Sonoelectroanalysis: Theory and Experiment

A thesis submitted for the
degree of Doctor of Philosophy
in the University of Oxford

By

Jonathan C. Ball

St John's College

Trinity Term 2000



Funded by the EPSRC and BP Chemicals Ltd

Abstract

This thesis reports the development of sonoelectrochemistry as a technique for sample analysis. Complementary modelling gives an insight into the mass transport and electrode reaction mechanisms. Separate studies were conducted as follows:

- Initially an copper(II) acetate buffer system was used as its speciation can be determined. In order to establish under which conditions analysis could be conducted the effect of speciation was examined. These were applied to the Anodic Stripping Voltammetry (ASV) determination of copper in the acetate solution and to facilitate the use of a traditionally inhospitable electrochemical medium: real ale with minimal pre-treatment. Both gave detection limits of the range (1-100) $\mu g\ L^{-1}$ and in quantitative agreement with Atomic Absorption Spectroscopy.
- The effect of acoustic streaming under mild insonation was studied by modelling Square Wave Voltammetry (SWV) of ASV and was found, when compared to experiment, to be the dominating factor. When the latter is strongly present two distinct mass transport regimes were identified. Studies of chemical and electrochemical processes suggested that the acoustic streaming model fails under more extreme conditions.
- SWV voltammetry was modelled for reversible electrochemical reactions leading to a refinement of existing analytical theory and the ASV modelling extended to account for surface morphology and finite electrode kinetics.

Droplets on an electrode surface subjected to a potential sweep give rise to voltammetric traces attributed to charge insertion. Three mechanisms for this are proposed: (i) charge injection at the droplets surface, (ii) charge injection at the three phase boundary and (iii) the droplet is saturated with counter ions and electron transfer occurs at the electrode surface. These are solved numerically and incorporate Regular Solution Theory to account for non-ideal interactions. Comparing with experimental data an approximate model identified the processes occurring for small droplets. A Marangoni-type convection is suggested for larger droplets.

Contents

CONTENTS i

ACKNOWLEDGEMENTS ix

GLOSSARY x

1. INTRODUCTION 1

1.1. GENERAL ELECTROCHEMISTRY 1

1.1.1. Origins 1

1.1.2. Redox Potentials and Thermodynamics 2

1.2. DYNAMIC ELECTROCHEMISTRY 5

1.2.1. Kinetics: Quasi-reversible and Irreversible Systems. Butler-Volmer Treatment 5

1.2.2. Kinetics: Mechanisms. Reinmuth and Testa notation. 8

1.2.2.1. CE Reaction (preceding reaction) 8

1.2.2.2. EC Reaction (Following Reaction) 9

1.2.2.3. Catalytic (EC') Reaction 10

1.2.2.4. ECE Reaction 10

1.2.3. Mass Transport 12

1.2.3.1. Diffusion 12

1.2.3.2. Convection 13

1.2.3.3. Migration 13

1.2.4. Linear Sweep Voltammetry (LSV) 15

1.2.5. Cyclic Voltammetry (CV) 17

1.2.6. Square Wave Voltammetry (SWV) 18

1.3. ANALYTICAL ELECTROCHEMISTRY 20

1.3.1. Stripping Voltammetry 20

1.3.1.1. Anodic Stripping Voltammetry (ASV) 21

1.3.1.2. Adsorptive Stripping Voltammetry (AdSV) 22

1.3.1.3. Cathodic Stripping Voltammetry (CSV) 23

1.4. ULTRASOUND AND SONOCHEMISTRY 24

1.4.1. Physical Effects of Ultrasound 25

1.4.2. Chemical Effects of Ultrasound 27

1.5. SONOELECTROCHEMISTRY 31

1.5.1. Historical Origins 31

1.5.2. Methods of Coupling 33

1.5.3. Mass Transport 34

1.5.3.1. Acoustic Streaming 35

1.5.3.2. Microjetting 36

1.5.3.3. Overall Picture 37

1.5.4. Surface Activation 38

1.5.5. Electroanalysis 39

1.5.6. Mechanistic and Synthetic Investigations 40

1.5.7. Frequency Effects 41

REFERENCES 43

2. EXPERIMENTAL METHODS 47

2.1. SONOELECTROCHEMISTRY 47

2.1.1. Calorimetric Calibration of Ultrasonic Horn Intensity 49

2.2. CHEMICALS USED 50

2.3. ELECTRONICS 50

2.4. ROTATING DISC ELECTRODE 50

2.5. ATOMIC FORCE MICROSCOPY 51

2.6. COMPUTATION 52

REFERENCES 53

3. THEORY 54

3.1. FINITE DIFFERENCE FORMULATION 54

3.1.1. Implicit vs. Explicit Formulations 56

3.2. BOUNDARY CONDITIONS 56

3.2.1. Dirichlet Boundary Conditions 57

3.2.2. Neumann Boundary Conditions 57

3.3. BACKWARDS IMPLICIT METHOD (BI) 57

3.3.1. Thomas Algorithm 58

3.4. CRANK-NICHOLSON (CN) METHOD 60

3.5. ALTERNATING DIRECTION IMPLICIT (ADI) 61

3.6. STRONGLY IMPLICIT PROCEDURE (SIP) 62

3.7. MULTIGRID TECHNIQUE (MGD1) 63

REFERENCES 66

4. COPPER ACETATE SOLUTIONS – SONO-ASV ON BARE GLASSY CARBON ELECTRODES AND THE SOLUTION KINETICS 67

4.1 INTRODUCTION 67

4.2 CHARACTERISATION OF THE SPECIATION OF COPPER (II) IN AQUEOUS ACETATE BUFFER 68

4.2.1 Formulation of Equations 68

4.2.2 Acetate Complexations and Dimerisations 70

4.2.3 Solution of Equations 71

4.2.4 World Wide Web (WWW) Solver 73

4.3 CALCULATION OF DIFFUSION COEFFICIENTS OF EACH SPECIES 76

4.4 Calculations of Insonated Diffusion Layer Thicknesses and Current Contribution per Species for Deposition 79

4.4.1 Outcome 82

4.5 Anodic Stripping Voltammetry (ASV) of Cu – Acetate Solutions. 82

4.6 Conclusions 84

References 85

5. THE ASV DETECTION OF COPPER IN BEER AT GLASSY CARBON ELECTRODES 86

5.1. Introduction 86

5.2. Experimental 89

5.3. Results and Discussion 91

5.3.1. Determination of Copper in Beer Using Mercury Thin Film Electrodes 91

5.3.2. Determination of Copper in Beer Using Solid Electrodes 93

5.3.3. Observations on the use of Solid Electrodes: Copper-lead Alloys 95

5.4. Conclusions 98

References 99

6. ANODIC STRIPPING VOLTAMMETRY: NUMERICAL THEORY FOR REVERSIBLE SYSTEMS AND EXPERIMENTAL VERIFICATION 101

6.1. Introduction 101

6.2. Theory 102

6.3. Results and Discussion 108

6.4. Experimental Verification 117

6.4.1. Experimental 117

6.4.2. Results and Discussion 120

6.5. CONCLUSIONS 125

REFERENCES 126

7. CAVITATION: SONOCHEMICAL AND SONOELECTROCHEMICAL EFFECTS. QUANTIFICATION AND SIMULATION OF INTERFACIAL CAVITATION 127

7.1. INTRODUCTION 127

7.2. THEORY 128

7.2.1. Cavitation Counter 128

7.2.2. Cavitation Simulator 130

7.2.2.1. Typical Output of the Simulator 133

7.3. EXPERIMENTAL 134

7.3.1. Reagents. 134

7.3.2. Instrumentation 135

7.4. RESULTS AND DISCUSSION 136

7.4.1. Detecting Cavitation Processes at the Macro-Electrode/Solution Interface 136

7.4.2. Effect of Cavitation Processes on Chemical Kinetics at the Electrode/Solution Interface 143

7.4.3. Correlation of Interfacial and Bulk Cavitation Processes. 147

7.5. CONCLUSIONS 149

REFERENCES 150

8. SIMULATION OF SQUARE WAVE VOLTAMMETRY: REVERSIBLE ELECTRODE PROCESSES 151

8.1. INTRODUCTION 151

8.2. THEORY 152

8.3. RESULTS AND DISCUSSION 158

8.4. CONCLUSIONS 165

REFERENCES 167

9. IONIC LIQUIDS: INVESTIGATION USING SIMULATION TECHNIQUES TO DETERMINE THE MECHANISM OF ELECTRON TRANSFER BY COMPARISON TO EXPERIMENT. 168

9.1. INTRODUCTION 168

9.2. THEORY 169

9.2.1. Regular Solution Theory 170

9.2.2. Mechanisms of Electron Transfer 172

9.2.2.1. Model 1: Droplet Surface Model. 172

9.2.2.2. Model 2: The Three Phase Boundary Model 175

9.2.2.3. Model 3: The Electrode Surface Model 178

9.2.3. Dual Reprocicity Method (DRM) 179

9.2.4. Dimensionless Variables 181

9.3. EXPERIMENTAL 182

9.4. RESULTS AND DISCUSSION 184

9.4.1. Theoretical 184

9.4.1.1. DRM Results 184

9.4.1.2. Failure of SIP and MGD1 187

9.4.1.3. Limitations of DRM 188

9.4.1.4. BI and Regular Solution Theory 189

9.4.2. Experimental 191

9.4.2.1. Electrochemically Induced Anion Insertion in Tetrahexylphenylenediamine 191

9.4.2.2. The Low Scan Rate Limit: Matching the Interaction Parameter Z 195

9.4.2.3. The Intermediate Scan Rate Regime: Transition from Thin Film to Diffusion Characteristics 197

9.4.2.4. The Fast Scan Rate Limit: Geometry Dependent Wave Shape Effects 201

9.5. CONCLUSIONS 202

REFERENCES 203

10. SQUARE WAVE ANODIC STRIPPING VOLTAMMETRY AT MERCURY PLATED ELECTRODES. SIMULATION OF SURFACE MORPHOLOGY EFFECTS 204

10.1. INTRODUCTION 204

10.2. THEORY 206

10.2.1. Uniform Thin Film 212

10.2.2. Computation 213

10.3. EXPERIMENTAL 214

10.3.1. Apparatus 214

10.3.2. Reagents 214

10.3.3. Experimental Procedure 214

10.4. EXPERIMENTAL RESULTS AND DISCUSSION 215

10.5. THEORETICAL RESULTS AND DISCUSSION 219

10.5.1. Validation 219

10.5.2. Quasi-reversible and Irreversible Response of Planar Electrodes 220

10.5.3. Hemispherical Electrodes 226

10.6. CONCLUSIONS 230

REFERENCES 231

A1 EFFLUENT DATA FROM BP CHEMICALS LTD, HULL SITE 232

A1.1. PH DATA 232

A1.2. COPPER DATA 233

A2 COMPUTER PROGRAM SOURCE CODE LISTINGS 234

A2.1. THE ONLINE BUFFER CALCULATOR (C/C++) 234

A2.2. REVERSIBLE ANODIC STRIPPING VOLTAMMETRY USING A SQUARE WAVE VOLTAMMETRIC SWEEP (FORTRAN 77) 239

A2.3. THE CAVITATION COUNTER (C/C++) 243

A2.4. THE CAVITATION SIMULATOR (C/C++) 245

A2.5. MODELLING OF SQUARE WAVE VOLTAMMETRY FOR REVERSIBLE SYSTEMS. 251

A2.6. OIL DROPLET (MODEL 1) WITH REGULAR SOLUTION THEORY (FORTRAN 77) 252

A2.7. MODELLING OF SQUARE VOLTAMMETRY ACCOUNTING FOR SURFACE MORPHOLOGY 254

A3 CHRONOAMPEROMETRY MODELLING AT UNIFORMLY ACCESSIBLE ELECTRODES WITH A FINITE DIFFUSION LAYER 255

A3.1. THEORY 255

A4 FICK'S LAWS 257

A4.1. FICK'S 1ST LAW OF DIFFUSION 257

A4.2. FICK'S 2ND LAW OF DIFFUSION 258

Acknowledgements

First and foremost I would like to thank my supervisor, Richard Compton, for giving me the opportunity to pursue my goal to complete a doctorate. He has not only been an inspirational person throughout the course of this work but has also been a friend outside the lab. My best regards go to Frank Marken who has helped me when I was stuck and found endless computer problems for me to fix, I wish him all the best at Loughborough. Also cheers to Barry Coles for C programming advice and web page problems (giving them to me).

My time here would have been less bearable without my colleagues in the lab. I will not mention you all by name but I will remember all of you fondly. Those of special mention are: Andy for those memorable library trips (especially to the ones with late opening hours); Jon Cooper for making it impossible for me to have a Tuesday without feeling ill; Richard Akkermans for taking me under his wing when I was new and showing me the delights of experimental electrochemistry; John Alden for introducing me to the acquired taste that is theoretical modeling; Shelley for interesting conversations (i.e. the ones not involving rowing or horses); Emma and Jo Aixill for setting me straight all too often; Cesar for his teletubby ways; the 'Theory Lab Boys' for making my final year fun and for watering the plants; Matthew Powell for aiding me this year with the huge monster known as the 'Compton Group Web Page'; Gavin for his constant verging on breakthroughs and Qiu for being undecipherable.

Outside the lab I would like to thank all my friends with whom I go *out to play*. Most notably of those are Jay and Nathan (and Mrs. Nathan); Karl and Ed; Willem for football and 007 conversations and many cigar tastings; Mick and his staff at St John's. Thanks also to Helen, you are a wonderful person and one of my best friends.

Finally a big thank to my family who have been nothing but supportive throughout my academic career. I love you.

Jon

Glossary

This is a summary of the terms used throughout this thesis.

Symbol	Meaning	Units
↻	mechanical stirring	
)))	application of ultrasound	
$[x]$	concentration of x	mol cm^{-3}
A, A_e	area of electrode	cm^2
A_1	rate constant	s^{-1}
Ac	Acetate (CH_3CO)	
ACS	American Chemical Standard	
ADI	Alternating Direction Implicit	
AdSV	Adsorptive Stripping Voltammetry	
AFM	Atomic Force Microscopy	
ASV	Anodic Stripping Voltammetry	
a_x	activity of x	mol cm^{-3}
BI	Backwards Implicit (method)	
Bu	butyl group (C_4H_9)	
c	concentration	mol cm^{-3}
c_x	concentration of x	mol cm^{-3}
C/C^{++}	programming language	
CN	Crank-Nicholson (method)	
C_p	specific heat capacity at constant pressure	J K^{-1} mol^{-1}
C_v	specific heat capacity at constant volume	J K^{-1} mol^{-1}
CPU	Central Processing Unit	
CSV	Cathodic Stripping Voltammetry	
CV	Cyclic Voltammetry	
D	diffusion coefficient	cm^2 s^{-1}
D_{ideal}	diffusion coefficient in an ideal solution	cm^2 s^{-1}
D_x	diffusion coefficient of x	cm^2 s^{-1}
DRM	Dual Reprocity Method	
E	electrode potential	V
E^0	standard potential	V
$E^{0'}$	formal potential	V
E_f	final voltage	V
E_i	initial voltage	V
E_p	peak potential	V
E_{p-p}	peak separation in voltage	V
E_{SW}	square wave voltage amplitude	V
$\tilde{E}$	dimensionless potential	
ΔE_s	square wave voltage step	V
F	the Faraday constant	C mol^{-1}
f	frequency	Hz
FORTRAN	programming language	
G	Gibb's free energy	J mol^{-1}
ΔG	Gibb's free energy change	J mol^{-1}
$\Delta G^{\ddagger}$	Gibb's free energy of activation	J mol^{-1}

ΔH	enthalpy change	J mol^{-1}
GCE	Glassy Carbon Electrode	
I	current	A
I_0	exchange current	A
I_{LIM}	limiting current	A
I^t	current at time $t\Delta t$	A
J	flux	mol cm^{-2} s^{-1}
K	reaction quotient	
k	rate constant	s^{-1}
k_0	standard rate constant	s^{-1}
k_b	backwards rate constant	s^{-1}
k_B	the Boltzmann constant	J K^{-1}
k_b^a	apparent backward rate constant	s^{-1}
K_D	dimerisation constant	
k_f	forward rate constant	
K_i	stability constant for i^{th} ligand addtion	
L	ligand	
l	mercury film thickness	cm
LSV	Linear Sweep Voltammetry	
M	molecular mass	g mol^{-1}
M	molarity	mol dm^{-3}
MGD1	Multigrid technique	
MTF	Mercury Thin Film	
n	number of electrons transferred	
NF	number of mercury film nodes	
NJ	number of solution nodes	
NK	number of solution nodes in 2^{nd} coordinate in 2 dimensional simulations	
NT	number of time nodes	
p	pressure	N m^{-2}
Ph	phenyl group	
pH	$-\log_{10}[H^+]$	
pK_a	acid constant ($-\log_{10}K_a$)	
R	Universal Gas constant	J K^{-1} mol^{-1}
r	radial coordinate in $r\theta\phi$ space	
R_{bubble}	radius of cavitational bubble	cm
Re	Reynolds number	
r_h	radius of hemisphere	cm
S	entropy	J K^{-1} mol^{-1}
ΔS	entropy change	J K^{-1} mol^{-1}
SCE	Saturated Calomel Electrode	
SET	Single Electron Transfer	
SIP	Strongly Implicit Procedure	
S_N1	unimolecular nuclear substitution reaction	
S_N2	bimolecular nuclear substitution reaction	
T	Absolute temperature	K
t	time	s
Δt	time interval	s
t_p	time of pulse in square wave voltammetry (½ a	s

	period)	
t_{sample}	time sample interval	s
THPD	tetrahexylphenyldiamine	
UHQ	Ultra High Quality	
v	velocity	cm s^{-1}
v_s	voltage scan rate	V s^{-1}
$\tilde{v}_s$	dimensionless scan rate	
w	no. of nearest neighbours	
WWW	World Wide Web	
x_x	mole fraction of x	
z	interaction parameter	J
Z	interaction constant defined as $\frac{zw}{k_B T}$	
α,β	Tafel coefficients of electron transfer	
β_i	stability constant for gross addition of i ligands	
δ	diffusion layer thickness	cm
ϕ	Potential	V
ϕ	coordinate in $r\theta\phi$ space	
φ	radial transformed space	
Γ_i	boundaries used in DRM	
γ	activity coefficients	
η	overpotential	V
ν	kinematic viscosity	cm^2 s^{-1}
θ	coordinate in $r\theta\phi$ space	
τ	Cottrellian time coordinate transfomation	
ω	rotation rate	rad s^{-1}
ξ	dimensionless space	
ψ	radial transformed space, tanh expanding grid	

1. Introduction

This chapter presents the concepts fundamental to the understanding of much of the experimental work presented in this thesis and also the electrochemical background to the simulations, the general theory of which will be explored in a later chapter.

1.1. General Electrochemistry

Electrochemistry is the study of reactions involving the transfer of an electron across a solution-electrode interface. The electrode in the majority of situations is solid with the obvious exception of mercury electrodes. More recently, other liquid electrodes have also become viable.[1,2]

1.1.1. Origins

The birth of electrochemistry was at the turn of the nineteenth century with the invention of Volta's 'pile'. Chemical species were consumed during the production of electricity and it was the crude precursor to modern day batteries.[3] Over the 19th century electrochemistry developed and evolved into many essential applications for the world today. Following the discovery of the electrolysis of water it was then shown by Grove that hydrogen and oxygen can be combined to form water with the production of electricity. This is the basis of the fuel cell technology being pursued by many industrial companies for greener fuel technology. Later, Planté devised the forerunner of the secondary battery or reversible battery which is now employed in all automobiles today to power the starter motor. Electrochemistry in the protection of metal corrosion was proposed by Davy and led to the electrolysis of molten electrolytes and the subsequent production of aluminium metal. The use of

electrochemistry in synthetic processes still provides novel products inaccessible by other methods.

1.1.2. Redox* Potentials and Thermodynamics

Consider the half-cell reaction:

$$Fe^{3+}(aq) + e^{-} \rightleftharpoons Fe^{2+}(aq) \qquad (1.1.)$$

where Fe(III) can be converted to Fe(II) by adding an electron and vice versa by the removal of an electron. To achieve this equilibrium a solution of Fe(II) and Fe(III) is needed which is supported by a counter ion X^- such that the solution remains electroneutral. If a wire is added to this solution, the wire can act as a sink of electrons; that is it could lose electrons to allow Fe(III) to be reduced to Fe(II) or alternatively accept electrons to oxidise Fe(II) to Fe(III). The equilibrium described in equation (1.1.) is quickly achieved at the wire surface. After equilibrium is attained there is going to be an electrical charge associated with both the phases. The charge of the phases is dictated by which side the equilibrium favours. If the equilibrium favours the right hand side the wire will be positive and conversely if the left hand side is favoured then the wire will be negative. This gives rise to a potential difference between the solution and wire and is dependent upon the concentrations of the Fe(II) and Fe(III) ions such that

$$\phi_M - \phi_{solution} = \text{constant} - \frac{RT}{F}\ln\left\{\frac{[Fe^{2+}]}{[Fe^{3+}]}\right\} \qquad (1.2.)$$

where ϕ_M is the potential of the metal and $\phi_{solution}$ is the potential of the solution. R is the universal gas constant, T the absolute temperature and F the Faraday constant. Equation (1.2.) is the famous Nernst equation for a single electrode-solution interface.

---

* Redox potential stands for Reduction Oxidation potential.

As there is no way of measuring this potential difference we need to create a reference electrode, set to an arbitrary value of 0.00V, allowing the measurement of the potential difference between the system being studied and the reference. The electrode conventionally used for this purpose is the hydrogen electrode. It consists of a platinum black electrode immersed in a solution of aqueous HCl and hydrogen gas bubbled over the surface. All half cell reactions in the literature have redox potentials quoted against this electrode. The redox potentials can also give a useful insight into the thermodynamics of the system. If all the cell components are at unit activity then the free energy change, ΔG^0, for the half cell reaction similar to equation (1.1.) is given by

$$\Delta G^0 = -nFE^0 \qquad (1.3.)$$

where n is the no. electrons transferred. From the measurement of cell potentials the free energy of a system can be determined and also since

$$dG = Vdp - SdT \qquad (1.4.)$$

and it can be concluded that

$$\left(\frac{\partial G}{\partial T}\right)_p = -S \qquad (1.5.)$$

and

$$\left(\frac{\partial \Delta G}{\partial T}\right)_p = -\Delta S \qquad (1.6.)$$

so that

$$nF\left(\frac{\partial E}{\partial T}\right)_p = \Delta S \qquad \text{and} \qquad nF\left(\frac{\partial E^0}{\partial T}\right)_p = \Delta S^0 \qquad (1.7.)$$

If the above are combined into the following relationship for enthalpy change

$$\Delta H^0 = \Delta G^0 + T\Delta S^0 \qquad (1.8.)$$

which then gives

$$\Delta H^0 = -nFE^0 + TnF\left(\frac{\partial E^0}{\partial T}\right)_p \qquad (1.9.)$$

thus from the redox potential, E^0, detailed information can be obtained about the enthalpy of the system. Finally in this section we will deal with a system in equilibrium and how its potential is affected by the concentration and derive the familiar Nernst equation for an electrode reaction. Consider the following reaction

$$\nu_O O + ne^- \rightleftharpoons \nu_R R \qquad (1.10.)$$

which is an instantly established equilibrium. The free energy is given from basic thermodynamics[4]

$$\Delta G = \Delta G^0 + RT \ln K \qquad (1.11.)$$

where K is the reaction quotient for the reaction in equation (1.10.). Using equation (1.3.) equation (1.11.) becomes

$$E = E^0 + \frac{RT}{nF} \ln \frac{a_R^{\nu_R}}{a_O^{\nu_O}} \qquad (1.12.)$$

where a_R and a_O represent the activity of R and O respectively. If concentrations are used we must introduce $E^{0'}$ the formal potential and the familiar Nernst equation becomes

$$\frac{[R]^{\nu_R}}{[O]^{\nu_O}} = \exp\left(-\frac{nF}{RT}\left(E - E^{0'}\right)\right) \qquad (1.13.)$$

The next section will go onto to deal with systems not in equilibrium and introduce the concepts of dynamic electrochemistry.

1.2. Dynamic Electrochemistry

In contrast to the previous section, this form of electrochemistry involves systems not in chemical equilibrium but involves the flow of an electric current.

1.2.1. Kinetics: Quasi-reversible and Irreversible Systems. Butler-Volmer Treatment

This section will focus solely on the electron transfer process and as a result will assume the solution is well stirred and the transport of the solution to the electrode is fast. It will also assume there is excess background electrolyte to prevent any double layer and migration effects. Considering the electron transfer reaction

$$O + e^- \rightleftharpoons R \tag{1.14.}$$

Assuming both forward and backward reactions are first order then the overall rate for R is given by

$$-\frac{d[O]}{dt} = \frac{d[R]}{dt} = k_f[O] - k_b[R] \tag{1.15.}$$

where k_f is the rate constant for the forwards reaction and k_b is the rate constant for the backwards reaction. The current is due to the net flux of O and directly proportional to it

$$I = FA\left(k_f[O] - k_b[R]\right) \tag{1.16.}$$

The temperature dependence of the rate constants are given by simple Arrhenius-type expressions.

$$k_f = Z \exp\left(\frac{-\Delta G_f^{\ddagger}}{RT}\right) \tag{1.17.}$$

and

$$k_b = Z \exp\left(\frac{-\Delta G_b^{\ddagger}}{RT}\right) \tag{1.18.}$$

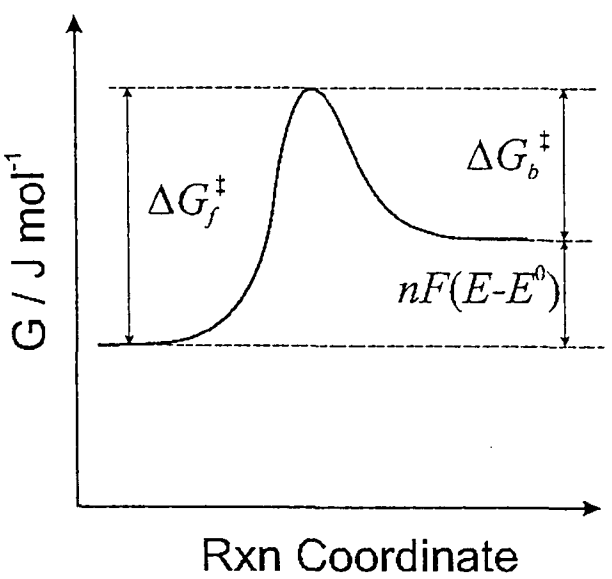


Figure 1.1 Free Energy *vs.* reaction coordinate diagram for an electron transfer process. E is the electrode potential.

where the $\Delta G_b^{\ddagger}$ and $\Delta G_f^{\ddagger}$ are the free energies of activation shown in Figure 1.1. The pre-exponential factors will be assumed to be equal due to the principle of microscopic reversibility. They have the units m s^{-1}. Considering the special case of equilibrium at the electrode surface where the net flux will be zero and consequently the current will also be zero. The surface and bulk concentrations will also be equal. Substituting equations (1.17.) and (1.18.) into (1.16.) gives

$$\ln\frac{[O]}{[R]} = \ln\frac{k_{b,0}}{k_{f,0}} = \frac{\Delta G_f^{\ddagger} - \Delta G_b^{\ddagger}}{RT} \tag{1.19.}$$

where $k_{b,0}$ and $k_{f,0}$ are the rate constants at zero current. The ratio of O and R concentrations is given by the Nernst equation in (1.13.) which combined gives

$$\Delta G_f^{\ddagger} - \Delta G_b^{\ddagger} = nF\left(E - E^{0'}\right) \tag{1.20.}$$

This is also shown graphically in Figure 1.1. This suggests that by varying the potential we can change the free energies of the species O and R at the electrode surface and consequently the activation energies must also depend on the potential. The next step assumes a simple linear relationship such that

$$\Delta G_f^{\ddagger} = \Delta G_0^{\ddagger} + \alpha nF\left(E - E^{0'}\right) \tag{1.21.}$$

and

$$\Delta G_b^{\ddagger} = \Delta G_0^{\ddagger} - \beta nF\left(E - E^{0'}\right) \tag{1.22.}$$

where α and $\beta = (1-\alpha)$ are the cathodic and anodic *transfer coefficients*, and $\Delta G_0^{\ddagger}$ is the activation energy of the process when $E = E^{0'}$. Assuming $\Delta G_0^{\ddagger}$ is constant at constant temperature then (1.17.) and (1.18.) become

$$k_{f,0} = k_0 \exp\left(\frac{-\alpha nF\left(E - E^{0'}\right)}{RT}\right) \tag{1.23.}$$

and

$$k_{b,0} = k_0 \exp\left(\frac{\beta nF\left(E - E^{0'}\right)}{RT}\right) \tag{1.24.}$$

where

$$k_0 = Z \exp\left(\frac{-\Delta G_0^{\ddagger}}{RT}\right) \tag{1.25.}$$

If a net current is flowing through the cell then the system is not at equilibrium. The deviation of the half-cell potential from the equilibrium value is called the overpotential η. The rate constants can now be redefined

$$k_f = k_{f,0} \exp\left(\frac{-\alpha nF\eta}{RT}\right) \tag{1.26.}$$

and

$$k_b = k_{b,0} \exp\left(\frac{\beta F\eta}{RT}\right) \tag{1.27.}$$

If the current I_0 termed the *exchange current*, is introduced as the current equal to the cathodic current at equilibrium then equation (1.16.) becomes

$$I = I_0\left[\exp\left(\frac{-\alpha nF\eta}{RT}\right) - \exp\left(\frac{\beta nF\eta}{RT}\right)\right] \tag{1.28.}$$

which is called the *Butler-Volmer* equation named after the two electrochemists who contributed to its formation[5] and experimental test[6] respectively.

1.2.2. Kinetics: Mechanisms. Reinmuth and Testa notation.

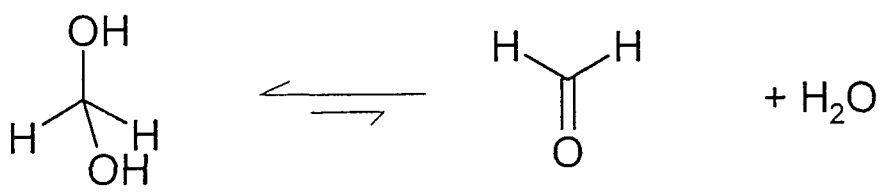
Previously, we dealt with reactions concerning solely heterogeneous electron transfer. In this section we will consider the cases when the electron transfer is coupled with a homogeneous chemical step. It convenient to classify the reaction schemes by using letters in the order that the steps occur. **E** is used to represent the heterogeneous electron transfer step and **C** to represent the homogeneous chemical step.[7] For example an electron transfer followed by a chemical reaction of the product would be term a **EC** reaction. The following are a selection of commonly encountered and interesting mechanisms.

1.2.2.1. CE Reaction (preceding reaction)

$$Y \rightleftharpoons O \qquad (1.29.)$$

$$O + ne^- \rightleftharpoons R \qquad (1.30.)$$

In this case the electroactive species is generated by a chemical reaction that precedes the electrode reaction. An example of the CE mechanism is the reduction of formaldehyde at a mercury electrode in aqueous solution.[8] In solution formaldehyde exists mainly in the non-reducible hydrated form $H_2C(OH)_2$ but in equilibrium with the reducible H_2CO form thus:



(1.31.)

Under some conditions the current will be controlled by the kinetics of the equilibrium giving rise to what is termed a *kinetic current*. Other examples are the reduction of weak acids such as acetic acid and metal complexes.

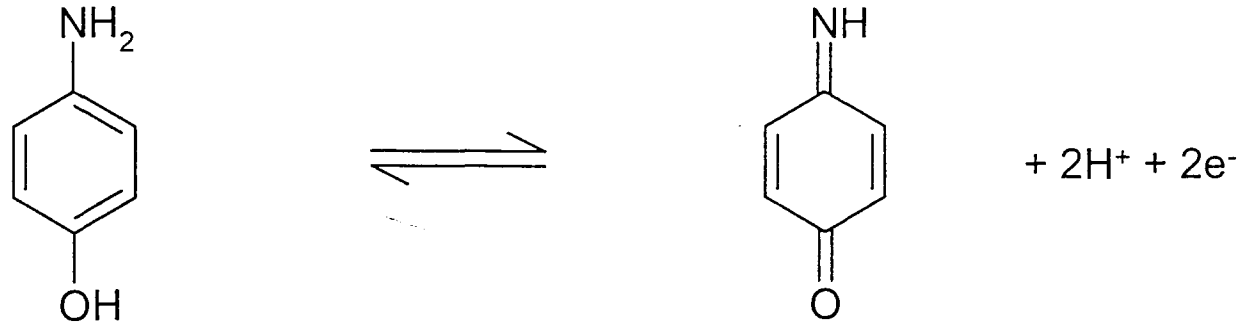
1.2.2.2. EC Reaction (Following Reaction)

In this case the chemical reaction follows the electron transfer reaction - the product of the electron transfer goes on to react further.

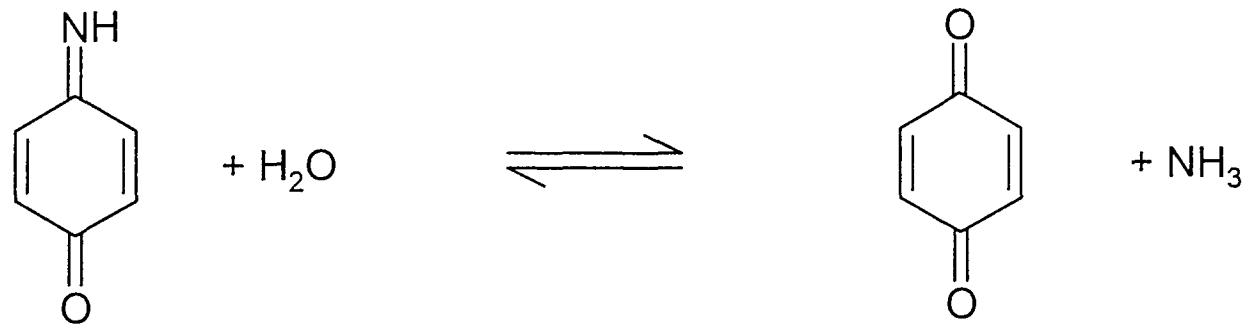
$$O + ne^- \rightleftharpoons R \qquad (1.32.)$$

$$R \rightleftharpoons X \qquad (1.33.)$$

The species X is not electroactive and does not interfere with the electrode reaction in (1.32.). An example of this is the oxidation of *p*-aminophenol at a platinum electrode in acidic media.[8]



(1.34.)



(1.35.)

The *p*-aminophenol is oxidised to the quinone imine and this undergoes a hydrolysis reaction to form benzoquinone which is neither oxidised or reduced at the potential required for the first electron transfer. This mechanism is very common as the electrochemical oxidation or reduction will often produce a very reactive species. A common example of this is the one electron reductions of suitable organic compounds in aprotic solvents such as DMF (*N,N*-dimethylformamide) or acetonitrile.[8] This produces radicals and/or radical ions may dimerise. This is designated an EC_2 reaction as the dimerisation step is second order.

1.2.2.3. Catalytic (EC') Reaction

In this specific type of *EC* reaction the product of the electron transfer reacts with an electroneutral species in the solution to give a product and regenerate the starting material.

$$O + ne^- \rightleftharpoons R \qquad (1.36.)$$

$$R + Z \rightarrow O + Y \qquad (1.37.)$$

A recent example of this type of reaction is the electrolytic generation of Pb(IV) from Pb(II) for the cleavage of 1,2-diols.[9]

$$Pb^{II} \rightleftharpoons Pb^{IV} + 2e^- \qquad (1.38.)$$

$$Pb^{IV} + diol \rightarrow Pb^{II} + products \qquad (1.39.)$$

1.2.2.4. ECE Reaction

In this mechanism the electron transfer reaction product is chemically active which reacts to form another electroactive species and this undergoes another electron transfer thus

$$O_1 + n_1e^- \rightleftharpoons R_1 \qquad (1.40.)$$

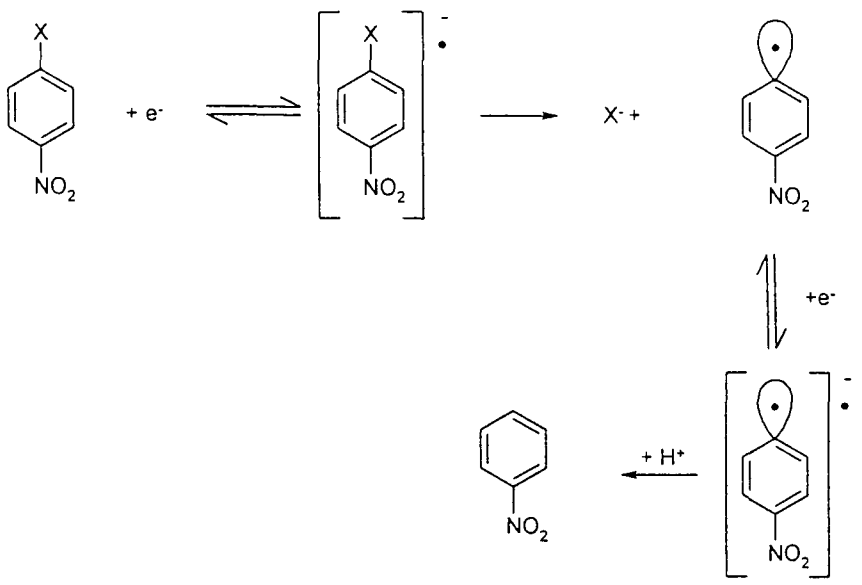
$$R_1 \xrightarrow{(+Z)} O_2 \qquad (1.41.)$$

$$O_2 + n_2e^- \rightleftharpoons R_2 \qquad (1.42.)$$

A good example of this reaction scheme is the reduction of a halonitroaromatic in an aprotic media. The reaction proceeds in the manner shown in Scheme 1.1. The assignment of the ECE mechanism is not as easy as it appears from the mechanism as the second E step occurs at a much higher potential and the species R_1 is capable of reducing O_2 whilst diffusing away in solution and thus another reaction can occur.[10]

$$XC_6H_4NO_2^{\bullet -} + {}^{\bullet}C_6H_4NO_2 \rightleftharpoons XC_6H_4NO_2 + {}^{-}C_6H_4NO_2 \qquad (1.43.)$$

This is sometimes referred to as the *DISP* mechanism. The *ECE* mechanism occurs when the electron transfer occurs at the electrode surface. A second variable of this type of reaction is the *ECE'* where the second electron transfer occurs at a more negative potential. In this case the first reaction behaves as an *EC* reaction but if the potential is taken to a more negative point we will find a second reduction wave and this will be characteristic of the *ECE'* reaction.



Scheme 1.1 The reaction mechanism for the reduction of a halonitroaromatic compound following an ECE mechanism.

Above are simple schemes but many others may also be built up. *EC* reactions can be further divided to distinguish between reversible (r), quasi-reversible (q) or irreversible (i) steps: e.g. E_rC_r, E_rC_i, E_qC_r etc. A complex example is the reduction of nitrobenzene to phenylhydroxylamine in liquid ammonia in the presence of a proton donor (ROH) which has been analysed in terms of an *EECCEEC* process.[11]

$$PhNO_2 + e^- \rightleftharpoons PhNO_2^{\bullet -} \qquad (1.44.)$$

$$PhNO_2^{\bullet -} + e^- \rightleftharpoons PhNO_2^{2-} \qquad (1.45.)$$

$$PhNO_2^{2-} + ROH \rightleftharpoons PhNOOH^- + RO^- \qquad (1.46.)$$

$$PhNOOH^- \rightarrow PhNO + OH^- \qquad (1.47.)$$

$$PhNO + e^- \rightleftharpoons PhNO^{\bullet -} \qquad (1.48.)$$

$$PhNO^{\bullet -} + e^- \rightleftharpoons PhNO^{2-} \qquad (1.49.)$$

$$PhNO^{2-} + 2ROH \rightarrow PhNHOH + 2RO^- \qquad (1.50.)$$

1.2.3. Mass Transport

In order for electrolysis to proceed reactant molecules must be transported from the bulk solution to the electrode surface. Thus various physical processes may contribute to the overall kinetics of any particular reaction. Therefore it is important to understand mass transport effects and their quantitative description is essential for the successful interpretation of experimental observations. There are three modes of mass transport of an electroactive species to and from an electrode; diffusion, convection and migration.

1.2.3.1. Diffusion

Macroscopically, diffusion is the movement of species under the influence of a concentration gradient which acts to maximise entropy by smoothing out inhomogeneities in composition. In microscopic terms, it is the statistical response of a system to an imbalance in the number of molecules in different regions of the system. A 'random walk' model[12] can be used to explain the movement of the molecules and a quantitative description is provided by Fick's Laws[13].

Fick's First Law describes the diffusive flux of material under the influence of a concentration gradient:

$$J_d(x,t) = -D\frac{\partial}{\partial x}[c(x,t)] \qquad (1.51.)$$

where D is the diffusion coefficient in $cm^2\ s^{-1}$, $c(x,t)$ is the concentration of the electroactive species in mol cm^{-3} and $J_d(x,t)$ is the diffusional flux in mol $cm^{-2}\ s^{-1}$ to the electrode in the x direction which is normal to the electrode surface.

Fick's Second Law describes rates of change of concentration:

$$\frac{\partial}{\partial t}c(x,t) = D\frac{\partial^2}{\partial x^2}[c(x,t)] \qquad (1.52.)$$

and is readily derived from the First Law (see Appendix A4).

1.2.3.2. Convection

Movement due to convection occurs when a mechanical force acts on or within a solution. Two types of convection may be usefully distinguished, natural convection and forced convection. Natural convection may be present in any solution and arises from thermal gradients and/or density differences within the solution. This type of convection is difficult to predict and is therefore undesirable. Forced convection arises from external forces such as pumping, stirring or hydrodynamic flow. This may be arranged to provide well defined hydrodynamic behaviour which allows the pattern of mass transport to the electrode to be rigorously predicted. In some electrochemical experiments forced convection may be introduced to swamp effects due to natural convection,[14] allowing more reliable and reproducible data. Alternatively current measurements may be taken rapidly before the onset of natural convection, as in cyclic voltammetry.

Quantitatively, the one-dimensional (x) convective flux is given by :

$$J_c(x,t) = c(x,t)v(x) \qquad (1.53.)$$

where $J_c(x, t)$ is the convective flux and $v(x)$ is the velocity of the solution in the x direction. The convective analogue of Fick's Second Law is therefore:

$$\frac{\partial c}{\partial t} = -\left[v_x \frac{\partial c}{\partial x} \right] \qquad (1.54.)$$

1.2.3.3. Migration

Migration is the movement of charged species due to electrical potential gradients[15] and it is by this mechanism that charge passes through the bulk electrolyte. The migratory flux due to a potential gradient $\partial\varphi/\partial x$ is given by:

$$J_m(x,t) = -\frac{zF}{RT} Dc(x,t) \frac{\partial \varphi}{\partial x} \qquad (1.55.)$$

where J_m is the flux due to migration in the x direction, z is the charge on the ion.

In a voltammetric experiment the combination of migration and electrolysis produces complex mass transport effects which are difficult to interpret. These effects are rendered negligible by use of an excess of electrolytically inert ions, known as the background electrolyte. Excess can then be defined in the context that in order to reduce the migration flux to one percent of the diffusive flux, a 33-fold excess of background electrolyte is required.[16] This results in the nullification of the $\partial\varphi/\partial x$ term in the equation, hence simplifying the mathematical treatment of electrochemical systems as only diffusion and convection need be considered. The addition of background electrolyte provides further advantages:

(i) It increases the solution's conductivity, thereby making the bulk solution less resistive to the flow of current. If this were not so then the response of the cell might be limited by the flow of current through the bulk solution and not by the phenomena of interest occurring at the electrode / solution interface.

(ii) It reduces the size of the double layer across which the interfacial potential drop occurs to approximately 10-20 Å. This permits electron transfer between electrode and electroactive species via quantum mechanical tunnelling.

(iii) The ionic strength of the solution remains the same throughout the experiment and this means that the activity coefficients of the reactants remain constant throughout the electrolysis.

In the following, concentrations are reported under fixed salt concentrations. Standard electrode potentials are thereby replaced by 'formal' electrode potentials. The formal

potential of a cell reaction, $E^{0'}$, is related to the standard potential, E^0 by the following equation:[17]

$$E^{0'} = E^0 + \frac{RT}{nF} \ln \frac{\Pi \gamma_{O_i}^{\nu_i}}{\Pi \gamma_{R_i}^{\nu_i}} \qquad (1.56.)$$

where $\gamma_{O_i}^{\nu_i}$ and $\gamma_{R_i}^{\nu_i}$ are the activity coefficients of the i^{th} oxidised and reduced species respectively in relation to molarity (mol dm^{-3}) and ν_i is the stoichiometry of the i^{th} species as it appears in the reaction.

1.2.4. Linear Sweep Voltammetry (LSV)

Linear sweep voltammetry is carried out in quiescent solution so that the only transport is diffusion to or from the electrode surface as predicted by equations (1.53.) and (1.54.). The potential of the working electrode is swept from an initial voltage, E_i, to an end voltage, E_f. This sweep is carried out at a rate ν_s which can be varied and the potential of the electrode at any time, t, is given by

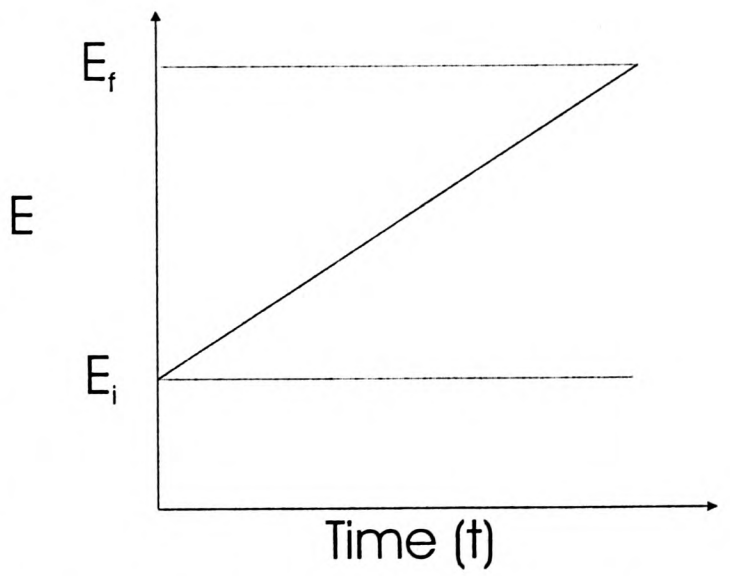


Figure 1.2 The potential sweep employed in LSV.

$$E(t) = E_i + \nu_s t \qquad (1.57.)$$

The waveform of the sweep is shown in Figure 1.2. Resulting voltammograms, plots of current against voltage, for both a reversible and irreversible electrode process are shown in Figure 1.3. The behaviour of the current voltage curve can be understood in the following manner. Initially no current flows since the applied potential is not sufficient to induce an electron transfer. As the potential is swept negative, to more reducing potentials, the reduction becomes more favourable and current begins to

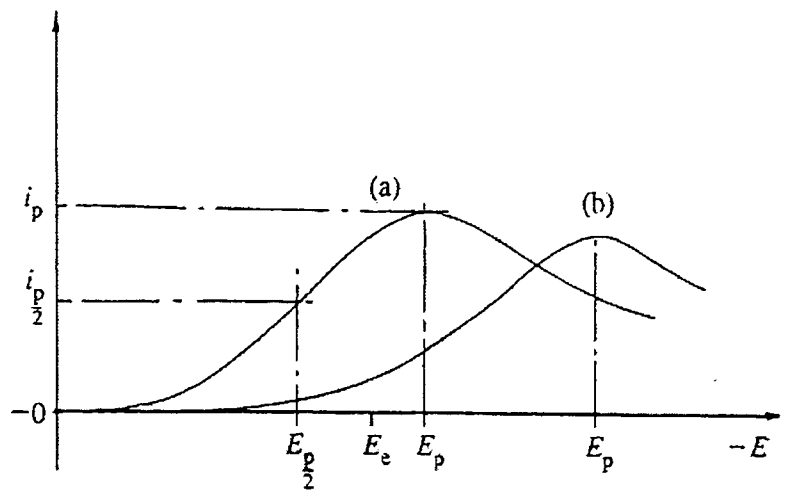


Figure 1.3 Linear sweep voltammogram for (a) a reversible elctron transfer and (b) an irreversible electrode reaction.

flow. The potential is swept more negative and the current will reach a maximum, known as the peak current i_p and then start to fall off. The current does not only reflect the rate of electron transfer, k_f, but also the surface concentration, c_0 of the oxidised species. Even though at more negative potentials the value of k_f increases the electrolysis of O decreases the surface concentration which is only partially replenished by diffusion from the bulk solution. The current is subsequently controlled by the rate at which O can diffuse to the electrode. The region of depletion near the electrode is defined as the diffusion layer. The current response is a balance of electrode kinetics and mass transport to the electrode.

The peak current for a reversible system is given by

$$\left|i_p\right| = 0.318nAFD^{\frac{1}{2}}v_s^{\frac{1}{2}}[\ ]_\infty\left(\frac{F}{RT}\right)^{\frac{1}{2}} \qquad (1.58.)$$

where A is the electrode area in cm^2 and $[\ ]_\infty$ is the bulk solution concentration in mol cm^{-3}. For the case of the irreversible reaction

$$\left|i_p\right| = 2.99\times10^5 n\alpha^{\frac{1}{2}}AD^{\frac{1}{2}}v_s^{\frac{1}{2}}[\ ]_\infty \qquad (1.59.)$$

where α is the transfer coefficient.

The diffusion layer is considered as the distance from the electrode where the concentration of the solution deviates from that of the bulk solution. If the scan rate is increased there is less time for the electrolysis and the depletion of O near the electrode and hence the diffusion layer is thinner. This gives rise to a larger

concentration gradient and hence increased flux as shown in (1.51.). This in turn gives rise to a greater current and peak current. Thus in (1.58.) and (1.59.) the value of i_p is related to the scan rate.

1.2.5. Cyclic Voltammetry (CV)

Cyclic voltammetry is an extension to LSV but in this case a triangular waveform is applied (see Figure 1.4). As with LSV the current is again recorded against the applied potential and scan rates of 10-1000mV s^{-1} are typically used. Although with microelectrodes rates of up 10^6 V s^{-1} have been achieved.[18] Considering the one electron reduction

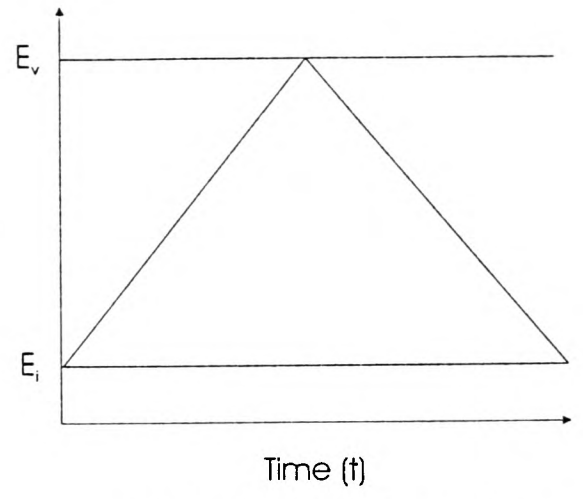


Figure 1.4 Variation of the potential applied.

$$O + e^- \rightleftharpoons R \qquad (1.60.)$$

The first part of the scan will follow the same pattern as that of the LSV voltammogram with the interplay of electrode kinetics and diffusion properties of the electroactive species *O*. When the direction of the potential sweep is reversed the cathodic current will decay to zero and the anodic current will increase due to the reoxidation of the reduction product *R*. The shape of the CV will depend mainly on the reversibility of the redox couple being studied and will also be

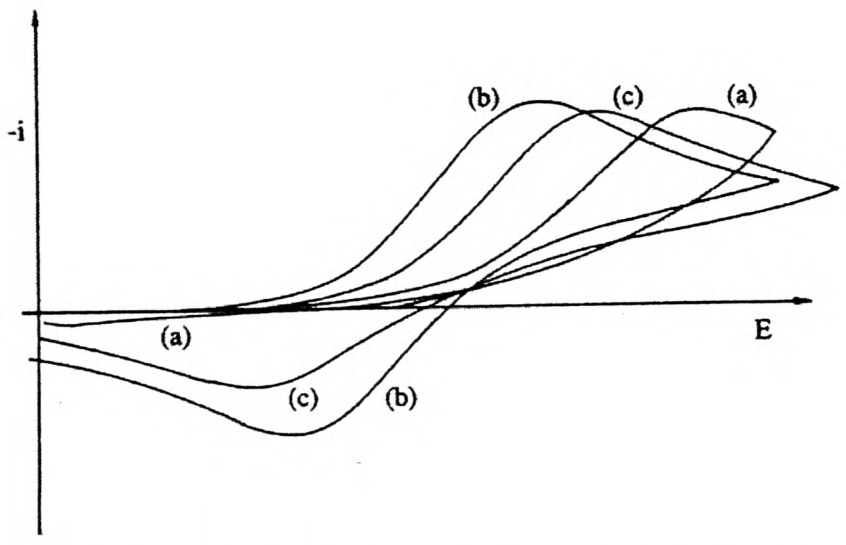


Figure 1.5 Cyclic voltammograms for (a) irreversible, (b) reversible and (c) quasi reversible electron transfer reactions.

modified due to homogeneous kinetics similar to those discussed in § 1.2.2. Figure 1.5 shows voltammograms for the three different types of electron transfer. The oxidative current flows at potentials positive of E^0 for both the reversible case and the quasi-reversible case. In the reversible case the peak separation, $E_{p\text{-}p}$, is independent of scan rate and has a value of

$$E_{p-p} = 2.218\frac{RT}{F} \tag{1.61.}$$

In the quasi and irreversible case the peak separation will be a function of the scan rate. The magnitude of the peak current will follow that of LSV and be scan rate dependent. Also the relative size of the reverse peak will be scan rate dependent for both the irreversible and quasi-reversible cases.

1.2.6. Square Wave Voltammetry (SWV)

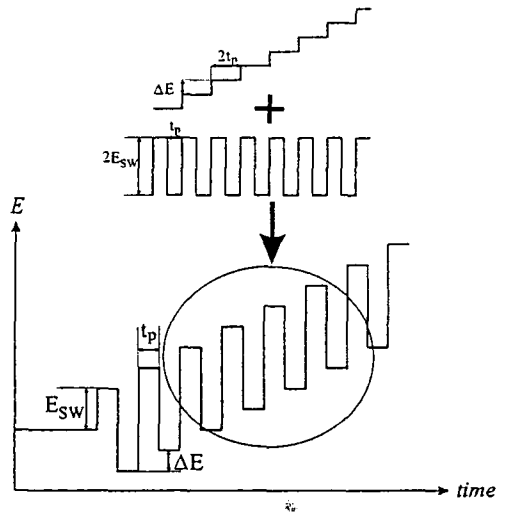


Figure 1.6 The SWV waveform.

This technique was developed by Barker *et al.* in the 1950s.[19] It involves the superimposition of a square wave pulse upon a slowly varying stepwise ramp. The current is measured at the end of each half cycle termed $I(1)$ and $I(2)$. The two currents measured are then combined to give the difference current, ΔI as detailed below

$$\Delta I = I(1) - I(2) \tag{1.62.}$$

which is the current observed on a SWV voltammogram and the potential of the average of the potentials of the pulses (see Figure 1.6). The potential at the end a half pulse m is given by

$$E_m = E_i - \left[\frac{m+1}{2}\right]\Delta E_S - E_{SW}\left(1+(-1)^{m+1}\right) \tag{1.63.}$$

The combination of currents and the sampling of currents is carried out to simplify the voltammogram. Figure 1.7 shows the normalised current time response, for a reversible system only, to the waveform as predicted by the analytical equation[20]

$$\psi_j = \frac{nFA\sqrt{D}[\ ]_\infty}{\sqrt{\pi t_p}} \sum_{m=1}^{j} \frac{Q_{m-1} - Q_m}{\sqrt{j-m+1}} \tag{1.64.}$$

where

$$Q_m = \frac{\varepsilon_m}{1+\varepsilon_m} \tag{1.65.}$$

and

$$\varepsilon_m = \exp\left[\frac{nF\left(E_m - E^0\right)}{RT}\right] \tag{1.66.}$$

and the dimensionless current ψ_j is defined as

$$\psi_j = i_j \frac{\sqrt{\pi t_p}}{nFA\sqrt{D}[\ ]_\infty} \tag{1.67.}$$

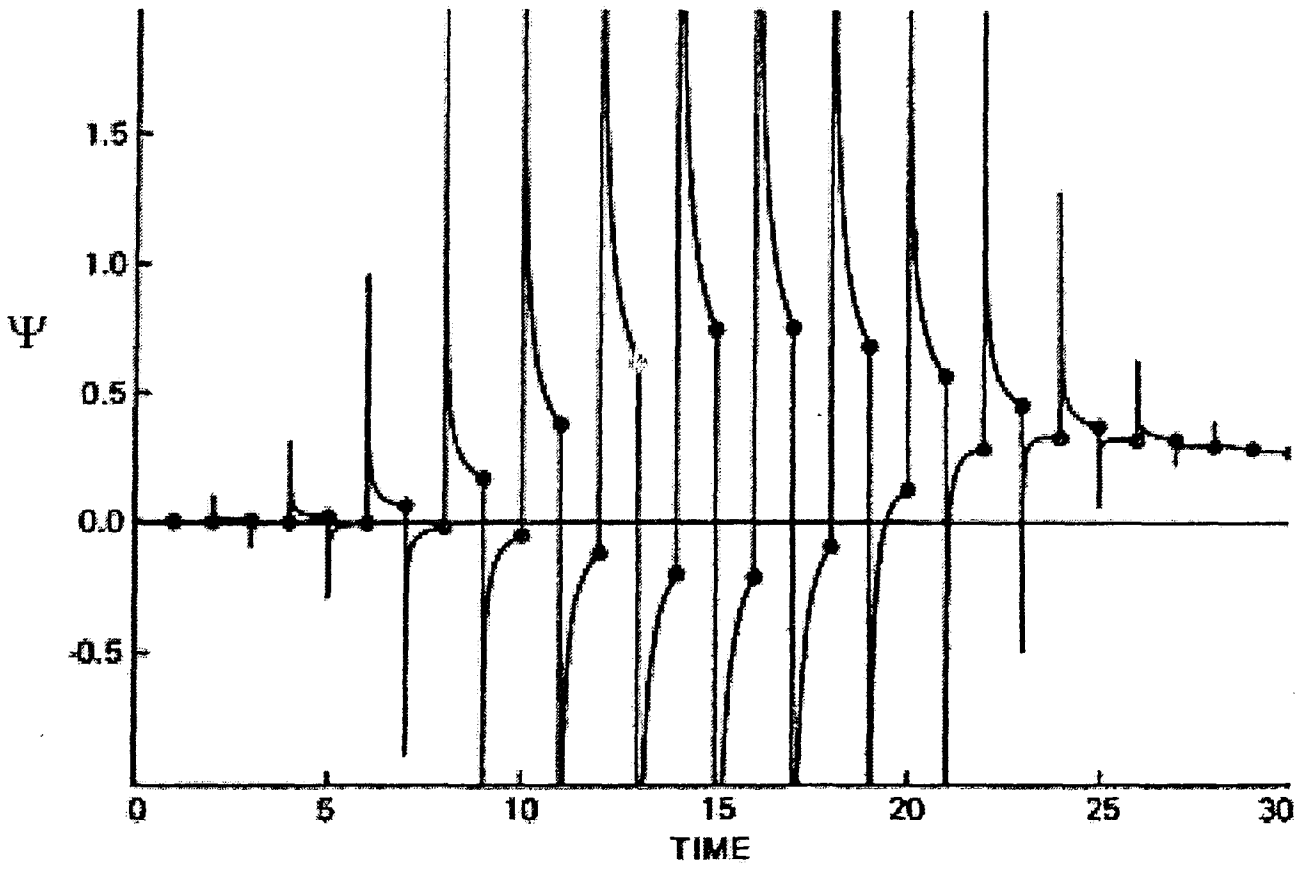


Figure 1.7 Normalised current response (Equ. (1.67.)) to the waveform in Figure 1.6. Time is dimensionless units of $j = \frac{(t - t_i)}{t_p}$ and the circled points are the currents at integer values of j given by equations (1.67.) and (1.64.). nE_{SW} = 50mV and $n\Delta E_s$ = 30mV

The points that are circled not only occur at the integer values of *j* they are also the points at which the current is sampled. The voltammogram is also symmetrical about the half wave potential which is exceptionally convenient for the quick inspection of the voltammograms. The main advantage of SWV is that because the current is sampled a short time after the effective potential step the current value is high and this makes the response much more sensitive than simple analogue sweep methods. As the frequency of the Square Wave pulse can be changed quite simply up to 2kHz, fast reactions can be probed for kinetic parameters.[21-23] This enhanced sensitivity is also employed in analytical techniques (covered in § 1.3) in order the enhance the detection limit and extend the range.

1.3. Analytical Electrochemistry

Electrochemistry can be used as a useful tool in the solution of real-life analytical problems. This next section will focus on some of the stripping techniques used, their advantages over more traditional methods and some examples of their usage.

1.3.1. Stripping Voltammetry

Stripping Voltammetry (SV) techniques all involve the same principles. The analyte is pre-concentrated at the electrode by a mechanism that is most suitable. There are many ways in which this may occur. One can reduce it onto the electrode in its metal or amalgam form as in Anodic Stripping Voltammetry(ASV). It can be adsorbed to the surface at a suitable potential as in Adsorptive Stripping Voltammetry (AdSV) or it can be oxidised to it corresponding oxide on the electrode surface as in Cathodic Stripping Voltammetry (CSV). The collected analyte is then stripped from the surface electrochemically by subjecting the electrode to potential sweep and the current voltage curves show peaks characteristic of the nature of the analyte and the

concentration. Selectivity for some ions can be achieved by modifying the electrode surface or substrate. The advantage of most electroanalytical techniques over more traditional methods is that the results are outputted in both currents and voltages and this allows the experiment to be completely computer controlled and the techniques automated. This subsequently provides the opportunity for on-line continuous monitoring. The techniques are also enhanced in sensitivity, are cheaper to produce, simple to operate and can be miniaturised to allow portability.

1.3.1.1. Anodic Stripping Voltammetry (ASV)

Anodic Stripping Voltammetry (ASV) is a commonly employed technique used in the detection of heavy metal cations. These are accumulated at the electrode by reduction to the zeroth oxidation state. Classically the electrode material used is a mercury film electrode[24] but more recently solid electrodes have been used successfully in the detection of some metals in solution.[25-27] This has the added benefits of not using mercury but can lead to intermetallic compounds being formed and interfering with the response.[28-31] This section will concentrate on the mercury based electrodes as the development of solid electrodes for ASV will be covered in chapters 4 and 5 of this thesis. Mercury was used for ASV because of two factors: first the negative potential range is greatly enhanced for mercury[24] and second that most heavy metals form amalgams with mercury.[40] The former point is very useful for example when trying to detect zinc which strips at approximately –1.2V *vs.* SCE (Saturated Calomel Electrode). Hanging drop electrodes were commonly employed for this techniques but nowadays the preferred method is the Mercury Thin Film Electrode (MTFE) as the peaks obtained are sharper and hence resolution and accuracy are increased. MTFE's require a substrate electrode and good examples of these are glassy carbon,[32,33] platinum[34] or iridium.[35] These are considered good substrates as the wetting ability is

good and they do not easily form amalgams with the mercury (as a gold electrode would). The mercury film is either prepared *ex-situ* or *in-situ*, that is to say in this case the film is either preformed on the electrode substrate or co-deposited with the analyte cations. The pre-concentration step is

$$M^{Z+} + Ze^{-} \rightleftharpoons M(Hg) \qquad (1.68.)$$

which is reversed in the stripping step. The stripping step can be accomplished by either a LSV sweep or a SWV sweep. The latter is found more often in the recent literature as it is more rapid and of higher sensitivity. In some cases the rapidity allows experiments to be carried out in the presence of oxygen[36] and is independent of the electrode geometry.[37] The important examples of metals that are detected in this way include copper, lead, cadmium and zinc at sub-ppb levels.

If a mixture of cations is analysed at mercury electrode, intermetallic compounds can be formed. In order to avoid this strategies can be developed for each case but may involve the deposition of a third element. As a good illustration the simple strategy for Cu^{2+} and Zn^{2+} will be used. This leads to Cu-Zn compounds in the mercury layer. If the solution is spiked with Ga^{3+} and co-deposited the preferential formation of Cu-Ga compounds allows the Zn^{2+} to be analysed without interference.[38] The Cu can be detected in a separate experiment by deposition at a more positive potential where Zn^{2+} is not reduced.

1.3.1.2. Adsorptive Stripping Voltammetry (AdSV)

Adsorptive stripping voltammetry (AdSV) is a well known electrochemical technique which has been applied to the detection of metals such as Co, Ni, Mo, U and V[39,40] and organic compounds such as heme, codeine, cocaine and digoxin.[40] In this methodology, pre-concentration of the metal is achieved by means of interfacial

accumulation of the target as a metal complex on the electrode. This pre-concentration step is crucial for AdSV analysis and its behaviour will affect the selectivity and sensitivity of the method.[41] the adsorbed species is then stripped off in the analytical step in the form of a Faradaic process. The charge passed in this step permits the inference of the concentration of the target. For instance, concentrations of vanadium as low as *ca.* 10^{-10} M have been analysed following the adsorptive accumulation of the $V^{(V)}$ complexes with catechol,[39,42] cupferron[43] and chloroanilic acid[41] on mercury electrodes.

1.3.1.3. Cathodic Stripping Voltammetry (CSV)

Cathodic stripping voltammetry of metal ions is the least commonly used of the three main electrochemical stripping techniques, which is surprising considering the potential benefits of CSV, including high specificity, mercury free and oxygen insensitive analyses. CSV is effectively the electrochemical inverse of ASV, where the analyte of interest is accumulated as an oxidised species on the electrode at a positive potential, and then quantified during the stripping step as the electrode potential is swept in a negative direction. The general form of the redox reaction is shown below

$$2M^{z+} + mH_2O \rightleftharpoons M_2O_m + 2mH^+ + 2(m-z)e^- \qquad (1.69.)$$

Although this technique can be applied to the detection of silver[44] it is most commonly employed for lead[45] and manganese[46,47] and the next section will concentrate on manganese as an example. Various CSV methods for directly analysing aqueous manganese have also been developed previously. These methods all employ the technique of first accumulating manganese from solution by electrodepositing MnO_2 anodically on the working electrode, and then stripping off

reduced Mn^{2+} ions by sweeping the potential negatively. Viltchinskaia *et al.*[46] and Labuda *et al.*[47] reported the use of graphite electrodes for CSV determination of manganese, with detection limits of the order of 10^{-8} M, and Khoo *et al.* obtained similar results using a 1-(2-Pyridylazo)-2-Napthol-modified carbon paste electrode.[48] Work in this area has also been carried out using platinum electrodes to determine the manganese content of steel,[49,50] and detection limits approaching nano-Molar (10^{-9} M) have been achieved using glassy-carbon electrodes.[51,52]

Although not exhaustive, the above list contains the best of the recently developed CSV techniques for manganese determination, and this is also evident in various review articles.[53,54] With such a limited range of applications for CSV existing at present, an investigation of new electrode materials and electrochemical techniques in this area is easily justified, in order to extend the range of CSV-based electroanalytical techniques and further develop what is an under-utilised methodology.

1.4. Ultrasound and Sonochemistry

Ultrasound is a high frequency longitudinal wave which is transmitted through the liquid in exactly the same manner as any other sound wave. Longitudinal waves are waves that travel in the same direction as the oscillation of the solution molecule. This causes the molecules to be pulled apart, known as 'rarefaction' and then pushed together, known as 'compression'. The pressure created at any point along the wave can be described by the sinusoidal equation below:

$$P = P_0 \sin(2\pi ft) \qquad (1.70.)$$

where P_0 is the applied pressure from the transducer, f is the frequency of the ultrasound and t is the time.

There are two distinct types of ultrasound which operate at very different frequencies: power ultrasound (20-100 kHz) and diagnostic ultrasound (1-10 MHz). The former is the one commonly employed in sonochemistry and the one with which this thesis is exclusively concerned. The latter is a non-invasive technique used in medicine for scanning the human body. The most common use is the scanning of foetuses during pregnancy.[55]

Ultrasound is also widely employed in industrial processes; it can be used to degas molten glass and metal; for producing finer and smaller crystals than silent conditions;[56] in the food industry for sterilisation processes and for environmental use by coagulating airborne particles thereby reducing polluting mists. A final application is the assistance of drilling, grinding and cutting of brittle materials such as glass or ceramics.[56]

1.4.1. Physical Effects of Ultrasound

The phenomenon of cavitation occurs when the sound wave undergoes rarefaction and the acoustic pressure P_0 is large enough to create a separation distance between the solution particles, approximately twice the Van der Waal's separation,[57,58] such that the liquid structure breaks down to form a cavity or bubble. These bubbles may survive many cycles (stable cavitation) or collapse after one or two cycles (transient cavitation). The energy required to create these bubbles is large so when these bubbles collapse the energy is released in the form of heat, causing a temperature rise in the solution, or in the form of light - termed sonoluminescence.[59] There are many different types of cavitation in solution and to understand the chemistry observed within these a full understanding of the nature of the bubble must be known. The following can be differentiated:

1. an empty cavity (true cavitation),

2. a solvent vapour filled cavity,
3. a dissolved gas filled cavity, or
4. a combination of gas and vapour filled cavity.

Cavitation in water requires large amounts of energy to obtain the critical separation - approximately 4 Å. To achieve this an acoustic pressure of 4000 atm[57] is required or an ultrasound intensity of 5 MW cm^{-2}. Whilst this is for true cavitation, in contrast if the cavitation bubble is filled with water vapour the required pressure is only 25% of that required before. Cavitation is also observed at much lower pressures due to 'weak spots' in the solution arising from dissolved gases and particles.

The amount of cavitation is related to a number of factors as follows

1. Frequency - if the frequency of the ultrasound is increased then cavitation will be reduced as bubbles have less time to form.
2. Temperature - increasing temperature raises the vapour pressure of the liquid and cavitation will occur at lower intensities.
3. Viscosity - the greater the intermolecular forces the more difficult it is to pull the molecules apart.
4. Type of dissolved gases - the greater the specific heat ratio ($\gamma = C_P / C_V$) the less the energy of cavitation will be absorbed and more marked effects will be seen.

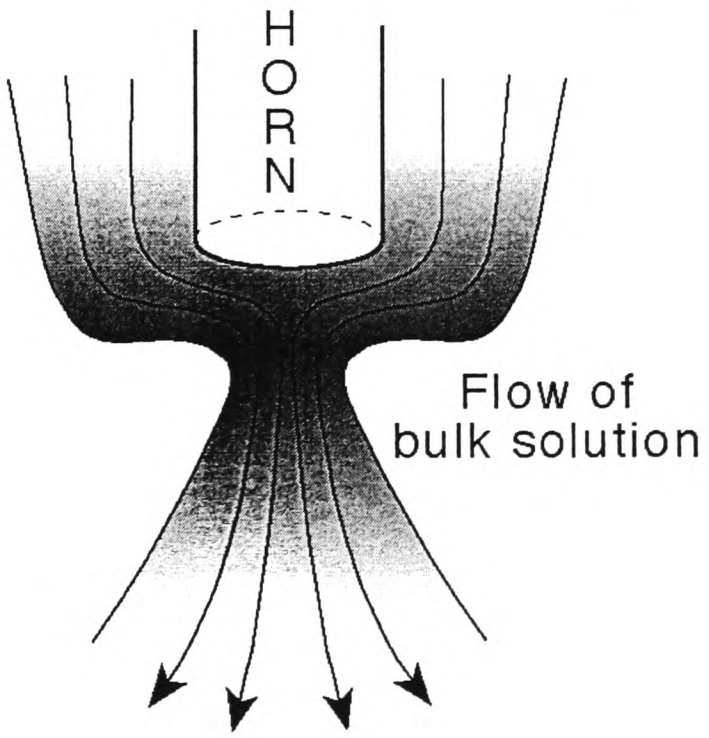


Figure 1.8 Schematic depiction of the flow pattern generated by the sonic horn.

5. External Pressure - a higher external pressure means that less bubbles will be formed but also increases the probability that the bubbles will collapse causing chemical reactions.[58]

6. Intensity - the number of molecules cavitationally displaced varies with ultrasound intensity.

Acoustic streaming[61] occurs when ultrasound enters a liquid and is dissipated by conversion into kinetic energy creating a shock wave in the bulk solution thereby increasing the convective motion of the solution away from the horn tip. The effect is visible to the naked eye and is dependent upon the intensity of the ultrasound (see Figure 1.8).

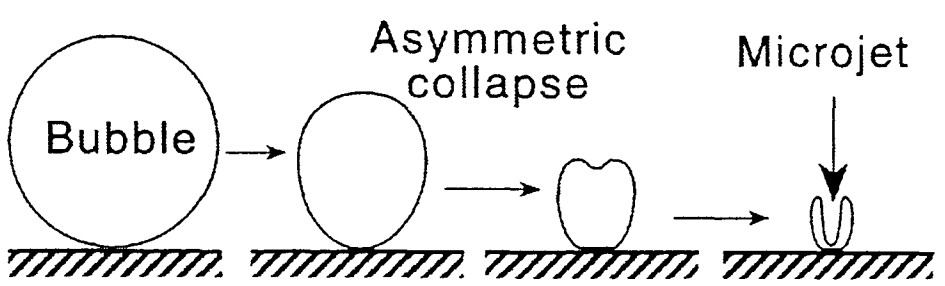


Figure 1.9 A cartoon of the collapse of a cavitation bubble causing a microjet.[60]

Microjet formation, or *microstreaming*,[60,131,132] results from the asymmetric collapse of the cavitation microbubbles and is seen in Figure 1.9. The result is to enhance the local mass transport as the jets of liquid may be travelling at speeds of up to 100 m s^{-1}.[60]

1.4.2. Chemical Effects of Ultrasound

Ultrasound can have many different effects on solutions depending on the frequency of the ultrasound and whether the solution is homogeneous or heterogeneous. The effects of frequency are considered first.

When cavitation occurs very high local temperatures may arise.[62-65] This in turn enables a more facile radical production. A common feature of ultrasound in chemistry is that it promotes radical reactions. In water the bubbles formed due to

cavitation are filled with vapour and dissolved gas; and are transient. The internal pressure and temperature can reach several hundred bars and several thousand degrees.[62-65] Under these extreme conditions the water molecule can cleave to give $H^{\bullet}$ and $OH^{\bullet}$ radicals respectively. If molecular oxygen is present it can also cleave to give O atoms:[66]

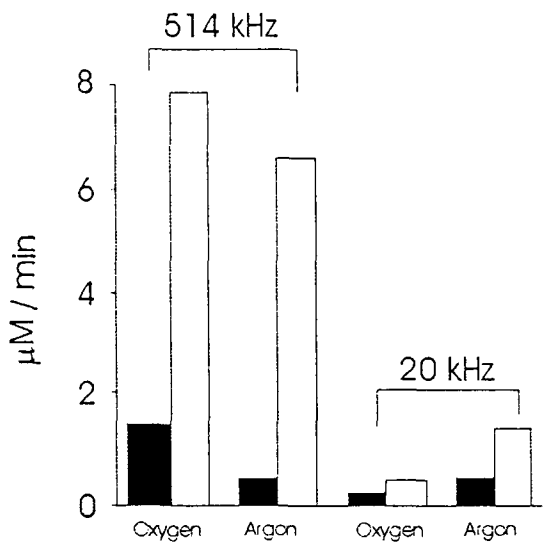


Figure 1.10 The rate of production of hydrogen peroxide (□) and that of the I_3^- ion (■). Power for each is adjusted such that the rate of I_3^- production in argon is 0.45 μM min^{-1}. Data taken from [66]

$$H_2O \rightarrow H^{\bullet} + OH^{\bullet}$$

$$O_2 \rightarrow 2O$$

The transient radicals can either escape from the bubble to react with dissolved molecules or recombine.

$$2OH^{\bullet} \rightarrow H_2O_2$$

The dependence of this on frequency has been monitored using aqueous KI solution and monitoring iodide ion oxidation and hydrogen peroxide production.[66] At higher frequency (514 kHz) hydrogen peroxide is more efficiently produced under oxygen but at lower frequency (20 kHz) the opposite is seen suggesting that the recombination reaction in the bubble is promoted by oxygen and, conversely, the transport out of the bubble is hindered by the presence of oxygen at higher frequencies.[66] This is illustrated in Figure 1.10.

The influence of ultrasound on solutions varies according to whether the reacting mixture is homogeneous or heterogeneous and can give different products compared to the analogous mechanically stirred reactions. The following guidelines for the effect on reactions have been summarised by Luche[67]

Homogeneous reactions: The chemistry of the reactions is influenced by the use of ultrasound by the collapse of the cavitation bubbles creating

hot spots and introducing novel intermediates such as co-ordinately saturated species or free radicals and thereby changing the course of the reaction.

Heterogeneous reactions: Three types of ultrasonic influence are observed:

i) If the reaction involves surface catalysis then the rate of reaction is increased as the ultrasound cleans the surface and promotes the reaction (for example Figure 1.11).

ii) If the reaction involves a radical intermediate or Single Electron Transfer (SET) this pathway is promoted[67] (see for example Figure 1.12).

iii) If the inhomogeneity comes from the immiscibility of two liquids ultrasound will enhance the rate of transport across the phase boundary.

In Figure 1.11 ultrasound activates the reaction between benzyl bromide and insoluble potassium cyanide at the alumina surface via an S_N2 type mechanism;[68] the normal solution reaction goes via an S_N1 type mechanism.[68] In Figure 1.12 the ultrasound serves both to promote the rate of the second SET and to provide radicals to trap the intermediate after the radical re-arrangement. Under insonation the more easily formed 5-membered ring (5-exo-trig) is trapped forcing the reaction to be irreversible and resulting in a kinetic product whereas in the mechanically stirred reaction the second SET is reversible and the thermodynamic 6-membered ring product results.[68] In heterogeneous solutions that contain an alkali metal, irradiation by ultrasound causes an emulsion of the metal to be produced.[69] If a piece of potassium metal is placed in xylene or toluene and exposed to ultrasound at approximately 10°C a silvery blue colour is obtained and the metal fragment disappears. This will not occur for lithium and will only occur for sodium in xylene.[69] Alkali metals are not the only

metals to be emulsified by ultrasound; it has been shown that the irradiation of a thin mercury film will yield an emulsion.[70,71] The powerful effect of ultrasound on heterogeneous reactions immediately suggests its use in electrochemistry to which we next turn.

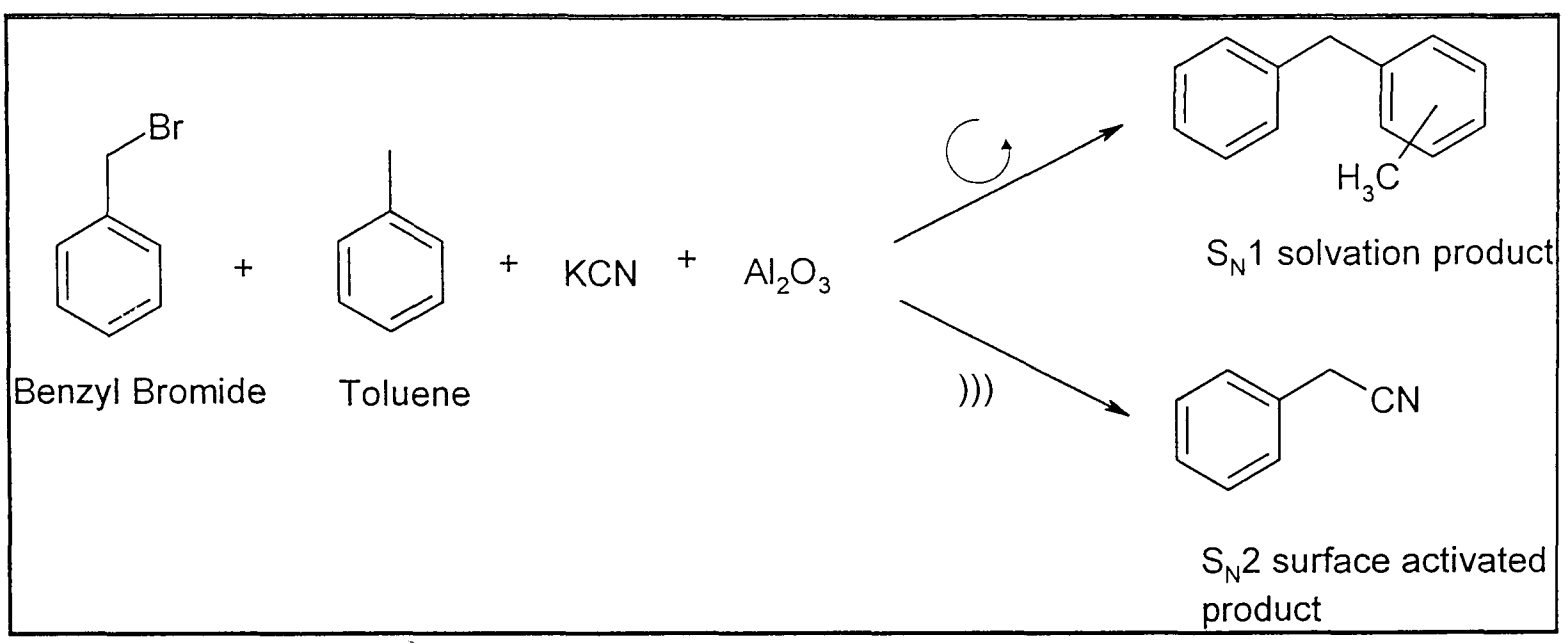


Figure 1.11 The surface activation effect of ultrasound. ↻ and))) denote mechanical and ultrasonic stirring respectively.

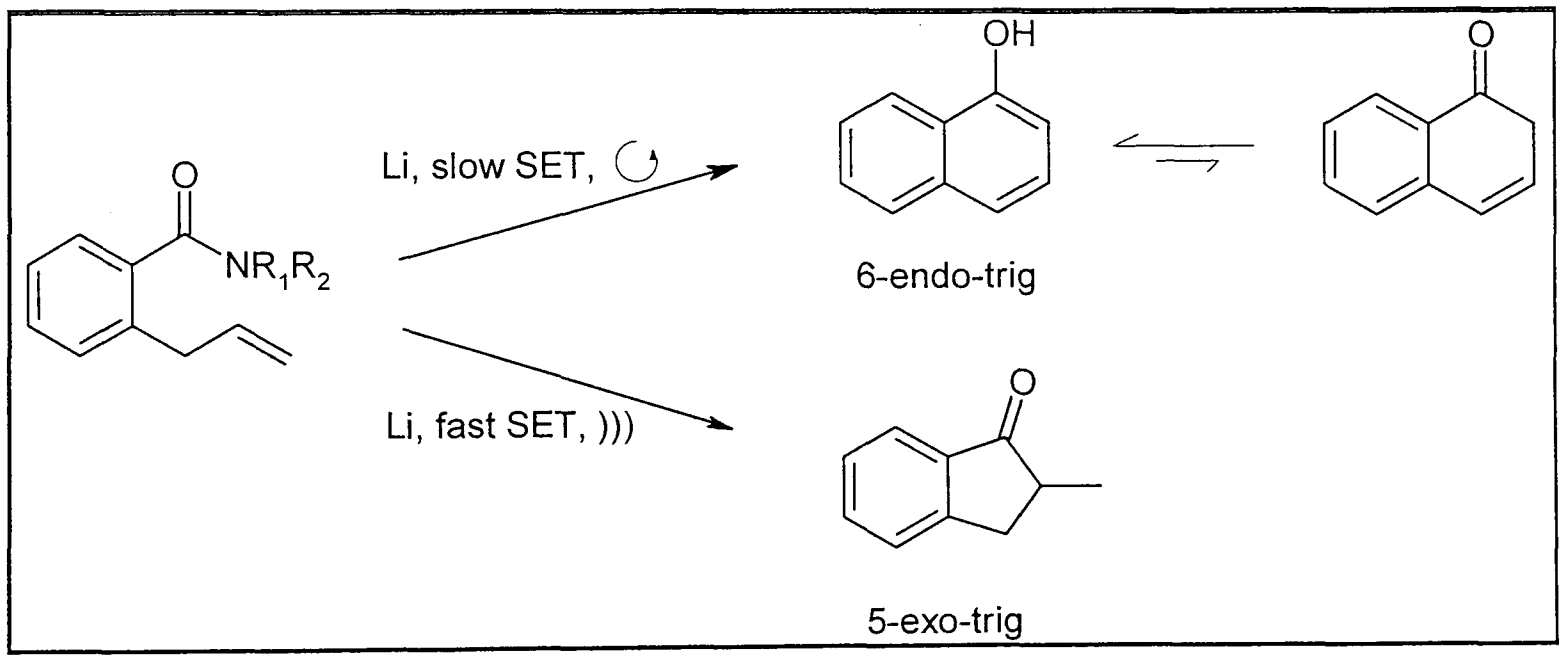


Figure 1.12 The radical promotion effect of ultrasound.

1.5. Sonoelectrochemistry

1.5.1. Historical Origins

Sonoelectrochemistry is re-emerging as an important and highly active interdisciplinary field of research.[72-76] Nevertheless the historical origins of the subject are early. Pioneering work was carried out by Nikitin[77-84] in Russia who studied the effect that sonic waves had on the polarised hydrogen electrode; subsequently the corresponding effects at ultrasonic frequencies were investigated by Yeager *et al.*[85,86] in the USA. The effect of ultrasound on the potential required for the hydrogen evolution reaction was investigated by Moriguchi[87] as early as 1934 and it was shown that this leads to a lowering of the potential required to reduce water at a bright platinum electrode an observation later reconfirmed by Yeager *et al.*.[88] These initial observations were developed by Schmid and Ehret[89] who examined the electrochemical formation of dihydrogen at a number of metal surfaces. Significant effects were observed at the onset of cavitation and independently observed by Piontelli.[90,91] Cavitational effects, where bubbles implode at or near the electrode surface, represent one possible important physical mechanism by which ultrasound can modify electrode processes. Of similar fundamental interest is the 1930's work of Moriguchi[92] who drew attention to the fact that ultrasound can decrease the thickness of the diffusion layer at the electrode; this observation represents a landmark in physical sonoelectrochemistry and mass transport effects will be seen below to be highly important in this area. Thus, for example, Moriguchi's work appears to the basis of the 1963 innovation of Bard[93] who reported the use of ultrasound in 'high

speed controlled potential coulometry' to decrease the exhaustive electrolysis time of silver(I) and iodide to under 100 seconds in a volume of 7.5 cm^3.

Other reports of early applications in sonoeletrochemistry concern the area of metal deposition; Dutt[94] claimed that it was possible to electroplate aluminium using ultrasound without causing solvent breakdown and Young and Kersten[95] investigated the effect of ultrasound on electroplating after the discovery of ripples formed during the insonation of warm paraffin on a glass tube.[96] These and other first works on the effects of ultrasound on electrochemical processes have been carefully summarised by Yeager and Hovorka[74] and by Littlewood;[97] the reader is directed to these reviews for more information about the above and also the influence of ultrasound on electrokinetic effects,[98,99] the behaviour of electrolytic solutions and the construction of early ultrasound transducers.[100,101]

The present day objectives of the coupling of power ultrasound with electrochemical systems are to develop new or improved electrode processes but also to provide a useful insight into the mechanism of electrode reactions. Ultrasound is not simply a source of chemical activation via collapse of cavitational bubbles but also a strong influence on the mass transport to and from the electrode-solution interface. Three recent reviews have been written about the explosion of work on sonoelectrochemistry[102-104] that has evolved in the last decade of the 20^{th} century. This section attempts to provide an overview detailing both physico-chemical aspects and applications.

1.5.2. Methods of Coupling

Ultrasound may be introduced into an electrochemical system in a variety of different ways. First and most simply an electrochemical cell may be placed in an ultrasonic bath. This method is simple but can be very irreproducible as the results are strongly dependent of the precise placement of the cell within the bath and the specific geometry of the cell being used.[105] In an extension of this approach the internal metal surface of the bath is coated with a non-conducting coating so that it is then possible to use the whole volume of the bath as the cell container.[106] A second method utilises a sonic horn; most popular is the '*face-on*' approach (see Figure 1.13a) where the ultrasonic horn is located opposite the electrode. The electrode-to-horn separation and the ultrasound power are both easily controlled allowing more complete characterisation of the cell; the effects seen are reproducible and easily interpreted. Another approach is the so-called '*sonotrode*' geometry (see Figure 1.13c). This is when the tip of the horn is used as the electrode[107,108] or is modified such that an electrode is physically introduced into the tip of the horn.[109] The sonotrode geometry, although in one sense the limiting case of the face-on geometry, has many different characteristics. As well as cavitational cleaning the vigorous 'shaking' of the horn can enhance the detachment of bulk electrodeposited surface species.[110] This has been elegantly exploited in the

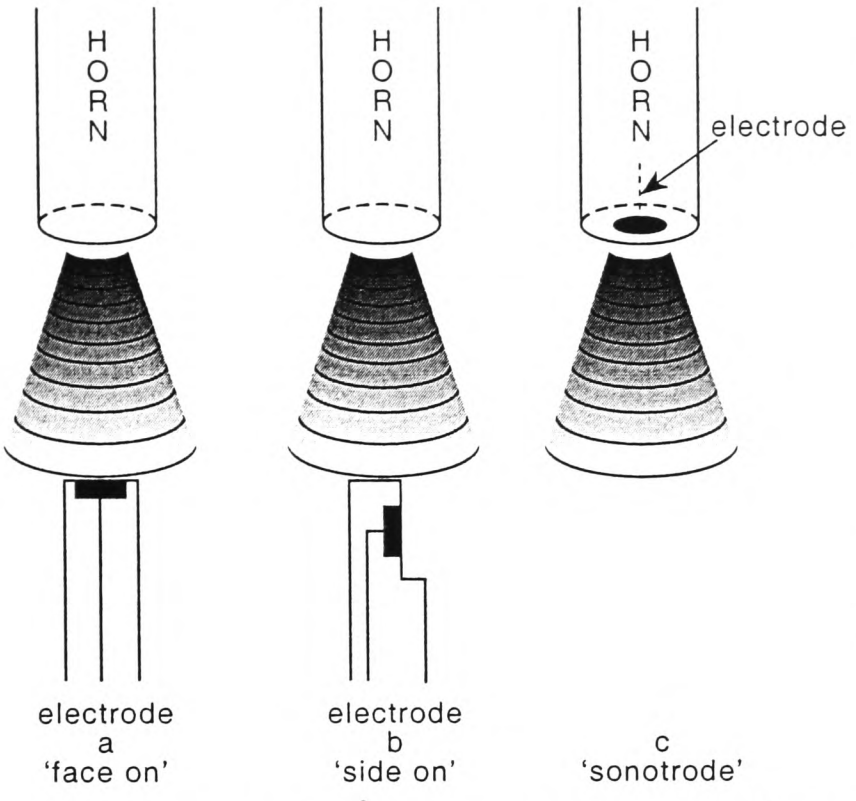


Figure 1.13 A schematic diagram showing different electrochemical cell arrangements usin a sonic horn. (a) the '*face-on*' (b)the 'side-on' and (c) the '*sonotrode*'

production of fine metal powders for metallurgical, catalysis and other purposes.[108,111,112] Effective diffusion layer sizes (see § 1.5.3.1) smaller than 1 μm can be obtained at a sonotrode even for relatively low ultrasound intensities allowing very fast electrode reactions to be easily perturbed. Finally another geometry, although not commonly employed, is the '*side-on*' approach (see Figure 1.13b) where the electrode is placed perpendicular to the horn in the centre of the flow due to acoustic streaming.[113] The hydrodynamics of this arrangement have been characterised as approximately resembling a flow over a plate.[113]

1.5.3. Mass Transport

The description of mass transport phenomena in ultrasound has been the subject of many papers.[106,114-117] Two major contributions to the mass transport exist: acoustic streaming (see Figure 1.8) and microjetting (see Figure 1.9) resulting from cavitational collapse. It was shown by Nonaka and others that the onset of cavitation has a threshold ultrasonic power[118)] and this is illustrated in Figure 1.14. It has also been shown that the threshold for cavitation is strongly dependent on pressure and the chemical nature of the pressurising atmosphere.[119]

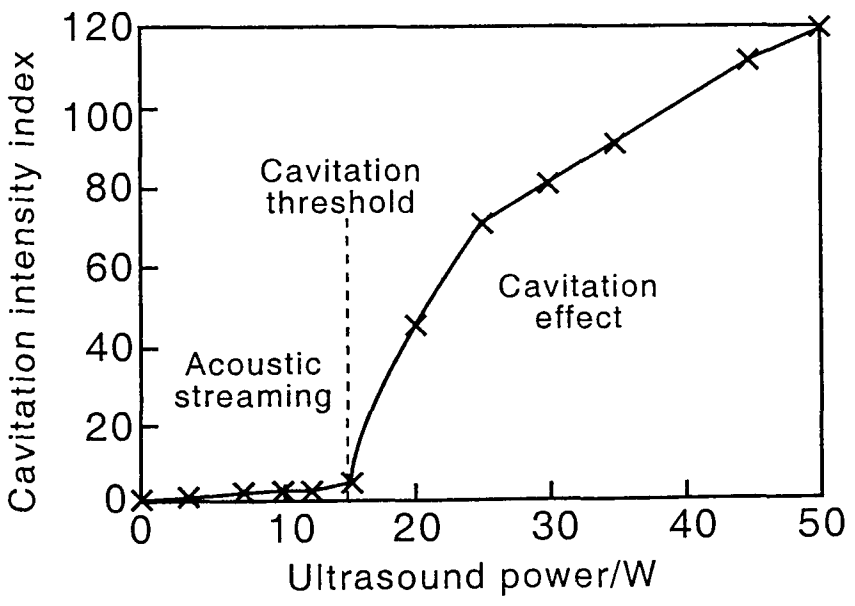


Figure 1.14 The relationship between the onset of cavitation and ultrasound power measured by the cavitation intensity index for the reduction of *p*-methlybenzaldehyde. Adapted from ref. 118.

1.5.3.1. Acoustic Streaming

It has been proposed separately by Marken *et al.*[120] and by Cooper and Coury Jr.[121] that acoustic streaming provides a major contribution on the rate of mass transport to electrodes of conventional dimensions. In Figure 1.15 a time resolved voltammogram is shown at a potential beyond the transport limited reduction of $Ru(NH_3)_6^{3+}$ at a very high ultrasound intensity. It can be clearly seen from Figure 1.15 that an average current is maintained relating to the acoustic streaming effect and the spikes are attributed to the cavitation collapse at the electrode surface (see §1.5.3.2 for more details). It was suggested by Yegnarman and Bharathi[122] that the former current was mass transport limited. Further experimental evidence showed that, at least for measurements conducted using acetonitrile solutions and for relatively low ultrasound powers, the magnitude of the current was dependent on the electrode area, A, the bulk concentration, $[\,]_\infty$, and the diffusion coefficient, D.[114] Many authors subsequently proposed a simple Nernstian model for the mass transport. This assumes that the concentration gradient is linear throughout the diffusion layer as shown in Figure 1.16 so that the limiting current, I_{LIM}, may be related to the diffusion layer thickness via

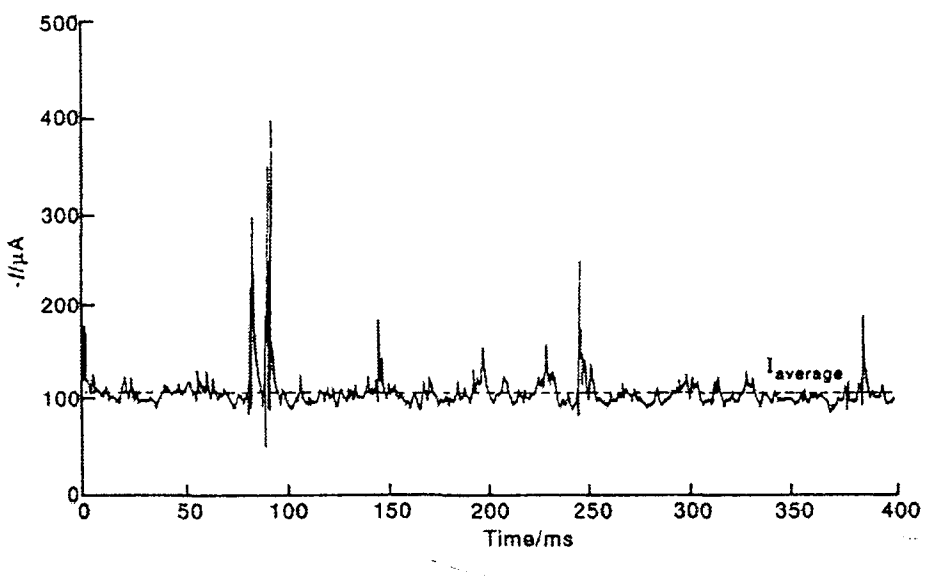


Figure 1.15 A time resolved voltammogram at an ultrasound intensity of 54 W cm^{-2} and a horn to electrode separation of 3mm for the one electron reduction of 1mM $Ru(NH_3)_6Cl_3$ (aq) at a 2mm mercury coated copper electrode.

$$I_{LIM} = \frac{nFAD[\,]_\infty}{\delta} \qquad (1.71.)$$

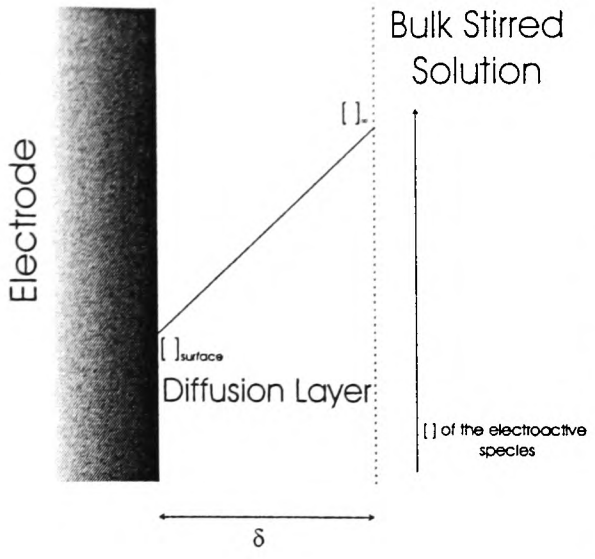


Figure 1.16 A schematic showing the Nernst diffusion layer model used in the derivation of equation (1.71.)

where n is the no. electrons, F is the Faraday constant and A is the electrode area. Further evidence for this model was recorded using AC impedance spectroscopy which gave rise to Cole-Cole plots indicative of a thinned diffusion layer of dimensions consistent with these inferred from DC measurements.[102,105,123] This model has been successfully employed in the elucidation of the kinetics in ECE,[124] EEC'[125] and EC'[126] mechanisms. Under stronger ultrasonic perturbations and in aqueous solution the diffusion layer has been shown to exhibit hydrodynamic behaviour as its size becomes proportional to the cube root of D[127] and equation (1.71.) has been rewritten.[125]

$$I_{LIM} = \frac{nFDA[]_{\infty}}{\delta(D)} \qquad (1.72.)$$

where

$$\delta \propto D^{1/3} \qquad (1.73.)$$

This relationship is shown in Figure 1.17. This is a general feature of convective systems[128] and suggests that the diffusion layer is not purely stagnant as suggested by the naïve Nernst model but contains a convective component.

1.5.3.2. Microjetting

Microjets are formed when a cavitational bubble implodes at or near a surface. These effects have been demonstrated by using both macro (diameter > 50μm) and microelectrodes. In work by Perusich and Alkire[129,130] a model of averaged microjet velocities gave only approximate agreement with experiment in the case of macroelectrodes. Work by Klíma *et al.*[60,131,132] and later by Birkin and Silva-

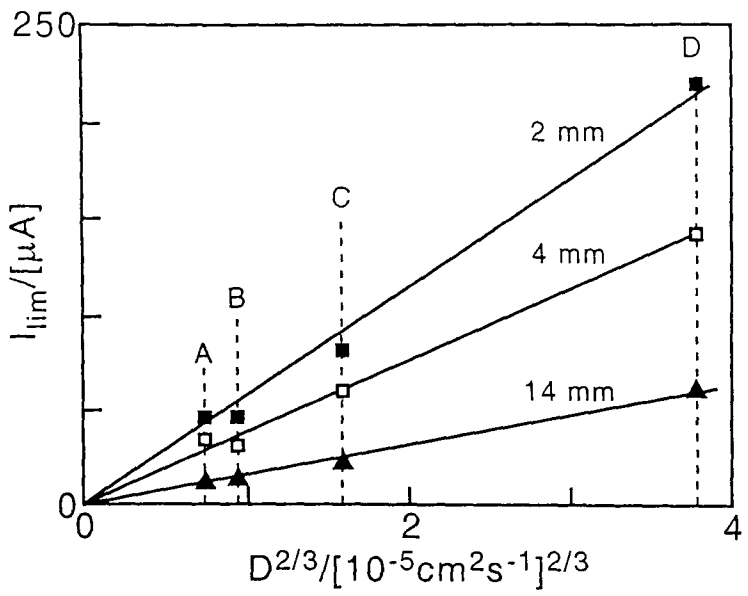


Figure 1.17 A plot of the limiting current obtained in sonovoltammetry of various species of differing diffusion coefficients in aqueous solution (A) $Fe(CN)_6^{4-}$ in 1M KCl (B) $Ru(NH_3)_6^{3+}$ in 0.1M KCl, (C) I^- in 0.125M H_2SO_4 and (D) H^+ in 1M KCl

Martinez[133-136] has shown that at microelectrodes the cavitational response can be modelled as a transient response akin to that observed at a 'wall-tube' geometry.[137-139] They also suggested that the mechanism for this response is that the imploding cavitational bubble compresses the diffusion layer but does not reach and expose the electrode surface.[134] After implosion the diffusion field around the electrode relaxes back to steady state giving rise to the transient behaviour observed. This approach has been used to investigate the effect of ultrasound on electron transfer reactions.[136]

1.5.3.3. Overall Picture

The micro electrode work of Klima[60,131,132] and others[133-136] elegantly illustrates the contribution of cavitational events to electrode currents and their importance for 'electrode cleaning' phenomena which, as discussed in the following section, are vital to many sonoelectrochemical processes. However, as the data in Figure 1.15 implies, the close similarity of the average currents to the baseline acoustic streaming induced values suggests that the dominant contribution at macroelectrodes, at least under conditions of moderate ultrasound power, maybe due to convective steady state currents. Due to the thinness of the diffusion layer due to acoustic streaming phenomena, as little as *ca.* 0.7μm at sonotrodes and often only a few microns under face-on conditions, the steady state diffusion layer is reformed within a few milliseconds if fully refreshed by a cavitation event. It follows that unless there is a

very large level of cavitational events (very high power and / or short horn-electrode distance) then at any particular individual location on the electrode surface the most usual mass transport environment will be of the steady convective diffusional nature rather than any from microjetting. A simple picture therefore emerges of sonoelectrochemical mass transport to a macroelectrode is that of a steady state acoustic streaming induced current very close to the average net current experienced over the electrode but occasionally punctuated by a cavitational event. The latter is, of course, essential to most sonoelectrochemical surface activation and it is to this we turn next.

1.5.4. Surface Activation

When a cavitation bubble collapses at an interface the resulting microjet, as well as an increase in mass transport, may clean the electrode surface by eroding material from the latter. This form of cleaning is implicit in the cavitational damage that is typically caused by ultrasound on electrode surfaces.[140] More usefully it was shown that insonated nickel electrodes were activated by a cleaning effect which removed the non-conducting oxide layer that forms on the electrode when the potential is scanned in a positive direction.[140] This cleaning effect has also been gainfully employed in the prevention of organic molecules adsorbing to the electrode surface and passivating the electrode[141] as for example in the activation of a glassy carbon electrode for the detection of copper in beer. Where under silent conditions no useful measurements can be made; in contrast insonation removes adsorbing organic materials intrinsically present in the beer and permits a quantitative electroanalytical method.[142] Similarly the work of Petrier showed that insonation hindered the electrodeposition of polypyrrole films at a platinum electrode.[143] More recently Reisse and co-workers have also exploited this powerful effect for the production of

highly reactive fine metal powders by pulsed sonoelectrochemical reduction.[107,108] for example they showed that zinc powder exhibited high reactivity in Barbier type reactions in aqueous media.[107] In contrast it has been shown that the electrodeposition of lead dioxide onto a glassy carbon electrode is unaffected by sonication albeit at low ultrasound intensities.[144] This is not the case in the deposition of lead onto copper foam electrodes which for long sonication times the lead deposits will detach themselves from the surface.

1.5.5. Electroanalysis

The enhanced mass transport to and surface activation of sonicated electrodes has suggested the coupling of power ultrasound to electroanalytical procedures. Madigan *et al.*[145] proposed a new form of stripping analysis whereby zero-valent metal particles were melted onto the electrode surface after being accelerated by microjets formed by acoustic cavitation. Marken *et al.* suggested the application of ultrasound to Anodic Stripping Voltammetry (ASV)[146] where not only does the improved mass transport aid the pre-concentration step but the electrode cleaning has been shown to permit the technique to work in dirty media which would otherwise passivate the electrode[141,142] as well as in model laboratory conditions.[110,147,148] This technique has been shown to increase sensitivity and usefully decrease analysis time by removing lengthy pre-treatments to destroy organic matrix effects.[149] The beneficial application of ultrasound has been reported for the Adsorptive Stripping Voltammetric (AdSV) detection of both metals and organic matter.[150,151] Recently, Saterlay *et al.*[45] have used Cathodic Stripping Voltammetry (CSV) in conjunction with ultrasound to simultaneously extract and determine lead in a river sediment.

The use of copper-nickel alloy electrodes has been used recently for the detection of oxygen[152-154] and these have also been successfully used under insonation via a ring-

disc electrode technique.[155] Walton *et al.* have shown that chlorine, hydrogen and oxygen may be detected at a platinised platinum electrode due to efficient ultrasound degassing at the electrode surface.[156] Similarly McMurray *et al.* have shown that both hydrogen and oxygen gave analytically useful signals at a titanium sonotrode.[157] Compton and Matysik reported the use of pulsed ultrasound for the detection of ascorbic acid by oxidation of the neutral species.[158] This method had been further developed recently by Akkermans *et al.* to incorporate the used of Laser Activated Voltammetry (LAV)[159] which allowed electrode cleaning by the laser and the enhanced mass transport from the ultrasound in the side-on approach.

1.5.6. Mechanistic and Synthetic Investigations

Extensive empirical investigations have been carried out on the effect of ultrasound on both organic and inorganic electrode processes. First the selectivity of the electroreduction of substituted benzaldehydes and related materials was found to be drastically affected to give more of the products which require less electron transfer.[160-163] Similarly ultrasound promoted the reduction of methyl halides at a reactive tin cathode to give similar products.[164,165] Further work has involved the preparation of polymer films[166] showing that more dense films were produced. Ultrasonic irradiation has also been shown to increase the current efficiencies for the formation of cupric carboxylates.[167] Recently, work building on the early electroorganic studies of Walton and Mason,[168] has investigated the effect of insonation of the Kolbe electrolysis of carboxylic acids.[169] The ultrasonic effects on preparative electrolysis of emulsions were examined by Marken *et al.* [170] and different cell geometries for electrosynthesis discussed.[171] Nonaka and co-workers, and others, have also studied the effects of ultrasound on the electrolysis of emulsions and suspensions.[170,172]

The mechanism of the Pb(IV) catalysed cleavage of diols has been investigated at graphite and glassy carbon electrode[125] and found to give excellent agreement with a EEC' mechanism calculated using Digisim™ 2.0[173] planar diffusion layer theory. Also the ECE mechanism of both 3-bromobenzophenone and *ortho*-bromonitrobenzene[124] has been shown to give good agreement with previous results[174] using a Nernst diffusion layer model (see §1.5.3.1). Preliminary results for the EC' mechanism of tris(*p*-bromophenyl)amine have also been reported.[126]

The application of a porous electrode under ultrasonic irradiation for the indirect oxidation of secondary alcohols has been reported by Belmont *et al.*[175] and also to the reduction of acetophenone.[176] The oxidation of phenol in wastewater by sonoelectrochemistry in NaCl media has been shown to give acetic and chloroacrylic acids as degradation products.[177] Degrand *et al.* reported the ultrasound-assisted oxidation of diuron[178] giving results consistent with a flat adsorbed species at the electrode surface. Dezhkunov and co-workers have explored the effect of cavitation on electrochemical processes within the Marcus Theory framework.[179]

1.5.7. Frequency Effects

The work on high frequency ultrasound coupled with electrochemistry, although there many examples of frequency effects in sonochemistry,[180-183] is very sparse. Petrier and co-workers proposed that the high frequency reactor acts as a completely stirrer tank from the instance of irradiation and they give a visual representation of the acoustic streaming.[184] Earlier work using methylviologen and ferricyanide reduction and pyrrole oxidation concluded that the most reproducible limiting currents were obtained when the electrode was placed near the gas liquid interface.[143] Conversely the best results for low frequency ultrasound occurred very near the source of irradiation. Work by Tatsumoto *et al.* compared the effect of 38 and 96 kHz on the

oxidation of chloropromazine.[185] It was found that the current observed was greater for 96 kHz and was considered to be due to the acceleration or increase in moving speed of the particles in the solution. Nevertheless it is clear that there is a need for rigorous studies in this area, particularly embracing full mass transport characterisation.

References for Chapter 1

[1] D.J. Fermin, H.D. Duong, Z.F. Ding, P.F. Brevet, H.H. Girault, *Phys. Chem. Chem. Phys.*, 1 (1999) 1461
[2] D.J. Fermin, H.D. Duong, Z.F. Ding, P.F. Brevet, H.H. Girault, *J. Am. Chem. Soc.*, 121 (1999) 10203
[3] W.F. Magie, *A Source Book in Physics* (Harvard University Press, Cambridge, 1965)
[4] I.M. Klotz, *Chemical Thermodynamics* (Benjamin, New York, 1964)
[5] J.A.V. Butler, *Trans. Faraday Soc.*, 19 (1924) 734
[6] T. Erdey-Gruz, M. Volmer, *Z. Phys. Chem.*, 150A (1930) 203
[7] A.C. Testa, W.H. Reinmuth, *Anal. Chem.*, 33 (1961) 1320
[8] A. J. Bard, L. R. Faulkner, *Electrochemical Methods*, Wiley, New York, (1980) pp. 430
[9] F. Marken, A.M. Squires, J.A. Alden, R.G. Compton, J.E.H. Buston, M.G. Moloney, *J. Phys. Chem. B*, 102 (1998) 1186
[10] A. J. Bard, L. R. Faulkner, *Electrochemical Methods*, Wiley, New York, (1980) pp. 432
[11] W. Smith, A.J. Bard, *J. Am. Chem. Soc.*, 97 (1975) 5203
[12] P. H. Reiger, *Electrochemistry*, Chapman and Hall, New York, (1994), pps. 128-129.
[13] A. Fick, *Philosophical Magazine and Journal of Science* 10 (1855) 30.
[14] A. J. Bard, L. R. Faulkner, *Electrochemical Methods*, Wiley, New York, (1980) pp. 280.
[15] M. S. Wrighton, D. L. Morse, L. Pdungsap, *J. Am. Chem. Soc.* 97 (1970) 3603.
[16] K. B Oldam, C. G. Zoski, *Comprehensive Chemical Kinetics*, Elsevier, Oxford, 26 (1986) 122.
[17] C. M. A. Brett, A. M. O. Brett, *Electrochemistry Principles, Methods, and Applications*, OUP, Oxford, (1993)
[18] R. Muller, J. Heinze, *J. Electrochem. Soc.*, 145 (1998) 1227
[19] G.C. Barker, I.L. Jenkins, *Analyst*, 77 (1952) 685
[20] J. Osteryoung, J.J. O'Dea, *Electroanal. Chem.*, 14 (1986) 209
[21] M.J. Nuwer, J.J. O'Dea, J.Osteryoung, *Anal.. Chim. Acta*, 251 (1991) 13
[22] J.J. O'Dea, J.Osteryoung, T. Lane, *J. Phys. Chem.*, 90 (1986) 2761
[23] J.J. O'Dea, J.Osteryoung, R.A. Osteryoung, *J. Phys. Chem.*, 87 (1983) 3911
[24] F. Vydra, K. Štulík, E. Juláková, *Electrochemical Stripping Analysis*, Ellis Horwood, Chichester, (1976)
[25] M.A. Baldo, S. Daniele, G.A. Mazzocchin, *Electroanal.*, 10 (1998) 410
[26] E. Kirowa-Eisner, M. Brand, D. Tzur, *Anal. Chim. Acta*, 385 (1999) 325
[27] M. Brand, I. Eshkenazi, E. Kirowa-Eisner, *Anal. Chem.*, 69 (1997) 4660
[28] H. Gunasingham, R. Dalangin, *Anal. Chim. Acta*, 246 (1991) 309
[29] S.Dong, Y. Wang, *Talanta*, 35 (1998) 819
[30] O.L. Kabanova, S.M. Beniaminova, *J. Anal. Chem.*, 26 (1970) 94
[31] E.Y.A. Neiman, L.G. Petrova, V.I. Ignaton, G.M. Dolgopolova, *Anal. Chim. Acta*, 113 (1980) 277
[32] F.-M. Matysik, S. Matysik, A.M. Oliveira Brett, C.M.A. Brett, *Anal. Chem.*, 69 (1997) 1651
[33] A.M. Oliveira Brett, C.M.A. Brett, F.-M. Matysik, S. Matysik, *Ultrason. Sonochem.*, 4 (1997) 123
[34] R.P. Akkermans, J.C. Ball, T.O. Rebbitt, F. Marken, R.G. Compton, *Electrochim. Acta*, 43 (1998) 3443
[35] C. Agra-Gutiérrez, M.F. Suaréz, R.G. Compton, *Electroanal.*, 11 (1999) 16
[36] M. Wojciechowski, W. Go, J. Osteryoung, *Anal. Chem.*, 57 (1985) 155
[37] K. Aoki, K. Tokuda, H. Matsuda, J. Osteryoung, *J. Electroanal. Chem.*, 207 (1986) 25
[38] C.M.A. Brett, A.-M. Oliveira Brett, *Electroanalysis*, OUP, Oxford (1998)
[39] C.M.G. van der Berg, Z.Q. Huang, *Anal. Chem.*, 56 (1984) 2383
[40] J. Wang, *Stripping Analysis. Principles, Instrumentation and Applications,* 1st Ed. VCH, New York, (1985) pp. 60
[41] S. Sander, G. Henze, *Fresenius J. Anal. Chem.*, 356 (1996) 259
[42] M. Vega, C.M.G. van der Berg, *Anal Chim. Acta*, 293 (1994) 19
[43] J. Wang, B. Tian, J. Lu, *Talanta*, 39 (1992) 1273
[44] A.J. Saterlay, F. Marken, J.S. Foord, R.G. Compton, submitted
[45] A.J. Saterlay, C. Agra-Gutiérrez, M.P.Taylor, F. Marken, R.G. Compton, *Electroanal.*, 11 (1999) 1083
[46] E.A. Viltchinskaia, D.M. Zeigman, D.M. Garcia and P.F. Santos, *Anal. Lett.*, 28 (1995) 1845.
[47] J. Labuda, M. Vaníčková and E. Beinrohr, *Mikrochim. Acta*, I (1989) 113.
[48] S.B. Khoo, M.K. Soh, Q. Cai, M.R. Khan and S.X. Guo, *Electroanalysis*, 9 (1997) 45.

[49] T. Ishiyama and T. Tanaka, *Tetsu To Hagane – J. Iron Steel Inst. Japan*, 82 (1996) 923.
[50] T. Ishiyama, *Bunseki Kagaku*, 46 (1997) 847.
[51] T. Tanaka, T. Muramatsu, N. Takada and A. Mizuike, *Bunseki Kagaku*, 42 (1993) 587.
[52] K.W. Bruland and J.S. Roitz, *Anal. Chim. Acta*, 344 (1997) 175.
[53] R.N. Goyal and A. Mittal, *J. Sci. Ind. Research.*, 53 (1993) 607.
[54] M. Esteban and C. Ariño, *Anal. Chim. Acta*, 285 (1994) 377.
[55] J. C. Birnholtz, E. E. Farrell, *American Scientist* 72 (1984) 608.
[56] T. J. Mason, J. P. Lorimer, *Sonochemistry: Theory, Applications and Uses of Ultrasound in Chemistry*, Ellis Horwood, Chichester, (1988).
[57] T. J. Mason, *Sonochemistry: the Uses of Ultrasound in Chemistry*, Royal Society of Chemistry Publications, London, (1990).
[58] A. Henglein, M. Gutiérrez, *J. Phys. Chem.* 97 (1993) 11368.
[59] R. Hiller, K. Weninger, S. J. Putterman, B. P. Barber, *Science* 266 (1994) 248.
[60] J. Klima, C. Bernard, C. Degrand *J. Electroanal. Chem.* 399 (1995) 147.
[61] F. Marken, R. P. Akkermans, R. G. Compton, *J. Electroanal, Chem.* 415 (1996) 55.
[62] K. S. Suslick, *Ultrasound, Its Chemical, Physical and Biological Effects*, VCH Weinheim, New York, (1988) pp. 138.
[63] A. J. Walton, G. T. Reynolds, *Adv. Phys.* (1987) 239.
[64] P. K. Chendke, H. S. Fogler, *J. Phys. Chem.* 89 (1985) 1673.
[65] K. S. Suslick, S. J. Cokktycz, E. B. Flint *Ultrasonics* 28 (1990) 280.
[66] C. Petrier, A. Jeunet, J.-L. Luche, G. Reverdy, *J. Am. Chem. Soc.* 114 (1992) 3148.
[67] J. L. Luche, C. Einhorn, J. Einhorn, J. V. Sinisterra-Gago, *Tetrahedron Let.*31 (1990) 4125.
[68] S. G. Davies, *Private Communication*, Oxford, March (1997).
[69] J.-L. Luche, C. Petrier, C. Dupuy, *Tetrahedron Let.* 25 (1984) 753.
[70] K. Söllner, C. Bondy, *Trans. Faraday Soc.* 32 (1936) 616.
[71] W. T. Richards, *J. Am. Chem. Soc.* 51 (1929) 1724.
[72] T.J. Mason, J.P. Lorimar, *Sonochemistry: Theory, Applications, Uses of Ultrasound in Chemistry*, Ellis Horwood, Chichester, (1988)
[73] P.D Lickiss, V.E. McGrath, *Chem. Britain*, 32 (1996) 47
[74] E. Yeager, F. Hovorka, *J. Acoust. Soc. Am.*, 25 (1953) 443
[75] A.A. Kaplin, V.A. Bramin, I.E. Stas, *Zh. Anal. Khim.*, 43 (1988) 921
[76] V. Yegnaraman, S Bharathi, *Bull. Electrochem.*, 8 (1992) 84
[77] L. Nikitin, *Compt. Rend. Acad. Sci. (URSS)*, 4 (1934) 309
[78] L. Nikitin, *J. Gen. Chem. (USSR)*, 6 (1936) 1393
[79] L. Nikitin, *J. Gen. Chem. (USSR)*, 6 (1936) 1401
[80] L. Nikitin, *J. Gen. Chem. (USSR)*, 10 (1940) 97
[81] L. Nikitin, *J. Gen. Chem. (USSR)*, 10 (1940) 636
[82] L. Nitikin, M. Rausch, *J. Phys. Chem.*, 20 (1946) 330
[83] L. Nitikin, *J. Phys. Chem.*, 22 (1948) 1090
[84] L. Nitikin, M. Rausch, *J. Phys. Chem.*, 20 (1946) 325
[85] E. Yeager, J. Bugosh, F. Hovorka, J. McCarthy, *J. Chem. Phys.*, 17 (1949) 411
[86] E. Yeager, J. Bugosh, H. Dietrich, F. Hovorka, *J. Acoust. Soc. Am.*, 22 (1950) 686(A)
[87] N. Moriguchi, *J. Chem. Soc. Jap.*, 55 (1934) 751
[88] E. Yeager, T.S. Oey, F. Hovorka, *J. Phys. Chem.*, 57 (1953) 268
[89] G. Schmid, L. Ehret, *Z. Elektrochem.*, 43 (1937) 597
[90] R. Piontelli, *Atti Accad. Lincei. Classe Sci. Fis. Mat. Nat.*, 27 (1938) 581
[91] R. Piontelli, *Atti Accad. Lincei. Classe Sci. Fis. Mat. Nat.*, 27 (1938) 357
[92] N. Moriguchi, *J. Chem. Soc. Jap.*, 55 (1934) 749
[93] A.J. Bard, *Anal. Chem.*, 35 (1963) 1125
[94] E.E. Dutt, *French Patent*, 749007 (1933); *Chem. Abstr.*, 27 (1933) 5657
[95] W.T. Young, H. Kersten, *J. Chem. Phys.*, 4 (1936) 426
[96] R.W. Wood, A.L. Loomis, *Phil. Mag.*, 4 (1927) 417
[97] K. Littlewood, *J. Roy. Inst. Chem.*, 86 (1962) 78
[98] H. Dietrick, E. Yeager, J. Bugoshi, F. Hovorka, *J. Acoust. Soc. Am.*, 25 (1953) 461
[99] S. Ueda, A. Wattanabe, F. Tsuji, *J. Electrochem. Ass. Jap.*, 19 (1951) 142
[100] A.E. Crawford, *Ultrasonic Engineering*, Butterworths Scientific Publications, London (1955)
[101] P. Vigoureux, *Ultrasonics*, Chapman, Hall, London (1950)

[102] R.G. Compton, J.C. Eklund, F. Marken, *Electroanal.*, 9 (1997) 509
[103] D.J. Walton, S.S. Phull, *Adv. Sonochem.*, 4 (1996) 205
[104] R.G. Compton, J.C. Eklund, F. Marken, T.O. Rebbitt, R.P. Akkermans, D.N. Waller, *Electrochim. Acta*, 42 (1997) 2919
[105] D.J. Walton, S.S. Phull, A. Chyla, J.P. Lorimer, T.J. Mason, L.D. Burke, M. Murphy, R.G. Compton, J.C. Eklund, S.D. Page, *J. Appl. Electrochem.*, 25 (1995) 1083
[106] H. Huck, *Ber. Bunsenges. Phys. Chem.*, 91 (1987) 648
[107] A. Durant, H. Francois, J.Reisse, A. Kirsch-de Mesmaeker, *Electrochim. Acta* 41 (1996) 277
[108] J. Reisse, H. Francois, J. Vandercammen, O. Fabre, A. Kirsch-de Mesmaeker, C. Maerschalk, J.-L. Delplancke, *Electrochim. Acta*, 39 (1994) 37
[109] R.G. Compton, J.C. Eklund, F. Marken, D.N. Waller, *Electrochim. Acta*, 41 (1996) 315
[110] R.P. Akkermans, J.C. Ball, F. Marken, R.G. Compton, *Electroanal.*, 10 (1998) 26
[111] A. Durant, J.-L. Delplancke, R. Winard, J. Reisse, *Tet. Let.*, 36 (1995) 4257
[112] J. Reisse, T. Caulier, C. Deckerheer, O. Fabre, J. Vandercammen, J.-L. Delplancke, R. Winnard, *Ultrason. Sonochem.*, 3 (1996) S147
[113] J. Eklund, F. Marken, D.N. Waller, R.G. Compton, *Electrochim. Acta*, 41 (1996) 1541
[114] R.G. Compton, J.C. Eklund, S.D. Page, T.J. Mason, D.J. Walton, *J. Appl. Electrochem.*, 26 (1996) 775
[115] D. Shoup, A. Szabo, *J. Electroanal. Chem.*, 160 (1984) 1
[116] R.G. Compton, J.C. Eklund, S.D. Page, *J. Phys. Chem.*, 99 (1995) 4211
[117] C.R.S Hagan, L.A. Coury Jr, *Anal. Chem.*, 66 (1994) 399
[118] M. Atobe, T. Nonaka, *Chem. Lett.*, (1997) 323
[119] D.L. Goldfarb, H.R. Corti, F. Marken, R.G. Compton, *J. Phys. Chem. A*, 102 (1998) 8888
[120] F. Marken, R.P. Akkermans, R.G. Compton, *J. Electroanal. Chem.*, 415 (1996) 55
[121] E.L. Cooper, L.A. Coury Jr., *J. Electrochem. Soc.*, 145 (1998) 1994
[122] V. Yegnarman, S. Bharathi, *Bull. Electrochem.*, 8 (1992) 84
[123] *for example see* A.J. Bard, L.R. Faulkner, *Electrochemical Methods*, John Wiley, Sons, New York, p.321 (1980)
[124] R.G. Compton, F. Marken, T.O. Rebbitt, *J.C.S. Chem. Commun.*, (1996) 1017
[125] F. Marken, R.G. Compton, J.E.H. Buston, M.G. Moloney, *Electroanal.*, 10 (1998) 1188
[126] Y. Kado, M. Atobe, T. Nonaka, *Abstracts of the Meeting of the Electrochemical Society of Japan*, April (1998) p365
[127] H.A.O. Hill, Y. Nagakawa, F. Marken, R.G. Compton, *J. Phys. Chem.*, 100 (1996) 17395
[128] C.M.A Brett, A.-M. Oliveira Brett, *Electrochemistry: Principles, Methods, Applications*, Oxford University Press, Oxford, UK (1993)
[129] S.A. Perusich, R.C. Alkire, *J. Electrochem. Soc.*, 138 (1991) 708
[130] S.A. Perusich, R.C. Alkire, *J. Electrochem. Soc.*, 138 (1991) 700
[131] J. Klíma, C. Bernard, C. Degrand, *J. Electroanal. Chem.*, 367 (1994) 297
[132] J. Klíma, C. Bernard, C. Degrand, *Chem. Listy*, 89 (1995) 587
[133] P.R. Birkin, S. Silva-Martinez, *J.C.S. Chem. Commun.*, (1995) 1807
[134] P.R. Birkin, S. Silva-Martinez, *J. Electroanal. Chem.*, 416 (1996) 127
[135] P.R. Birkin, S. Silva-Martinez, *Anal. Chem.*, 69 (1997) 2055
[136] P.R. Birkin, S. Silva-Martinez, *Ultrasonics Sonochem.*, 4 (1997) 121
[137] D.T. Chin, C.H. Tsang, *J. Electrochem. Soc.*, 125 (1978) 1461
[138] J.V. Macpherson, S. Marcar, P.R. Unwin, *Anal. Chem.*, 66 (1994) 2175
[139] W.J. Albery, S. Bruckenstein, *J. Electroanal. Chem.*, 144 (1983) 105
[140] R.G. Compton, J.C. Eklund, S.D. Page, G.H.W. Sanders, J. Booth, *J. Phys. Chem.*, 98 (1994) 12410
[141] R.P. Akkermans, J.C. Ball, T.O. Rebbitt, F. Marken, R.G. Compton, *Electrochim. Acta*, 43 (1998) 3443
[142] C. Agra-Gutiérrez, J.L Hardcastle, J.C. Ball, R.G. Compton, *Analyst*, 124 (1999) 1053
[143] A. Benahcene, C. Petrier, G. Reverdy, P. Labbe, *New J. Chem.*, 19 (1995) 989
[144] J. González-García, J. Iniesta, A. Aldaz, V. Montiel, *New J. Chem.*, 22 (1998) 343
[145] N.A. Madigan, T.J. Murphy, J.M. Fortune, C.R.S. Hagan, L.A. Coury Jr., *Anal. Chem.*, 67 (1995) 2781
[146] F. Marken, T.O. Rebbitt, J. Booth, R.G. Compton, *Electroanal.*, 9 (1997) 19
[147] F.-M. Matysik, S. Matysik, A.-M. Oliveira Brett, C.M.A. Brett, *Anal. Chem.*, 69 (1997) 1651
[148] A.-M. Oliveira Brett, C.M.A. Brett, F.-M. Matysik, S. Matysik, *Ultrason. Sonochem.*, 4 (1997) 123
[149] M.A. Baldo, C. Bragato, S. Daniele, *Analyst*, 122 (1997) 1

[150] C. Agra-Gutiérrez, R.G. Compton, *Electroanal.*, 10 (1998) 204
[151] C. Agra-Gutiérrez, R.G. Compton, *Electroanal.*, 10 (1998) 603
[152] L. Nei, *Electroanal.*, 7 (1995) 471
[153] L. Nei, R.G. Compton, *Sens, Actuators B*, 30 (1996) 83
[154] L.Nei,, R.G. Compton, *Anal. Commun.*, 33 (1996) 319
[155] L. Nei, F. Marken, Q. Hong, R.G. Compton, *J. Electrochem. Soc.*, 144 (1997) 3019
[156] D.J. Walton, L.D. Burke, M.M. Murphy, *Electrochim. Acta*, 41 (1996) 2747
[157] H.N. McMurray, D.A. Worsley, B.P. Wilson, *J.C.S. Chem. Commun.*, (1998) 887
[158] R.G. Compton, F.-M. Matysik, *Electroanal.*, 8 (1996) 218
[159] R.P. Akkermans, M. Wu, C.D. Bain, M. Fidel-Suárez, R.G. Compton, *Electroanal.*, 10 (1998) 613
[160] K. Matsuda, M. Atobe, T. Nonanka, *Chem. Lett.*, (1994) 1619
[161] M. Atobe, K. Matsuda, T. Nonaka, *Electroanal.*, 8 (1996) 784
[162] M. Atobe, T. Nonaka, *Chem. Lett.*, (1995) 669
[163] M. Atobe, T. Nonaka, *J. Electroanal. Chem.*, 425 (1997) 161
[164] M. Atobe, K. Matsuda, T. Nonaka, *Denki Kagaku*, 12 (1994) 1298
[165] M. Atobe, T. Nonaka, *Bull. Chem. Soc. Jpn.*, 71 (1998) 397
[166] M. Atobe, S. Fuwa, N. Sato, T. Nonaka, *Denki Kagaku*, 6 (1997) 495
[167] M. Atobe, T. Nonaka, *Ultrason. Sonochem.*, 4 (1997) 17
[168] T.J. Mason, J.P. Lorimar, D.J. Walton, *Ultrason.*, 28 (1990) 333
[169] H. Fujiwara, M. Atobe, H. Kanetsuna, T. Nonaka, *J. Chinese Chem. Soc.*, 45 (1998) 175
[170] F. Marken, R.G. Compton, S.D. Bull, S.G. Davies, *J.C.S. Chem. Commun*, (1997) 995
[171] F. Marken, R.G. Compton, S.G. Davies, S.D. Bull, T. Thiemann, M. L. Sá e Melo, A. Campos Neves, J. Castillo, C.G. Jung, A. Fontana, *J. Chem. Soc. Perkin Trans. II*, (1997) 2055
[172] M. Atobe, P.-C. Chen, T. Nonaka, *Denki Kagaku*, 66 (1998) 554
[173] M. Rudolph, D.P. Reddy, S.W. Feldberg, *Anal. Chem.*, 66 (1994) A589
[174] R.G. Compton, R.G. Wellington, P.J. Dobson, P.A. Leigh, *J. Electroanal. Chem.*, 370 (1994) 129
[175] C. Belmont, P. Cognet, J. Berlan, G. Lacoste, P.-L. Fabre, J.-M. Jud, *Bull. Soc. Chim. Fr.*, 134 (1997) 159
[176] C. Belmont, P. Cognet, J. Berlan, G. Lacoste, P.-L. Fabre, J.-M. Jud, *J. Appl. Electrochem.*, 28 (1998) 185
[177] F. Trabelsi, H. Aït-Lyazidi, B. Ratsimba, A.M. Wilhelm, H. Delmas, P.-L. Fabre, J.Berlan, *Chem. Eng. Sci.*, 51 (1996) 1857
[178] K. Macounova, J.Klíma, C. Bernard, C. Degrand, *J. Electroanal. Chem.*, 457 (1998) 141
[179] N.V. Dezhkunov, A.I. Kulak, A. Francescutto, *Ultrason.*, 34 (1996) 551
[180] C. Petrier, B. David, S. Laguian, *Chemosphere*, 32 (1996) 1709
[181] G. Cum, G. Galli, R. Gallo, A. Spadaro, *Ultrason.*, 30 (1992) 267
[182] A Francony, C. Petrier, *Ultrason. Sonochem.*, 3 (1996) S77
[183] C. Petrier, A. Jeunet, J.-L. Luche, G. Reverdy, *J. Am. Chem. Soc.*, 114 (1992) 3148
[184] N. Gondrexon, V. Renaudin, C.Petrier, M. Clement, P. Boldo, Y. Gonthier, A. Bernis, *Ultrason. Sonochem.*, 5 (1998) 1
[185] N. Tatsumoto, S. Fujii, N. Kawano, *Ultrason. Sonochem.*, 4 (1997) 9

2. Experimental Methods

This chapter covers the fundamental aspects of the experimental methodology employed in the following chapters. More details on each experiment and how it was performed will be given in the relevant chapters.

2.1. Sonoelectrochemistry

Sonoelectrochemical cells shown in Figure 2.1 were used. The horn used was a Sonics and Materials ultrasonic horn (model VCX 400) and operates at 20kHz (see Figure 2.2).

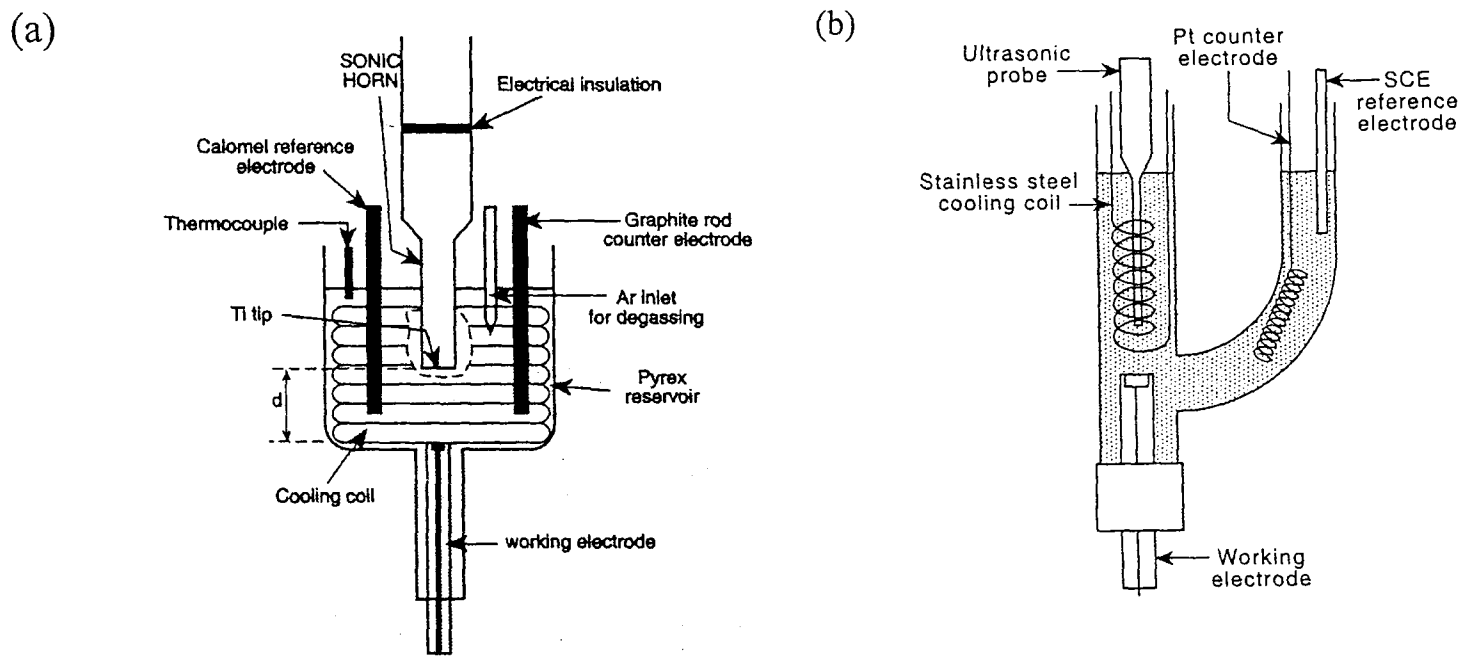


Figure 2.1 Two examples of the sonoelectrochemical cells used in this thesis (a) the large version with volume *ca.* 250ml and (b) has a volume of *ca.* 25ml.

The ultrasonic intensity was calibrated calometrically by the procedure detailed by Mason *et al.*[1,2] giving powers of up to 60 W cm^{-2} for the large horn tip and 400 W cm^{-2} for the small horn tip. The small horn tip is titanium rod of length 127 mm (1/2 wavelength) with a smaller cross sectional area whereas the large horn tip is made of titanium alloy (Ti 90%, Al 6% and V 4%) and has a diameter of 13 mm. The use of this alloy is for the following reasons

- high fatigue strength
- low acoustic loss
- chemical inertness (very significant as the horn tip must be immersed in the solution whilst operating.

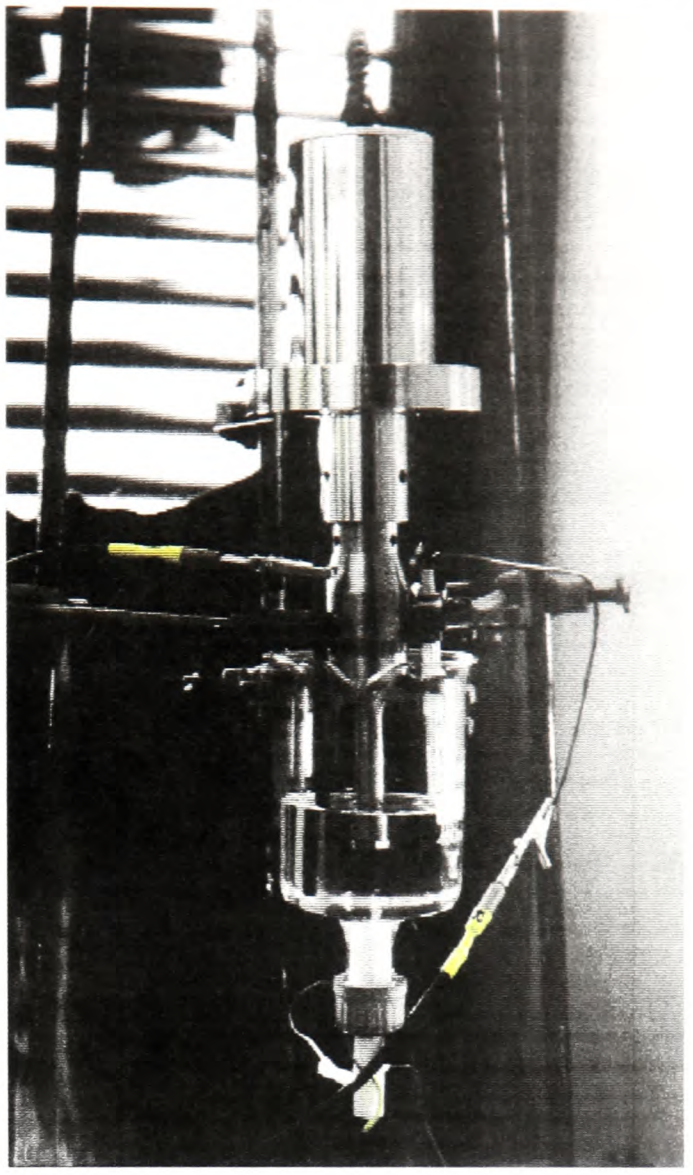


Figure 2.2 Photograph of the Ultrasonic Horn described in the text immersed in an electrochemical cell. The cooling coil is omitted for clarity.

The probe has a threaded end to allow the tip to be replaced when worn (see Figure 2.3). It also allows the insertion of '*in-house*' modified tips with platinum or gold inserts to give '*sonotrodes*' discussed in §1.5.2. The horn must be tuned for each power setting to ensure that the unit is drawing the minimum electrical power and the results obtained are more reproducible. If the horn is difficult to tune then there is a fault within the system such as a worn tip or loose connection. The ultrasound is generated by a piezoelectric crystal transducer.[3-5] When a rapidly alternating potential is applied to a piezoelectric material (e.g. $BaTiO_3$ or $PbNb_2O_6$) mechanical distortion occurs which is translated into vibrations of whatever is in contact with the material (most commonly metal blocks which additionally conduct away heat and protect the crystal). Transducers are of half wavelength multiples long such that the power is focussed at the horn tip.

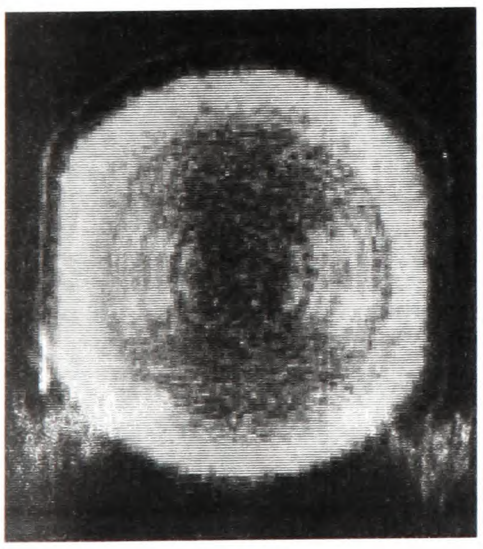


Figure 2.3 A horn tip showing considerable cavitation damage.

The cell contains a stainless steel cooling coil which

serves to regulate the temperature of the cell to ±2 °C in bulk solution. The electrodes used were glassy carbon (BAS) of 3 mm diameter measured using a travelling microscope and were polished before use using diamond lapping compounds (Kemet, Kent, UK) of decreasing size down from 25 to 1 μm, in order to eliminate the introduction of impurities into the solution from the electrode. A saturated calomel electrode (SCE) (Radiometer, Copenhagen) acted as a reference in all experiments throughout this work unless where stated while platinum or gold coil usually acted as the counter electrode. Graphite rods were occasionally also used for this purpose.

2.1.1. Calorimetric Calibration of Ultrasonic Horn Intensity

The intensity of the ultrasonic horn is simply related to the horn tip and the power supplied and is described below.

$$Intensity = \frac{power}{area} \tag{2.1.}$$

The power is dependent on the mass, m, the specific heat capacity, C_p, of the solvent and the initial slope of the temperature, T, time, t, graph

$$power = mC_p\left(\frac{dT}{dt}\right)_{t=0} \tag{2.2.}$$

To measure the temperature of the solution a Pt thermocouple was used and readings taken every 30 s for 10 minutes for different horn amplitudes. Typical results are shown in Figure 2.4.

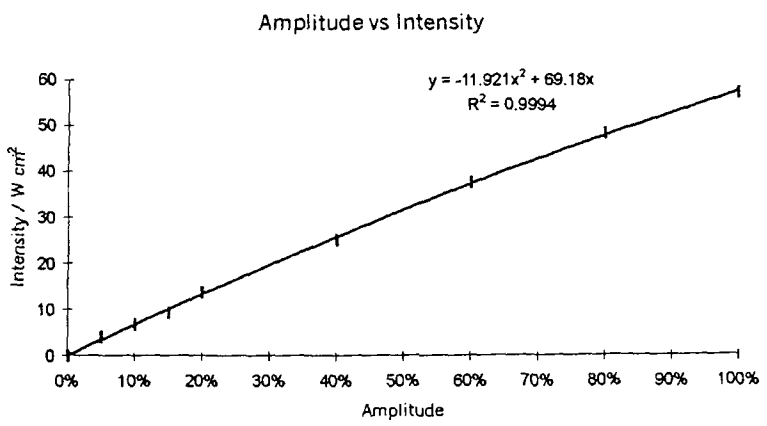


Figure 2.4 Calibration graph of ultrasound intensity against the amplitude of vibration in water.

At high amplitudes the intensity tends to stray from linearity as the ability to tune the horn decreases and the transmission of power becomes less

efficient. It can be seen from the graph that the maximum power obtainable with a large horn tip is 60 W cm^{-2} but in the '*face-on*' geometry the most common power was 30 W cm^{-2} and in the '*sonotrode*' set-up was below 10 W cm^{-2}.

2.2. Chemicals Used

See each chapter for the relevant chemicals and suppliers.

2.3. Electronics

The electronic apparatus used in the sonochemical experiments were either a Autolab® PGSTAT20 or μ-autolab (Utrecht, Netherlands). In the oil droplet work an Oxford Electronics potentiostat and a Lloyd Instruments PL3 chart recorder (Lloyd Instruments, Southampton) were used.

2.4. Rotating Disc Electrode

The electrode used in this thesis was made of glassy carbon (BAS) and sheathed in Teflon™; similar to the electrodes used in Sonoelectrochemistry but had a brass thread to allow connection to a motor for rotation (see Figure 2.5). Before use the electrode was polished in the same manner as earlier (§2.1). The electrode is rotated at different speeds (0-30 Hz) along the axis perpendicular to the electrode. The vessel is thermostatted as a change in temperature will give rise to change in viscosity and

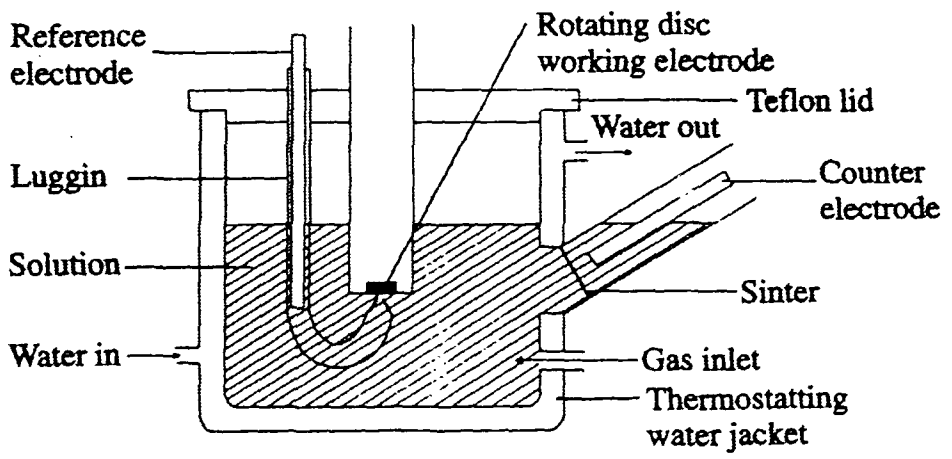


Figure 2.5 Schematic of a typical rotating disc experiment

then the Levich equation,[6] shown below, will not be any use without a known viscosity.

$$I_{lim} = 0.62nFA[x]_{\infty} D^{\frac{2}{3}} \nu^{-\frac{1}{6}} \omega^{\frac{1}{2}} \qquad (2.3.)$$

where I_{lim} is the limiting current observed n is the number of electron transferred, F is the Faraday constant, A the area of the electrode, $[x]_{\infty}$ the bulk concentration, D the diffusion coefficient of the electroactive species, ν the kinematic viscosity and ω the rotation rate (in rad s^{-1}). One can see that if the limiting current is plotted against the square root of the rotation rate a straight line graph will be obtained and the diffusion coefficient may then be determined for the gradient of the graph.

2.5. Atomic Force Microscopy

In all atomic force microscopy (AFM) experiments a Topometrix (Santa Barbara, CA) TMX 200 'Discover' SPM (scanning probe microscope) was used in contact mode by maintaining a constant deflection of laser beam from the microlever using a feedback loop (see Figure 2.6). The scans were of various sizes with a maximum vertical range of 10μm.

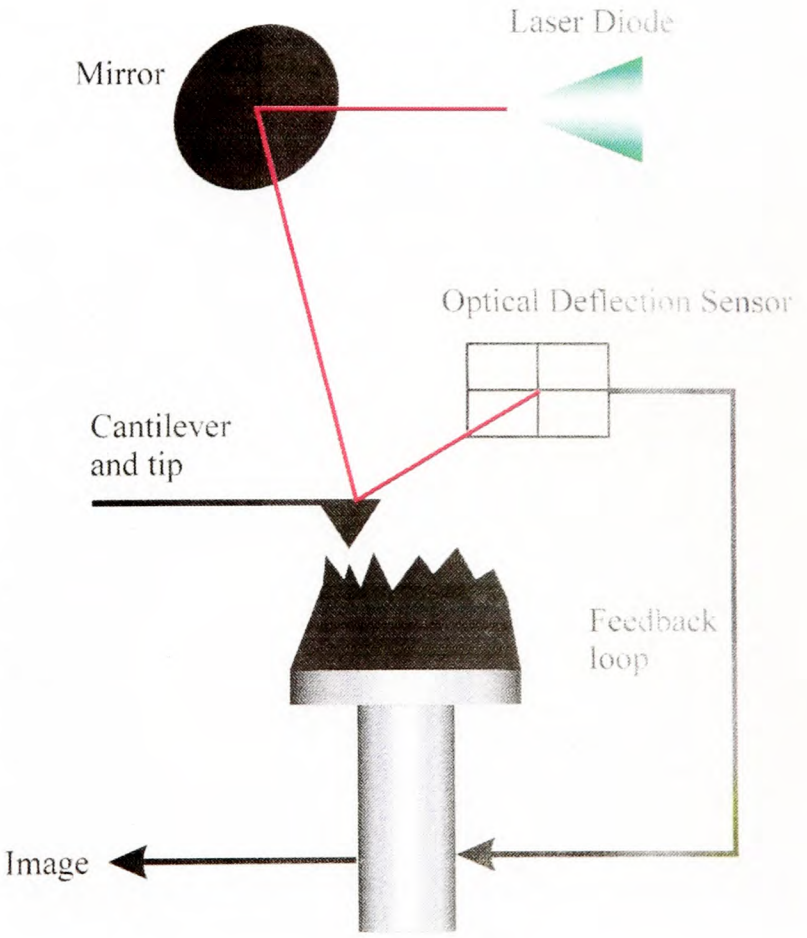


Figure 2.6 A schematic of the AFM machine.

2.6. Computation

All programs were written in either FORTRAN 77 or C/C++ and executed on a Silicon Graphics Origin™ 2000 server. Full listing of the programs used can be found in Appendix A2.

References for Chapter 2

[1] T.J. Mason, J.P. Lorimer, D.M. Bates, *Ultrasonics*, 30 (1992) 40
[2] M.A. Margulis,A.N. Mal'tsev, *J. Russ. Phys. Chem.*, 43 (1969) 592
[3] T.J. Mason, J.P. Lorimer, *Sonochemistry: Theory, Applications and Uses in Chemistry*, Ellis Horwood (1988)
[4] T.J. Mason, *Sonochemistry: the Uses of Ultrasound in Chemistry*, Royal Society of Chemistry Publications, London, (1990)
[5] T.J. Mason, J.P. Lorimer, *Practical Sonochemistry, User's Guide to Applications in Chemistry and Chemical Engineering*, Ellis Horwood (1989)
[6] V.G. Levich, *Acta Physicochim. URSS* 17 (1942) 257

3. Theory

This chapter explains the general theory used in the majority of the simulations in this thesis and discusses the relative merits of different techniques used to accomplish simulations and why the ones used in this thesis are chosen.

3.1. Finite Difference Formulation

What is meant by finite difference and how are they created? A finite difference, as its name suggests, is the difference between two distinct points in space or time. It is a mathematical tool that is used to turn a continuous, unknown function into a discretised series of points that can be fed in to a computer program and manipulated.

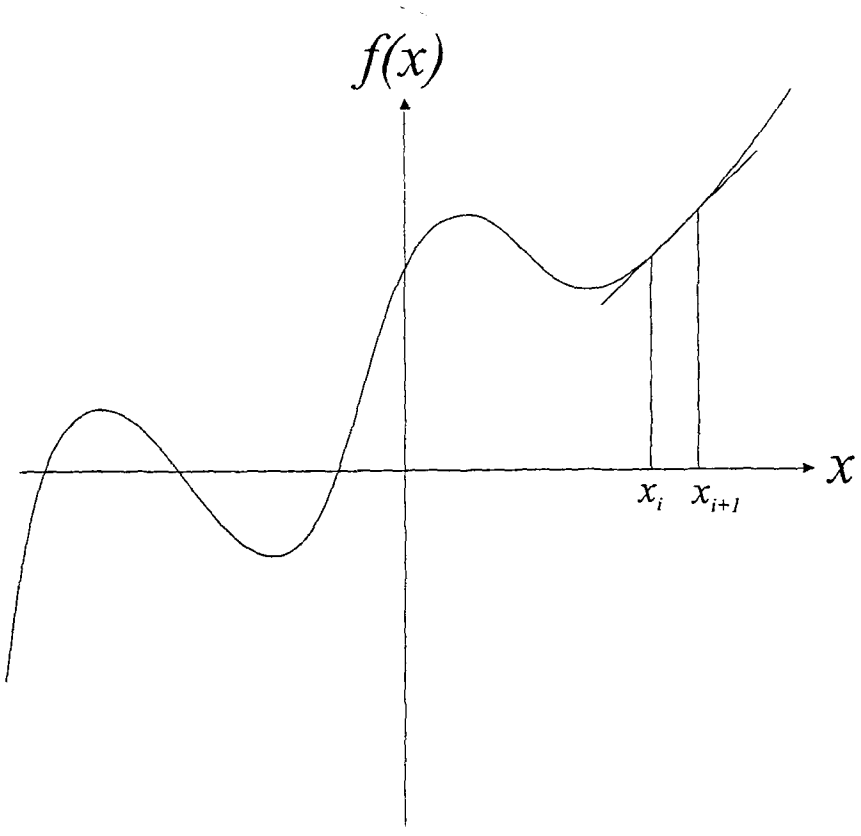


Figure 3.1 A diagram of an unknown function showing the approximation of the gradient between two points.

The origin of these stems back to the definition of a derivative in terms of two closely spaced points. Consider a function, $f(x)$, where its value at some points are known but the equation that describes it is not. An example function is shown in Figure 3.1. The gradient at any point would usually be given to us by the derivative of the function at that point. As there is no known expression for this function then the gradient must be approximated. If the value of the function is known at two points that are close in space then an approximate value for the gradient can be obtained. In this case the value of $f(x)$ is known at the points x_{i+1} and x_i. If the distance

between them is small enough then the gradient between the two points is equal to the gradient at the point that lies halfway between them. i.e.

$$f'\left(x_{i+\frac{1}{2}}\right)=\left.\frac{df}{dx}\right)_{x=x_{i+\frac{1}{2}}}\approx\frac{f(x_{i+1})-f(x_i)}{\Delta x} \tag{3.1.}$$

where

$$\Delta x = x_{i+1}-x_i \tag{3.2.}$$

Equation (3.1.) now gives a relationship between the first derivative and the values of the points of the function. There is also a finite difference formulation for the second derivative. This is easy to formulate if it is borne in mind that the second derivative is the first derivative of the gradient. i.e.

$$f''(x)=\frac{d^2f}{dx^2}=\frac{d}{dx}\cdot\frac{df}{dx} \tag{3.3.}$$

from equations (3.1.) and (3.3.) it can be inferred

$$f''(x_i)=\frac{\left(\frac{df}{dx}\right)_{x=x_{i+\frac{1}{2}}}-\left(\frac{df}{dx}\right)_{x=x_{i-\frac{1}{2}}}}{\Delta x} \tag{3.4.}$$

and turning the derivatives into finite differences using equation (3.1.)

$$f''(x_i)=\frac{f(x_{i+1})-2f(x_i)+f(x_{i-1})}{(\Delta x)^2} \tag{3.5.}$$

In the next two equations the notation used in this thesis will be defined:

$$c=c(x) \tag{3.6.}$$

i.e. c is a function of x and thus

$$\frac{d^2c}{dx^2}=\frac{c_{i+1}-2c_i+c_{i-1}}{(\Delta x)^2} \tag{3.7.}$$

where the subscript, i, of c represents the value of c at x_i and Δx the distance in the x direction between consecutive and evenly spaced points.

3.1.1. Implicit vs. Explicit Formulations

If the function to be turned into finite differences is a function of two variables there are two ways of doing this to give either an implicit or explicit relationship. e.g. consider Fickian diffusion in one dimension, x, w.r.t. to time, t (Fick's 2nd Law see § 1.2.3.1.).

$$\frac{\partial c}{\partial t} = D\frac{\partial^2 c}{\partial x^2} \tag{3.8.}$$

maybe turned in to *implicit* finite differences thus

$$\frac{c_i^t - c_i^{t-1}}{\Delta t} = D\frac{c_{i+1}^t - 2c_i^t + c_{i-1}^t}{(\Delta x)^2} \tag{3.9.}$$

where the only known value is c_i^{t-1} and the rest are unknown. The *explicit* formulation is shown below

$$\frac{c_i^t - c_i^{t-1}}{\Delta t} = D\frac{c_{i+1}^{t-1} - 2c_i^{t-1} + c_{i-1}^{t-1}}{(\Delta x)^2} \tag{3.10.}$$

and in this there is only one unknown, c_i^t. On the first glance the explicit equations appear much easier to solve than the implicit one, which to some extent they are. The major advantage is that the implicit equations are unconditionally stable whereas the explicit equations will break down if too large a time step is used.[1] A third option of mixing implicit and explicit terms will be covered later in this chapter.

3.2. Boundary Conditions

In order to make differential equations soluble *boundary conditions* must be applied along the edges of the area to be solved. These exist in two broad categories termed *Dirichlet* and *Neumann* boundaries.

3.2.1. Dirichlet Boundary Conditions

Dirichlet boundaries are when a value is imposed on the edge as in the case at the edge of a diffusion layer the concentration would be expected to be that of the bulk concentration or at the electrode the concentration would follow that of the Nernst equation or be complete destruction or generation of the species. This is applied by incorporation the value imposed into the known (t-1) side of equations (3.9.) or (3.11.).

3.2.2. Neumann Boundary Conditions

Neumann boundaries are when the boundary conditions are applied in the form of a derivative. This is most common at a cell wall when a no-flux boundary is imposed i.e.

$$\left(\frac{\partial c}{\partial x}\right)_{x=wall} = 0 \qquad (3.12.)$$

This is applied by making the concentration at the wall equal to the concentration one node in from the wall. The explicit formulation of these and how they are formally incorporated will be explained further in the chapters involving simulations.

3.3. Backwards Implicit Method (BI)

Sometimes referred to as the fully implicit Laasonen method,[2] in this method the finite differences are formulated implicitly as shown previously in (3.9.). The basis of the backwards implicit method is that we have three unknown points in general related to a known value or zero. There must be boundary conditions at the edges to allow the problem to be soluble. These may be either Neumann, Dirichlet or a combination of both.

3.3.1. Thomas Algorithm[3,4]

This is a simplified version of a Gaussian elimination for a tridiagonal matrix. The Gaussian elimination algorithm is as follows:

1. LU Decomposition: $\boldsymbol{d} = \mathbf{M}\boldsymbol{u}$; $\mathbf{M} = \mathbf{LU}$
2. Back substitution through an intermediate vector: $\boldsymbol{d} = \mathbf{L}\boldsymbol{f} \Rightarrow \boldsymbol{f} = \mathbf{L}^{-1}\boldsymbol{d}$
3. Forward substitution to give the solution: $\boldsymbol{f} = \mathbf{U}\boldsymbol{u} \Rightarrow \boldsymbol{u} = \mathbf{U}^{-1}\boldsymbol{f}$

1. An **LU** decomposition of a tridiagonal matrix may take the form:

$$\begin{bmatrix} b_1 & c_1 & & \\ a_2 & b_2 & c_2 & \\ & \ddots & \ddots & \ddots \\ & & a_N & b_N \end{bmatrix} = \begin{bmatrix} \alpha_1 & & & \\ a_2 & \alpha_2 & & \\ & \ddots & \ddots & \\ & & a_N & \alpha_N \end{bmatrix} \begin{bmatrix} 1 & \beta_1 & & \\ & 1 & \beta_2 & \\ & & \ddots & \ddots \\ & & & 1 \end{bmatrix} \tag{3.13.}$$

from the multiplication of the **L** and **U** matrices we can see:

$$b_i = a_i\beta_{i-1} + \alpha_i \qquad \text{apart from} \qquad b_1 = \alpha_1 \tag{3.14.}$$

and

$$c_i = \alpha_i\beta_i \tag{3.15.}$$

therefore the coefficients of the **LU** matrices are given by

$$\alpha_1 = b_1 \tag{3.16.}$$

$$\beta_i = \frac{c_i}{\alpha_i} \qquad \text{for} \qquad i = 1,2,\ldots,N-1 \tag{3.17.}$$

$$\alpha_i = b_i - a_i\beta_{i-1} \qquad \text{for} \qquad i = 2,3,\ldots,N \tag{3.18.}$$

2. The back substitution goes as follows:

$$\begin{bmatrix} d_1 \\ d_2 \\ \vdots \\ d_N \end{bmatrix} = \begin{bmatrix} \alpha_1 & & & \\ a_2 & \alpha_2 & & \\ & \ddots & \ddots & \\ & & a_N & \alpha_N \end{bmatrix} \begin{bmatrix} f_1 \\ f_2 \\ \vdots \\ f_N \end{bmatrix} \tag{3.19.}$$

The inversion of **L** can be accomplished by the explicit matrix multiplication of each line and rearrangement of the resulting equations thus:

$$d_1 = \alpha_1 f_1 \tag{3.20.}$$

$$d_i = a_i f_{i-1} + \alpha_i f \qquad \text{for} \qquad i = 2,3,\ldots,N \tag{3.21.}$$

therefore $\boldsymbol{f}$ is given by:

$$f_1 = \frac{d_1}{\alpha_1} \tag{3.22.}$$

$$f_i = \frac{d_i - a_i f_{i-1}}{\alpha_i} \qquad \text{for} \qquad i = 2,3,\ldots,N \tag{3.23.}$$

3. The forward substitution goes as follows

$$\begin{bmatrix} f_1 \\ f_2 \\ \vdots \\ f_N \end{bmatrix} = \begin{bmatrix} 1 & \beta_1 & & \\ & 1 & \beta_2 & \ddots \\ & & \ddots & \ddots \\ & & & 1 \end{bmatrix} \begin{bmatrix} u_1 \\ u_2 \\ \vdots \\ u_N \end{bmatrix} \tag{3.24.}$$

Again the inversion of **U** is done 'by hand' as for **L**.

$$f_N = u_N \tag{3.25.}$$

$$f_i = u_i + \beta_i u_{i+1} \qquad \text{for} \qquad i = 1,2,\ldots,N-1 \tag{3.26.}$$

therefore by rearranging we get values for the resultant vector $\boldsymbol{u}$.

$$u_N = f_N \tag{3.27.}$$

$$u_i = f_i - \beta_i u_{i+1} \qquad \text{for} \qquad i = 1,2,\ldots,N-1 \tag{3.28.}$$

The Thomas algorithm first solves in a forwards direction for $\boldsymbol{f}$ and then backwards direction for $\boldsymbol{u}$. The final solution being in the backwards directions is where this technique derives its name, the *Backwards Implicit* (BI) method.

The Thomas algorithm is stable for all values of *a, b* and *c* and is now the method of choice for solving tridiagonal matrices for linear systems or two dimensional systems that can be formulated in either a BI or ADI manner (see below). It was first

employed in electrochemistry by Anderson[5] and has received much attention in recent years.

3.4. Crank-Nicholson (CN) Method[6]

This method was invented by Crank and Nicholson[6] in 1947 and has been named after them. In the general explicit scheme the discretisation of the time derivative behaves poorly. If the derivative is centralised around $t + ½$ we can write the finite difference formulation:

$$\left.\frac{\partial c}{dt}\right)_{t=t+\frac{1}{2}} = \frac{c_i^{t+1} - c_i^t}{\Delta t} \tag{3.29.}$$

The second derivative shown below refers to centralised formulation at time t .

$$\left.\frac{\partial^2 c}{\partial x^2}\right)_{t=t} = \frac{c_{i+1}^t - 2c_i^t + c_{i-1}^t}{(\Delta x)^2} \tag{3.30.}$$

This, in the Crank-Nicholson (CN) scheme, can be shifted to $t + ½$ using a linear interpolation.

$$c_i^{t+\frac{1}{2}} = \frac{c_i^{t+1} + c_i^t}{2} \tag{3.31.}$$

thus equation (3.30.) becomes at $t + ½$

$$\left.\frac{\partial^2 c}{\partial x^2}\right)_{t=t+\frac{1}{2}} = \frac{1}{2}\left(\frac{c_{i+1}^{t+1} - 2c_i^{t+1} + c_{i-1}^{t+1} + c_{i+1}^t - 2c_i^t + c_{i-1}^t}{(\Delta x)^2}\right) \tag{3.32.}$$

thus the diffusion equation becomes

$$\frac{c_i^{t+1} - c_i^t}{\Delta t} = \frac{D}{2(\Delta x)^2}\left(c_{i+1}^{t+1} - 2c_i^{t+1} + c_{i-1}^{t+1} + c_{i+1}^t - 2c_i^t + c_{i-1}^t\right) \tag{3.33.}$$

The above equation states we are not explicitly interested at the concentrations at $t + ½$ but use it as a centre of symmetry to get good approximations on either side. Equation (3.33.) rearranges for all i as below:

$$c_{i-1}^{t+1} + ac_i^{t+1} + c_{i-1}^{t+1} = b_i^t \tag{3.34.}$$

where

$$a = -\frac{2}{\lambda}(\lambda + 1) \tag{3.35.}$$

and

$$b_i^t = -c_{i-1}^t + \frac{2(\lambda - 1)}{\lambda} c_i^t - c_{i+1}^t \tag{3.36.}$$

This is a tridiagonal system of equations which can again be solved using the Thomas Algorithm (§ 3.3.1). This method is less stable but more accurate than the BI method and has been recommended for general 1-dimensional simulations.[7] Britz[8] also reports improved efficiency by incorporating the CN scheme into Rudolph's FIFD.[9]

3.5. Alternating Direction Implicit (ADI)

This method for 2-dimension simulations was developed by Peaceman and Rachford[10] in 1955 and applied to diffusional problems by Lapidus and Pinder[11] in 1982. Considering the 2-dimensional diffusion equation:

$$\frac{\partial c}{\partial t} = D\left[\frac{\partial^2 c}{\partial x^2} + \frac{\partial^2 c}{\partial y^2}\right] \tag{3.37.}$$

In this case at a time t the discretisation in the x direction is carried out in a fully implicit manner. In the y direction this is carried out in a fully explicit manner.

$$\frac{c_{i,j}^t - c_{i,j}^{t-1}}{\Delta t} = D\left[\left(\frac{c_{i+1,j}^t - 2c_{i,j}^t + c_{i-1,j}^t}{(\Delta x)^2}\right) + \left(\frac{c_{i,j+1}^{t-1} - 2c_{i,j}^{t-1} + c_{i,j-1}^{t-1}}{(\Delta y)^2}\right)\right] \tag{3.38.}$$

which gives rise to a tridiagonal system similar to that detailed for the CN and BI schemes detailed above. At the next pass, $t + 1$, the discretisation occurs in the reverse manner, i.e. the x direction is fully explicit and y direction is fully implicit thus

$$\frac{c_{i,j}^{t+1} - c_{i,j}^{t}}{\Delta t} = D\left[\left(\frac{c_{i+1,j}^{t} - 2c_{i,j}^{t} + c_{i-1,j}^{t}}{(\Delta x)^2}\right) + \left(\frac{c_{i,j+1}^{t+1} - 2c_{i,j}^{t+1} + c_{i,j-1}^{t+1}}{(\Delta y)^2}\right)\right] \tag{3.39.}$$

This method is also detailed by Jain[12] as half time steps such that the time interval is 1/2Δt. In this case the solution of interest occurs after two iterations, i.e. from $t = t$ to $t = t + 1$. This means in practice the implementation is half as efficient but more accurate than the Lapidus and Pinder application. This method is stable and easy to implement.

3.6. Strongly Implicit Procedure (SIP)

This method, invented by Stone,[13] solves a five diagonal matrix equation of the form

$$\mathbf{q} = \mathbf{At} \tag{3.40.}$$

where **q** is a known vector of size NJ × NK and **t** is an unknown vector of size NJ × NK. **A** is pentadiagonal matrix of size (NJ × NK) × (NJ × NK) where NJ and NK are the number of nodes in the x and y direction respectively. Unlike the ADI method detailed above this is a totally implicit method. The differential equations should be cast into the following form

$$q_{i,j} = A_{i,j}t_{i,j-1} + B_{i,j}t_{i-1,j} + C_{i,j}t_{i,j} + D_{i,j}t_{i+1.j} + E_{i,j}t_{i,j+1} \tag{3.41.}$$

This method was widely used for solving heat transfer problems[14-17] but has recently been applied to electrochemistry problems.[18] The solution is obtained by modifying **A** by the addition of a matrix **B** such that **A** + **B** can be LU decomposed. The matrix equation can the be solved iteratively from an initial guess, $\mathbf{t}^{i}$, supplied by the user.

$$(\mathbf{A} + \mathbf{B})\mathbf{t}^{i+1} = \mathbf{q} + \mathbf{B}\mathbf{t}^{i} \tag{3.42.}$$

The choice of matrix **B** is discussed elsewhere.[13-17] The algorithm is available from the NAG library[19] and is converged to two criteria supplied by the user: (i) the change in residual errors between successive iterations and (ii) the residual errors after each

iteration. It is worth noting that there is a 3-dimensional analogue for this that involves a seven point system but this is computationally intensive.[20]

3.7. Multigrid Technique (MGD1)

This method was detailed by Brandt[21] in the late '70s and is an efficient way of solving a set of finite difference equations. The basis of the method is the interpolation between different grids. These are often the *optimal* method for solving these linear systems.[22] The basis of this method is that it is very easy to solve the equation of a course grid which can be interpolated to an approximation to a fine grid. The matrix equation can be written as before.

$$\mathbf{Mu} = \mathbf{b} \tag{3.43.}$$

where **M** is the known banded matrix, **u** is the unknown vector and **b** is the known vector. The equation (3.43.) can be solved iteratively from a starting approximation $\mathbf{u}_0$. the residual at the i^{th} iteration is given by

$$\mathbf{r}_i = \mathbf{b} - \mathbf{M}\mathbf{u}_i \tag{3.44.}$$

The residual is related to the error, $\mathbf{e}_i$,

$$\mathbf{e}_i = \mathbf{M}^{-1}\mathbf{r}_i \tag{3.45.}$$

Equation (3.45.) can also be expressed as a linear system analogous to (3.43.) and can also be solved iteratively (or directly). The error is then applied to the i^{th} approximation to get a new approximation.

$$\mathbf{u}_{i+1} = \mathbf{u}_i + \mathbf{e}_i \tag{3.46.}$$

This is repeated until the residual and error have values within those specified by the user. In a linear multigrid method the residuals and errors are restricted to the course grid, i.e. $\mathbf{Me} = \mathbf{r}$ is only solved on the course grid, and then interpolated up to the fine

grid and used to correct the solution. To allow the reader to visualise this method it is easier to describe the solver for a 2-level scheme, i.e. a coarse and fine grid only.

- An initial value of $\mathbf{u}_0$ for the fine grid is provided.
- $\mathbf{u}_0$ is 'smoothed' usually by using a few iterations of linear solver such as Gauss-Siedel.
- The residual is then calculated.
- The residual is then mapped onto the coarse grid using a weighted average technique. Also **M** must be mapped to the course grid by either using the finite differences for course grid or by use of a Galerkin operator:
- The system is then solved for equation (3.45.) to give the errors for the coarse grid.
- The errors are then interpolated up to the fine grid, usually the opposite of the mapping procedure used for the residual.
- $\mathbf{u}_1$ is then calculated from (3.46.) and the next iteration begins. This repeats until the value of $\mathbf{r}_i$ falls below a threshold value.
- The final solution is smoothed at the end to 'clean-up' the vector.

In many multigrid methods instead of just two levels, the steps are repeated onto increasingly coarser meshes. The greater the number of mesh levels, the greater the efficiency. Multigrid methods are not always appropriate for solving some systems. If the system is off diagonally dominant, i.e. the terms from the first derivation contribute more than the second derivative the method may fail. This is expressed for a finite difference stencil of

$$\begin{aligned} b_{j,k} = {} & A^6_{j,k}u_{j+1,k-1} + A^7_{j,k}u_{j+1,k} \\ & A^3_{j,k}u_{j,k-1} + A^4_{j,k}u_{j,k} + A^5_{j,k}u_{j,k+1} \\ & + A^1_{j,k}u_{j-1,k} + A^2_{j,k}u_{j-1,k+1} \end{aligned} \qquad (3.47.)$$

the condition for diagonal dominance is

$$\left|A^4_{j,k}\right| > \sum_{i\neq 4}\left|A^i_{j,k}\right| \qquad \text{for all } j \text{ and } k \tag{3.48.}$$

If this condition is strongly violated then divergence may occur. The NAG FORTRAN library supplies a multigrid routine.[23] For the condition in (3.48.) it is recommended by NAG to try the routine to see if it works rather than calculate if it is true for all j and k.

References for Chapter 3

[1] J.A. Alden, R.G. Compton, *J. Electroanal. Chem.*, 402 (1996) 1
[2] P Laasonen, *Acta Maths*, 81 (1949) 309
[3] G.H. Bruce, D.W. Peaceman, H.H. Rachford, J.D. Rice, *Trans. Am. Inst. Min. Engrs. (Petrol Div.)*, 198 (1953) 79
[4] L.H. Thomas, *Elliptic problem in linear difference equations over a network*, Watson Sci. Comput. Lab. Rept., Columbia University, New York (1949)
[5] J.L Anderson, S. Moldoveanu, *J. Electroanal. Chem.*, 179 (1984) 107
[6] J. Crank, P.Nicholson, *Proc. Cam. Phil. Soc.*, 43 (1947) 50
[7] M. Stözbach, J. Heinze, *J. Electroanal. Chem.*, 346 (1993) 1
[8] D. Britz, *J. Electroanal. Chem.*, 352 (1993) 17
[9] M. Rudolph, *J. Elctroanal. Chem.*, 314 (1991) 13
[10] D.W. Peaceman, H.H. Rachford, *J. Soc. Industr. Appl. Maths*, 3 (1955) 28
[11] L. Lapidus, G.F. Pinder, *Numerical Solutions of Partial Differentials Equations in Science and Engineering*, (John Wiley, New York, 1982)
[12] M.K. Jain, *Numerical Solution of Differential Equations* (2nd Ed, Wiley Eastern Ltd, 1984)
[13] H.L. Stone, *SIAM J. Num. Anal.*, 5 (1968) 530
[14] R.W. Walters, D.L. Dwoyer, H.A. Hassan, *AIAA Journal*, 24 (1986) 6
[15] K.H. Chen, R.H. Pletcher, *AIAA Journal*, 29 (1991) 1241
[16] M. Zedan, G.E. Schneider, *Num. Heat Transfer*, 8 (1985) 537
[17] G.E. Schneider, M. Zedan, *Num. Heat Transfer*, 4 (1981) 1
[18] R.G. Compton, R.A.W. Dryfe, R.G. Wellington, J. Hirst, *J. Electroanal. Chem.*, 383 (1995) 13
[19] Subroutine D03EBF – © NAG, Oxford.
[20] J.A. Alden, *Part II Thesis*, University of Oxford, (1995)
[21] A. Brandt, *Math. Comp.*, 31 (1977) 333
[22] W.H. Press, S.A. Teukolsky, W.T. Vetterling, B.P. Flannery, *Numerical Recipes in C* (2nd Ed, CUP, Cambridge, 1992) pp871-888
[23] Subroutine D03EDF – © NAG, Oxford.

4. Copper Acetate Solutions – Sono-ASV on Bare Glassy Carbon Electrodes and the Solution Kinetics

4.1 Introduction

The use of mercury electrodes for Anodic Stripping Voltammetry (ASV) is widespread. With legislation pending in the EU[1] and the complete ban on the use of mercury in Japan[2] and Sweden[3,4] an alternative for mercury must be found. The aim of this chapter is to explore the possibility of using bare glassy carbon electrodes for the ASV of copper in chemically complex media. In particular acetate buffer was chosen as the system in which copper forms many complexes and so allows an investigation into how these complexes may affect the results. Although this is not a true 'dirty' (i.e. real world) system, we can effectively characterise the system and it can provide a model for a real system such as effluent from an acetic acid plant. This assumption is discussed in appendix A1 using real data from BP Chemicals Ltd acetate plant in Hull, UK. This chapter will take a stepwise approach to the problem: first, a general solution will be derived for the speciation of a multi-complex system and then applied to the copper acetate system. Second, the results will then be applied in order to determine the relative and actual diffusion coefficients of each species present. Third, a simple kinetic study is carried out to determine whether the speciation will affect the ASV determination and then finally the validity of the ASV approach adopted in light of the conclusions from the earlier sections will be verified.

4.2 Characterisation of the Speciation of Copper (II) in Aqueous Acetate Buffer

In the first instance a general solution to the complexation question will addressed. In solutions there is considered to be the following species: the simple hydrated ion which we will term M^{Z+} and the substituted ions from the mono substituted to the n-substituted ion, i.e. $ML^{(Z-1)+}$ to $ML_n^{(Z-n)+}$,[5-8] where L^- denotes the complexing counter ion.

4.2.1 Formulation of Equations

In order to characterise the speciation we must first consider the equilibrium below

$$M^{Z+} + LH \rightleftharpoons L^- + H^+ + \ldots + ML_i^{(Z-i)+} + \ldots + ML_n^{(Z-n)+} \qquad (4.1.)$$

where $i = 1,2,\ldots,n$ and n is the maximum number of ligands that can be complexed to the metal ion. The initial concentrations of M^{Z+}, LH and L^- are known and assigned the concentrations x, y and z respectively. At equilibrium the concentrations of M^{Z+}, LH, L^- and H^+ are unknown and are assigned the variables a, b, c and d respectively. The concentration of a species $ML_i^{(Z-i)+}$ is assigned the variable u_i. These variables are summarised in Table 4.1.

Species	M^{Z+}	LH	L^-	H^+	$ML_i^{(Z-i)+}$
Initial Concentration	x	y	z	0	0
Concentration at equilibrium	a	b	c	d	u_i

Table 4.1 Summary of the variables representing concentrations

At equilibrium we formulate relations for a, b and c in terms of x, y, z, d and u_i thus:

$$a = x - \sum_{i=1}^{n} u_i \qquad (4.2.)$$

$$b = y - d \tag{4.3.}$$

$$c = z + d - \sum_{i=1}^{n} \frac{u_i}{i} \tag{4.4.}$$

The concentration u_i is given by

$$u_i = K_i u_{i-1} c \tag{4.5.}$$

where K_i is the stability constant and is defined.[9]

$$K_i = \frac{\left[ML_i^{(Z-i)+}\right]}{\left[ML_{i-1}^{(Z-i+1)+}\right]\left[L^-\right]} = \frac{u_i}{u_{i-1}c} \tag{4.6.}$$

For the gross addition of ligands we introduce β_i where:

$$\beta_i = \frac{\left[ML_i^{(Z-i)+}\right]}{\left[M^{2+}\right]\left[L^-\right]^i} = \frac{u_i}{ac^i} \tag{4.7.}$$

where β_i can also be defined as

$$\beta_i = \prod_{j=1}^{i} K_j \qquad \text{and} \qquad u_i = \beta_i a c^i \tag{4.8.}$$

We also need to account for the acid constant, pK_a, which is defined as*

$$pK_a = -\log_{10} \frac{\left[H^+\right]\left[L^-\right]}{\left[HL\right]} \tag{4.9.}$$

For a monobasic acid in terms of d we get:

$$d = \frac{b}{c} \cdot 10^{-pK_a} \tag{4.10.}$$

If all the above equations are combined to a single equation in terms of c only we get a function $f(c)$:

---

* The activity coefficients are neglected in the definition of the pK_a and the stability constants as this is the manner in which they are defined in Sillén.[9]

$$f(c) = z + \frac{y \cdot 10^{-pK_a}}{(c + 10^{-pK_a})} - \frac{x\sum_{i=1}^{n} \frac{\beta_i c^i}{i}}{1 + \sum_{i=1}^{n} \beta_i c^i} - c = 0 \qquad (4.11.)$$

This allows the equation to be solved for c in the manner described in §4.2.3 .

4.2.2 Acetate Complexations and Dimerisations

In acetate buffer solutions the situation becomes more complex due to dimerisation reactions that must also be considered.[10] These are shown below:

$$HA + A^- \overset{K_{12}}{\rightleftharpoons} HA_2^- \qquad (4.12.)$$

$$H^+ + HA_2^- \overset{K_{22}}{\rightleftharpoons} H_2A_2 \qquad (4.13.)$$

and

$$2HA \overset{K_D}{\rightleftharpoons} H_2A_2 \qquad (4.14.)$$

where A^- denotes the acetate counter ion, CH_3COO^- and replaces L^- from the previous section. The constants K_{12}, K_{22} and K_D are also related to the pK_a of the acid.

$$[H^+] = \frac{K_a[HA]}{[A^-]} \qquad and \qquad [H^+] = \frac{[H_2A_2]}{K_{22}[HA_2^-]} \qquad (4.15.)$$

where $[H_2A_2] = K_D[HA]^2$ and $[HA_2^-] = K_{12}[HA][A^-]$

such that $K_a = \frac{K_D}{K_{22}K_{12}}$ and therefore

$$pK_a = -\log_{10}\frac{K_D}{K_{22}K_{12}} \qquad (4.16.)$$

Copper in acetate buffer is known to have up to five different species ranging from the unsubstituted ion, Cu^{2+}, to the quadruply substituted ion, CuA_4^{2-}.[5-9,11] When the metal concentration is small compared to the acetate concentration then the fifth species can

be ignored as it exists in only very small amounts in solution (typically <0.1%).[5] The value of the dimerisation constants for acetate and the dissociation constants for Cu^{2+} in acetate buffer are listed in Table 4.2.

$\log_{10} K_1$	1.65±0.02[5]
$\log_{10} K_2$	1.00±0.06[5]
$\log_{10} K_3$	0.36±0.13[5]
$\log_{10} K_{12}$	-0.34±0.03[10]
$\log_{10} K_{22}$	4.63±0.01[10]
$\log_{10} K_D$	-0.73±0.03[10]
pK_a	4.61±0.02[11]

Table 4.2 The stability constants for Cu^{2+} in acetate buffer solution at 298K.

In this case the solutions can again be solved but the function is much more complicated:

$$f(c) = b + K_a \frac{b}{c} + K_{12} bc + 2K_D b^2 - y \tag{4.17.}$$

where

$$b(c) = \left[z - c - \frac{x \sum_{i=1}^{n} \frac{\beta_i c^i}{i}}{1 + \sum \beta_i c^i} \right] \Bigg/ \left(K_{12} c - \frac{K_a}{c} \right) \tag{4.18.}$$

and c denotes the equilibrium concentration of A^-.

4.2.3 Solution of Equations

The two situations above can both be solved numerically by the Newton-Raphson method.[12] This method is the most celebrated method for one-dimensional root

routines. The method derives from the familiar Taylor series expansion of a function in the neighbourhood of a point,

$$f(x+\delta) \approx f(x) + f'(x)\delta + \frac{f''(x)}{2}\delta^2 + \ldots \qquad (4.19.)$$

For small values of δ and a well behaved function the non-linear terms can be ignored, hence if $f(x + \delta) = 0$ then

$$\delta = -\frac{f(x)}{f'(x)} \qquad (4.20.)$$

If we start far from the root this may include a local maximum or minimum which is the death of the method so the initial guess must be close to the root. This is because the higher order terms are important and equation (4.20.) is grossly inaccurate. If the function chosen is suitable then the method is very powerful as it converges very quickly but there are cases when this is not true. These two cases are:

i) when the method solves a root to be a maximum or minimum and the solution shoots off into space. See Figure 4.1

ii) when the solution enters a non-convergent cycle. See Figure 4.2. These can both be avoided by a better initial guess.

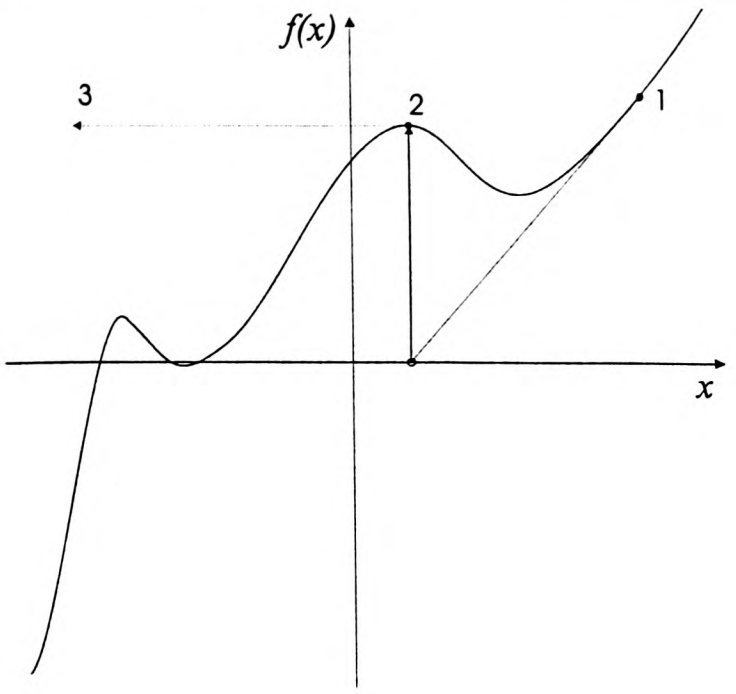


Figure 4.1 Case where Newton's method encounters a local extremum and shoots off into space

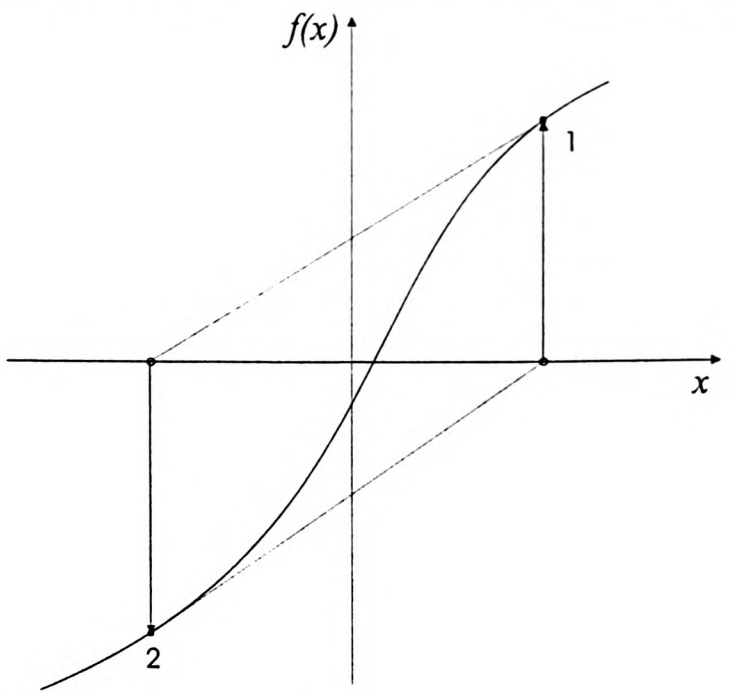


Figure 4.2 Case when Netwon's method enters a non-convergent cycle.

To avoid these situations the solver's return value is set to be between two limits. In this case the limits are $z + y$ and $z - x$. The upper limit corresponds to the conservation of matter and the lower limit to complete complexation of the metal and no acid dissociation. If the metal concentration is greater than that of the complexing ion the lower boundary will be set to zero. The solver will also check if these upper and lower boundaries fall either side of the root. If convergence is not met from one boundary then the other is used.

4.2.4 World Wide Web (WWW) Solver

These solvers have been written in C (listing can be found in appendix A2). The program strategy is shown in Figure 4.3 using a pre-written routine for the Newton-Raphson solver,[13] and can be run from the World Wide Web (WWW) at http://physchem.ox.ac.uk:8000/research/buffer/buffer_menu.shtml.

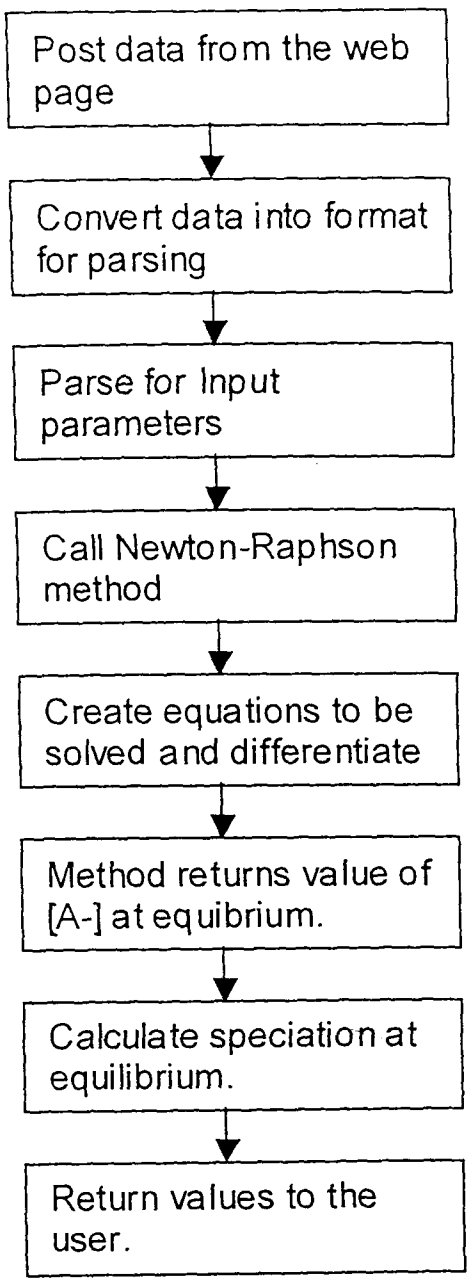


Figure 4.3 The strategy of the web solver.

The web page itself is relatively simple to use. The user inputs the initial concentrations of the acid, counter ion and the metal ion; the user must also input the stability constants for all the metal complexes and then send the data. The computer in Oxford then runs the solvers and returns the relative speciation and also, in the carboxylic acid case, the acetate speciation. The solver can solve any number of metal species as the program has a built-in differentiation routine for power terms. Some sample results are shown in Table 4.3.

These results can be compared to speciation curves from the values of K_i given in ref. 5 and at the predicted values of pH good agreement is observed in the relative concentrations. Figure 4.4 shows a speciation profile for 0.1 M AcONa / 0.05 M AcOH buffer solution and the buffer calculator gives a pH of 4.91 which then gives rise to excellent agreement (within 1%) with the relative copper speciation given by the curves in Figure 4.4. Slight discrepancies occur as the speciation curves do not take into account the dimerisation of the acetic acid as does the buffer calculator.

	$-\log_{10}[H^{+}]$	$\%Cu^{2+}$	$\%CuA^{+}$	$\%CuA_2$	$\%CuA_3^{-}$	$\%H_2A_2$	$\%HA_2^{-}$
[AH] = 0.05 M $[A^{-}]$ = 0.1 M $[Cu^{2+}]$ = 5 mM	4.91	10.1	42.1	39.4	8.4	0.3	1.3
[AH] = 0.05 M $[A^{-}]$ = 0.1 M $[Cu^{2+}]$ = 1 mM	4.92	9.6	41.4	40.2	8.9	0.3	1.4
[AH] = 0.025 M $[A^{-}]$ = 0.05 M $[Cu^{2+}]$ = 5 mM	4.89	24.5	50.1	22.9	2.4	0.2	0.7
[AH] = 0.025 M $[A^{-}]$ = 0.05 M $[Cu^{2+}]$ = 1 mM	4.91	23.0	50.0	24.3	2.7	0.2	0.7
[AH] = 0.05 M $[A^{-}]$ = 0.1 M $[Cu^{2+}]$ = 0.05 M	4.69	18.8	48.9	28.5	3.8	0.3	0.9

Table 4.3 A table of sample results for copper speciation in acetate buffer. %Cu is calculated as the percentage of species present compared with the total amount of copper present. $\%H_2A_2$ and $\%HA_2^{-}$ are the percentage present of the total concentration of A, i.e. $[HA]+[A^{-}]$.

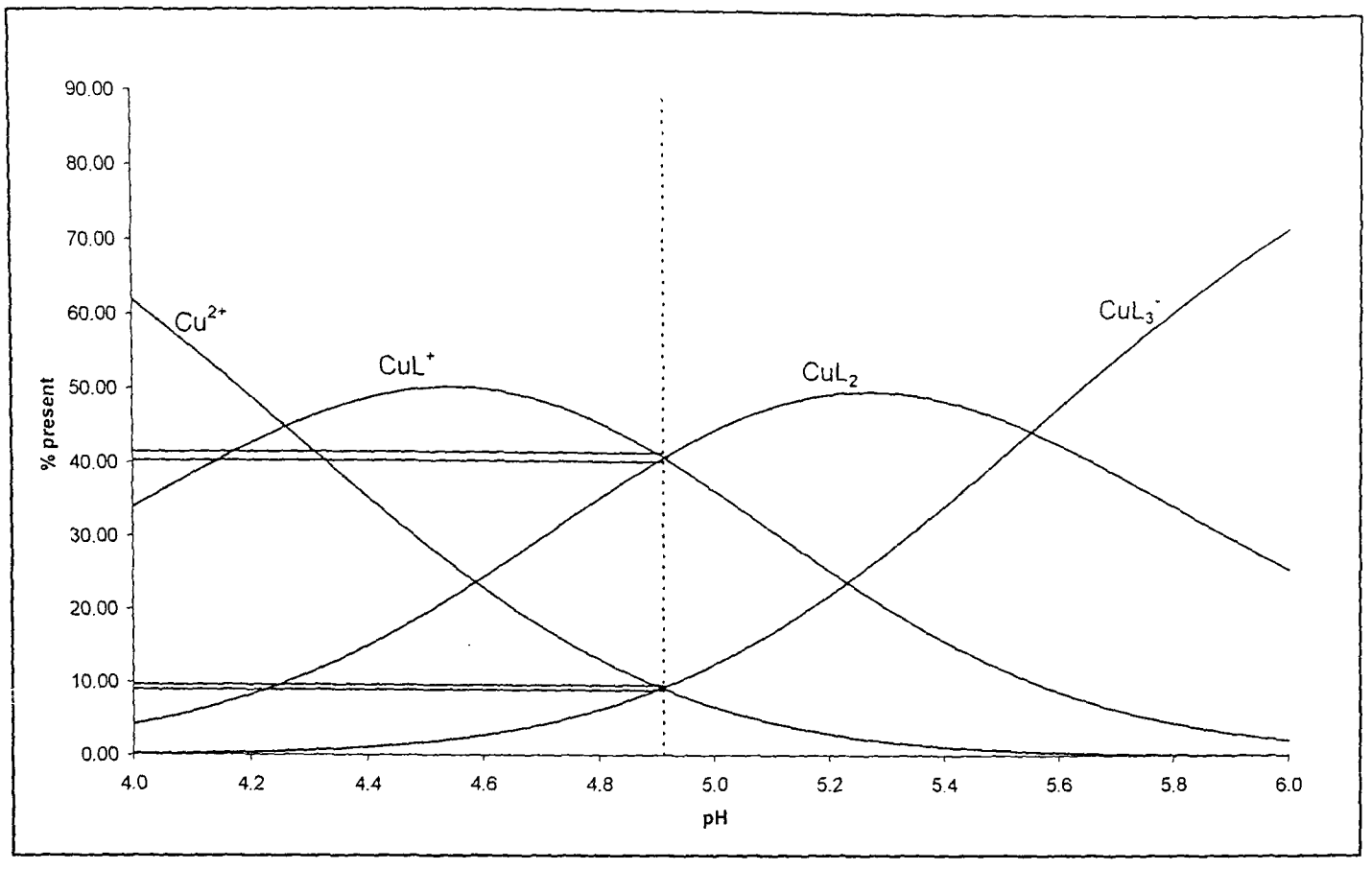


Figure 4.4 Speciation profile for 0.1M AcONa, 0.05M AcOH with Cu^{2+} present. The concentration of Cu^{2+} affects the pH of the solution which would be measured experimentally.

4.3 Calculation of Diffusion Coefficients of each Species

To calculate the diffusion coefficient of the copper species a Rotating Disc Electrode (RDE) was used. This is a commonly employed hydrodynamic electrode due its simplicity to use. The experimental details can be found in a preceding chapter. The rotating action spins solutions from the surface of the electrode and consequently draws free solution towards the disc. This maintains a steady supply of the electroactive material to the electrode surface. The Reynolds number for the RDE is defined

$$\mathrm{Re} = \frac{\omega r_c^{\,2}}{\nu} \qquad (4.21.)$$

where ν the kinematic viscosity of the solution ($cm^2\ s^{-1}$), r_c is the radius of the cylinder within which the electrode is housed (cm) and ω is the rotation speed of the electrode (rad s^{-1}). Provided Re does not exceed 10^5 the flow within the solution is laminar[14] and has the pattern shown in Figure 4.5. The convective flow can be characterised

precisely but of particular importance is the component of the flow normal to the electrode surface. The velocity in the *z*-direction, v_z, close to the surface is known to be:

$$v_z \approx -Cz^2 \qquad (4.22.)$$

where $C = 0.510\omega^{\frac{3}{2}}\nu^{\frac{1}{2}}D^{-\frac{1}{3}}$ which shows that as the rotation speed increases, so does the velocity to the surface. Under steady state conditions the diffusion and convection of material is given by

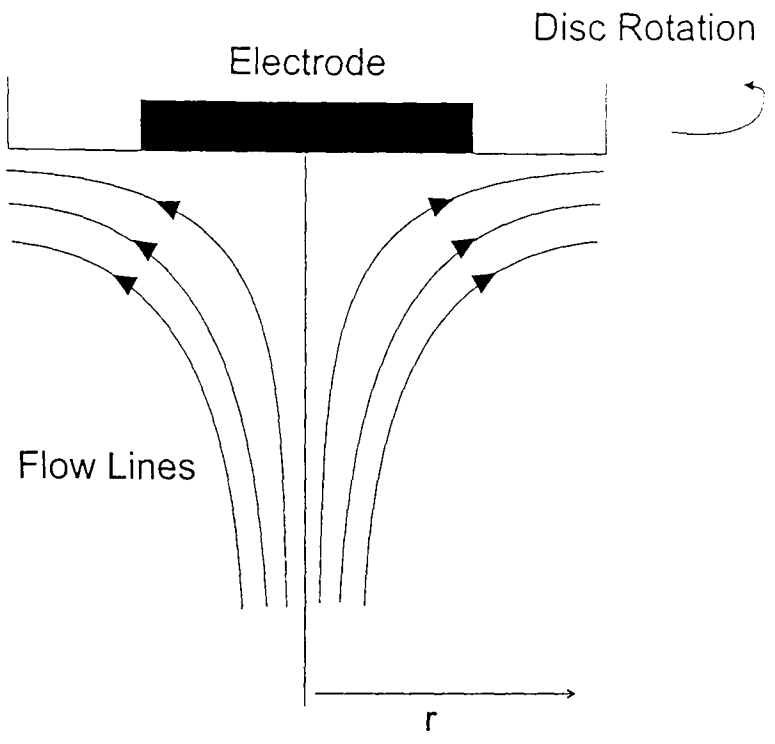


Figure 4.5 Laminar Flow lines at the rotating disc electrode.

$$\frac{\partial[\ ]}{\partial t} = D\frac{\partial^2[\ ]}{\partial z^2} - v_z\frac{\partial[\ ]}{\partial z} = 0 \qquad (4.23.)$$

Assuming the concentration of the active species to be zero at the electrode surface the transport limited current is described below

$$I_L = 0.62nFA[\ ]_\infty D^{\frac{2}{3}}\nu^{-\frac{1}{6}}\omega^{\frac{1}{2}} \qquad (4.24.)$$

where n is the no. electrons involved, F is the Faraday constant (96485 C mol^{-1}), A is the area of the electrode (cm^2), $[\ ]_\infty$ the bulk concentration (mol cm^{-3}) and D the diffusion coefficient (cm^2 s^{-1}). This is the Levich equation for the RDE.[15] Next the Levich equation is adapted to aid the interpretation of the limited current observed for the copper acetate complex system.

We will assume that each species present will contribute to the limiting current in the Levich manner according to their equilibrium concentrations. i.e. the Levich equation for the observed limiting current becomes a sum of the individual currents for each species:

$$I_L = 0.62FA\nu^{-\frac{1}{6}}\omega^{\frac{1}{2}}\sum_{i=0}^{n}\left[ML_i^{(Z-i)+}\right]D_i^{\frac{2}{3}} \qquad (4.25.)$$

where i is the number of ligands and D_i is the Diffusion coefficient of species i. $D_{Av.}$ is defined by the following equation

$$D_{Av.}^{\frac{2}{3}}\left[M_{(tot)}\right] = \sum_{i=0}^{n}\left[ML_i^{(Z-i)+}\right]D_i^{\frac{2}{3}} \qquad (4.26.)$$

where $[M_{(tot)}]$ is the total concentration of metal ion species. From experiment the only discernible parameter is the value of $D_{Av.}$. In order to find this value the following experiments were performed. Two solutions of 5 mM Cu^{2+} were made up in acetate buffer in purified water. One solution was 1 M AcONa, 0.5 M AcOH and the second 0.5 M AcONa, 0.25 M AcOH. The apparatus was set up as detailed in chapter 2. To perform the experiments the electrode was rotated at various speeds and a linear voltammetric sweep performed for each speed between 0.5 V and -0.8 V at a scan rate of 10 mV s^{-1}. These gave rise to sigmoidal shaped curves with a transport limited current, I_L. The value of $D_{Av.}$ is calculated from the RDE experiment by plotting I_L against $\omega^{0.5}$ with the gradient of the straight line plot being a function $D_{Av.}$. Then using the buffer calculators developed in §4.2 we find the relative concentrations of the species and then consequently the diffusion coefficients of the individual species using an iterative method. The method used is the Generalised Reduced Gradient (GRG2) non-linear optimisation which can be operated simply using Microsoft (MS) Excel's solver function. The boundaries set for the results were solved by incorporating them into above GRG2 solver using the Simplex method.[16,17] The boundaries set on the solutions were as follows: As the value for $D_{Av.}$ was always less than that expected for unsubstituted copper then it could be assumed that substituted copper species have slower diffusion coefficients. The next assumption was that the

more substituted the metal ion the larger its size and hence the slower it diffuses i.e. $D_0 > D_1 > D_2 > D_3$ and that D_0 was taken to be the literature value.† Using these assumptions approximate values for the diffusion coefficients of the metal ion species were obtained (see Table 4.4). The use of two solutions was to gain two different values for $D_{Av.}$ and complete the iteration procedure to give two sets of values for D_i. These were found to be similar and the results quoted in Table 4.4 are the average values for the two experiments.

i	D_i / (10^{-5} cm^2 s^{-1})
0	0.800 ± 0.05
1	0.680 ± 0.05
2	0.615 ± 0.05
3	0.123 ± 0.05

Table 4.4 The calculated diffusion coefficients for Cu^{2+} species in acetate buffer. Calculated by taking into account acetate dimerisations.[10]

In the results presented in Table 4.4 the value for D_3 is anomalously low. This might be attributed to kinetic processes of a CCCE nature inhibiting the electrode process; nevertheless the reasonable values for D_0 through to D_2 suggest the validity of the approach at least to the first order. The method used for calculating the diffusion coefficients has accounted for the kinetic parameter within the diffusion coefficient for CuL_3^- ion. Calculating four values from two experiments was achieved using a simple curve fitting mechanism readily available through MS Excel and detailed earlier in this section. This in turn will then affect the later figures in §4.4. The true limiting current will be larger and the contribution from the CCCE mechanism much

† 0.8×10^{-5} cm^{2}s^{-1} J.C. Ball, *Part II Thesis*, University of Oxford, (1997)

greater. This will be acknowledged later.

4.4 Calculations of Insonated Diffusion Layer Thicknesses and Current Contribution per Species for Deposition.

The coupling of ultrasound with electrochemistry has been detailed in §1.5. In this section we wish to discover if the speciation will affect the deposition stage. The ultimate aim is to see whether the ASV determination will work from a calibration curve or an *in situ* micro-addition approach. In order to evaluate this a simple kinetic study must be carried out. The most probable mechanisms to be encountered would be a mechanism of the CE type, when there is one or more chemical steps before the electrochemical step, such that the metal ion must shed its complexation sphere before being reduced. i.e.

$$CuA_4^{2-} \rightleftharpoons CuA_3^{-} \rightleftharpoons CuA_2 \rightleftharpoons CuA^{+} \rightleftharpoons Cu^{2+} \xrightarrow{+2e^-} Cu \qquad (4.27)$$

To determine which equilibrium is slow on the timescale of the deposition, i.e. the complex at which the C mechanism begins, the following approach is taken. The diffusion layer thickness must be calculated using a calibration species. Using these thicknesses we can calculate the expected contribution per species to the insonated limiting current. If the limiting current is then plotted against the inverse of the diffusion layer it will show where the observed current lies and give an indication of where the chemical step becomes important. To calibrate the diffusion layer it has been shown that the ultrasonic diffusion layer follows Nerstian behaviour[18] and in aqueous solutions exhibit hydrodynamic behaviour.[19] This suggests using a calibration solution of a species with a well defined diffusion coefficient, in this case

$Ru(NH_3)_6^{2+}$,‡ to approximate the diffusion layer for different ultrasound powers and horn to electrode separations using the Nernst diffusion layer equation

$$I_L = \frac{nFAD[\ ]_\infty}{\delta} \qquad (4.28.)$$

where δ is the diffusion layer thickness (cm). Once having calibrated the diffusion layer thickness, using the diffusion coefficients in Table 4.4, the contribution to the limiting current expected due to insonation can then be easily calculated. Figure 4.6 and Figure 4.7 both show plots of limiting current I_L against δ^{-1} for all the species and the experimental results. For large diffusion layers the experimental points fall between the CuL_2 and the CuL_3 lines suggesting a CE mechanism. Conversely for small diffusion layers they lies below the CuL_2 line suggesting a CCE mechanism. Although the data presented does not allow rigorous kinetic parameters to be extracted it proposes some very fundamental points to be borne in mind for the next stage, the sono-ASV detection of copper in complex systems.

As mentioned earlier, the diffusion coefficient of D_3 value is likely to be too low. The effect in the present calculations is that the limiting current for the non-kinetic case would be larger and the contribution to the current from the CuL_3^- ion would be greater. The points would therefore all lie in the CCE mechanism region and this will be the dominant kinetic control imposed on the experiment.

---

‡ 0.91×10^{-5} cm^2 s^{-1}:

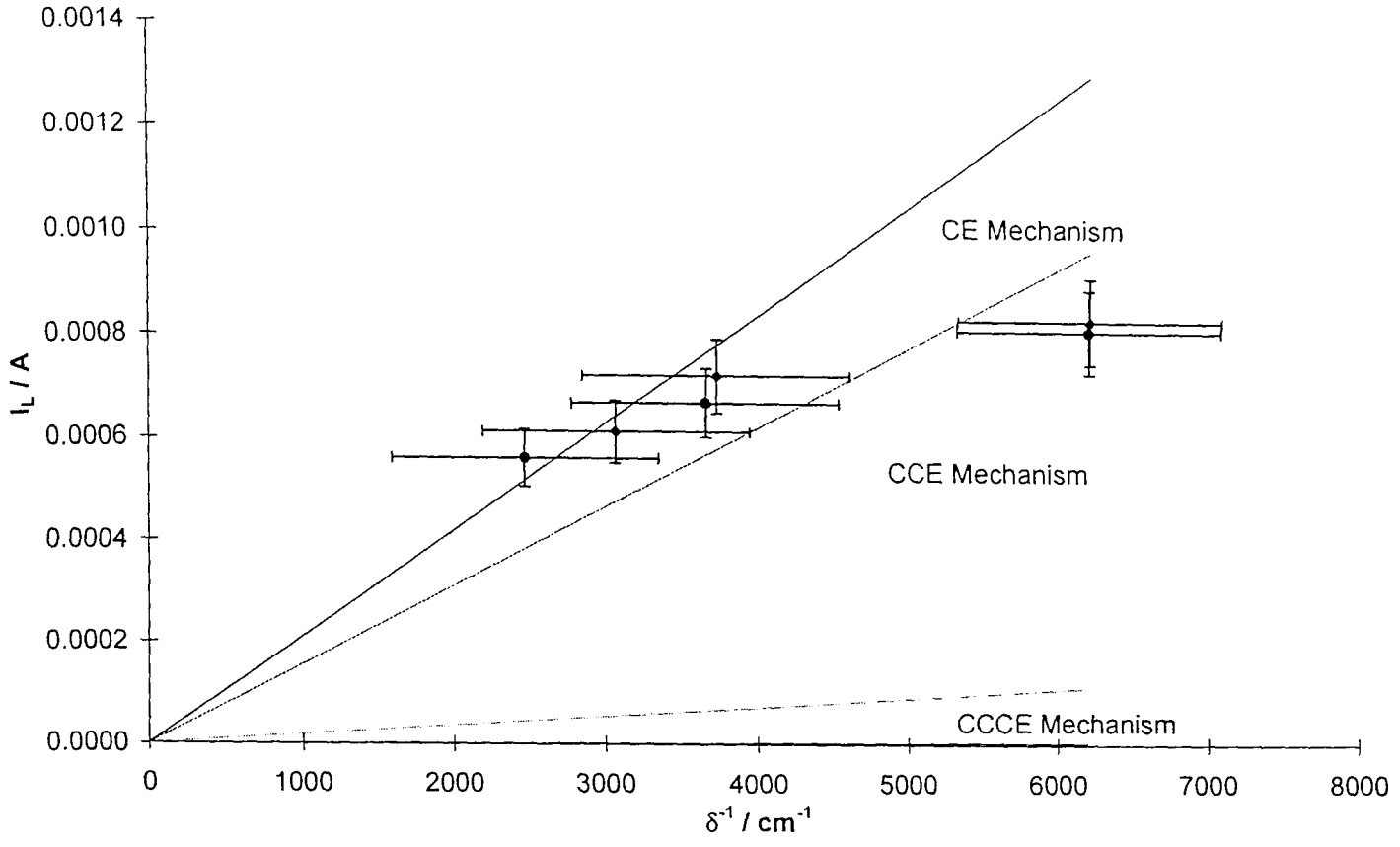


Figure 4.6 A plot of Limiting Current (I_L) / A *vs.* δ^{-1} / cm^{-1} for 0.5 M AcO^-, 0.25 M AcOH, 5 mM Cu^{2+}

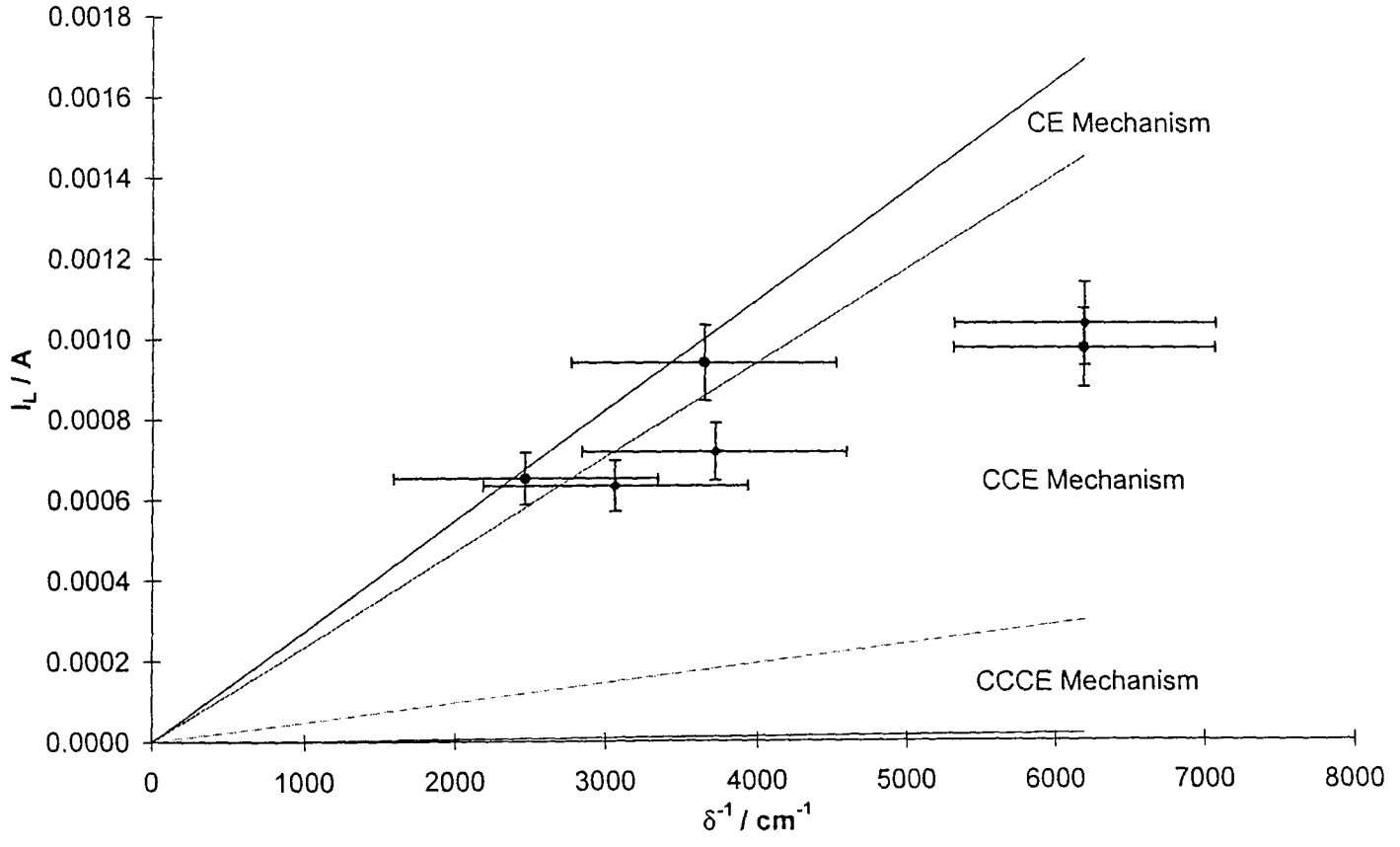


Figure 4.7 A plot of Limiting Current (I_L) / A *vs.* δ^{-1} / cm^{-1} for 1.M AcO^-, 0.5 M AcOH, 5 mM Cu^{2+}.

4.4.1 Outcome

The conclusions one should make before preceding to undertake sono-ASV of the complex solution are as follows. The use of a μ-addition approach is essential as a

calibration curve will not account for the possibility of differing speciation. The speciation varies only slightly with the concentration of the complexed metal except when the buffer concentration is of the same order as the metals, so whilst performing μ-additions one must not add too much in order not to change the speciation ratios drastically. To prevent the complication of CCE type mechanisms instead of the CE type mechanisms a small horn-electrode separation should be avoided and/or high powers of ultrasound.

4.5 Anodic Stripping Voltammetry (ASV) of Cu – Acetate Solutions.

Anodic Stripping Voltammetry (ASV) is an increasingly popular tool for analytical chemistry. Traditionally carried out on mercury electrodes this technique can easily distinguish between various metal ions and quantify concentrations quickly and efficiently. As mentioned earlier, the use of mercury is becoming severely restricted and an alternative must be found. In this final section we will show that bare glassy carbon electrodes can be employed successfully in the detection of copper in a clean system and that the inclusion of ultrasound will enhance the process. In the next chapter these

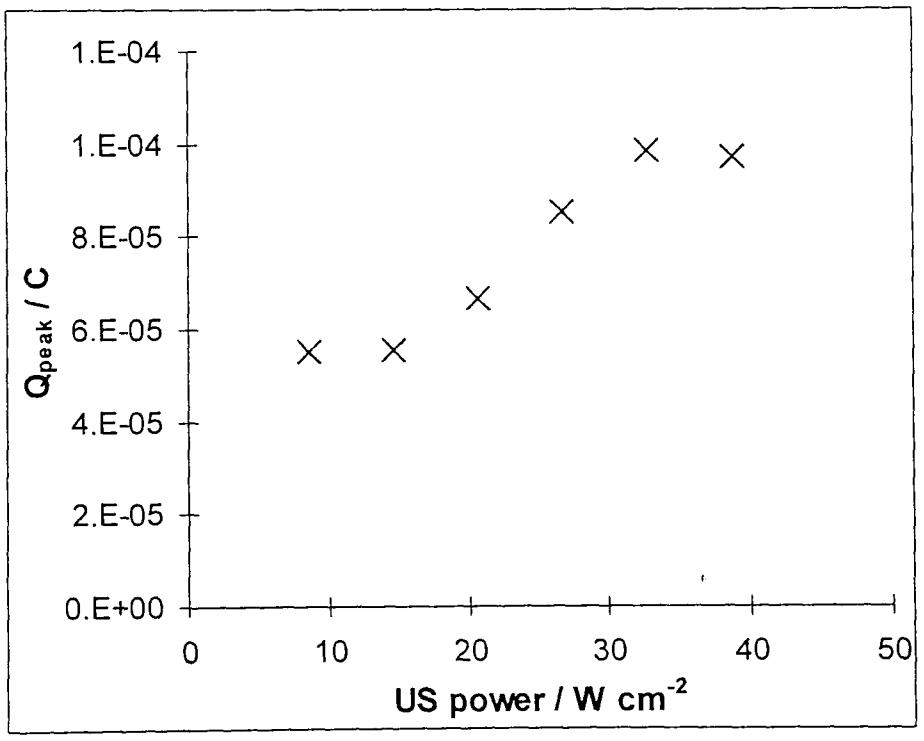


Figure 4.8 A graph showing the charge stripped for various ultrasound powers with 60 s deposition at –1.0 V.

results will be applied to a real world example and shown to be accurate in detecting the amount of copper in real ale.

The experimental set up is similar to that detailed in §2.1. The ultrasonic horn was placed opposite a bare glassy carbon electrode. The power of the ultrasonic horn was calibrated as explained in §2.1.1. The deposition step was carried out at –1.0 V (*vs.* SCE) for various powers of ultrasound and times and the charge stripped compared. Figure 4.8 shows charge stripped for various ultrasound intensities in 5 μM Cu^{2+} solution for 60 s. As one can easily see there is a limiting value for the deposition. The optimal value for the intensity is approximately 30 W cm^{-2}, as even though more charge is stripped above that intensity, the solution temperature would be hard to regulate at 25±2°C. Figure 4.9 shows the effect of deposition time with charge stripped. One can see this is linear and the sensitivity can be increased by increasing the time. As the aim of this is to keep the experiments short, 60 s is deemed to be appropriate for the required Limit of Detection (LOD). Figure 4.10 shows the micro addition plot for 30W cm^{-2} US and 60 s deposition time. This gives an actual limit of detection of 10^{-7} M and a theoretical limit of the order of 10^{-8} M. The electrode horn separation was kept constant at 10 mm in accordance with the conclusions of the previous section.

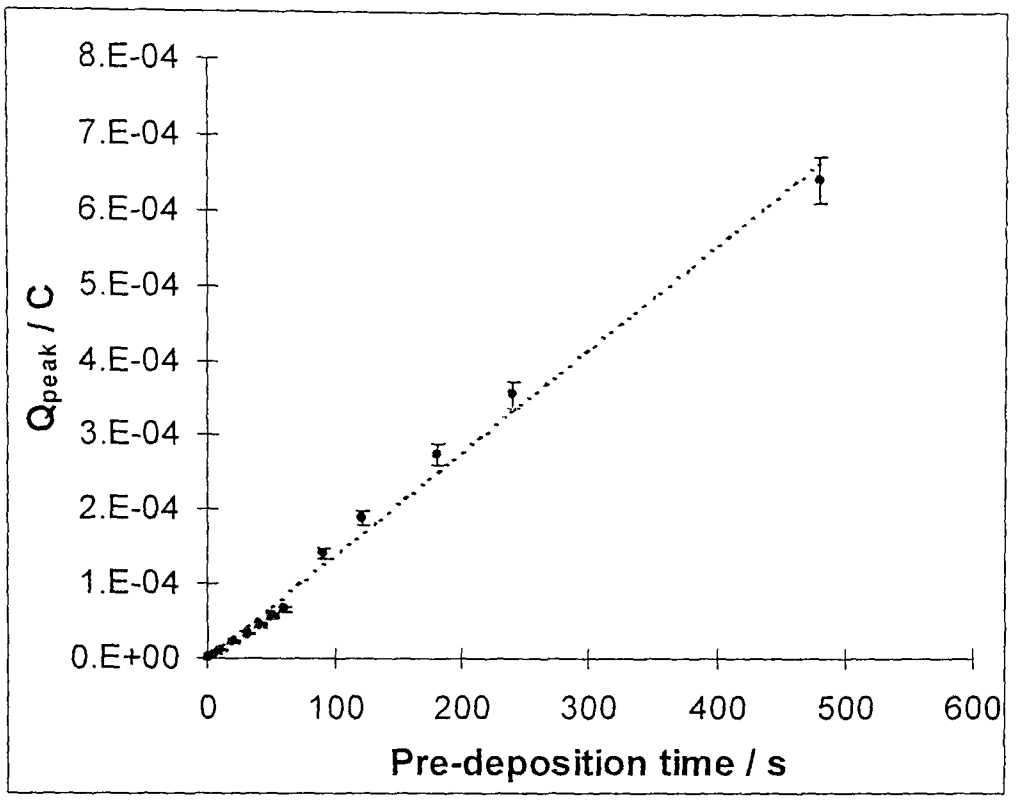


Figure 4.9 The effect of deposition time on the charge stripped for Cu at an ultrasound intensity of 30W cm^{-2}.

4.6 Conclusions

ASV may be carried out in speciated solutions if one is careful to not change the speciation due to micro additions. One cannot set up a calibration curve as the speciation will change the value expected. One also has to be careful not set up too small a diffusion layer as the kinetics of the dissociation of the ligands may affect the results. This will be applied in the next chapter to the ASV of copper in beer where much speciation will be encountered and will be unknown and impossible to model as before.

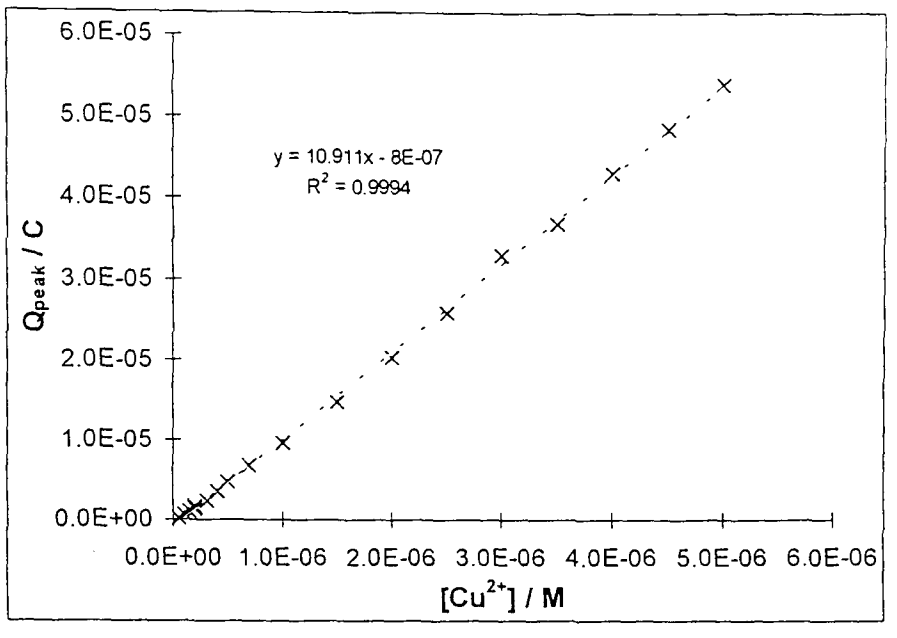


Figure 4.10 A micro addition plot for the detection of Cu in acetate buffer.

References for Chapter 4

[1] http://www.planetark.org/dailynewsstory.cfm?newsid2382&newsdate=06-Nov-1998
[2] A.J. Saterlay, J.S. Foord, R.G. Compton, *Analyst*, 124 (1999) 1791
[3] http://vest.gu.se/~bosse/Mercury/Nature/Swedishflow/default.html
[4] E. Gustafsson, *Water and Soil Pollution*, 80 (1995) 99
[5] S. Fronæus, *Acta Chem. Scand.*, 5 (1951) 859
[6] K.J. Pedersen, *Kgl. Danske Vidensk. Selskab, Math-fys. Medd.*, 22 (1945) No. 12
[7] H.P. Gregor, L.B. Luttinger, E.M. Loebl, *J. Phys. Chem.*, 59 (1955) 34
[8] M. Lloyd, V. Wycherley, C.B. Monk, *J. Chem. Soc.*, (1951) 1786
[9] L.G. Sillén, J Bjerrum, A.E. Martell, *Stability Constants of Metal-ion Complexes: 2. Organic Ligands*, (2nd Ed., Chem. Soc., London, 1964) pp xii
[10] D.L. Martin, F.J.C. Rossotti, *Proc. Chem. Soc.* (1959) 60
[11] S. Fronæus, *Doctoral Diss.*, Lund (1948) 42
[12] E. Steiner, *The Chemistry Maths Book* (OUP, Oxford, 1996) pp448-450
[13] W.H. Press, S.A. Tuekolsky, W.T. Vettring, B.P. Flannery, *Numerical Recipes in C* (2nd Ed. CUP, Cambridge, 1996) pp362-367
[14] A.C. Fisher, *Electrode Dynamics* (OUP, Oxford, 1996) pp21
[15] P.H. Rieger, *Electrochemistry* (2nd Ed., Chapman and Hall, New York, 1994) pp211
[16] L.S. Lasdon, A. Waren, A. Jain, M. Ratner, *ACM Transactions on Mathematical Software* 4 (1978) 34
[17] L.S. Lasdon, S. Smith, *ORSA Journal on Computing*, 4 (1992) 2
[18] C. Agra-Gutiérrez, J.C. Ball, R.G. Compton, *J. Phys. Chem.*, 102 (1998) 7028
[19] H.A.O. Hill, Y. Nakagawa, F. Marken, R.G. Compton, *J. Phys. Chem.*, 100 (1996) 17395

5. The ASV Detection of Copper in Beer at Glassy Carbon Electrodes

The work reported in this chapter has been published in *The Analyst* 124 (1999) 1053.

5.1. Introduction

Anodic Stripping Voltammetry (ASV) is a very sensitive and quick electroanalytical technique[1] which has been successfully applied to the detection and quantitative determination of various metals such as Pb, Sn, Cu, Zn, Cd, Bi, Sb, Au, Cr and Hg.[1,2] ASV involves two stages. First is the pre-concentration step where the electrode is held at a suitably negative potential such that the target is reduced onto the electrode surface to form either an amalgam, if using a mercury electrode, or an adsorbed layer of the target, if using a solid electrode. Second, the electrode is subjected to a positive potential sweep causing the target on or in the electrode to be oxidised. This results in an anodic peak which is characteristic of the target being analysed. The position of the peak reveals the identity of the target and the area or height of the peak is related to its concentration. The technique is very sensitive and under favourable conditions can detect as low as 10^{-11} M.[1,2]

Mercury thin film electrodes (MTFE) are well established electrode materials for ASV.[2-6] These electrodes offer a large surface area to volume ratio and, as a result, greater sensitivity and resolution of neighbouring signals than those obtained with a mercury drop electrode are observed.[2] Glassy carbon is used as a common electrode substrate for MTFE's. Its advantages include,[3-6] the ease of preparation, high sensitivity, large potential window and low interaction with the mercury. However, the weak adhesion to mercury often results in poor mechanical properties.[4,6,7] Other electrode materials such as platinum, copper and silver give rise to mercury thin films

with more stable mechanical properties. However, the dissolution of these substrates in mercury and the resulting formation of intermetallic compounds with analyte metals deposited into the film can limit their utility.[8,9] Mercury thin films on iridium have been shown to overcome this problem, due to the very low solubility of iridium in mercury.[8-10] However, recent studies[11] have shown iridium-based mercury film electrodes to be less sensitive for the determination of lead and cadmium than Nafion®-coated glassy carbon mercury film electrodes. Environmental and health issues concerning mercury and its toxicity, as mentioned in the previous chapter have prompted the development of mercury-free solid electrodes, especially for on-line monitoring of foodstuff, clinical and field tests.[12-14] Carbon disk microelectrodes have been used for trace analysis of lead and copper in rain and wine samples using ASV.[14] This technique has also been used to determine heavy metals in aqueous media using carbon screen-printed electrodes. Potentiometric stripping analysis for on-line monitoring has been successfully applied using gold-coated screen-printed carbon electrodes;[15] interactions among the metals with the naked solid electrode still present problems. For example, unexpected or unexplained stripping voltammetric responses have been observed for electrodeposited copper and lead on glassy carbon and graphite electrodes due to intermetallic interactions.[16-19] Both the enhancement[16,17] and decrease or total suppression[18,19] of the lead stripping peak have been observed in solutions with large copper to lead ratio.

A commonly problem encountered in ASV is the deactivation of the electrode surface. The presence of organic substances in the sample matrix can cause peak depression or even complete fouling of the electrode.[20-30] This leads to low sensitivity and poor reproducibility. As a consequence, it is often necessary to mineralise the sample to eliminate these interferences. These treatments consists of acidification or UV

irradiation in the presence of an oxidant.[24] However, they complicate and lengthen the analytical protocol and introduce contamination risks. One method employed to prevent electrode fouling is to electrochemically activate or modify the electrode.[31-36] A more efficient way of overcoming this problem is to use ultrasound-assisted electrochemistry (see §1.5.5). The use of ultrasound in electrochemistry has been exploited and is now emerging as a powerful technique in electroanalytical chemistry.[37-46] Its major advantages include the extremely enhanced mass transport[38,42,45,46] to and from the electrode surface and the activation and cleaning[38,43,44,46] of electrode surfaces achieved under insonation. In particular, ultrasound has been successfully applied in ASV. For example, well defined and very sharp stripping responses have been obtained for lead, copper and cadmium using mercury containing electrodes in aqueous media and alcoholic beverages.[37-39,41,47] Another way of overcoming electrode fouling is to use membrane-coated electrodes. Dialysis membranes, cellulose acetate and Nafion® have been used[20-22,39-49] for this purpose. In particular Nafion®-coated electrodes have been successfully applied to the detection of heavy metals in aqueous[11,47] and real media[21,22,48,49] using ASV. These Nafion®-coated mercury thin film electrodes, usually on glassy carbon, often exhibit higher sensitivity and resistance to electrode fouling by excluding negatively charged organic species. In addition, the polymer coating provides a more mechanically stable mercury film under the presence of ultrasound.[11,47] A major advantage of sono-electroanalysis is that cavitation effects can clean the surface during the pre-concentration stage preventing electrode fouling and also that insonation increases the mass transport to the electrode and hence the sensitivity of the experiment.

The aim of this chapter is to assess the applicability of *sono*-ASV to the determination of total metal contents in complex, organic rich and non-traditional electrochemical

media using mercury-free electrodes, building on the previous chapters results in which other electroanalytical techniques fail to give accurate and reproducible results due to electrode fouling and matrix effects. For this purpose, a comparison of methodologies using both mercury thin film and glassy carbon electrodes is conducted using beer as a model '*dirty*' media.

5.2. Experimental

The cell used is shown in Figure 5.1. It has a volume of *ca.* 25 cm^3. The working electrode is placed directly opposite the ultrasonic horn (Model CV26, Sonics and Materials) and located near the cell bottom with a transducer probe to working electrode distance of 5 mm. The horn was equipped with a titanium alloy micro-tip (of diameter *ca.* 3 mm, Aldrich) and was operated at 20 kHz. The ultrasonic intensity was calibrated calorimetrically according to the procedure of Margulis *et al.*[50,51] over the range 40 - 550 W cm^{-2}. The sono-ASV experiments were carried out at 200 ± 5 W cm^{-2} unless otherwise stated. Thermostatting of the cell was accomplished by means of a stainless steel cooling coil inserted in the solution through which water was circulated from a constant temperature bath. By limitation of sonication time to less than 5 min this arrangement enabled the voltammetric measurements to be conducted at constant temperature (25 °C) to within ± 2°C.

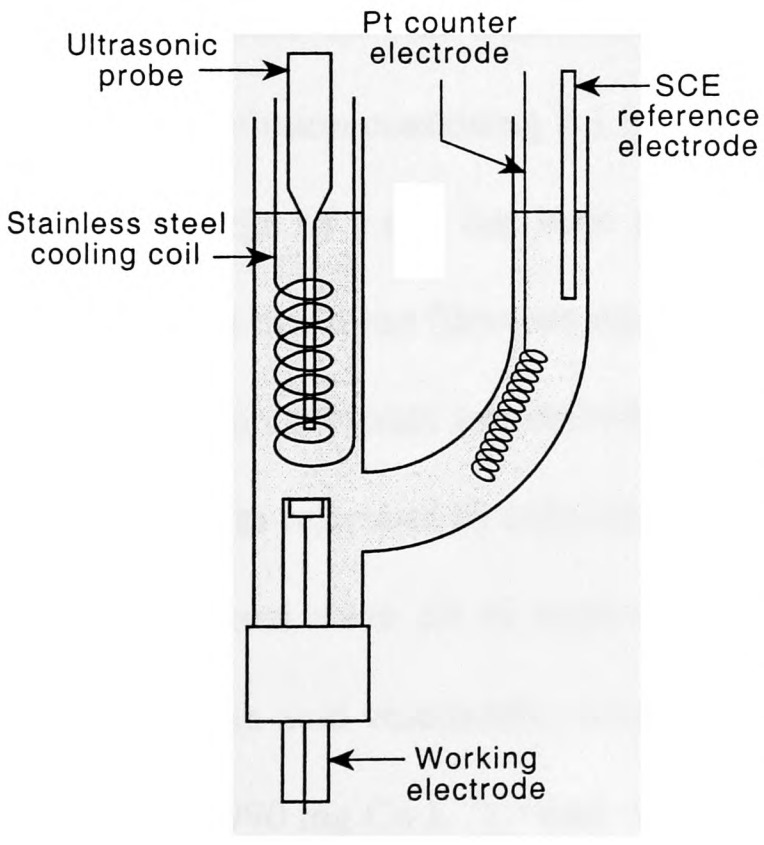


Figure 5.1 Schematic diagram of the electrochemical cell employed in the *sono*-ASV determination of metals in beer.

An Eco-Chemie μAUTOLAB® (Utrecht, Netherlands) was employed to control the potential of the working electrode. The need for bipotentiometric[52] control of the titanium horn was eliminated by insulating the transducer from the probe with a thin Teflon™ disc and connecting the two with a screw thread machined from Delrin™ instead of titanium.

Experiments were conducted using two types of electrode materials. A bare glassy carbon electrode and an *ex situ* mercury-plated Nafion®-coated glassy carbon electrode. The substrate (a 3 mm diameter glassy carbon disc supplied by BAS, US) was carefully polished using diamond lapping compounds (Kemet, Kent, UK) of decreasing size down to 0.1 μm before use. A platinum counter electrode was used throughout the experiments. All potentials are quoted with respect to the saturated calomel electrode, SCE (Radiometer, Copenhagen). Nafion® coating was achieved following the procedure described previously.[11,39] Mercury plating of this electrode was conducted *ex situ* immediately before use. Mercury was deposited from a deaerated solution containing 0.1 M $HClO_4$ and 0.01 M $Hg(ClO_4)_2$ at –1.0 V *vs.* SCE until a charge of 1 mC has been passed through the electrode. Previous studies[11,39] have shown that these films are composed of mercury micro-droplets deposited on the glassy carbon substrate and embedded in a compact, transparent Nafion® matrix. The electrode was refreshed by repeating this procedure for each measurement.

Reagents used were all of analytical grade or the highest commercially available purity. Nitric acid volumetric standards (1.0 M and 0.1 M), copper atomic absorption standard (990 mg Cu L^{-1}), lead volumetric standard (0.1 mg Pb L^{-1}), mercury(II) perchlorate, perchloric acid and dimethylformamide were supplied by Aldrich. Pedigree Bitter was purchased from Marston's Brewery (Burton-on-Trent, UK). A Nafion® solution of 5 % weight in low-weight alcohols (Sigma) was diluted with

ethanol (analytical grade) prior to application. Solutions were prepared using UHQ grade water of resistivity not less than 18 MΩ cm (Elgastat, High Wycombe, Bucks, UK). Test solutions were prepared by adding 88 cm^3 of beer to 162 cm^3 of 0.1 M nitric acid unless otherwise stated. All solutions were thoroughly purged of oxygen by bubbling argon (PureShield) through the solution prior to electrolysis.

For the comparison of total copper content, samples were analysed (standard addition method) using electrothermal atomic absorption spectrometry with no sample pretreatment. This was conducted by Rooney Laboratories Ltd. (Basingstoke, UK).

5.3. Results and Discussion

5.3.1. Determination of Copper in Beer Using Mercury Thin Film Electrodes

Anodic stripping square voltammograms for Cu^{2+} were obtained in a solution obtained by mixing 88 cm^3 0.1 M HNO_3 and 162 cm^3 Pedigree Bitter beer using a mercury thin film electrode. Deposition of the lead amalgam was conducted for 240 s at −1.0 V *vs.* SCE under power ultrasound of intensity 200 W cm^{-2} emitted from a horn probe placed at 5 mm above a 3 mm diameter *ex situ* mercury-plated Nafion®-coated glassy carbon electrode (see Figure 5.1). The square wave sweep parameters were as follows: pulse amplitude of 25 mV, potential step of 5 mV and a frequency of 60 Hz. Typical square wave voltammograms are shown in Figure 5.2. The anodic stripping peak at *ca.* 0.0 V *vs.* SCE increases and shifts anodically with increasing added copper. This wave corresponds to the oxidation of copper amalgam. Standard copper micro-addition experiments were conducted to determine the amount of copper in the beer using the method described above. A typical standard micro-addition plot is shown in Figure 5.3, as a plot of the anodic stripping peak current *vs.*

the amount of copper added per volume of beer. Results are shown in Table 5.1 and compared with analyses provided by an independent laboratory using electrothermal atomic absorption spectrometry. The standard addition method provides a copper content of 265 ± 65μg Cu per litre of beer (background corrected). A value for the total copper content in the beer sample was provided by an independent laboratory and shows excellent agreement (Table 5.1). Analysis of the standard addition data provided a theoretical limit of detection of 0.15 μg Cu per litre of beer, although practical detection limits are somewhat higher depending on the minimum detectable peak and the purity of the reagents.[39]

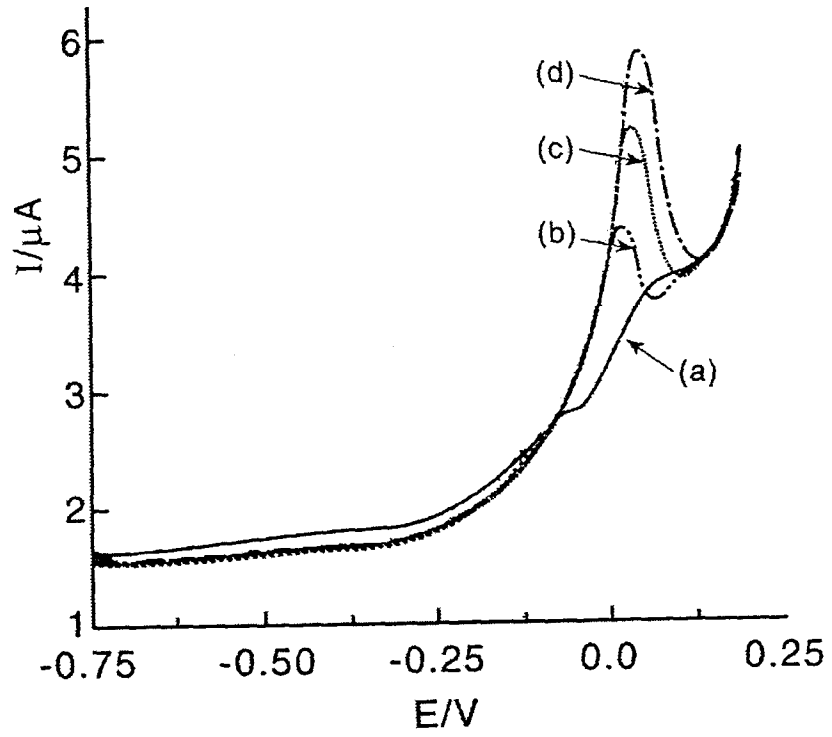


Figure 5.2 Square wave anodic stripping voltammograms of aqueous solutions prepared by mixing 88 cm^3 0.1 M HNO_3 and 162 cm^3 Pedigree beer: (a) blank, and after addition of (b) 507 μg Cu L^{-1}, (c) 1014 μg Cu L^{-1}, and (d) 1522 μg Cu L^{-1}. The deposition step was conducted for 240 s at −1.0 V vs. SCE under power ultrasound of intensity 200 W cm^{-2} emitted from a horn probe placed at 5 mm opposite a 3 mm *ex situ* mercury-plated Nafion®-coated glassy carbon electrode. Square wave sweep parameters: pulse amplitude of 25 mV, potential step of 5 mV and a frequency of 60 Hz.

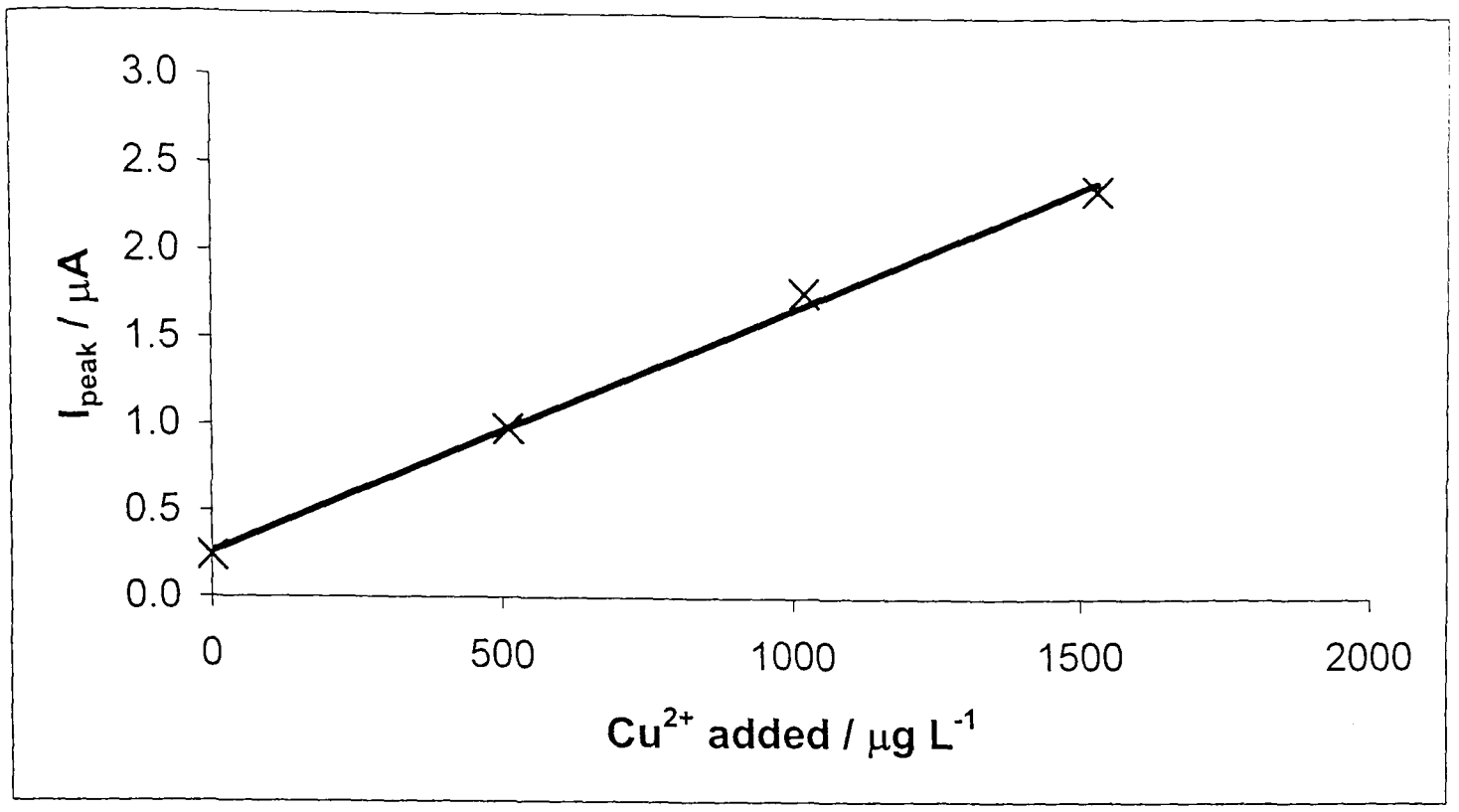


Figure 5.3 Standard micro-addition plot for copper(II) in a solution prepared by mixing 88 cm^3 0.1 M HNO_3 and 162 cm^3 Pedigree beer. The deposition step was conducted for 240 s at –1.0 V *vs.* SCE under power ultrasound of intensity 200 W cm^{-2} emitted from a horn probe placed at 5 mm opposite a 3 mm *ex situ* mercury-plated Nafion®-coated glassy carbon electrode. Square wave sweep parameters as in Figure 5.2.

5.3.2. Determination of Copper in Beer Using Solid Electro des

Mercury-free electrodes were used to determine the amount of copper in Pedigree bitter using a 3 mm diameter glassy carbon electrode. Pre-conditioning of the electrode was conducted at –2 V *vs.* SCE for 10 s. This treatment reduces the fouling of the electrode improving the stability and the size of the signal. Deposition of copper on the glassy carbon substrate was conducted at –1.5 V *vs.* SCE under power ultrasound of intensity 200 W cm^{-2} emitted from a horn probe placed at 5 mm above the working electrode (see scheme in Figure 5.1). The stripping step was carried out using a square wave scan with the same parameters as for experiments in section 3.1. Typical square wave voltammograms for a solution containing 162 cm^3 0.1 M HNO_3 and 88 cm^3 Pedigree Bitter with and without added copper are shown in Figure 5.4. Note the different current scale than for Figure 5.2 for analysis using different electrode substrates. Results in the absence of ultrasound are shown for comparison.

The wave at *ca.* 0 V *vs.* SCE increases with increasing concentration of added copper and corresponds to the anodic stripping peak of solid copper deposited on the glassy carbon electrode. The wave at *ca.* –0.3 V *vs.* SCE also increases with added copper concentration and is related to copper-lead interactions which will be further discussed in the next section. In the absence of ultrasound both the copper and copper-lead alloy stripping peaks are not observed; application of ultrasound is essential for the ASV procedure. This is due to the surface activation[38,41,42] observed in the presence of ultrasound which removes organic adsorbates thought to preclude measurement under silent conditions.

This highlights one major benefit of using ultrasound coupled to ASV; in addition the high mass transport ensures that large SWV signals are seen for relatively short accumulation times.

Several determinations of copper in Pedigree beer were obtained as described above and analysis of the standard addition data provided the values shown in Table 5.1 together with values provided by an independent laboratory. The excellent agreement between the two methods confirms the reliability of *sono*-SWASV to give the total copper content in beer.

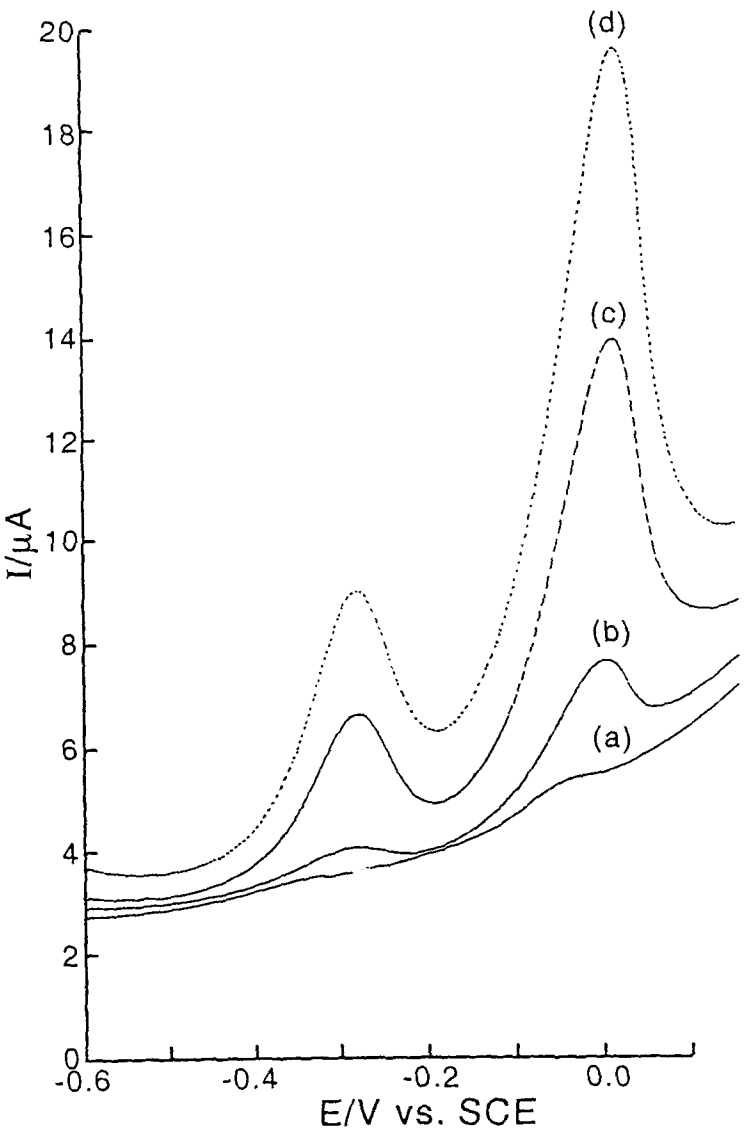


Figure 5.4 Square wave anodic stripping voltammograms of aqueous solutions prepared by mixing 162 cm^3 0.1 M HNO_3 and 88 cm^3 Pedigree beer and (a), (b) 47.7 μg Cu L^{-1}(per litre of solution), (c) 143 μg Cu L^{-1}, and (d), 190.6 μg Cu L^{-1}. The deposition step was conducted for 240 s at –1.5 V *vs.* SCE under (a) under silent conditions, and (b), (c), and (d), under power ultrasound of intensity 200 W cm^{-2} emitted from a horn probe placed at 5 mm opposite a 3 mm glassy carbon electrode. Square wave sweep parameters as in Figure 2.

Electrode	Sample	[Cu][a] / μg Cu L^{-1}	[Cu][b] / μg Cu L^{-1}
NCMFGCE	Pedigree sample 1	265 ± 65	230
GC	Pedigree sample 1	222 ± 31	230
GC	Pedigree sample 2	139 ± 4	140

[a]- as determined by *sono*-SWASV; [b]- as determined by independent laboratory.

Table 5.1 Determination of copper in Pedigree beer using *sono*-SWASV. Results for two types of electrodes are shown: NCMFGCE corresponds to an *ex situ* mercury-plated Nafion®-coated glassy carbon electrode; GC corresponds to a glassy carbon electrode. Deposition was carried out at –1.5 V *vs.* SCE in the case of GC and at –1 V *vs.* SCE in the case of the NCMFGCE for 240 s under ultrasound of intensity 200 W cm^{-2} at a horn to electrode distance of 5 mm (see scheme in Figure 1). Glassy carbon electrodes were pre-conditioned at –2 V *vs.* SCE for 5 s. Values are expressed as the average values for 3 determination ± their standard deviation.

5.3.3. Observations on the Use of Solid Electrodes: Copper-lead Alloys

Figure 5.4 shows a wave at *ca.* -0.3 V *vs.* SCE which is attributed to a copper-lead alloy. Further experiments were conducted to corroborate this inference. *Sono*-ASV experiments were conducted in a solution containing 0.1 M HNO_3 and 0.5 μM Pb^{2+} to which certain amounts of Cu^{2+} and Pb^{2+} were successively added using a glassy carbon electrode. The working electrode was preconditioned at -2 V *vs.* SCE for 5 s. The deposition step was then conducted at –1.5 V *vs.* SCE for 120 s under power ultrasound of intensity 200 W cm^{-2} emitted from a horn probe placed at 5 mm of the working electrode. The stripping step was carried out using a linear sweep voltammetric scan at a scan rate of 50 mV s^{-1}. Results are shown in Figure 5.5 as a plot of current *vs.* applied potential for (a) microadditions of Cu^{2+}, and (b) microadditions of Pb^{2+} solutions. Figure 5.5a shows linear sweep voltammograms upon additions of Cu^{2+} solutions. The peak at *ca.* 0.0 V *vs.* SCE corresponds to the oxidation of copper deposited on the glassy carbon electrode and increases with the

microadditions. The peak at *ca.* -0.5 V corresponds to the oxidation of lead deposited on the electrode and decreases with increasing amount of copper added. The third wave, at *ca.* -0.3 V, increases with increasing concentration of copper added and corresponds to the oxidation of a lead copper alloy. Figure 5.5b shows linear sweep voltammograms upon additions of Pb^{2+} to a solution containing 0.1 M HNO_3, 0.5 μM Pb^{2+} and 3 μM Cu^{2+}. The anodic copper peak at *ca.* 0.0 V remains initially constant upon addition of up to 150 μg Pb L^{-1}. Further addition of lead results in a decrease of the copper peak and in an increase of both the lead and alloy peaks which broaden and merge. These results clearly indicate the occurrence of an copper-lead alloy, in the form of an intermetallic compound or a solid solution. These observations are in agreement with earlier reports about the deposition of copper and lead on solid electrodes.[14,19,24] Comparison with the results obtained using mercury film electrodes reported in this chapter it can be concluded that copper-lead interactions are less important in the presence of mercury. This is in agreement with previous observations.[16,19] Nonetheless, the occurrence of these interactions does not affect the applicability of sono-ASV to the detection of total copper in beer using mercury-free glassy carbon electrodes, as evidenced by the excellent agreement with copper content values provided by the independent laboratory.

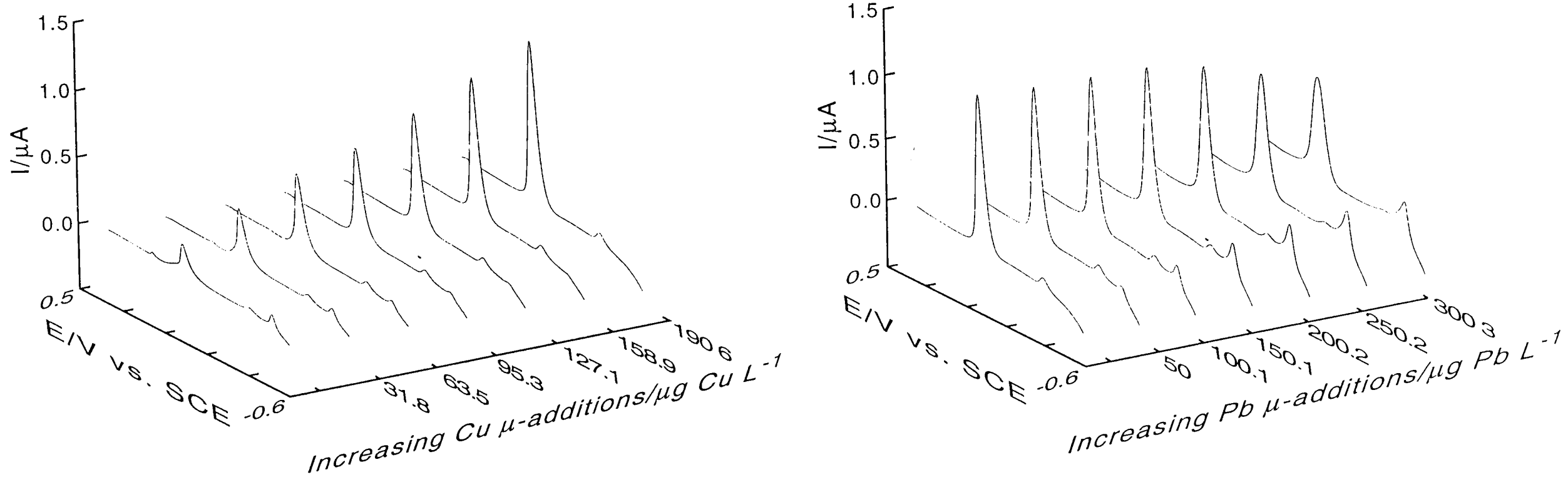


Figure 5.5 Linear sweep voltammograms (50 mV s^{-1}) obtained in aqueous solutions of 0.1 M HNO_3, 0.5 μM $Pb^{2+}$and: (a) after several micro-additions of copper (0 to 190.6 μg Cu L^{-1}); (b) 190.6 μg Cu $L^{-1}$and several microadditions of lead (0 to 300.3 μg Pb L^{-1}). The deposition step was conducted for 120 s at –1.5 V *vs.* SCE under power ultrasound of intensity 200 W cm^{-2} emitted from a horn probe placed at 5 mm opposite a 3 mm glassy carbon electrode.

5.4. Conclusions

Sono-ASV has been shown to be an effective electroanalytical technique to determine total copper contents in dirty media using both mercury thin film and unmodified glassy carbon electrodes. Both electrodes give excellent agreement with values obtained using atomic absorption spectroscopy conducted by an independent laboratory. In the absence of ultrasound electrode passivation by organic species and lower rates of mass transport prevent the observation of any measurable signals. *In-situ* cavitational cleaning of the electrode by insonation maintains the electrode activity and is fundamental to the success of the experiment.

References for Chapter 5

[1] F. Vydra, K. Štulík, E. Juláková, *Electrochemical Stripping Analysis*, Ellis Horwood, 1976 *and references cited therein*
[2] J. Wang, *Stripping Analysis. Principles, Instrumentation, and Applications*, VCH Publishers, 1985
[3] J.-M. Zen, N.-Y. Chi, F.-S. Hsu, M.-J. Chung, *Analyst* 120 (1995) 511
[4] H. P. Wu, *Anal. Chem.* 66 (1994) 3151
[5] W. Frenzel, *Anal. Chim. Acta* 273 (1993) 123
[6] M. Štulíková, *J. Electroanal. Chem.* 48 (1973) 33
[7] N.F. Zakharchuk, Kh.Z. Brainina, *Electroanalysis* 10 (1998) 379
[8] L. Nyholm, F. Björefors, *Anal. Chim. Acta* 327 (1996) 211
[9] S.P. Kounaves, W. Deng, *J. Electroanal. Chem.* 301 (1991) 77
[10] S.P. Kounaves, J. Buffle, *J. Electroanal. Chem.* 216 (1987) 53
[11] C. Agra-Gutiérrez, M. F. Suárez, R. G. Compton, *Electroanalysis*, 11 (1999) 16
[12] D. Desmond, B. Lane, J. Alderman, M. Hill, D. W. M. Arrigan, J. D. Glennon, *Sens. and Actuators B* 48 (1998) 409
[13] P. J. S. Barbeira, N. R. Stradiotto, *Talanta* 44 (1997) 185
[14] M. A. Baldo, S. Daniele, G. A. Mazzocchin, *Electroanalysis* 10 (1998) 410
[15] J. Wang, B. Tian, *Anal. Chem.* 65 (1993) 1529
[16] E. Y. A. Neiman, L. G. Petrova, V. I. Ignaton, G. M. Dolgopolova, *Anal. Chim. Acta* 113 (1980) 277
[17] O. L. Kabanova, S. M. Beniaminova, *J. Anal. Chem.* 26 (1970) 94
[18] S. Dong. Y. Wang, *Talanta* 35 (1998) 819
[19] H. Gunasinghan, R. Dalangin, *Anal. Chim. Acta* 246 (1991) 309
[20] B. Hoyer, N. Jensen, *Talanta* 42 (1995) 767
[21] B. Hoyer, T.M. Florence, G. E. Batley, *Anal. Chem.* 59 (1987) 1608
[22] B. Hoyer, T.M. Florence, *Anal. Chem.* 59 (1987) 2839
[23] A. Aliakbar, M. Popl, *Coll. Czech. Chem. Commun.* 50 (1985) 1141
[24] M.A. Baldo, C. Bragato, S. Daniele, *Analyst* 122 (1997) 1
[25] S.K.C. Chang, E. Holm, J. Schwarz, P. Rayas-Duarte, *Anal. Chem.* 168 (1979) 353
[26] L. Sipos, J. Golimoski, P. Valenta, H.W. Nurnberg, *Fresenius Z. Anal. Chem.* 298 (1979) 1
[27] J. Golimoski, K. Golimoski, *Anal. Chim. Acta* 325 (1996) 111
[28] S. Mannino, *Riv. Vitic. Enol. Conegiano* 6 (1982) 297
[29] D. Jagner, S. Westerlund, *Anal. Chim. Acta* 117 (1980) 159
[30] G.N. Chen, G.R. Scollary, V.A. Vicente-Beckett, *Am. J. Enol. Vitic.* 45 (1994) 305
[31] A.G. Fogg, M.A. Fernández-Arciniega, R.M. Alonso, *Analyst* 110 (1985) 851
[32] A.G. Fogg, M.A. Fernández-Arciniega, R.M. Alonso, *Analyst* 110 (1985) 1201
[33] A.G. Fogg, R.M. Alonso, M.A. Fernández-Arciniega, *Analyst* 111 (1986) 249
[34] A.G. Fogg, R.M. Alonso, *Analyst* 112 (1987) 1071
[35] A.Y. Chamsi, A.G. Fogg, *Analyst* 113 (1988) 1723
[36] K.-K. Shiu, K. Shi, *Electroanalysis* 10 (1998) 959
[37] A.M. Oliveira Brett, C.M.A. Brett, F.-M. Matysik, S. Matysik, *Ultrason. Sonochem.* 4 (1997) 123
[38] R. G. Compton, J. C. Eklund, F. Marken, *Electroanalysis* 9 (1997) 509
[39] F.-M. Matysik, S. Matysik, A.M. Oliveira Brett, C.M.A. Brett, *Anal. Chem.* 69 (1997) 1651
[40] N.A. Madigan, T.J. Murphy, J.M. Fortune, C.R.S. Hagan, L.A. Coury, Jr. *Anal. Chem.* 67 (1995) 2781
[41] F. Marken, T.O. Rebbitt, J. Booth, R.G. Compton, *Electroanalysis* 9 (1997) 19
[42] R.G. Compton, J.C. Eklund, S.D. Page, T.J. Mason, D.J. Walton, *J. Appl. Electrochem.* 26 (1996) 775
[43] R.G. Compton, J.C. Eklund, S.D. Page, G.H.W. Sanders, J. Booth, *J. Phys. Chem.* 98 (1994) 12410
[44] A.M. Oliveira Brett, F.-M. Matysik, *Bioelectrochem. Bioenerg.* 42 (1997) 111
[45] C. Agra-Gutiérrez, R.G. Compton, *Electroanalysis* 10 (1998) 204
[46] C. Agra-Gutiérrez, R.G. Compton, *Electroanalysis* 10 (1998) 603
[47] R.P. Akkermans, J.C. Ball, T.O. Rebbitt, F. Marken, R.G. Compton, *Electrochim. Acta* 43 (1998) 3443
[48] J.C. Vidal, R.B. Viñao, J.R. Castillo, *Electroanalysis* 4 (1992) 653
[49] S. Jaenicke, R.M. Sabarathinam, B. Fleet, H. Gunasingham, *Talanta* 45 (1997) 703
[50] M.A. Margulis, A.N. Maltsev, *Russ. J. Phys. Chem.* 43 (1969) 592

[51] T.J. Mason, J.P. Lorimer, D.M. Bates, *Ultrason.* 30 (1992) 140
[52] F. Marken, R.G. Compton, *Ultrason. Sonochem.* 2 (1996) S131

6. Anodic Stripping Voltammetry: Numerical Theory for Reversible Systems and Experimental Verification

The work presented in this chapter has been published in the *Journal of Physical Chemistry* 102 (1998) 3967 and 102 (1998) 7028

6.1. Introduction

In previous work[1-5] simulation techniques have been developed to permit the description of anodic stripping voltammetry (ASV) at hydrodynamic electrodes. ASV is commonly applied to the analytical determination of a wide range of trace metals and generally employs mercury electrodes.[6,7] The method has two stages. First, a pre-concentration step is applied in which electro-deposition of the target metal ion(s) in solution leads to the accumulation of metal in the (mercury) electrode usually through the formation of an amalgam. Second the electrode potential is swept positive so inducing the oxidation of the metal(s) in the mercury electrode resulting in a characteristic voltammetric peak(s) which permits the determination of the target(s). The merits of using hydrodynamic conditions for the first or both stages of ASV include enhanced sensitivity and reproducibility in addition to the attractions of conducting the experiment under continuous flow conditions.[8-16] However theory[1-3,17-20] has indicated that under conditions of merely modestly enhanced transport the associated reduction in the diffusion layer thickness can lead to significant deviations from the theory developed for conditions of semi-infinite diffusion. The purpose of a recent series of papers[1-3] was to explore the effects of diffusion layer contraction through the simulation of voltammetric responses.

The simulation of linear sweep ASV has been carried out at uniformly accessible electrodes for both electrochemically reversible and quasi-reversible processes;[2,3] such

theory is approximately applicable to rotating disc and hanging mercury drop electrodes and possibly to insonated electrodes.[21] Theory has been extended to the case of channel[5] and wall-jet[1] electrodes. However many applications of ASV are, in experimental practice, conducted using square wave voltammetry (SWV) since this offers many advantages as evaluated by Brett and Oliveira Brett;[22] speed of analysis, lower consumption of electroactive species, reduced problems with electrode passivation and the possibility of conducting measurements without the need for the removal of dissolved oxygen.[23] The present chapter seeks to develop simulation approaches for SWV since although analytical theory is well-developed for the case of semi-infinite diffusion conditions[24-26] this may be less amenable to a general treatment of SWV for hydrodynamic electrodes.[27]

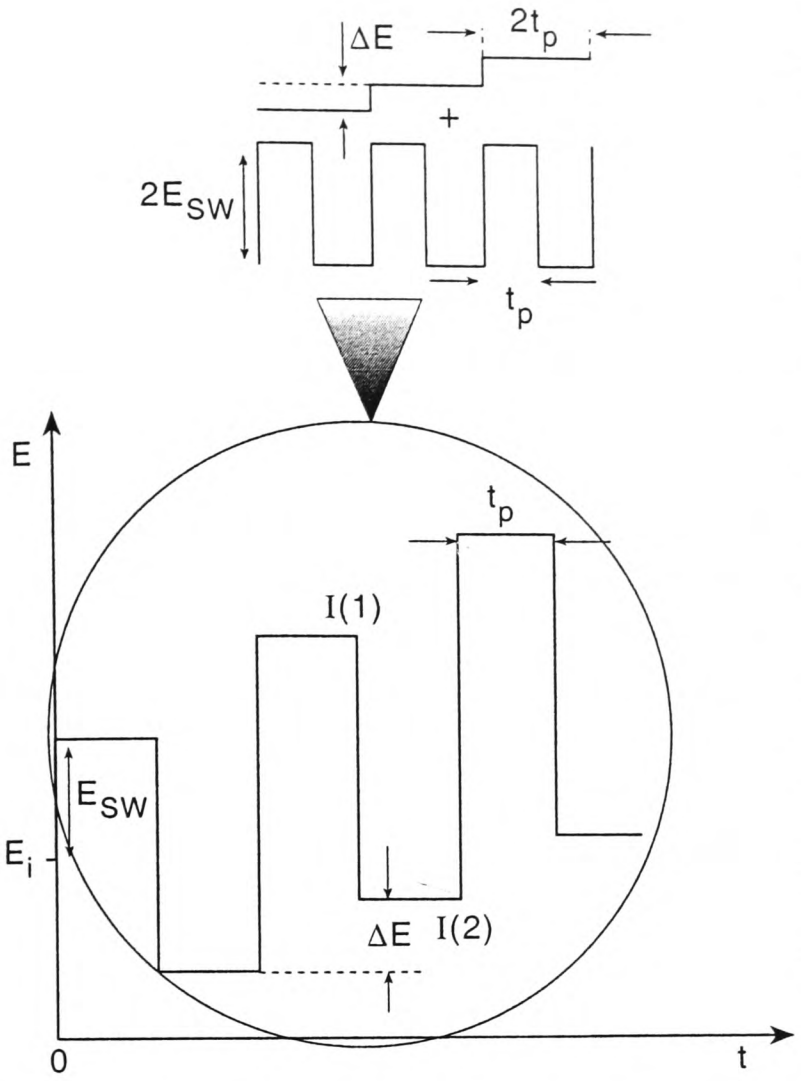


Figure 6.1 A schematic diagram showing a Square Wave Voltammetric sweep.

6.2. Theory

Considering the electrode process

$$RED_{(Hg)} - ne^- \rightleftharpoons OX_{(aq)} \qquad (6.1.)$$

corresponding to an ASV stripping peak in which the electrode potential is subjected to an anodic square wave voltammetric sweep as shown in Figure 6.1 where ΔE is the

step voltage of staircase, E_{SW} is the pulse amplitude, $I(1)$ is the forward current, $I(2)$ is the backward current and t_d is the deposition time. The time of pulse, t_p, is related to the frequency, f, of the pulse

$$t_p = \frac{1}{2f} \tag{6.2.}$$

The electrode process is next assumed to be electrochemically reversible such that the Nernst Equilibrium applies

$$\frac{[RED]_{(Hg)}}{[OX]_{(aq)}} = \exp\left[-\left(\frac{nF}{RT}\right)\left(E - E^{0'}\right)\right] \tag{6.3.}$$

where E is the potential on the square wave scan and $E^{0'}$ is the formal potential of the redox couple.

In the following it is either first supposed that the film is sufficiently thin that diffusion of the reduced material through the film is so fast that no concentration gradients build up within the film. In this case the following boundary conditions applies.

$$l\frac{\partial[RED]}{\partial t} = D_O \frac{\partial[OX]}{\partial y}\bigg|_{y=0} \tag{6.4.}$$

where y is the Cartesian co-ordinate normal to the electrode surface, l is the mercury film thickness and D_O is the diffusion coefficient of the oxidised species. Second and conversely as the pulse duration is typically very short, we might expect that film diffusion needs to be included in the model as suggested by the work of Osteryoung and co-workers.[25,26] To do this the above equation must be replaced by two separate equations. At the film surface the flux of RED and OX must be equal such that

$$D_R \frac{\partial[RED]}{\partial y}\bigg|_{y=0} = D_O \frac{\partial[OX]}{\partial y}\bigg|_{y=0} \tag{6.5.}$$

where D_R is the diffusion coefficient of the reduced species within the film. The transport within the film can be assumed to be controlled by Fick's 2nd law of Diffusion:

$$\frac{\partial[RED]}{\partial t} = D_R \frac{\partial^2[RED]}{\partial y^2} \tag{6.6.}$$

Finally the transport of OX in solution is similarly controlled.

$$\frac{\partial[OX]}{\partial t} = D_O \frac{\partial^2[OX]}{\partial y^2} \tag{6.7.}$$

At the diffusion layer edge

$$y = \delta$$

the concentration of OX is set to $[OX]_{bulk}$. It also assumed that no intermetallic compounds are formed in the amalgam described above.

Considering the formulation of the above problem in finite difference terms and exploring first the possibility of conducting simulations in real time. Due to the nature of the potential sweep, there is much more movement of OX at the beginning of the pulse than at the end where, if both a low enough frequency is employed and the diffusion layer is thin enough, approximately steady state conditions apply. For this transport to be probed quantitatively a prohibitively large number of real time nodes per pulse would be required as discussed further below. Therefore to make the simulations more computationally efficient expanding time grids were adopted. Two grids were required as each cycle corresponds approximately to a double potential step where the diffusion of OX away from or to the electrode follows two different natural timescales. For the 'forward' or 'oxidising' pulse we introduce "Cottrellian time" such that[28]

$$\tau_f = \frac{a}{\sqrt{t}} \tag{6.8.}$$

where τ_f is the transformed time on the forward pulse, t is the real time and a is a constant. Accordingly for the 'backward' or 'reducing' pulse "reverse Cottrellian time"[29] was employed such that the transform time co-ordinate, τ_b, is given by

$$\tau_b = a\left[\frac{1}{\sqrt{(t - t_p)}} - \frac{1}{\sqrt{t}}\right] \tag{6.9.}$$

where t is the time elapsed from the start of the forward pulse.

The transport equations must be transformed to these new co-ordinate systems. The forward time derivative becomes thus

$$\frac{\partial}{\partial t} = -\frac{\tau_f^{\,3}}{2a^2} \cdot \frac{\partial}{\partial \tau_f} \tag{6.10.}$$

The backward time co-ordinate transformation is less easy as there is no explicit form for t in terms of τ_b. Using the chain rule the following relationship is obtained

$$\left.\frac{\partial}{\partial t}\right]_y = \frac{\partial \tau_b}{\partial t} \cdot \left.\frac{\partial}{\partial \tau_b}\right]_y \tag{6.11.}$$

In the following to evaluate the derivative with respect to time at any point an Adam's variable order variable step method was used in the computation described below.[30]

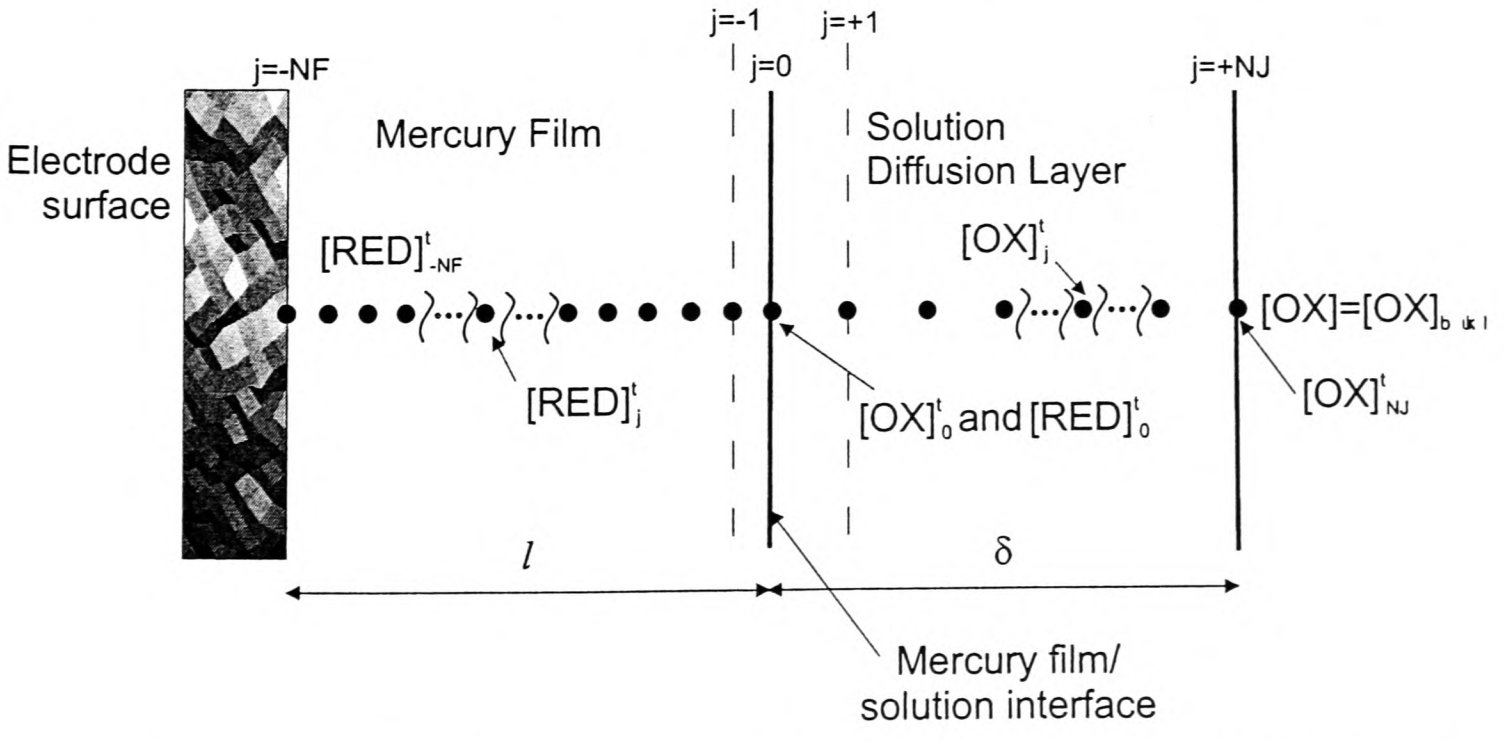


Figure 6.2 A schematic diagram showing the spatial node distribution used in the film diffusion model.

Considering the most general case where film diffusion is simulated. The finite difference forms of the relevant equations become:

$$-\lambda^{Hg}[RED]^t_{j-1}+\left(1+2\lambda^{Hg}\right)[RED]^t_j-\lambda^{Hg}[RED]^t_{j+1}=[RED]^{t-1}_j \tag{6.12.}$$

$$-\lambda^{s}[OX]^t_{j-1}+\left(1+2\lambda^{s}\right)[OX]^t_j-\lambda^{s}[OX]^t_{j+1}=[OX]^{t-1}_j \tag{6.13.}$$

Notationally the superscript t for real time is used rather than τ for Cottrellian time to avoid the confusion that increasing τ counts backwards in real time. The subscript j refers to the spatial nodes shown in Figure 6.2. At the electrode surface

$$-[RED]^t_{-1}+\left\{e^{-\theta}+\kappa\right\}[OX]^t_0-\kappa[OX]^t_1=0 \tag{6.14.}$$

In equations (6.12.) - (6.14.) for the forward pulse

$$\lambda^{Hg}_{\tau_f}=\frac{2D_R a^2\Delta\tau_f}{{\tau_f}^3(\Delta l)^2} \qquad \lambda^{s}_{\tau_f}=\frac{2D_O a^2\Delta\tau_f}{{\tau_f}^3(\Delta y)^2} \tag{6.15.}$$

Likewise for the backward pulse

$$\lambda^{Hg}_{\tau_b}=-\frac{D_R\Delta\tau_b}{(\Delta l)^2}\cdot\left(\frac{1}{\left(\frac{\partial\tau_b}{\partial t}\right)}\right) \qquad \lambda^{s}_{\tau_b}=-\frac{D_O\Delta\tau_b}{(\Delta y)^2}\cdot\left(\frac{1}{\left(\frac{\partial\tau_b}{\partial t}\right)}\right) \tag{6.16.}$$

and for both pulses

$$\kappa=\frac{D_O\Delta l}{D_R\Delta y} \qquad \theta=\frac{nF}{RT}\left(E-E^{0'}\right) \qquad \Delta l=\frac{l}{NF} \qquad \Delta y=\frac{\delta}{NJ}$$

It should be noted that the constants above take into account the fact that $\Delta\tau$ in the computations discussed below is always defined as positive when corresponding to forward going time. It is calculated thus

$$t_i=\frac{t_p}{NT} \qquad \Delta\tau_{f\,or\,b}=\frac{\tau_i-\tau_p}{NTAU} \tag{6.17.}$$

where τ_t and τ_p are transformed values of t_i and t_p according to equations (6.8.) and (6.9.). NT is the number of real time nodes required for convergence and $NTAU$ is the

number of transformed time nodes required. The approximate efficiency of the transformed grid in comparison to real time computation is estimated by the ratio of *NT*:*NTAU* which for most cases was found to be in excess of 50 times faster for full convergence.

The following boundary conditions apply to the transport equations:

$$
\begin{aligned}
&t = 0 \\
&\qquad [OX]_j = [OX]_{bulk} \qquad for\ j = 0,1,2,\ldots,NJ \\
&\qquad [RED]_j = [RED]_i \qquad for\ j = -NF,\ldots,-2,-1,0 \\
&y = \delta \\
&\qquad [OX]_{NJ} = [OX]_{bulk} \\
&y = -l \\
&\qquad [RED]_{-NF} = [RED]_{-NF+1}
\end{aligned}
\tag{6.18.}
$$

where $[RED]_i$ is the initial concentration of reduced material in the film. To allow a readily soluble tridiagonal matrix to be formed the mercury film-solution interface boundary condition must also be incorporated into the solution diffusion equation at j = -1 such that

$$-\lambda^{Hg}[RED]^t_{-2} + \left(1+2\lambda^{Hg}\right)[RED]^t_{-1} - \lambda^{Hg}e^{-\theta}[OX]^t_0 = [RED]^{t-1}_{-1} \tag{6.19.}$$

All the relevant equations may now be grouped together as a single matrix equation.

$$
\begin{bmatrix}
[RED]^{t-1}_{-NF+1} \\ \cdot \\ \cdot \\ \cdot \\ [RED]^{t-1}_{-2} \\ [RED]^{t-1}_{-1} \\ 0 \\ [OX]^{t-1}_0 \\ [OX]^{t-1}_1 \\ \cdot \\ \cdot \\ \cdot \\ [OX]^{t-1}_{NJ-1} + \lambda'[OX]_{bulk}
\end{bmatrix}
=
\begin{bmatrix}
\left(1+\lambda^{Hg}\right) & -\lambda^{Hg} & 0 & \cdot & \cdot & \cdot & \cdot & \cdot & \cdot & \cdot & \cdot & \cdot & \cdot & \cdot \\
\cdot & \cdot & \cdot & \cdot & \cdot & \cdot & \cdot & \cdot & \cdot & \cdot & \cdot & \cdot & \cdot & \cdot \\
\cdot & \cdot & \cdot & \cdot & \cdot & \cdot & \cdot & \cdot & \cdot & \cdot & \cdot & \cdot & \cdot & \cdot \\
\cdot & \cdot & \cdot & \cdot & \cdot & \cdot & \cdot & \cdot & \cdot & \cdot & \cdot & \cdot & \cdot & \cdot \\
\cdot & \cdot & \cdot & \cdot & \cdot & \cdot & \cdot & \cdot & \cdot & \cdot & \cdot & \cdot & \cdot & \cdot \\
\cdot & \cdot & \cdot & 0 & -\lambda^{Hg} & \left(1+2\lambda^{Hg}\right) & -\lambda^{Hg}e^{-\theta} & 0 & \cdot & \cdot & \cdot & \cdot & \cdot & \cdot \\
\cdot & \cdot & \cdot & \cdot & 0 & -1 & e^{-\theta}+\kappa & -\kappa & 0 & \cdot & \cdot & \cdot & \cdot & \cdot \\
\cdot & \cdot & \cdot & \cdot & \cdot & 0 & -\lambda' & \left(1+2\lambda'\right) & -\lambda' & 0 & \cdot & \cdot & \cdot & \cdot \\
\cdot & \cdot & \cdot & \cdot & \cdot & \cdot & \cdot & \cdot & \cdot & \cdot & \cdot & \cdot & \cdot & \cdot \\
\cdot & \cdot & \cdot & \cdot & \cdot & \cdot & \cdot & \cdot & \cdot & \cdot & \cdot & \cdot & \cdot & \cdot \\
\cdot & \cdot & \cdot & \cdot & \cdot & \cdot & \cdot & \cdot & \cdot & \cdot & \cdot & \cdot & \cdot & \cdot \\
\cdot & \cdot & \cdot & \cdot & \cdot & \cdot & \cdot & \cdot & \cdot & \cdot & 0 & -\lambda' & \left(1+2\lambda'\right)
\end{bmatrix}
\cdot
\begin{bmatrix}
[RED]^t_{-NF+1} \\ \cdot \\ \cdot \\ \cdot \\ [RED]^t_{-2} \\ [RED]^t_{-1} \\ [OX]^t_0 \\ [OX]^t_1 \\ [OX]^t_2 \\ \cdot \\ \cdot \\ \cdot \\ [OX]^t_{NJ-1}
\end{bmatrix}
\tag{6.20.}
$$

This is easily solved by using the Thomas Algorithm.[31,32]

The component currents *I(1)* and *I(2)* (shown in Figure 6.1) are calculated from the flux at the surface of the electrode using Fick's 1st law

$$I(x) = nFAD_O \left\{ \frac{[OX]_0^{tp} - [OX]_1^{tp}}{\Delta y} \right\} \quad where \;\; x = 1,2 \tag{6.21.}$$

The current observed in experimental practice is the difference current ΔI which is calculated by subtracting the backward current, *I(2)*, from the forward current, *I(1)*.

All programs were written in FORTRAN 77 or C, the source code can be found in appendix A2, and executed on a Silicon Graphics Origin 2000 server. Results were analysed using Microsoft Excel 7.0 or IDL 5.0. The simulations were converged to 1%. Typical values of $NTAU = 200$, $NT = 10\,000$, $NJ = 8000$ and $NF = 4000$ were found to be appropriate.

6.3. Results and Discussion

Starting with the consideration of the results of the simulations for the case of semi-infinite diffusion ($\delta \rightarrow \infty$) where the expected behaviour has been thoroughly characterised by means of analytical theory.[25] In particular Kounaves and co-workers showed[25] that the SWV peak for reversible systems can be characterised by three parameters as follows. First the dimensionless peak current,

$$\Delta\varphi_p = \frac{\Delta I_p (\pi\tau)^{\frac{1}{2}}}{nFAD_R^{\frac{1}{2}}[RED]_i} \tag{6.22.}$$

Second the shift in peak potential, E_p, from the true formal potential,

$$nE_{shift} = n\left(E_p - E^{0'}\right) \tag{6.23.}$$

Third the peak width at half-height,

$$nW_{\frac{1}{2}} = n\left(E_{\frac{1}{2}}^R - E_{\frac{1}{2}}^L\right) \tag{6.24.}$$

where $E_{\frac{1}{2}}^{R}$ is the potential at the point to the right of the peak where the current is half the peak current and correspondingly $E_{\frac{1}{2}}^{L}$ is the potential at the same current on the left of the peak. All these three parameters were shown to be unique functions of a single parameter,

$$\Lambda = l\left(\frac{f}{D_R}\right)^{\frac{1}{2}} \qquad (6.25.)$$

for the simulated case of semi-infinite diffusion conditions.[25] Figure 6.3, Figure 6.4* and Figure 6.5 show a comparison of the simulations described above with the analytical theory as reported in reference 25. The parameters E_{SW} and ΔE were fixed corresponding to optimal sensitivity.[24] In all three cases very satisfactory agreement is seen so vindicating both the basis and implementation of our computational approach.*

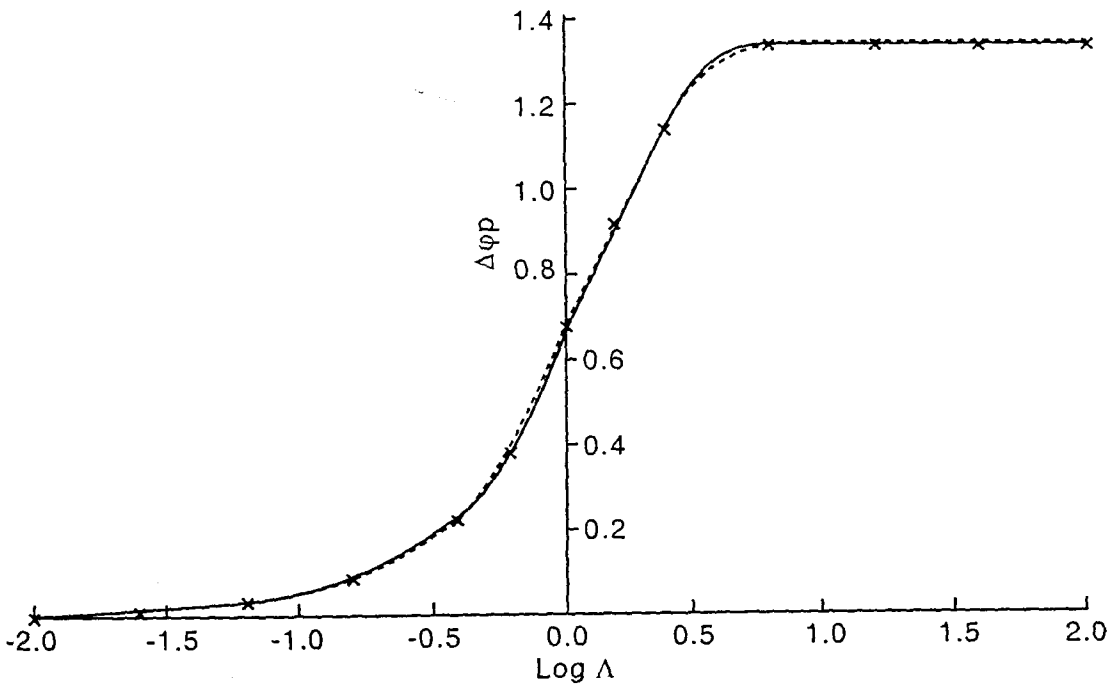


Figure 6.3 Dependence of the current-function peak height, $\Delta\varphi_p$, on log Λ. $n\Delta E = 10$ mV and $nE_{sw} = 50$ mV. Other parameters are described in the text The solid line shows the simulated behaviour whilst the dotted line corresponds to the work of Kounaves and co-workers.[25]

* The error bars in Figure 6.4 arise from the fact that the voltage steps in the simulation are of 5 mV amplitude so that the potential shift values associated with any value of Λ have a maximum uncertainty of this size. For all the points, the analytical theory of Kounaves *et al.* lie within the error bars.

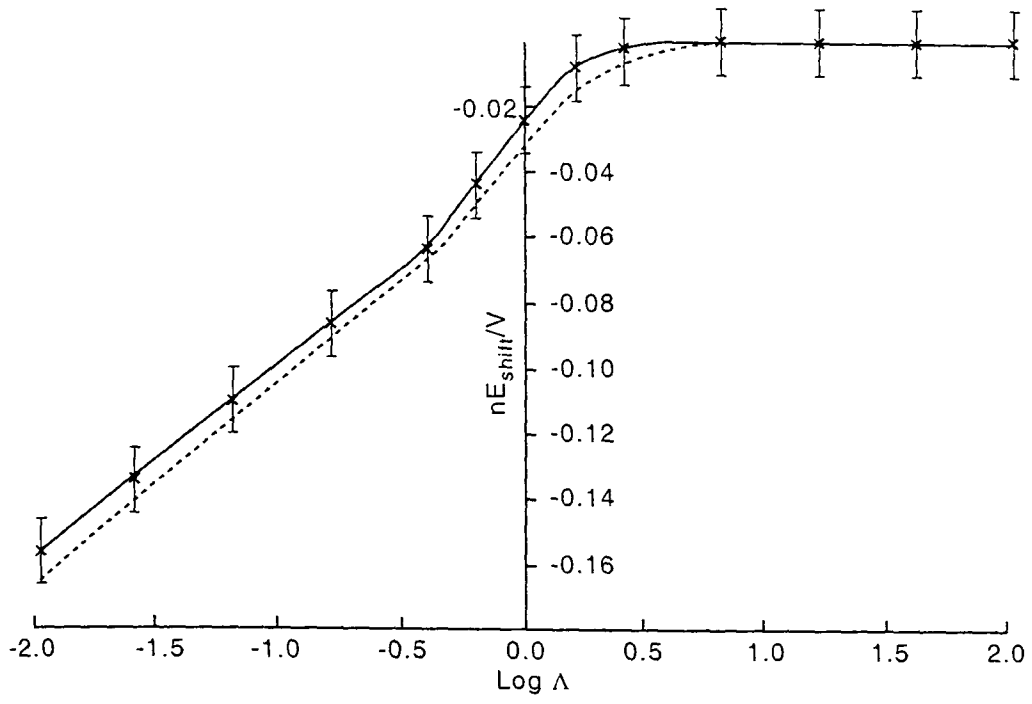


Figure 6.4 Dependence of the peak potential on log Λ. $n\Delta E$ = 10 mV and nE_{sw} = 50 mV. Other parameters are described in the text The solid line shows the simulated behaviour whilst the dotted line corresponds to the work of Kounaves and co-workers.[25]

Next is the consideration of the SWV response as a function of the diffusion layer thickness. Figure 6.6 shows the SWV peak simulated for typical experimental parameters as follows: $E^{0'}$ = -0.50 V, l = 0.1μm, $D_R = 2\text{x}10^{-5}$ cm^{2}s^{-1}, $D_O = 10^{-5}$ cm^{2}s^{-1}, $A = (0.15)^2\pi$ cm^2, n = 2 and f = 200 Hz where D_O and D_R relate to reported values for lead.[33] A range of diffusion layer thicknesses between 1 and 20 μm were simulated together with, for comparison, the response for semi-infinite diffusion. The current, ΔI, displayed is the difference between *I(1)* and *I(2)*. Note that the current first decreases as the diffusion layer shrinks but then passes through a minimum near a diffusion layer thickness of *ca.* 2 μm after which the peak current again rises!

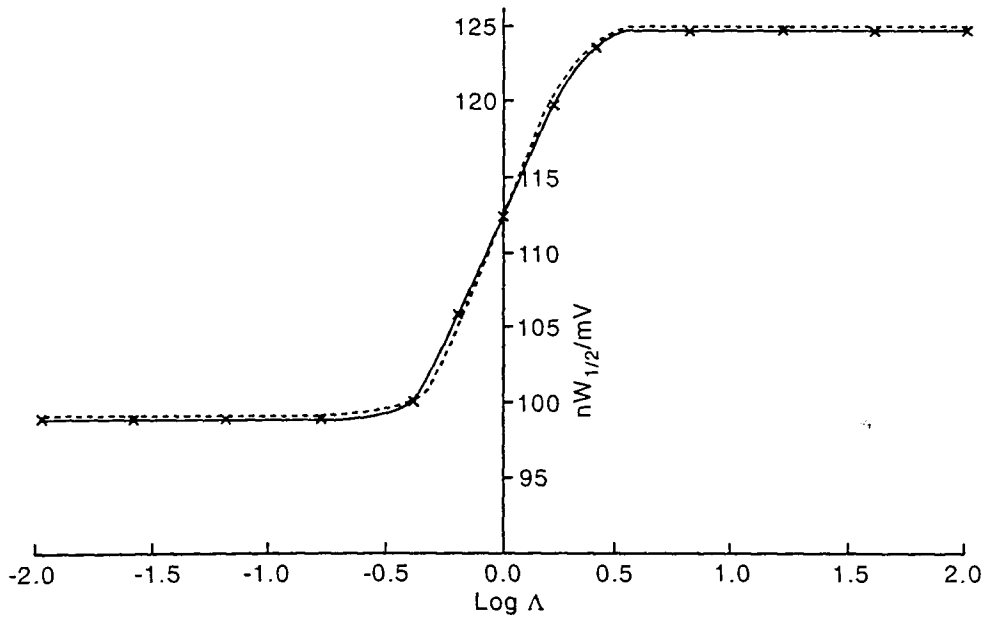


Figure 6.5 Dependence of the peak width at half height on log Λ. $n\Delta E$ = 10 mV and nE_{sw} = 50 mV. Other parameters are described in the text The solid line shows the simulated behaviour whilst the dotted line corresponds to the work of Kounaves and co-workers.[25]

The behaviour in Figure 6.6 can be rationalised by examining the spatial and temporal distributions of both OX (in solution) and RED (in the mercury film) at different

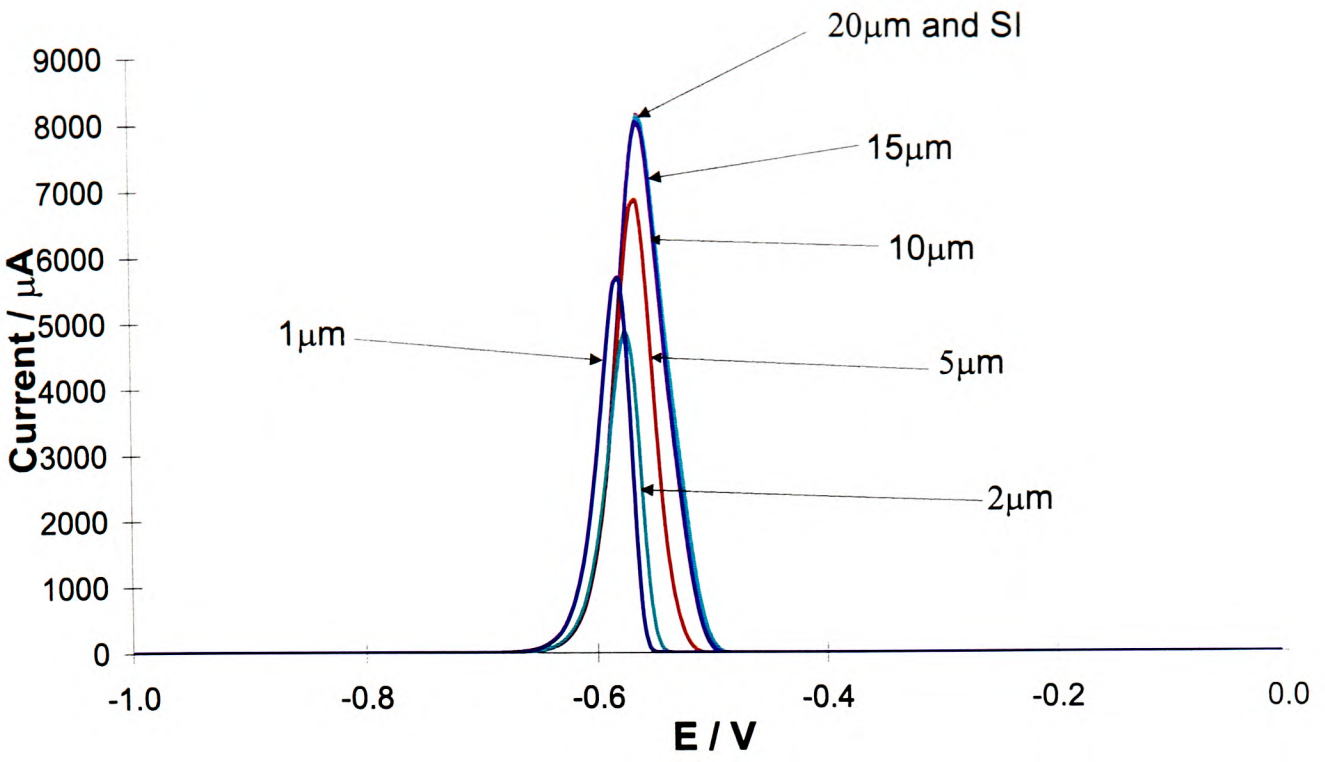


Figure 6.6 Square wave voltammograms for the case where $l = 0.1\mu m$, $n\Delta E$ = 10 mV and nE_{sw} = 50. f = 200 Hz and $[RED]_i$ = 1M for various diffusion layer thickness. SI corresponds to semi-infinite diffusion.

potentials on the current-voltage curve. Figure 6.7 shows these profiles for E = -0.60 and -0.56 V respectively corresponding to the start of the peak and to approximately the peak potential respectively.

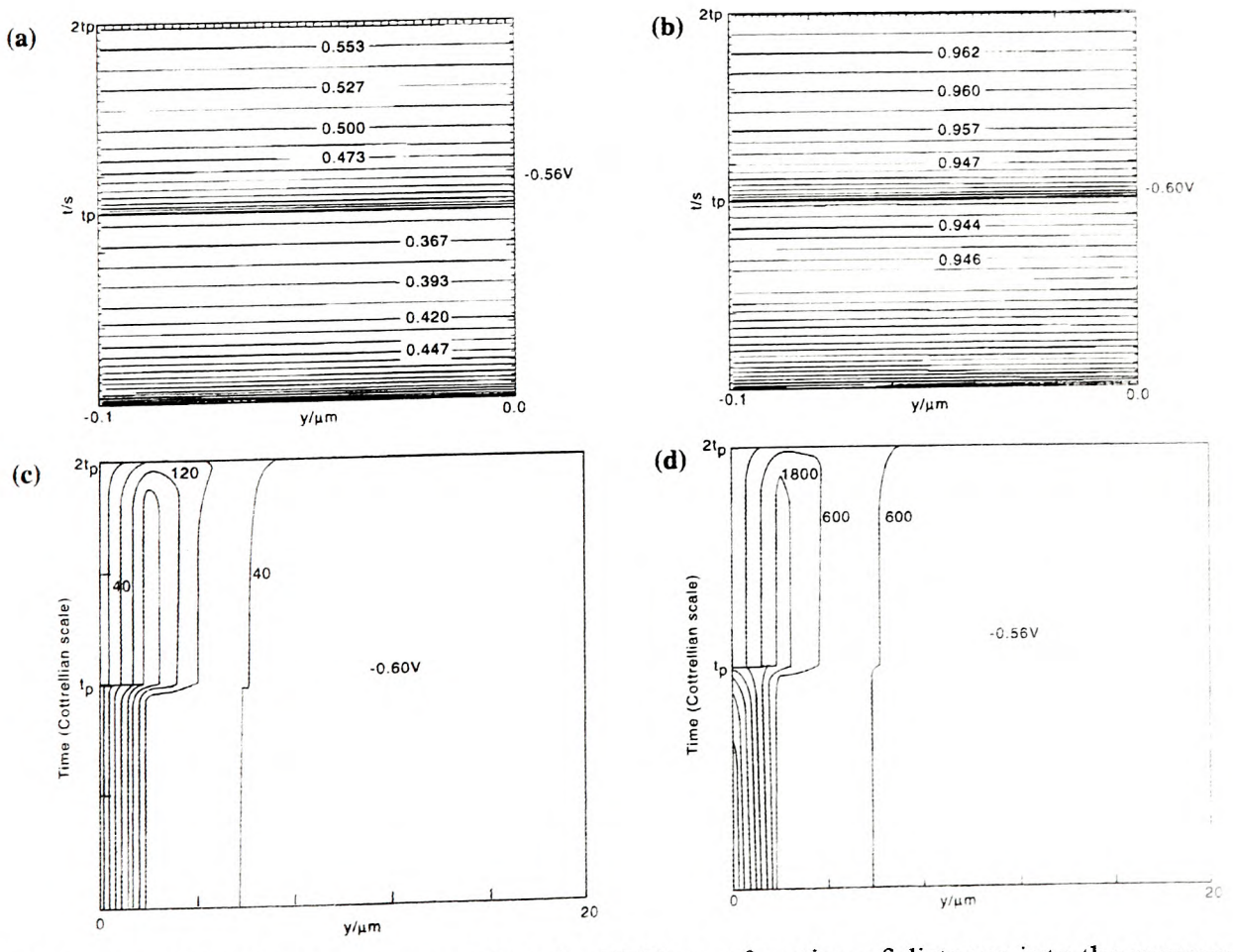
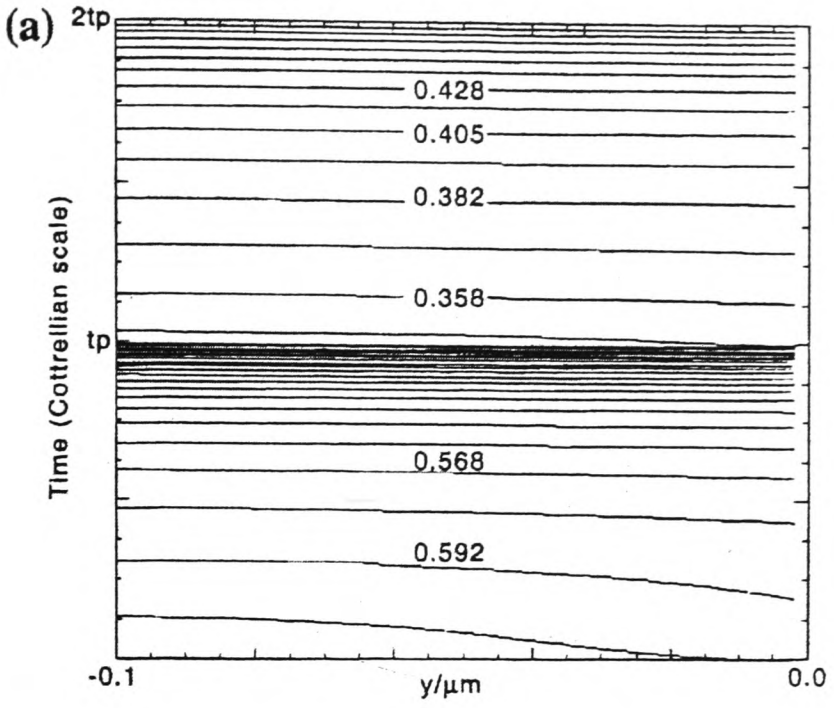


Figure 6.7 (a) and (b) Concentration profiles for RED as a function of distance into the mercury film and of (real) time throughout a complete potential cycle at E = -0.60 V and -0.56 V respectively. (c) and (d) Dimensionless profiles of $[OX]/[OX]_{bulk}$ as a function of distance away from the electrode and of Cottrellian time throughout a complete potential cycle at E = -0.60 V and -0.56 V respectively. In all cases semi-infinite diffusion was assumed; the relevant simulation parameters are given in the text.

In both cases the concentration of RED in the film, although smaller at the more positive potential, is very nearly uniform pointing to the relatively efficient film transport in this case. For OX a greater concentration is seen at -0.56 V as compared to -0.60 V and the oxidised form has diffused further into the solution since the time elapsed since the start of the full peak is longer. Note that the concentration of OX passes through a maximum on the reverse pulse since the material that has been ejected from the electrode on the forward peak undergoes partial re-reduction at the electrode surface.



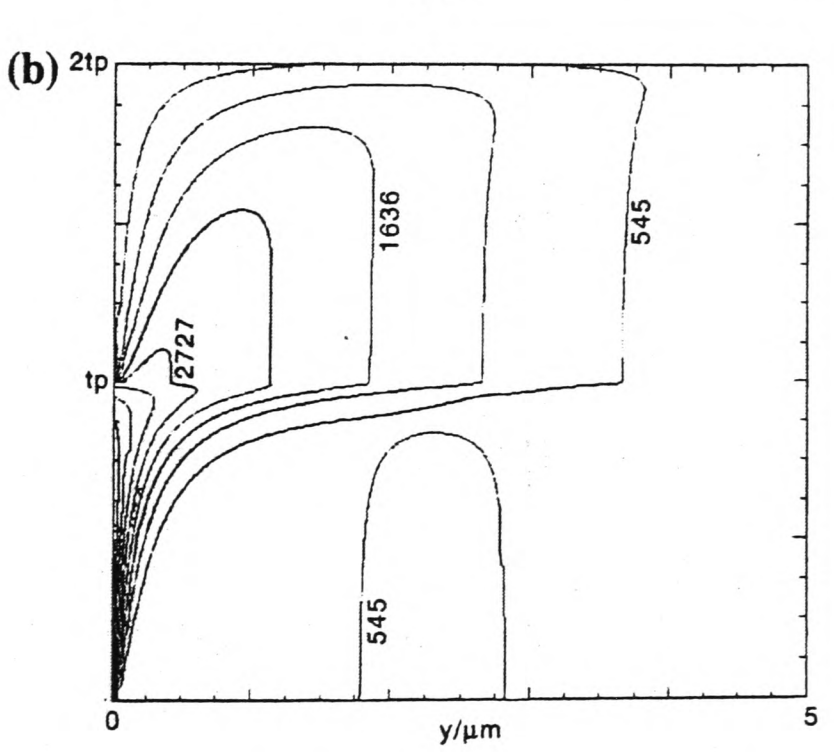


Figure 6.8 (a) Concentration profile for RED as a function of distance into the mercury film and of Cottrellian time throughout a complete potential cycle at E = -0.56 V corresponding to the SWV peak potential. (b) Dimensionless profile of $[OX]/[OX]_{bulk}$ as a function of distance away from the electrode and of Cottrellian time throughout a complete potential cycle at E = -0.56 V. In both cases a diffusion layer thickness of 5 µm was assumed; the other simulation parameters are given in the text.

Figure 6.8 shows data corresponding to that in Figure 6.7 except that a diffusion layer thickness of 5 µm has been assumed. The data depicted relates to the peak potential shown in Figure 6.6 (-0.56 V). Comparison shows primarily that the absolute amount of material in solution is less and that some of the diffusing species has reached the edge of the diffusion layer and hence

has been lost to the solution bulk. This accounts for the decreased current difference seen in Figure 6.6 as this effect decreases the magnitude of *I(2)*.

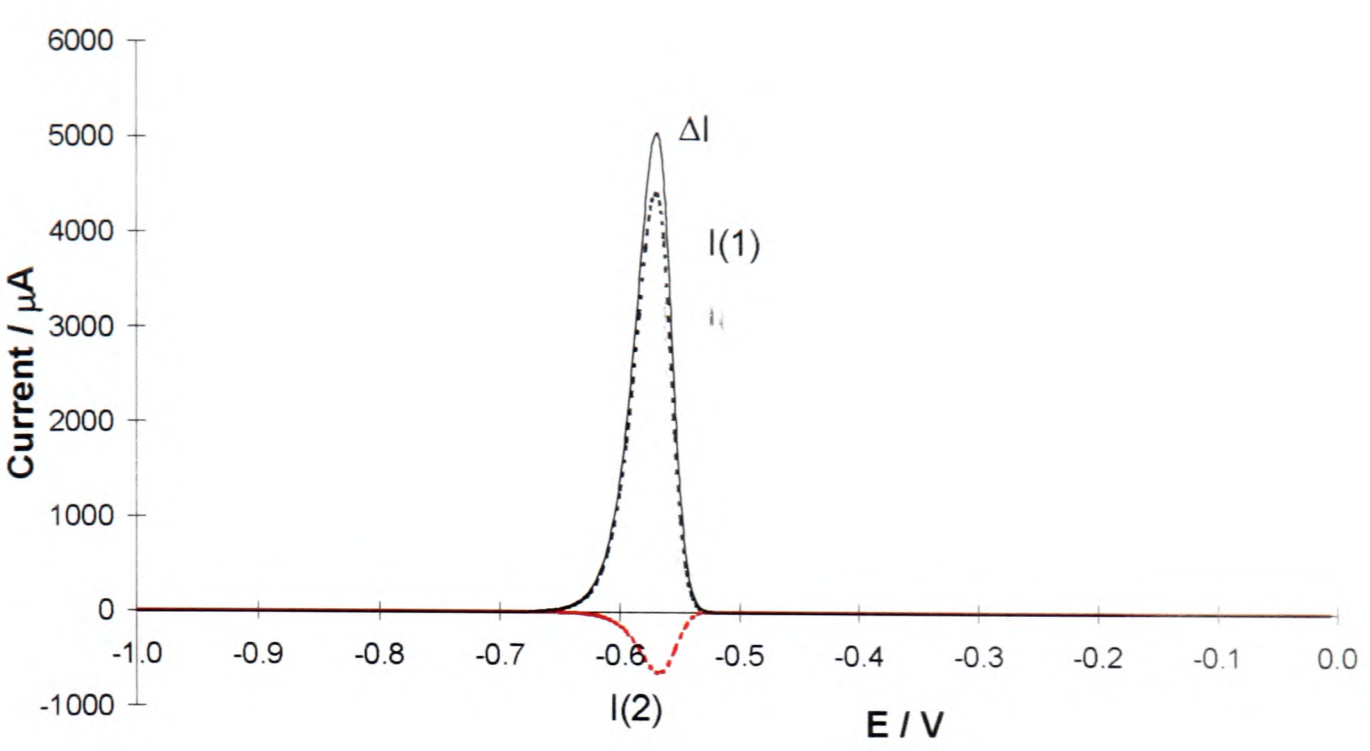


Figure 6.9 Plots of ΔI, *I(1)* and *I(2)* for diffusion layer thicknesses of (a) 3 and (b) 5 μm respectively. The other simulation parameters are as for Figure 6.6.

This is illustrated in Figure 6.9 where ΔI, *I(1)* and *I(2)* are shown for diffusion layer thicknesses of 3 and 5 μm respectively. A significant relative decrease in *I(2)* is seen for the smaller diffusion layer. Note that in Figure 6.8 the distribution of RED in the film remains closely uniform although this is less accurately so than for the cases shown in

Figure 6.7.

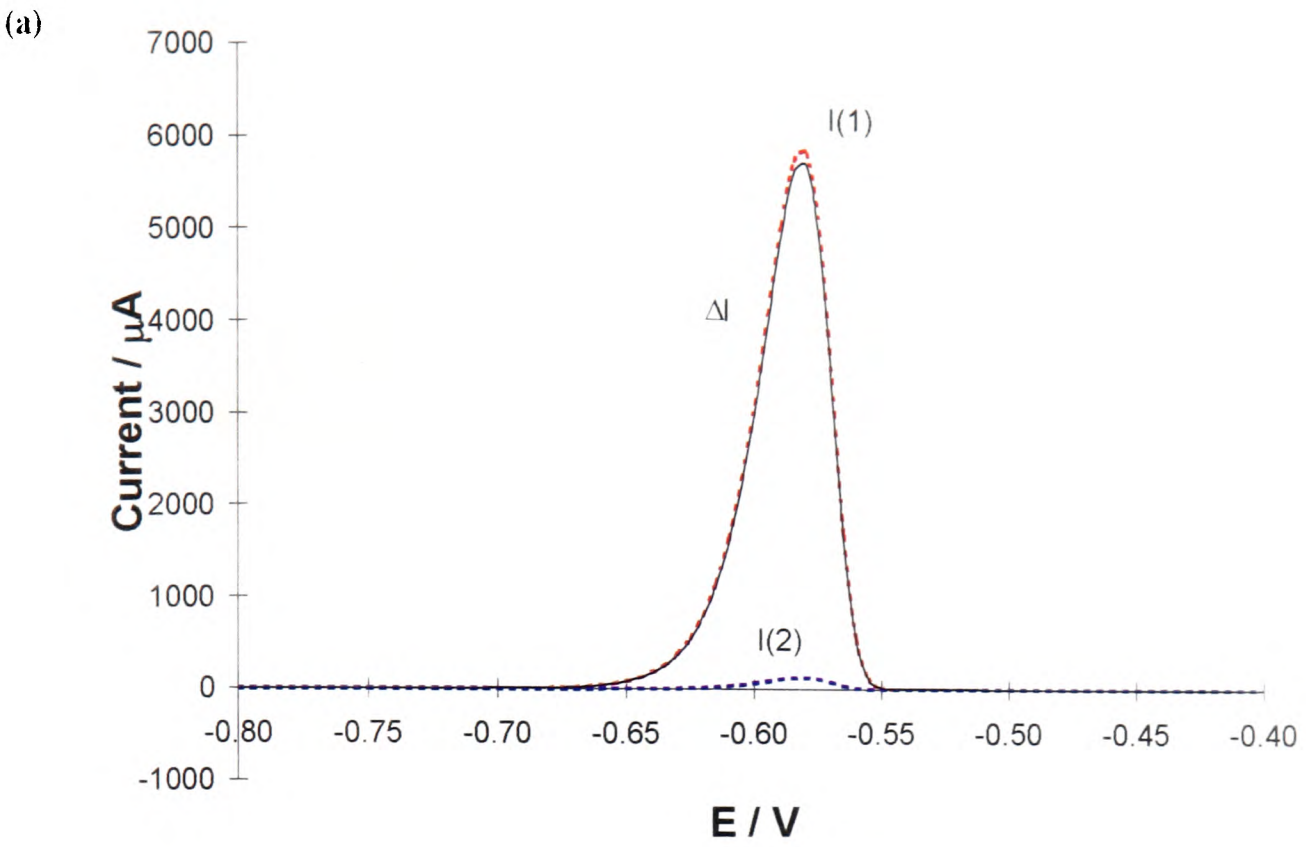


Figure 6.10 Plots of ΔI, $I(1)$ and $I(2)$ for a diffusion layer thicknesses of (a) 1 μm and (b) 2 μm. The simulation parameters are as for Figure 6.6; $f = 200$ Hz.

Figure 6.10 shows ΔI, $I(1)$ and $I(2)$ for a diffusion layer thicknesses of 1 and 2 μm with all other parameters having the same value as for Figure 6.9. Note that Figure 6.6 shows the 1 μm case to have a larger value of ΔI than for the thicker diffusion layers simulated. Figure 6.10 reveals this again arises from the behaviour of $I(1)$ which, in comparison

with Figure 6.9, is seen to progressively increase as the diffusion layer thickness is decreased. In contrast the behaviour of *I(2)* is such that it changes sign as the diffusion layer thickness is reduced!

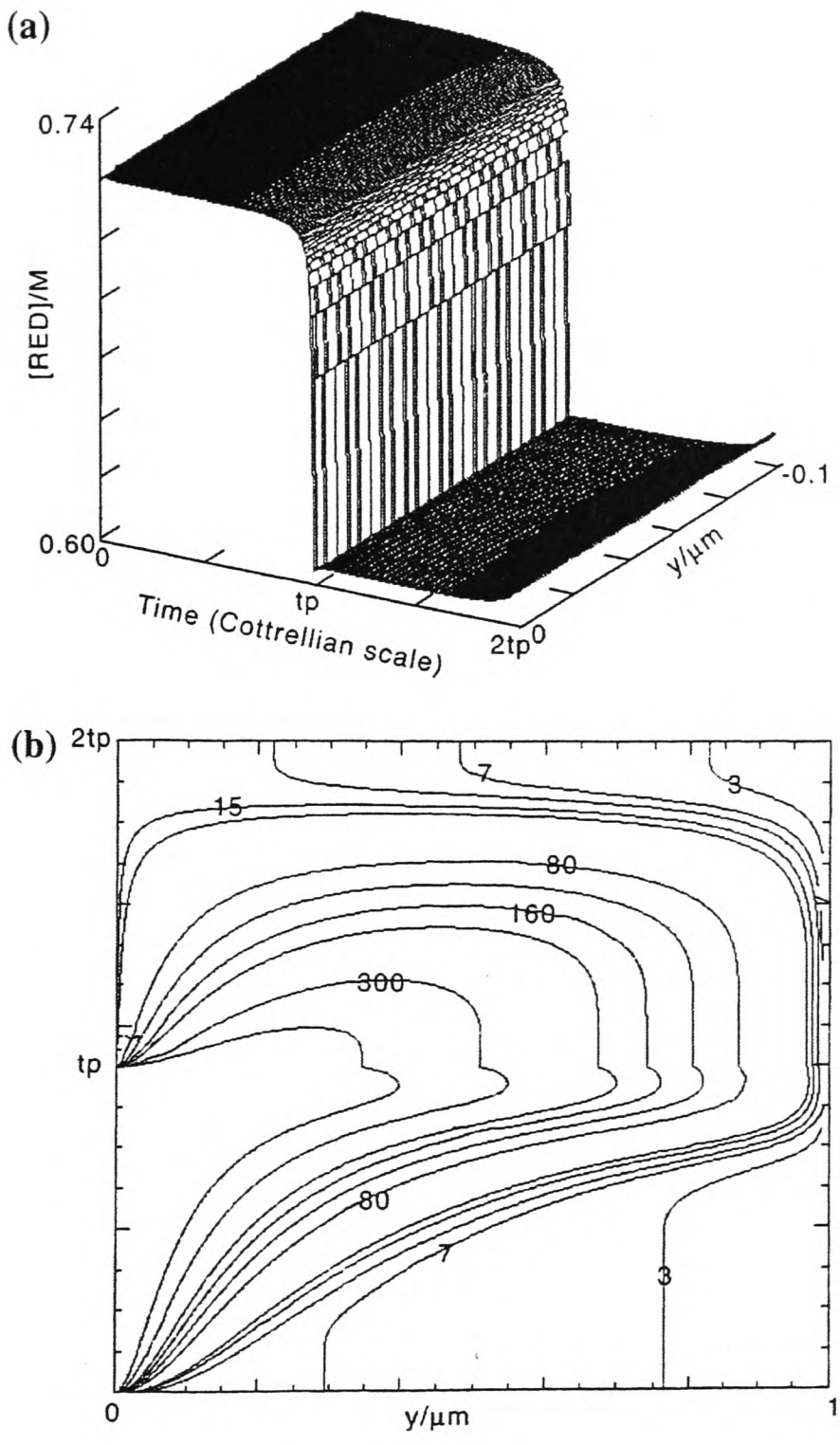


Figure 6.11 (a) Concentration profile for RED as a function of distance into the mercury film and of Cottrellian time throughout a complete potential cycle at E = -0.59 V. (b) Dimensionless profile of $[OX]/[OX]_{bulk}$ as a function of distance away from the electrode and of Cottrellian time throughout a complete potential cycle at E = -0.59 V. In both cases a diffusion layer thickness of 1 µm was assumed; the other simulation parameters are given in the text.

Examination of Figure 6.11 shows that this arises since for the pulse times studied *I(2)* is sampled so late in comparison with the rate of diffusion into bulk solution that material released from the electrode in the forward going pulse has almost quantitatively been lost from the diffusion layer. The contours in Figure 6.11(a) correspond to the return of material into the electrode for most of the pulse but to expulsion later on. Accordingly at times late in the reverse pulse the current direction is oxidative corresponding to the continued release of material from the electrode. This interpretation is confirmed if the simulations are repeated for a much high pulse frequency of 2000 Hz as shown in Figure 6.12 where the behaviour of *I(2)* has returned to being reductive, as expected.

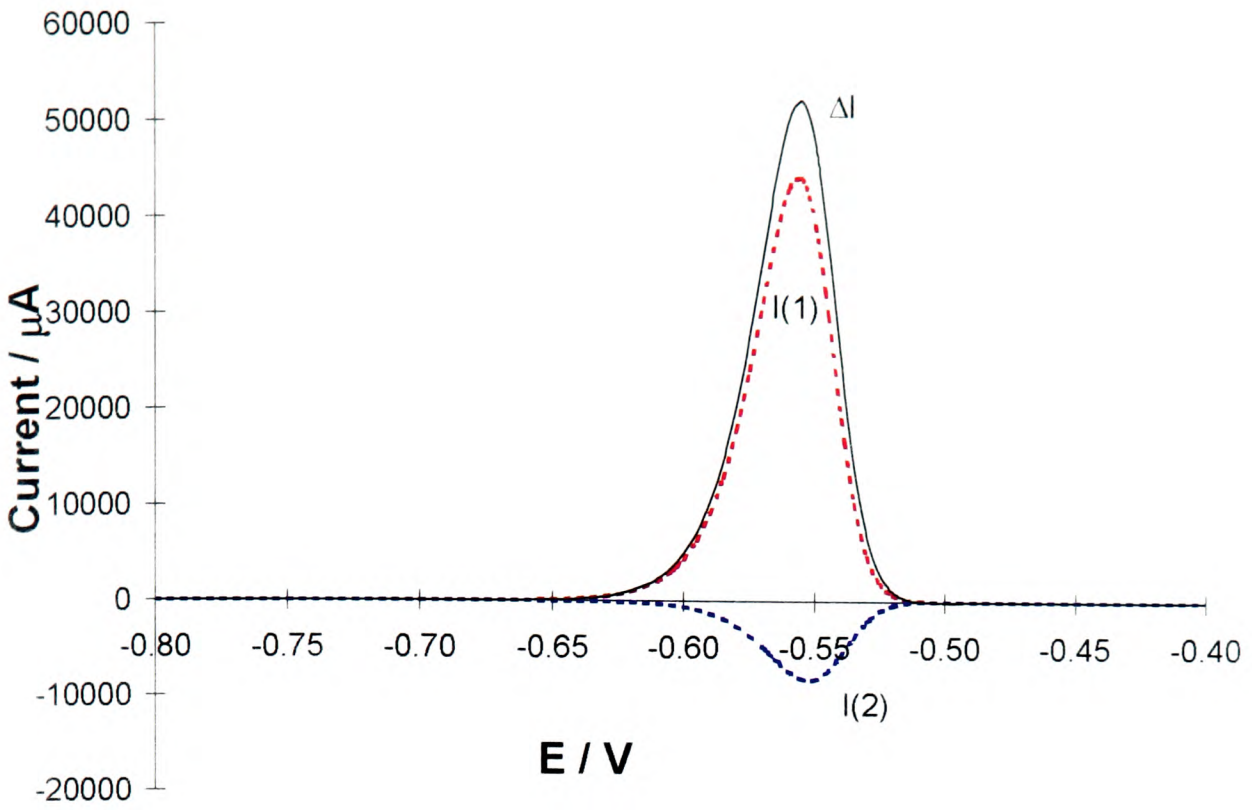


Figure 6.12 Plots of ΔI, *I(1)* and *I(2)* for a diffusion layer thicknesses of 1 μm. The simulation parameters are as for Figure 6.6 with the exception that f = 2000 Hz.

Next considering a case where film diffusion is important. Figure 6.13 shows data simulated for the semi-infinite diffusion case where D_O and D_R correspond to $1x10^{-5}$ and $2x10^{-5}cm^2s^{-1}$ respectively and l = 5μm. Non-uniformities of the RED concentration can be clearly discerned in the film. Notice, in particular, that shortly after each half pulse there can exist either a maximum or minimum according to whether the new pulse either re-

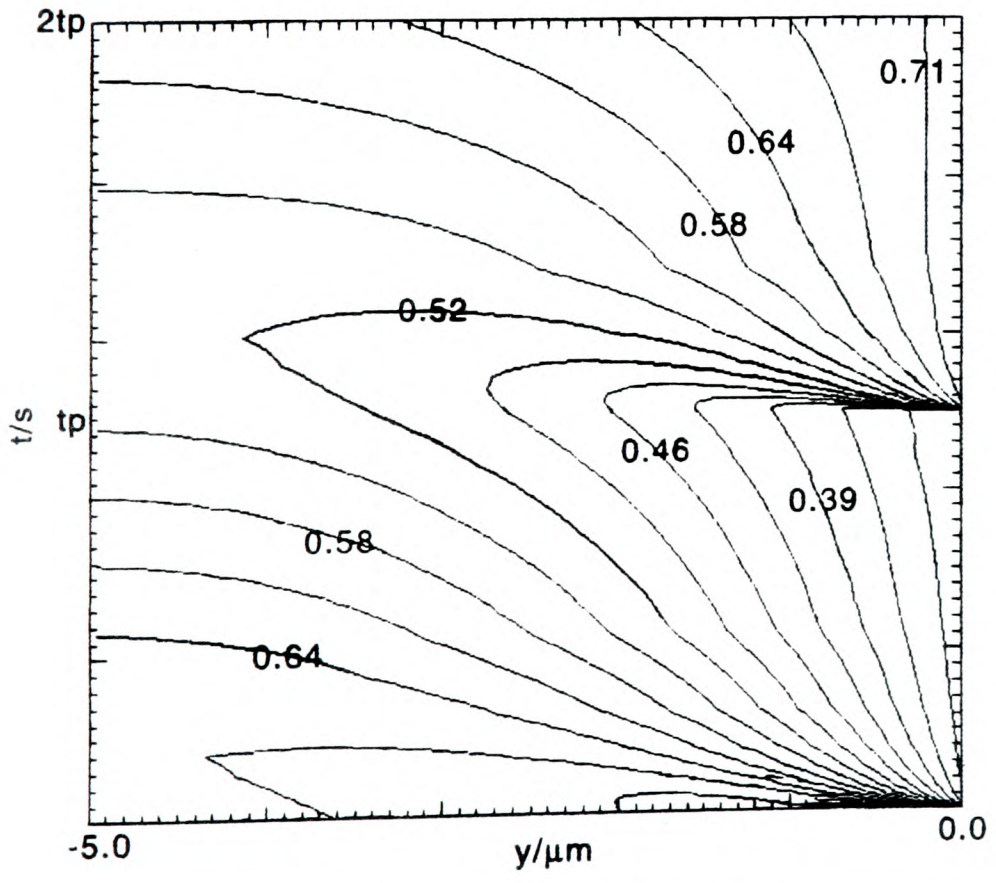


Figure 6.13 The concentration profile for RED within the mercury film as a function of distance and (real) time throughout a complete potential cycle at E = -0.56 V with f = 200 Hz. Diffusion coefficients were assumed for D_O and D_R of $1x10^{-5}$ and $2x10^{-5}$ cm^2s^{-1} respectively.

deposits or strips RED from the film. Clearly under these conditions the experimental response is sensitive to the value of D_R and so hydrodynamic studies of thick mercury films should permit access to the measurement of diffusion coefficients of metals in mercury.

The above results indicate that when SWV is conducted under hydrodynamic conditions significant modifications of the current response may be observed as compared to semi-infinite diffusion conditions. It is pertinent to ask as to the experimental circumstances where this is likely to be seen. For rotating disc electrodes (uniform) diffusion layers of between 10 and 100 μm thick are typically obtained in aqueous solutions for rotation speeds between 50 and 1 Hz so that deviations from semi-infinite conditions would be minimal (see for example Figure 6.6). In contrast for the wall-jet electrode, commonly used in analytical practice,[8-16] *average* diffusion layer thicknesses between 1 and 300 μm can be obtained for flow rates in the range 1 to 10^{-3} cm^3s^{-1} implying the need for caution if presuming semi-infinite diffusion theory. Likewise microelectrodes of sufficiently small size will have sufficiently thin diffusion layers as to require elaboration of the simple theory.

6.4. Experimental Verification

6.4.1. Experimental

The well characterised and thermostatted (25 ± 2 °C) electrochemical cell used for voltammetric and sonovoltammetric experiments has been described in detail previously[34] and in chapter 2. The positioning of the working electrode in this cell is directly opposite the transducer probe and located near the cell bottom. The transducer probe to working electrode distance was 3 mm in all experiments reported below. The ultrasound generator employed was a VCX400 model sonic horn (Sonics and

Materials, USA) equipped with a 13 mm titanium diameter probe emitting 20 kHz ultrasound. The sound intensity was varied between 0 to 40 W cm^{-2} as determined calorimetrically using the method originally suggested by Margulis.[35,36] All experiments were performed using a computer-controlled PGSTAT20 Autolab potentiostat (Eco-Chemie, Utrecht, The Netherlands). The need for bipotentiometric[37] control of the titanium horn itself was eliminated by insulating the transducer from the probe with a thin Teflon disc and connecting the two with an insulating screw thread machined from Delrin™ instead of titanium. Thermostatting of the cell (25 ± 2 °C) was accomplished by means of a glass cooling coil inserted in the solution through which water is circulated from a constant temperature bath.

The working electrode consisted of a 2 mm copper electrode polished using diamond pastes of successively finer size down to 1 μm (Kemet, Kent, UK) which was then electrochemically coated with mercury following a procedure described in the literature.[38] Electroplating was carried out using a 0.01 M mercury(II) perchlorate and a 0.1 M perchloric acid solution at an applied potential of –0.6 V vs. SCE where hydrogen evolution is not observed. This permitted the calculation of the thickness of the mercury film, which was 1 ±0.03 μm in all cases. This choice of substrate produces uniform mercury films which are not obtained on other electrode substrates such as platinum or glassy carbon where small mercury droplets are formed.[38,39] The films are also appropriate for using under sonication, since they remain largely unaffected.[40,41] In addition, modelling of simple linear scan ASV of various metals using mercury-coated copper electrodes has shown[38] good correlation between theory and experiments in the case of Pb^{2+}. In this modelling no interactions were assumed to occur between copper and lead in the mercury film as required by the theory described above.

Reagents used were of analytical grade or the highest commercially available purity. Hexaaminеruthenium(III) chloride, mercury(II) perchlorate, perchloric acid, a lead(II) standard (0.483 mM) and a hydrochloric acid standard (0.974 M) were supplied by Aldrich, sodium chloride and potassium nitrate by BDH and were used as received. Solutions were prepared using UHQ grade water of resistivity not less than 18 MΩ cm (Elgastat, High Wycombe, Bucks, UK). All solutions were deaerated with Pureshield Argon prior to experiments.

The ASV procedure was a modified version of that described by Donten and Kublik.[38] 250 mL of a solution containing 0.5 M NaCl, 0.1 M HCl and 5 μM Pb^{2+} were placed in the sono-electrochemical cell described above. The solution was then deaerated by purging with pureshield Argon for 15 min while the electrode was held at –0.3 V vs. SCE, where any lead present in the mercury film is stripped off while the film remains unaffected. The working electrode was then set at the deposition potential of –0.8 V *vs*. SCE for 60 s. The anodic stripping voltammetry scan, square wave, was then started during which ultrasound was applied to the system as described above. Square wave parameters were as follows: amplitude 25 mV, step voltage of 5 mV, and frequencies varying between 20 to 1000 Hz. Time-resolved experiments were conducted in a solution containing 0.1 M KNO_3 and 1mM $Ru(NH_3)_6Cl_3$ with the working electrode held at –0.5 V *vs*. SCE where the mass-transport limited reduction current of $Ru(NH_3)_6^{3+}$ can be obtained to calibrate the diffusion layer thickness.[42]

6.4.2. Results and Discussion

In the previous section (§ 6.2) a simulation approach to electrochemically reversible systems undergoing square wave voltammetry at hydrodynamic electrodes was developed. Significant deviations from semi-infinite diffusion theory were predicted for small diffusion layer thicknesses.

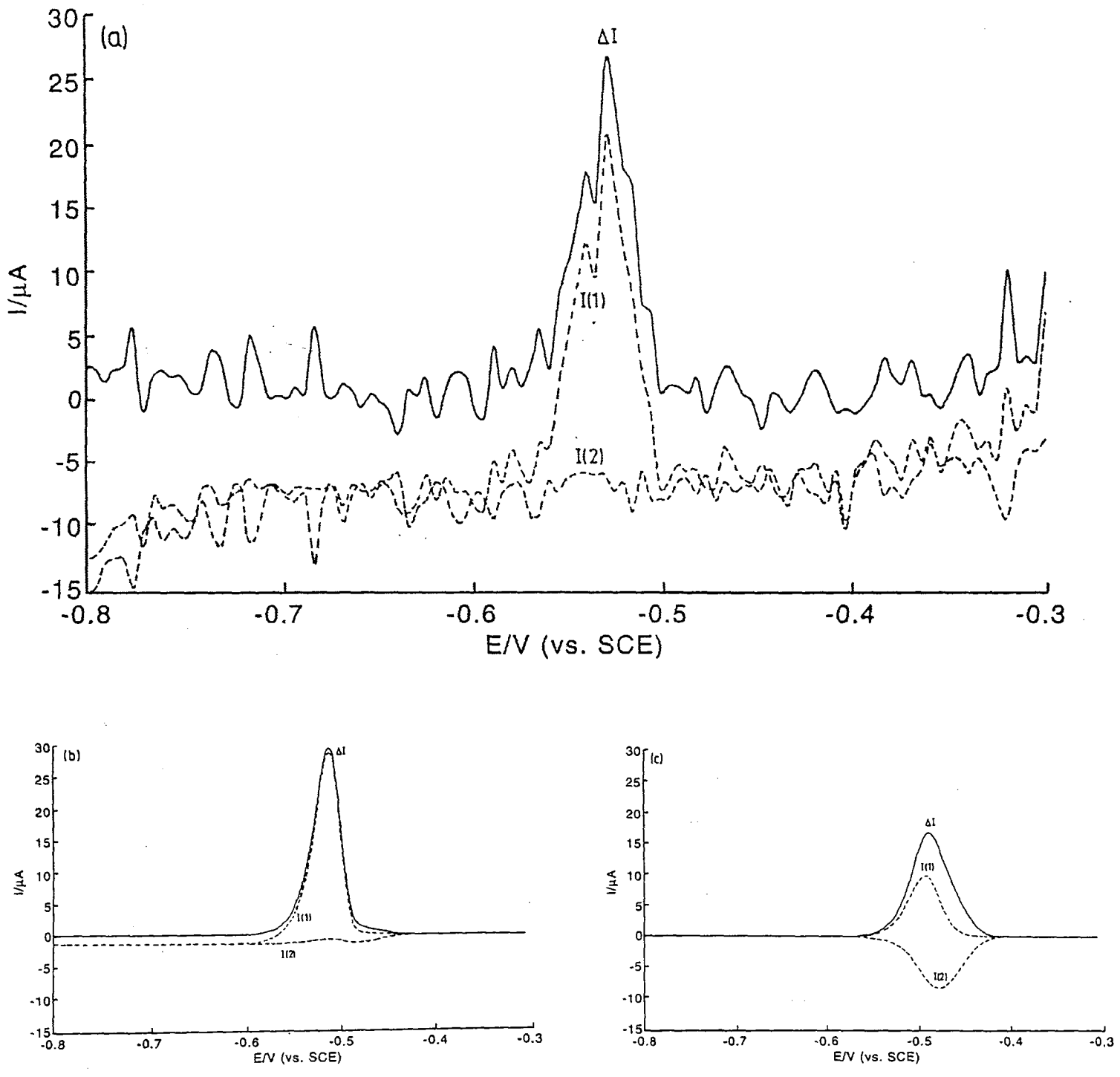


Figure 6.14 Square wave voltammograms for a frequency of 20 Hz obtained: (a) experimentally in a 0.5 M NaCl, 0.1 M HCl and 5 μM Pb^{2+} solution following a pre-concentration time of 60 s at –0.8 V *vs.* SCE using a 1 μm mercury film on copper under sonication of intensity 54 W cm^{-2} from a ultrasonic probe placed at 3 mm of the working electrode; (b) via simulation using a diffusion layer thickness of 2.4 μm; and (c) via simulation under conditions of semi-infinite diffusion. Square wave parameters: pulse amplitude, E_{SW} = 25 mV and a step voltage, ΔE, of 5 mV.

Therefore, a series of experiments were carried out in which square wave voltammograms for a frequency of 20 Hz were obtained experimentally (Figure 6.14a) under applied ultrasound of intensity 54 W cm^{-2} emitted from a ultrasonic probe placed at 3 mm opposite a 2 mm mercury-coated copper electrode. The diffusion layer thickness under these conditions was calculated using equation (6.26.) and the mass-transport-controlled current obtained during time-resolved experiments (shown in Figure 6.15) for the one-electron reduction of $Ru(NH_3)_6^{3+}$ in 0.1 M KNO_3 on a 2 mm mercury-coated copper electrode held at an applied potential of –0.5 V *vs.* SCE (mass-transport-controlled current) under otherwise identical conditions of sonication.

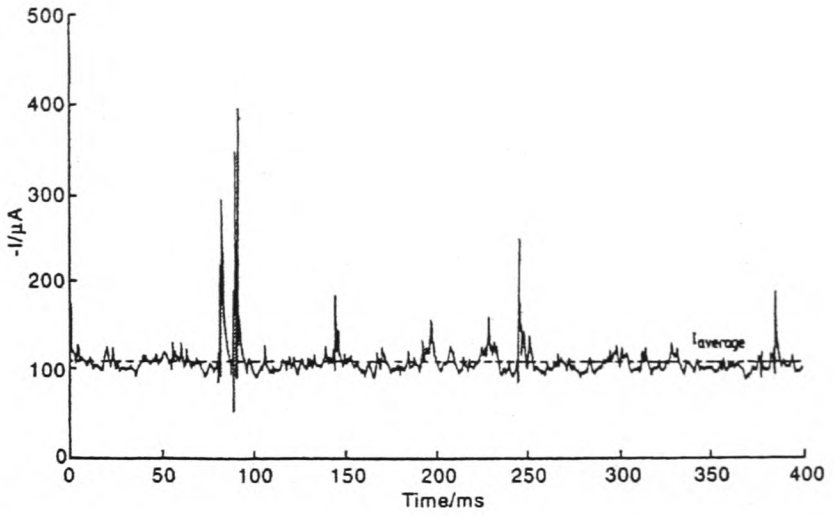


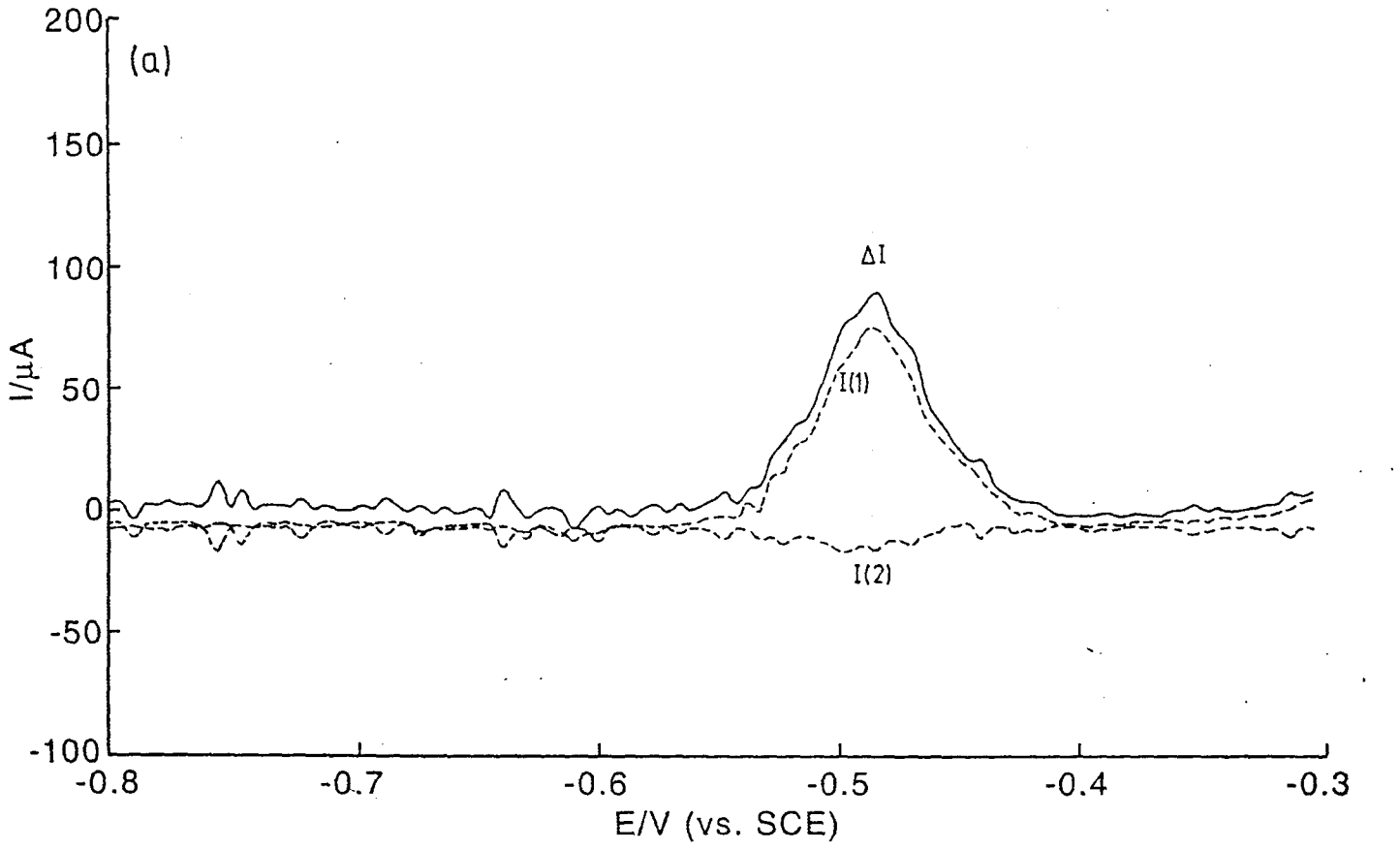
Figure 6.15 Time-resolved current signal for the reduction of 1 mM $Ru(NH_3)_6^{3+}$ in aqueous 0.1 M KNO_3 at an applied potential of –0.5 V *vs.* SCE recorded in the presence of ultrasound of intensity 54 W cm^{-2} emitted from an ultrasonic probe placed at 3 mm of a 2 mm mercury-coated copper electrode.

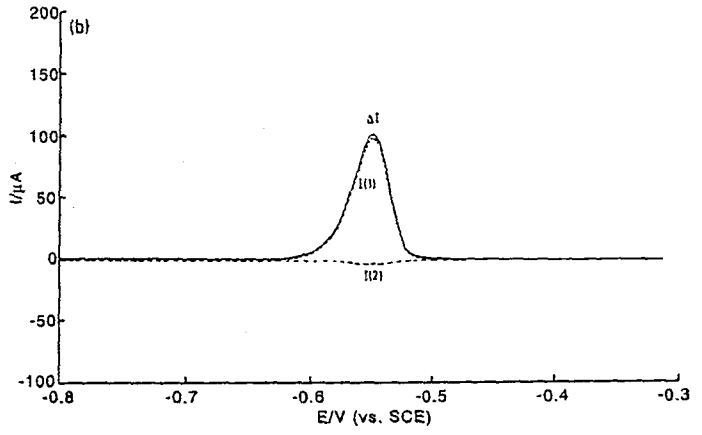
$$I_{\lim} = \frac{nFAD[OX]}{\delta} \qquad (6.26.)$$

where I_{lim} is the limiting current, n is the number of electrons involved, A is the electrode area, 3.14 mm^2, F the Faraday constant, D the diffusion coefficient of the ruthenium(III) complex in water, 9.1×10^{-5} cm^2 s^{-1} and [Ox] its concentration, 1 mM. A value of δ of 2.4 μm is obtained for an ultrasound intensity of 54 W cm^{-2} at a horn to electrode distance of 3 mm. Results (where ΔI is the difference between I(1) and I(2), the forward and backward currents during the square wave scan) were compared to the theoretical values predicted by the theory both under high mass-transport using the calculated value of δ reported above, Figure 6.14b, and under conditions of semi-

infinite diffusion, Figure 6.14c. An excellent agreement is observed between experiment and the theoretical values predicted using the model of the 'uniformly accessible electrode' for a diffusion layer thickness of 2.4 μm, Figure 6.14a and Figure 6.14b, respectively. Both differ considerably from the value predicted under conditions of semi-infinite diffusion. In particular, the magnitude and sign of I(2) in Figure 6.14a correlates well with the predicted values. This observed behaviour of I(2) as the diffusion layer thickness decreases had been predicted by the theory and reported in the previous section. It was attributed to the fact that at small diffusion layer thickness the pulse times studied I(2) is sampled so late in comparison with the rate of diffusion of Pb^{2+} into the bulk of the solution that the Pb^{2+} released from the electrode in the forward going pulse has been partially lost from the diffusion layer and cannot be reduced in the backward going scan I(2). It is worth pointing out that this strong agreement between theory and experiment occurs despite the strong cavitational events which occur under power ultrasound as shown by individual current spikes in Figure 6.15. Theory has been developed[42] which satisfactorily approximates the effect of ultrasound on the mass transport at the electrode surface by considering only the effect of 'acoustic streaming' and by treating the system similar to related cases in hydrodynamic voltammetry as has been the case for the theory used in these simulations. The contribution of the underlying physical processes responsible for the huge increase in mass transport under insonation conditions are (i) acoustic streaming, (ii) jets caused by cavitational collapses, (iii) turbulent convection, (iv) microstreaming in the presence of oscillating bubbles, and (v) to some degree the fluctuating current density which might -owing to the calibration procedure- average to an apparent δ_{app} smaller than the geometric average. However, the present results

are further evidence for a dominant effect of acoustic streaming on the mass transport at the electrode surface.





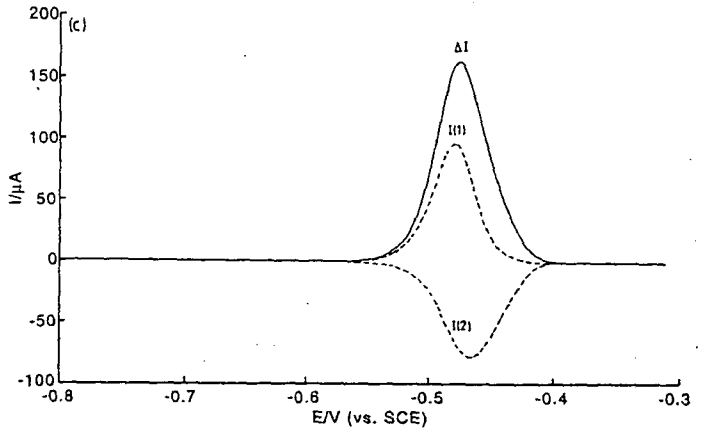


Figure 6.16 Square wave voltammograms for a frequency of 200 Hz obtained: (a) experimentally in a 0.5 M NaCl, 0.1 M HCl and 5 μM Pb^{2+} solution following a pre-concentration time of 60 s at –0.8 V *vs.* SCE using a 1 μm mercury film on copper under sonication of intensity 54 W cm^{-2} from a ultrasonic probe placed at 3 mm of the working electrode; (b) via simulation for a diffusion layer thickness of 2.4 μm; and (c) via simulation under conditions of semi-infinite diffusion. Other square wave parameters as in Figure 6.14.

The effect of the frequency of the pulse can be observed in Figure 6.16 and Figure 6.17, where square wave voltammograms obtained in the same conditions as those in Figure 6.14 are shown for the higher frequencies of 200 and 1000 Hz. As predicted by the theory (Figure 6.16b) I(2) becomes slightly reductive as the pulse frequency is increased to 200 Hz. Further increase of the pulse frequency renders I(2) more

reductive. As discussed above experimental results obtained under power ultrasound deviate from simulation under conditions of semi-infinite diffusion and are best described using the 'uniformly accessible electrode' model with a diffusion layer thickness of 2.4 μm. This observation can be explained along with the discussion provided above for the magnitude and sign of I(2). As the frequency increases the Pb^{2+} released during the forward scan has less time to be diffuse away into the bulk of the solution and therefore is more readily available for reduction in the backward scan I(2).

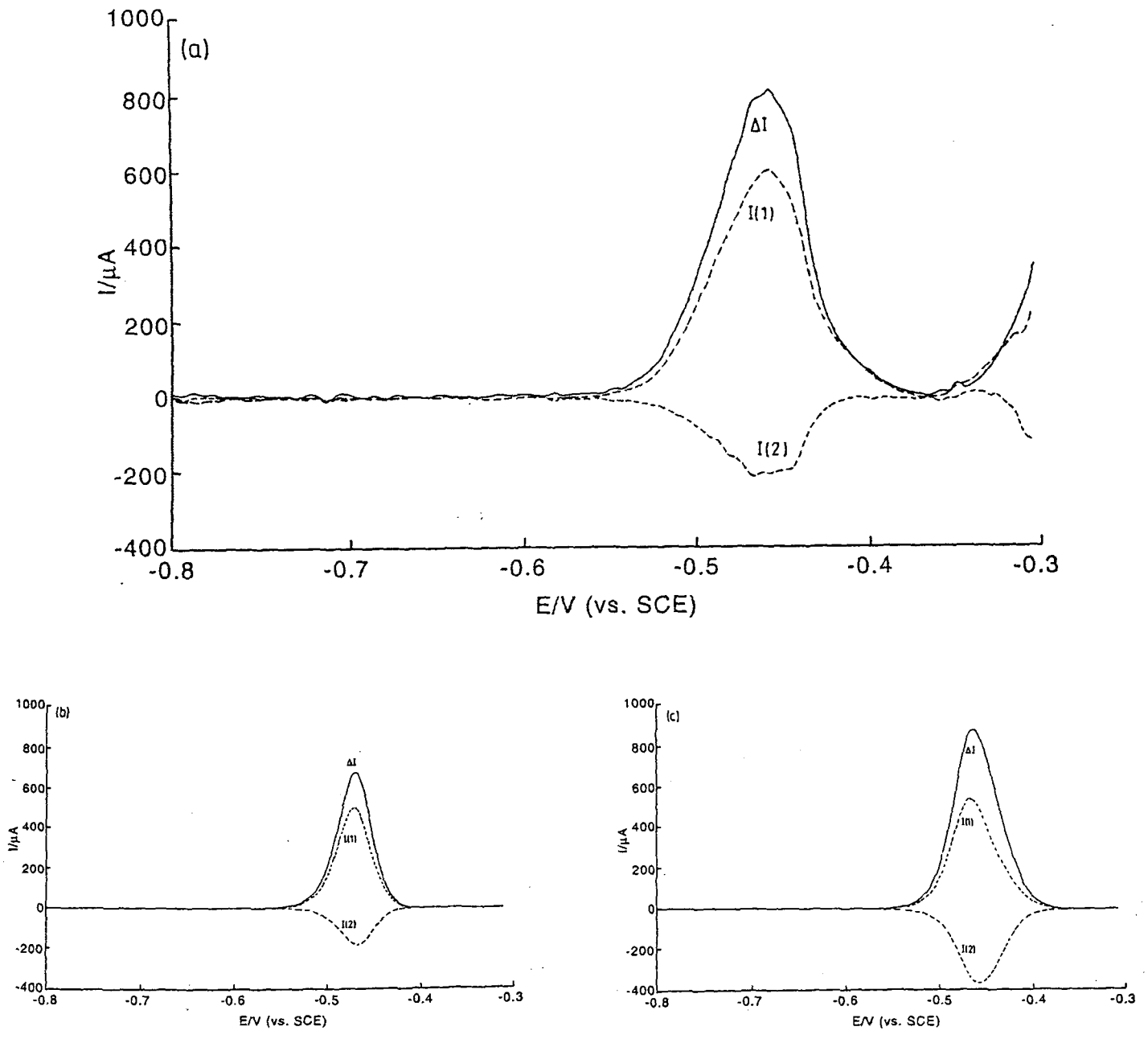


Figure 6.17 Square wave voltammograms for a frequency of 1000 Hz obtained: (a) experimentally in a 0.5 M NaCl, 0.1 M HCl and 5 μM Pb^{2+} solution following a pre-concentration time of 60 s at –0.8 V *vs.* SCE using a 1 μm mercury film on copper under sonication of intensity 54 W cm^{-2} from a ultrasonic probe placed at 3 mm of the working electrode; (b) via simulation using a diffusion layer thickness of 2.4 μm; and (c) via simulation under conditions of semi-infinite diffusion. Other square wave parameters as in Figure 6.14.

6.5. Conclusions

In the above a simulation approach to electrochemically reversible processes undergoing SWV at a hydrodynamic electrode is developed and significant deviations from semi-infinite diffusion conditions predicted. The theory developed for SWV as applied to electrochemically reversible processes undergoing ASV at planar mercury electrodes has been corroborated with experiments in the presence of ultrasound. In particular, deviations from semi-infinite theory predicted under conditions of high mass transport correlated well with experiments in which small diffusion layer thicknesses was attained by the application of power ultrasound. These results provided further evidence for a dominant effect of 'acoustic streaming' on the mass transport at the electrode surface. Finally, care should be taken when choosing the frequency in SWVASV experiments under small diffusion layer thicknesses since partial reduction of the metal ion species in the backward scan may be lost due to diffusion of the metal ion species away from the electrode

References for Chapter 6

[1] J.C. Ball, R.G. Compton, C.M.A. Brett, *J. Phys. Chem.* 102 (1998) 162
[2] J.C. Ball, R.G. Compton, *Electroanalysis* 9 (1997) 765
[3] J.C. Ball, *Sonoelecroanalysis*, Part II thesis, Oxford (1997)
[4] J.C. Ball, R.G. Compton, *Electroanalysis* 9 (1997) 1305
[5] J.C. Ball, J.A. Cooper, R.G. Compton, *J. Electroanal. Chem.* 435 (1997) 229
[6] Kh. Brainina, E. Neyman, *Electroanalytical Stripping Methods*; John Wiley and Sons: New York, 1993
[7] J. Wang, *Analytical Electrochemistry*; VCH: Weinheim, 1994
[8] G.E. Batley, T.M. Florence, *J. Electroanal. Chem.*, 55 (1974) 23
[9] V.I. Bakaanov, M.S. Zakharov, V.A. Antip'eva,; A.P. Grigorchenko, *Zh. Anal. Khim.*, 29 (1974) 421
[10] C.M.A. Brett, J.L.F.C.Lima, M.B. Quinaz Garcia, *Analyst* 119 (1994) 1229
[11] C.M.A. Brett, M.M.P.M. Neto, *J. Electroanal. Chem.* 258 (1989) 345
[12] C.M.A. Brett, A.M. Oliveira Brett, J.L.C. Pereira, *Electroanalysis* 3 (1991) 83
[13] M.M.P.M Neto, M.M.G.S. Rocha, C.M.A. Brett, *Talanta* 41 (1994) 1597
[14] C.M.A. Brett, M.B. Quinaz Garcia, J.L.F.C. Lima, *Electroanalysis* 8 (1996) 1169
[15] S.H. Lieberman, A. Zirino, *Anal. Chem.* 46 (1974) 20
[16] R.W. Andrews, D.C. Johnson, *Anal. Chem.* 48 (1974) 1057
[17] D.K. Roe, J.E.A. Toni, *Anal. Chem.* 37 (1965) 1503
[18] C.M.A. Brett, A.M. Oliveira Brett, *J. Electroanal. Chem.* 262 (1989) 83
[19] J. Schiewe, K.B. Oldham, J.C. Myland, A.M. Bond, V.A. Vicente-Beckett, S. Fletcher, *Anal. Chem.* 69 (1997) 2673
[20] W.T. de Vries, E. van Dalen, *J. Electroanal. Chem.* 14 (1967) 315
[21] R.G. Compton, J.C. Eklund, F. Marken, *Electroanalysis* 9 (1997) 509
[22] C.M.A. Brett, A.M. Oliveira Brett, *Electrochemistry. Principles, Methods and Applications*; Oxford University Press: Oxford, UK, 1993
[23] M. Wojciechowski, W. Go, J. Osteryoung, *Anal. Chem.* 57 (1985) 155
[24] J. Osteryoung, J.J. O'Dea, in A.J. Bard, (Ed.) *Electroanalytical Chemistry*; Marcel Dekker: New York, 14 (1986) 209
[25] S.P. Kounaves, J.J. O'Dea, P. Chandresekhar, J. Osteryoung, *Anal. Chem.* 59 (1987) 386
[26] S.P. Kounaves, J.J. O'Dea, P. Chandresekhar, J. Osteryoung, *Anal. Chem.* 58 (1986) 3199
[27] K. Aoki, K. Tokuda, H. Matsuda, J. Osteryoung, *J. Electroanal. Chem.*, 207 (1986) 25
[28] F.G. Cottrell, *Z. Phys. Chem.* 42 (1903) 385
[29] T. Kambara, *Bull. Chem. Soc. Japan* 27 (1954) 523
[30] D02CAF subroutine in the NAG library (Mark 17)
[31] A.C. Fisher, R.G. Compton, *J. Appl. Electrochem.* 22 (1992) 38
[32] A.C. Fisher, R.G. Compton, *J. Phys. Chem.* 95 (1991) 7538
[33] F. Vydra, K. Štulík, E. Juláková, *Electrochemical Stripping Analysis*; Ellis Horwood: Chichester, UK, 1976
[34] R.G. Compton, J.C. Eklund, S.D. Page, *J. Phys. Chem.* 99 (1995) 4211
[35] M.A. Margulis, A.N. Mal'tsev, *Russ. J. Phys. Chem.* 43 (1969) 592
[36] T.J. Mason, J.P. Lorimer, D.M. Bates, *Ultrasonics* 30 (1992) 40
[37] F. Marken, R.G. Compton, *Ultrasonics Sonochemistry* 2 (1996) S131
[38] M. Donten, Z. Kublik, *J. Electroanal. Chem.* 196 (1985) 275
[39] F. Marken, T.O. Rebbitt, J. Booth, R.G. Compton, *Electroanalysis*, 9 (1997) 19
[40] C. Agra-Gutiérrez, R.G. Compton, *Electroanalysis*, 10 (1998) 204
[41] C. Agra-Gutiérrez, R.G. Compton, *Electroanalysis*, 10 (1998) 603
[42] F. Marken, R.P. Akkermans, R.G. Compton, *J. Electroanal. Chem.* 415 (1996) 55

7. Cavitation: Sonochemical and Sonoelectrochemical Effects. Quantification and Simulation of Interfacial Cavitation.

The work in this chapter has been published in *Ultrasonics Sonochemistry* 7 (2000) 7. The work reported in section 7.4 was done in collaboration with Joanna Hardcastle of the Physical and Theoretical Chemistry Laboratory, Oxford and Dr. Steven D. Bull and Prof. Stephen Davies of the Dyson Perrins Laboratory, Oxford.

7.1. Introduction

In recent years much attention has been focussed on the development of fundamental knowledge and new applications in sonoelectrochemistry.[1,2] The methodology of introducing a source of high intensity ultrasound into an electrochemical cell has benefited from the availability of horn type transducers which enable high intensity ultrasound to be applied locally to the working electrode of a conventional three electrode system[3,4] or four electrode system,[5] see Chapter 2 for more details. In this arrangement[2] effects from the reactor geometry and reference electrode damage become negligible and the ultrasound intensity at the location of the working electrode can conveniently be altered by both the horn to electrode distance at constant power or the ultrasound intensity at a fixed distance.[6,7]

In work conducted with microelectrodes[8,9] cavitation effects were found to significantly contribute to the mass transport and therefore to the nature of the electrode process and an elegant statistical analysis of current data has been suggested by Birkin *et al.*[10] Experiments at macro-electrodes revealed an apparently much simpler model to account for the mode of mass transport. In many cases a simple planar diffusion layer model may be employed to analyse current data and even quantitative kinetic analysis has been shown to be possible.[11-13] In studies concerned

with the cleavage of a carbon-bromide bond[11] and with the diol cleavage process induced by electrogenerated Pb(IV)[12] the sonoelectrochemical limiting current has been used directly to determine and compare chemical rate constants for ECE-type and EC'-type reaction schemes.

For conditions at the electrode/solution interface, which are dominated by *both* macroscopic turbulent streaming[14] *and* cavitation/microstreaming, a rather more complex mass transport model may be anticipated and there must be a threshold of cavitation activity at which the simple mass transport model fails. In this chapter investigation into the factors which dominate the presence and force of cavitation events at the interface of a macro-electrode has been undertaken based on an electrochemical detection procedure. A simple and elegant computational strategy is also developed to allow both the quantification and simulation of the effects of cavitation for a simple electrode system. The results of these are then used to show the level of interfacial cavitation activity causes the model of a planar diffusion layer at macro-electrodes to fail only under very extreme conditions. Further, a correlation between the electrochemically detected interfacial cavitation activity and the rate of sonolysis processes in the bulk solution phase are demonstrated for the case of cyanide degradation in aqueous 0.1 M NaOH.

7.2. Theory

7.2.1. Cavitation Counter

The cavitation counter is a simple and quick program written, in house, in C that will interrogate a data file from an Autolab® to calculate the mean of the data points and subsequently calculate how many of the data points deviate by a defined factor from the mean. The output from the program is both on screen and as a data file. The

original data file remains unchanged by the program. The program is written primarily for use on a UNIX or Linux operating system but can be readily adapted to run via MS-DOS or similar operating system.

The program works along the simple linear algorithm shown in Figure 7.1. Initially the program calculates the number of points in the file. The memory is dynamically allotted for these points and read from the file. The source file is then closed and the data within it remains intact. The data is then parsed to a subroutine and its mean and standard deviation are calculated (the subroutine is adapted from ref 15). The points are then parsed to a second routine to calculate their deviation from the mean value and to count the frequency of this deviation. The program then outputs the percentage that deviate for differing values from the mean to both the GUI and a file.* This gives a very useful indication of the number of cavitational spikes present within the voltammogram of similar ilk to Figure 7.7. This small program will prove to be

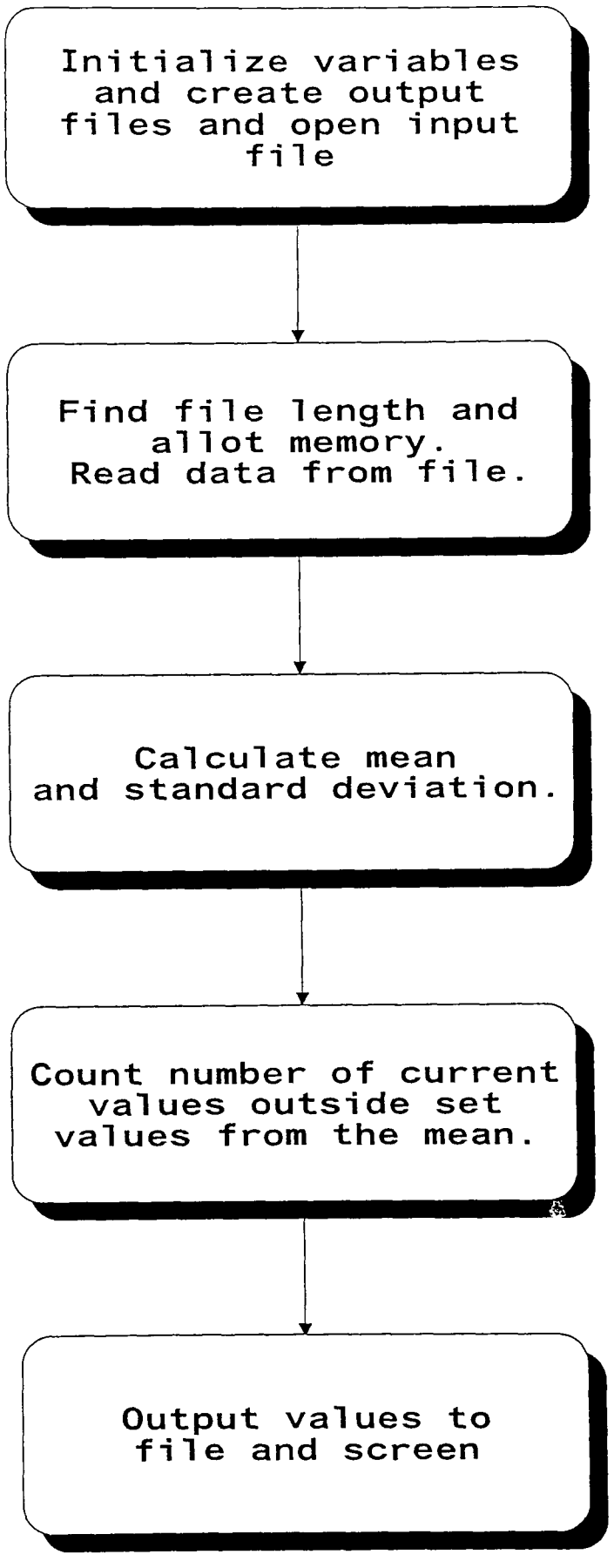


Figure 7.1 The sequence of events within the Cavitation Counter's algorithm.

* The output filename is *originaldatafilename*`res.dat`.

reliable during the next few sections and is a cost effective alternative to the commercial cavitation meters available. These consist of a pressure and heat sensor which can detect both cavitational collapse and the heating from the ultrasonic power. They allow mapping of intensity throughout the liquid but do not give an accurate handle on the electrochemical cavitation and its effects which the method developed above allows. They are also comparatively expensive with prices range between $1500 and $5000. A full listing of the program's source code can be found appendix A2.

7.2.2. Cavitation Simulator

In this section a cavitation simulator will be developed in order to allow qualitative discussion of the observed voltammograms seen later. To do this the electrode is assumed to be square. It is then divided up into N x N areas which have an area of equivalent magnitude to the Cross Sectional Area (CSA), at the diameter, of a cavitation bubble. The areas are addressed in a 2-dimensional vector format as shown in Figure 7.2. Initially the mass transport to the electrode is assumed to be due solely to acoustic streaming. If a cavitational event occurs then the event will be addressed to one of the elements of the electrode and assumed to react in a Cottrell like manner for a fixed diffusion layer. Considering the beginning of the simulation, each element is at steady state with a uniform diffusion layer.

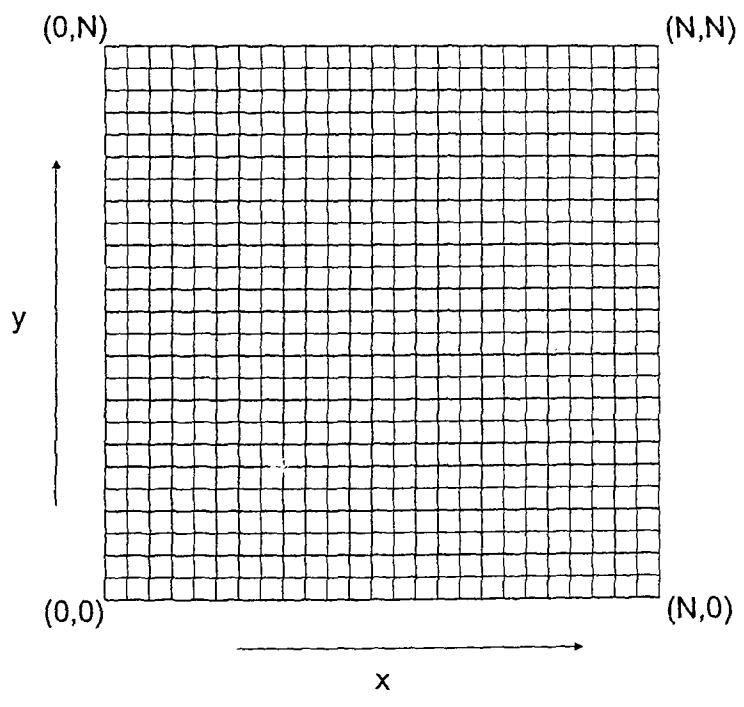


Figure 7.2 The square electrode used in the cavitation simulator.

$$\frac{\partial^2[\ ]}{\partial z^2} = 0 \qquad (7.1.)$$

It is also assumed for the elements at the extremes of the electrode experience no edge effects even though they are each a microelectrode this can be ignored as they are added together. The current is given by the sum of all the elements' currents.

$$I_{tot} = \sum_{j=0}^{N}\sum_{i=0}^{N} I_{(i,j)} \qquad (7.2.)$$

where $I_{(i,j)}$ is the current of the element (i,j). As the current due to acoustic streaming is known to be a uniform diffusion layer then it's value is calculated using the Nernst diffusion layer theory.

$$I_{(i,j)} = \frac{nFA_{el}D[\ ]_{\infty}}{\delta} \qquad (7.3.)$$

where n is the number of electrons transferred, F, the Faraday constant, A_{el} the area of the element, D the diffusion coefficient, $[\ ]_{\infty}$ the bulk concentration and δ the diffusion layer thickness. To determine if a cavitation event occurs first, the program calculates the probability that an event will occur at each element from the data supplied by

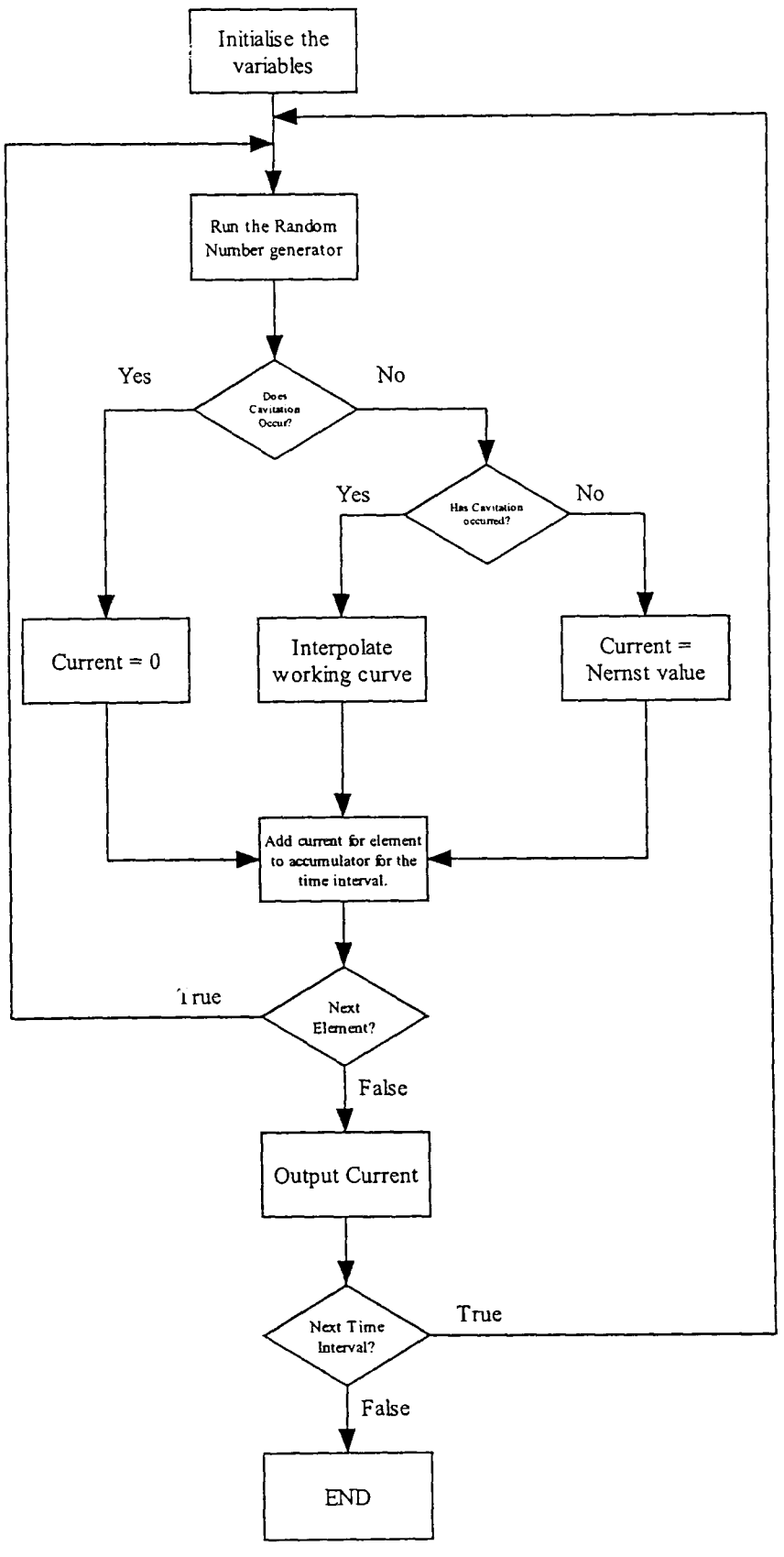


Figure 7.3 Simplified version of the cavitation simulator.

the user i.e. cavitation frequency and relative bubble size cf. to electrode size. The program then uses a random number generator (RNG) at each element to determine if the element will experience a cavitation event. To do this the simulator compares the result from the RNG and if it is lower than the probability for cavitation, an event is recorded. Random number generation is not a simple task and requires complex mathematics to produce a routine that is completely *random* and will continue to be stable over a long period of time (i.e. for the production of a large number of random numbers). The routine used was taken from a numerical recipe in ref. 16. Most simple RNGs need to be initialised by an integer number and for each number will give out the same and unique sequence of '*random*' numbers. To overcome this apparent lack of randomness, introduced by using the same initialisation number, the simulator uses its PID (Process IDentification) number to initialise the RNG (unfortunately limiting its operation to UNIX platforms only). This number is not chosen by the operator but assigned by the operating system using an unknown, to the author or operator, allocation algorithm and therefore adds a further degree of randomness to the RNG. This suggests, and was found to be true, that if the simulator is run with the same parameters the output will more than likely not be exactly the same as it was before, as with real cavitation voltammograms (see later). Although they may be visually different they are in fact statistically the same.

If a cavitation event is recorded then the element's response will modelled as a transient (Cottrell like) response for a completely refreshed diffusion layer (modelled by J.A. Alden, PTCL, Oxford).[17] For more information on this see Appendix A3. In the case of the simulator this is only true for the time interval after the event is initiated as initially no current from that element will be recorded as the bubble is sitting there blocking the electrode. This also prevents the need for extrapolation of

the transient at $t = 0$, usually infinity.. The simulator remembers the address of each element that has experienced a cavitational event and on the next time interval will find the appropriate current from the working curve in reference 17. A simplified version of the program is shown in Figure 7.3. A full listing of the program written in C can be found in Appendix A2.

7.2.2.1. Typical Output of the Simulator

This section will present some typical voltammograms from the simulator program. As will be seen later on, the voltammograms are not exact matches to the experimental voltammograms but do give an insight to the processes occurring during the later 'steady state' voltammograms recorded. Figure 7.4 shows a time dependent voltammogram for an easily accessible diffusion layer thickness (3 μm) and an acceptable bubble diameter (50 μm). All the other parameters are shown in the figure caption. According to Leighton the bubble diameter may be between 20-250 μm.[18] Thus the simulated voltammogram in Figure 7.4 is for a fairly small bubble. If a larger bubble diameter is used then the voltammogram shown in Figure 7.5 is obtained. All the other parameters are the same as in Figure 7.4. Note that although the shape of the voltammogram is similar to that of Figure 7.4 the current scale is significantly different. The implications of this is that

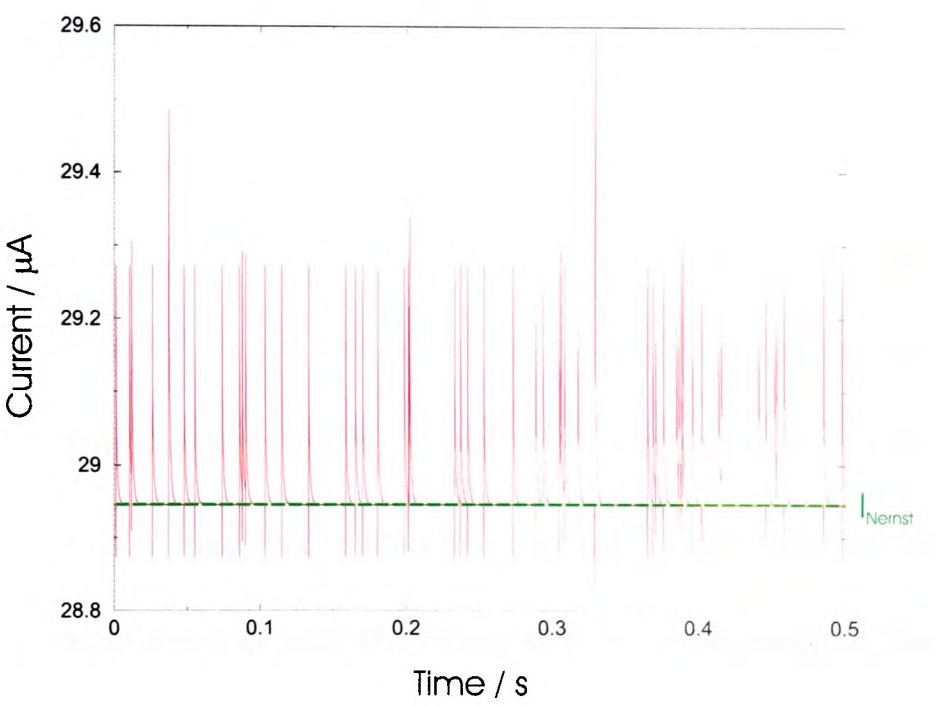


Figure 7.4 A simulated time dependent voltammogram from the cavitation simulator. the parameters are as follows: $\delta = 3$ μm; $R_{bubble} = 25$ μm; $D = 0.9 \times 10^{-5}$ cm^{2}s^{-2}; $[\,]_\infty = 1$ mM; $A_{el.} = 0.01$ cm^2; $t_{sample} = 0.1$ ms and $f_{cav.} = 100$ s^{-1}.

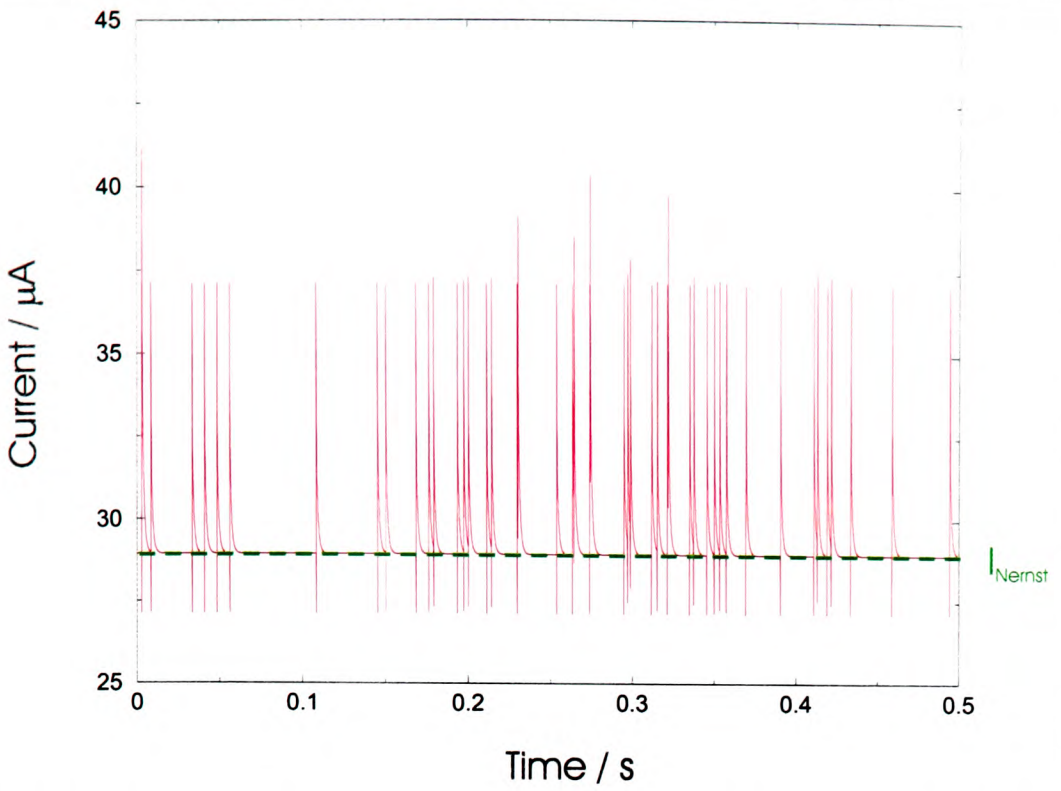


Figure 7.5 Simulator output with the same parameters as Figure 7.4 but with R_{bubble} = 125 µm.

the cavitation counter detailed in §7.2.1 will not detect small bubbles imploding at the electrode but will identify when large bubbles implode. The main failing of the cavitation simulator is that assumptions that the bubbles imploding at the surface are of uniform diameter whereas in the experimental case a variety of bubble sizes would be expected. This gives rise to the *uniform* appearance of the output. The negative currents (current below the Nernst current value) observed in both experimental and the simulator is explained by the fact the bubble has arrived at the electrode and is blocking the current for that element.

7.3. Experimental

7.3.1. Reagents.

Chemical reagents used were $Ru(NH_3)_6Cl_3$, ferrocene, KCN, NaOH (all Aldrich), dimethylformamide (HPLC grade, Aldrich), NBu_4PF_6 (electrochemical grade, Fluka), and have been obtained commercially in analytical or the purest available grade and used without further purification. 3-bromobenzophenone was prepared according to a literature procedure.[19]

Pure water was taken from a Elgastat filter system (Elga, High Wycombe, UK) and had a resistivity of not less than 18 MΩ cm. Solutions used in electrochemical experiments were degassed with argon (Pureshield, BOC gases) for at least 15 minutes prior to recording data.

7.3.2. Instrumentation.

Electrochemical experiments were conducted with an Autolab® PGSTAT20 or a μ-Autolab® system (Ecochemie, Netherlands). The concentration of cyanide was monitored with an Orion model 9606 sure-flow combination cyanide ion selective electrode connected to a Jenway 3030 pH/mV meter (Jencons, UK). For ultrasound experiments a Sonics & Materials VCX 400 transducer system equipped with a 13 mm diameter horn tip or a 3 mm diameter stepped horn tip was used. The horn tip immersed in the solution was electrically insulated via a Teflon foil (100 μm) and a Delrin screw connection. The power output of the transducer has been calorimetrically calibrated[20,21] for each experimental configuration. Sonochemical experiments were conducted in a thermostated sonochemical cell (jacketed Pyrex cell) which is described in detail elsewhere.[22]

The sonoelectrochemical cell[2] consisted of a conventional three electrode cell with a saturated Calomel reference electrode (SCE, Radiometer, Kopenhagen), a working electrode mounted in the bottom part of the reactor, and a Pt-coil counter electrode. The ultrasonic horn was placed from the top at a fixed distance from the working electrode, which was measured manually with approximately ± 0.2 mm accuracy. The system was thermosstatted to $20 \pm 3^{\circ}C$ with a stainless steel cooling coil and degassing with argon (Pureshield®, BOC) was used to deaerate the system. A lid and a continuos flow of argon prevented air from coming into contact with the sample

solution. The data analysis for the determination of the number of data points in a set of 5000 points deviating by a given margin from the average was performed using the program discussed and developed in §7.2.1 on a Silicon Graphics Origin™ 2000 server.

7.4. Results and Discussion

7.4.1. Detecting Cavitation Processes at the Macro-Electrode/Solution Interface.

A major factor in ultrasound induced processes is the presence of cavitation both in the bulk solution and at interfaces. The phenomenon, caused by voids or gas bubbles in the solution phase being coupled to the oscillating pressure field, is responsible for 'hot spot' processes and erosion.[23] There are different types of cavitation such as stable cavitation (violently oscillating bubble) or transient cavitation (collapsing bubble)[24] and the ultrasound frequency as well as the intensity determines the type and violence of the process.[8]

Cavitation at a solid/solution interface should occur more readily compared to cavitation in the bulk solution due to the weaker molecular interactions at the interface. At the interface, crevices and active sites exist at which gas bubbles readily form. Further, in the presence of hydrodynamic flow the

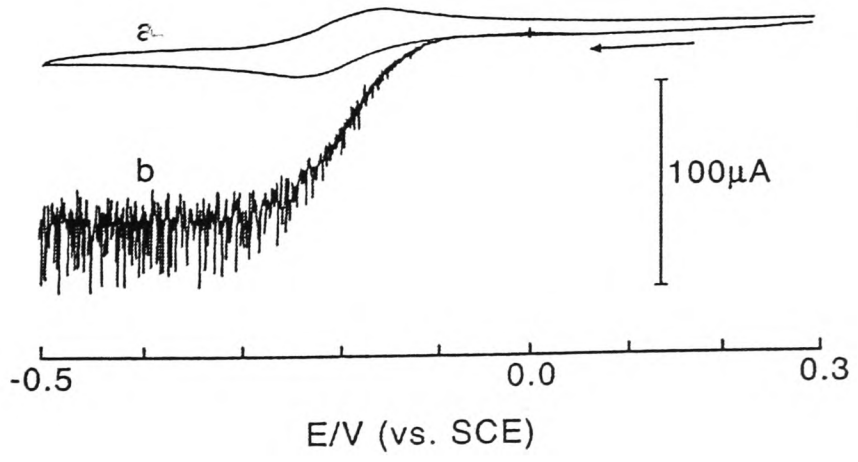


Figure 7.6 Cyclic voltammogram (a) and sonovoltammogram (b) for the reduction of 1 mM $Ru(NH_3)_6^{3+}$ in aqueous 0.1 M KCl at a 6 mm diameter Pt disc electrode (scan rate 10 mV s^{-1}, 13 mm diameter horn, 20 mm electrode to horn distance, ultrasound intensity 15 W cm^{-2}).

interfacial tension is further increased and cavitation becomes even more facile. A direct comparison between the different types of cavitation and their effects on chemical systems is a complex undertaking and often an empirical cavitation index has been introduced for standardisation purposes. This cavitation index may be based on commercially available instrumentation,[25,26] the mechanical effect of ultrasound,[27] or characteristic acoustic emission[28] associated with cavitation.

In electrochemistry the beneficial effects of ultrasound have been exploited in areas as diverse as electrosynthesis[29] and electroanalysis.[30,31] Major factors in power ultrasound affecting electrochemical processes are the change in mass transport and the cavitation processes at the electrode/solution interface. In Figure 7.6 a cyclic voltammogram (Figure 7.6a) and a sonovoltammogram (Figure 7.6b) for the reduction of $Ru(NH_3)_6^{3+}$ in aqueous 0.1 M KCl, given by equation (7.4.), are shown.

$$Ru(NH_3)_6^{3+} + e^- \rightleftharpoons Ru(NH_3)_6^{2+} \qquad (7.4.)$$

The cyclic voltammogram obtained at a 6 mm diameter Pt disc electrode is consistent with a reversible and well-defined one electron reduction process with a half wave potential $E_{1/2}$ = -0.20 V *vs*. SCE. The corresponding sonovoltammogram shows both the considerable increase in current density induced by fast mass transport at the electrode/solution interface and the characteristic noise superimposed on the limiting current caused by cavitation processes at the interface.

The aim of the present study is to address the nature of sonoelectrochemical processes under the more vigorous conditions than earlier studies so that the source of the high intensity ultrasound emitted from ultrasonic horn probes is brought very close to the electrode surface. It has been noted by Coury *et al.*[32] that distances in the millimetre range are required for strong thermal and erosion effects. By employing microelectrode methods Birkin[8,33] was able to show how cavitation at the

electrode/solution interface became more violent for closer electrode to horn distances and how microelectrodes can be damaged under the most violent conditions.

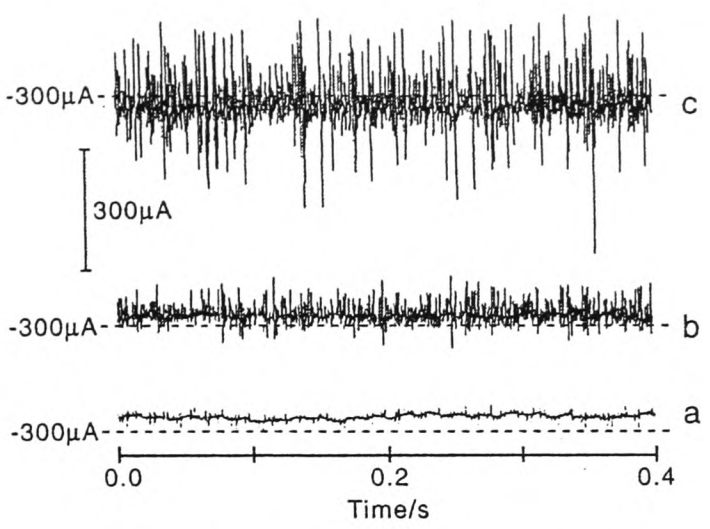


Figure 7.7 Current response traces for the sonoelectrochemical (3 mm diameter horn probe, 1 mm electrode to horn distance) reduction of 1 mM $Ru(NH_3)_6^{3+}$ in aqueous 0.1 M KCl at a 6 mm diameter Pt disc electrode with the potential fixed at E_{app} = -0.5 V *vs.* SCE, (a) W 110 cm^{-2}, (b) 300 W cm^{-2}, (c) 550 W cm^{-2}, sampling time 0.1 ms.

In order to investigate sonoelectrochemical processes under the more violent conditions, in the present study macroelectrodes are used with the advantage of only small effects of the local erosion damage on the overall current response. In the sonovoltammogram shown in Figure 7.7 it can be seen that in the region in which a mass transport controlled current response (limiting current) is detected, two factors govern the characteristics of the reponse: (i) the magnitude of the limiting current (I_{lim}) and (ii) the amount of noise superimposed on the signal. Traditionally, the limiting current has been the most important parameter because it could be shown to directly give a measurement of the mass transport at the electrode surface. The simplistic approach of a planar diffusion layer model has been employed in several studies and is shown in equation (7.5.). Note the similarity to equation (7.3.) which refer to the current of an element of the electrode.

$$I_{lim} = \frac{nFAD[\ ]_{\infty}}{\delta} \qquad (7.5.)$$

In this equation, n denotes the number of electrons transferred per molecule, F is the Faraday constant, D the diffusion coefficient, A the electrode area, and $[\ ]_{\infty}$ the concentration. With the diffusion layer thickness, δ, known, it is possible to quantify the kinetics of chemical processes coupled to the electron transfer.

In Figure 7.7 traces observed for the limiting current for the reduction of $Ru(NH_3)_6^{3+}$ in aqueous 0.1 M KCl at a 6 mm diameter Pt disc electrode and over a short period of time are shown and compared for a very close electrode to horn distance, 1 mm, and various power settings. It can be seen that under these conditions a considerable change in power has only very little effect on the limiting current. This effect has been described before[14] and may be attributed to a limit in the macroscopic flow of liquid across a surface in the presence of ultrasound induced pressure fluctuations. Therefore, although of considerable importance in the analysis of chemical processes at the electrode/solution interface, the limiting current observed under extreme ultrasound conditions is *not* in itself a good measure of the physical nature of the process. However, it can also be seen that the level of noise superimposed on the current signal significantly changes. Very short current spikes in the sub-millisecond time scale are detected and are indicative of substantial cavitational action at the electrode surface. In order to understand the characteristics of the observed current peaks (i) the ratio of the total electrode area to the area affected by the cavitation process and (ii) the time for the Cottrell relaxation process[10] following the cavitation process have to be taken into consideration. The approximate time, τ, required for a concentration gradient between the electrode surface and the outer diffusion layer, δ, to be established may be given by equation (7.6.).

$$\tau = \frac{\delta^2}{D} \qquad (7.6.)$$

Under the experimental conditions of the sonovoltammograms shown in Figure 7.7 and with $D_{Ru} = 0.91 \times 10^{-9}$ m^2 s^{-1},[34] it follows that τ is of the order of 10 ms. This time scale is not consistent with the duration of the very short current spikes detected in the measurement (see Figure 7.7). However, due to the large area of the electrode and the

anticipated change of the diffusion layer thickness going from the centre to the outer regions only the most violent initial period of the cavitational collapse may be detected. That is, the larger the electrode the more violent the cavitation process has to be to affect the limiting current. The magnitude of the observed current spike is related to the amount of liquid volume, which has been replaced by the cavitation process at the electrode surface and therefore may be regarded as a good relative measure for the violence of cavitation processes. The quantitative analysis of the current traces would require a time-resolved response in which the decay of the peak and the area can be determined.[35] For the data presented in this study a higher level of analysis is unwarranted but a useful correlation of the current peak height and sonochemical and sonoelectrochemical processes can be shown. This effect can also be explained using the cavitation simulator. Figure 7.8a shows a response for a bubble of diameter ~100 μm for a small diffusion layer (approximately 1 μm at the centre of the electrode) Figure 7.8b shows the response for a diffusion layer of 10 μm (corresponding to the edge of the electrode). The spikes are sharper and slightly larger for the smaller diffusion and mirror the situation in Figure 7.7a. All the other simulator parameters are as in Figure 7.4.

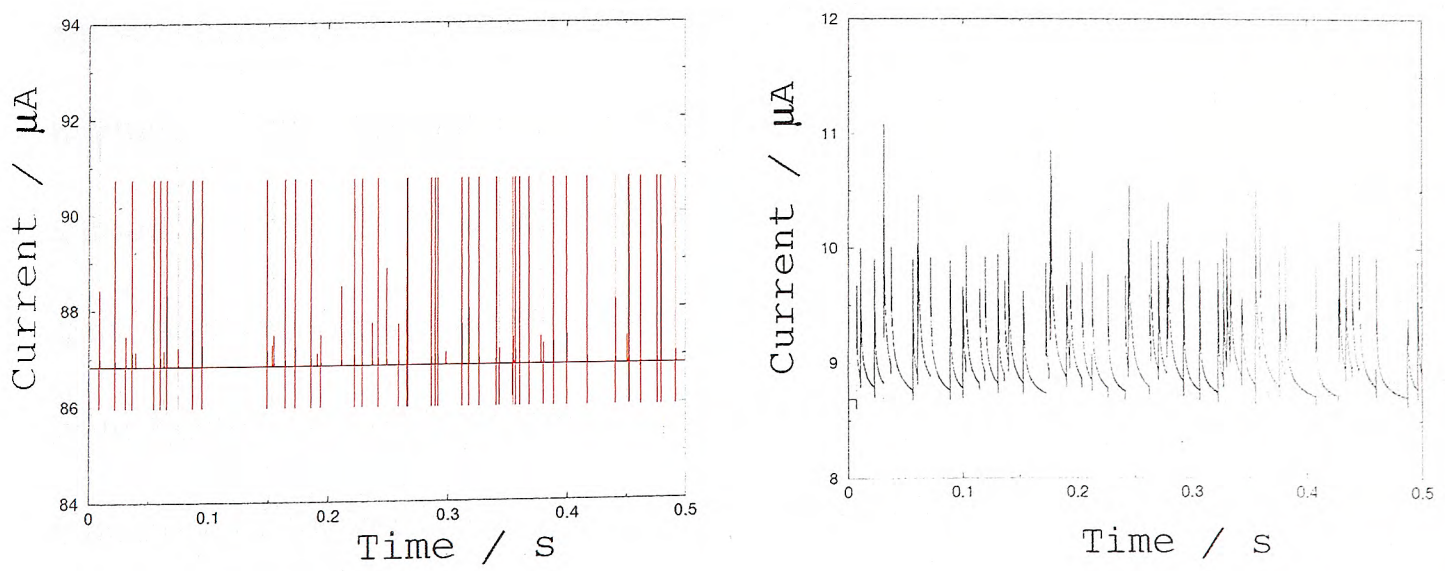


Figure 7.8 Simulated data for a cavitation bubble of size 100 μm for different diffusion layer thickness a) 1 μm and b) 10 μm. All other parameters as in Figure 7.4.

In Figure 7.9 the analysis of current peak data observed in measurements analogous to those shown in Figure 7.7 is presented. The plots show the number of current data points in percentage of the total number of data points recorded over a period of 0.4 s with a 0.1 ms resolution. For an electrode to horn distance of 1 mm the number of current data points deviating more than 10% from the mean can be seen to considerably increase at a ultrasound intensity level of ca. 200 W cm^{-2} (Figure 7.9a). Current data points deviating more than 20% increase markedly at ca. 300 W cm^{-2} (Figure 7.9b). In the second plot the effect of changing the distance between electrode and horn tip is shown. A decrease in this distance from 1 mm (Figure 7.9e) to 4 mm (Figure 7.9h) causes a complete change in the characteristics although the magnitude of the limiting current is not altered significantly. It can be seen that electrode to horn distance as well as the ultrasound power used have a dramatic impact on changing the process from a smooth average limiting current to massive current fluctuations under extreme cavitation conditions. It is interesting to note that the number of the peak currents with a given magnitude increase in a highly non-linear fashion with a strong increase of very violent processes at a power level much higher than that expected for the cavitation threshold.[36]

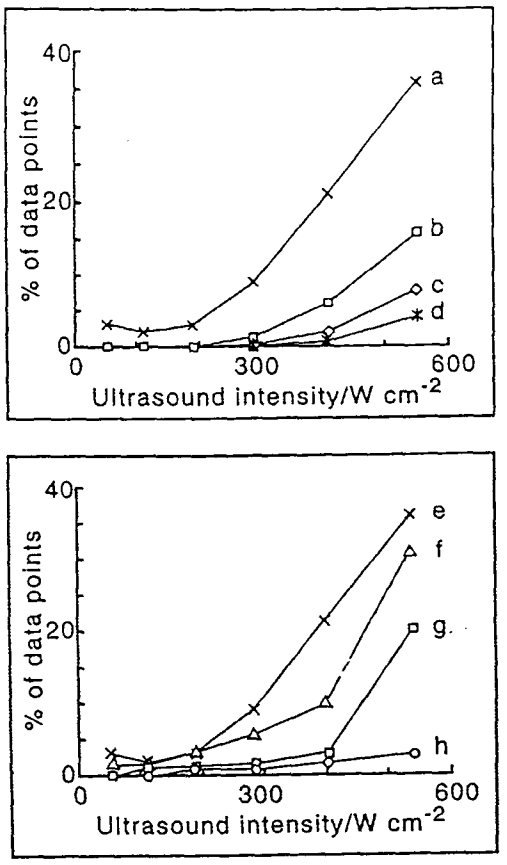


Figure 7.9 Plot of the fraction of current readings for the sonoelectrochemical (3 mm diameter horn probe) reduction of 1 mM $Ru(NH_3)_6^{3+}$ in aqueous 0.1 M KCl at a 6 mm diameter Pt disc electrode with a deviation from the average current response (the mean) of more than (a) 10 %, (b) 20 %, (c) 30 %, (d) 40 % (electrode to horn distance 1 mm) versus the ultrasound intensity employed and for a fixed 10 % deviation from the mean threshold and an electrode to horn tip distance of (e) 1 mm, (f) 2 mm, (g) 3 mm, and (h) 4 mm.

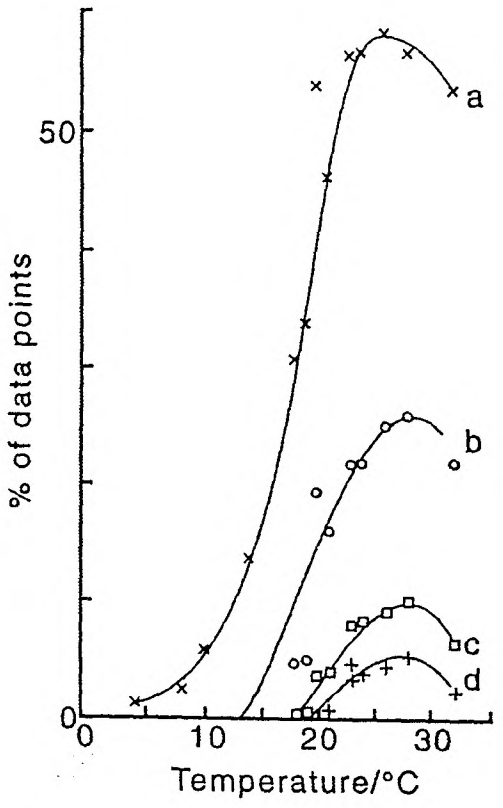


Figure 7.10 Plot of the fraction of current readings for the sonoelectrochemical (3 mm diameter horn probe) reduction of 1 mM $Ru(NH_3)_6^{3+}$ in aqueous 0.1 M KCl at a 6 mm diameter Pt disc electrode with a deviation from the average current response of more than 10 % (electrode to horn distance 1 mm) versus the temperature in the sonoelectrochemical cell.

The effect of temperature on the detection of cavitation events is shown in Figure 7.10. As may be anticipated, the number of strong cavitation events increases with temperature, but it also shows saturation behaviour at around 50 to 60% high current events deviating more than 10% from the mean. A possible physical explanation of this observation is that in the presence of a dense cloud of cavitation bubbles individual bubbles start to interact and the resulting process may become less violent and less efficient.[24]

An analogous study of cavitation events at the electrode /solution interface in a dimethylformamide solution of 1 mM ferrocene/0.1 M NBu_4PF_6 has been conducted to allow some insight into the mass transport conditions at the electrode surface and to allow the electrochemical cavitation index to be correlated with the possible break down of the simplistic model of a planar diffusion layer.

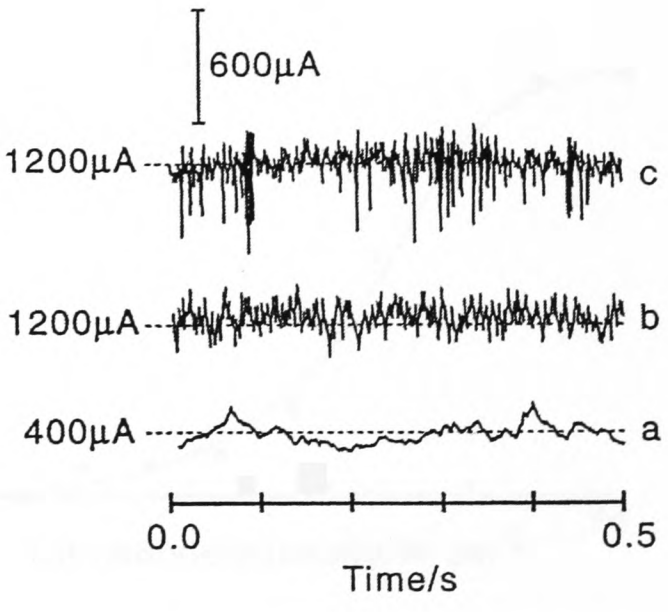


Figure 7.11 Current response traces for the sonoelectrochemical (13 mm diameter horn probe, 3 mm electrode to horn distance) oxidation of 1 mM ferrocene in dimethylformamide/ 0.1 M NBu_4PF_6 at a 4 mm diameter Pt disc electrode with the potential fixed at E_{app} = 0.7 V *vs.* SCE ((a) 5 W cm^{-2}, (b) 33 W cm^{-2}, (c) 68 W cm^{-2}, sampling time 0.1 ms).

In Figure 7.11 typical current traces recorded over a short period of time with 0.1 ms resolution are shown. The potential applied to

the working electrode was set to 0.7 V *vs.* SCE in order to stay in the potential region positive of the half wave potential for the oxidation of ferrocene, $E_{1/2}$ = 0.38 V *vs.* SCE, where the mass transport controlled limiting current is detected. The data shown in Figure 7.11 has been recorded for a 3 mm electrode to horn tip distance and the trends observed in aqueous media can be again detected. Under extreme conditions of close distance and high ultrasound intensity the limiting current appears not to further increase. However, the magnitude of current spikes clearly increases. A plot shown in Figure 7.12 shows how the number of current points detected for the ferrocene oxidation deviating more than 10% from the mean steadily increase at higher ultrasound intensity.

7.4.2. Effect of Cavitation Processes on Chemical Kinetics at the Electrode/Solution Interface.

It has recently been shown that under conditions of sonoelectrochemical measurements chemical processes which are coupled to electron transfer at the electrode/solution interface may be analysed quantitatively[11] by assuming the validity of the simple planar diffusion layer model. This kind of methodology opens up possibilities to measure the rate constants of the rate determining steps of a wide variety of chemical processes in the presence

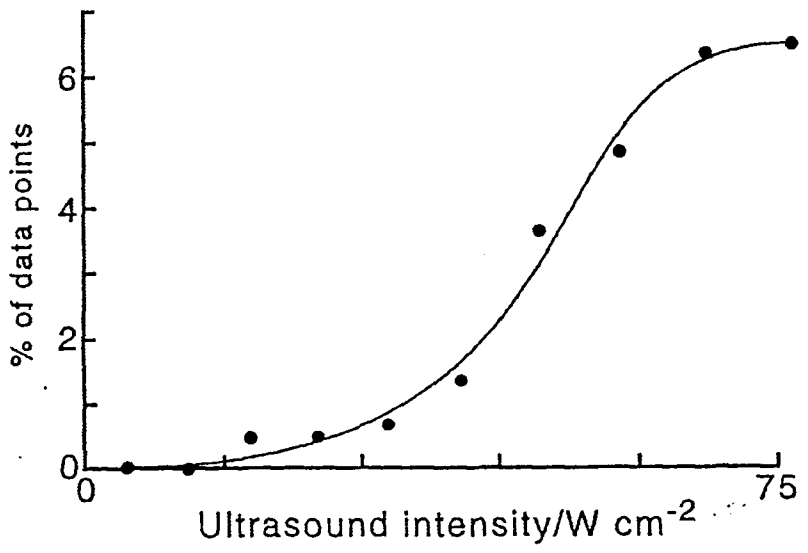


Figure 7.12 Plot of the fraction of current readings for the sonoelectrochemical (13 mm horn diameter, 3 mm electrode to horn distance) oxidation of 1 mM ferrocene in dimethylformamide/ 0.1 M NBu_4PF_6 at a 4 mm diameter Pt disc electrode with a deviation from the average current response of more than 10 % versus the ultrasound intensity employed.

of intense ultrasound simply by analysis of the limiting current observed for sonovoltammograms at a range of different average diffusion layer thickness.

It may be argued that the model of a planar diffusion layer is very over simplified and should break down even when calibration of the diffusion layer thickness is employed. The transition to a more complex mass transport model would obviously be expected for very extreme conditions with strong cavitation interference. That is, by going to conditions of extremely high ultrasound intensity there should be a deviation in the data observed for the rate constant from the theoretical model.

The model reaction studied here is the reduction of 3-bromobenzophenone, which is known to follow an ECE type mechanism.[11,37] The reaction steps, which characterise the overall process are given in equations (7.7.)-(7.10.).

$$RBr + e^- \rightleftharpoons RBr^{\bullet -} \qquad (7.7.)$$

$$RBr^{\bullet -} \rightarrow R^{\bullet} + Br^- \qquad (7.8.)$$

$$R^{\bullet} + SH \rightarrow RH + S^{\bullet} \qquad (7.9.)$$

$$RH + e^- \rightleftharpoons RH^{\bullet -} \qquad (7.10.)$$

Following the initial electron transfer (equation (7.7.)) a rate determining chemical process, the cleavage of the carbon - bromide bond (equation (7.8.)) occurs and leads to the formation of another redox active species, RH. Under conditions of fast mass transport only the first electron transfer step occurs and the product, R-$Br^{\bullet -}$, escapes from the diffusion layer before the chemical step (H-atom transfer) with SH (a solvent molecule or NBu_4^+) can occur. Therefore a transition from a one electron transfer process (E-process) under conditions of fast mass transport to a two electron transfer (ECE-process) under conditions of very slow mass transfer will occur, and the correlation of the number of effectively transferred electrons, n_{eff}, and the diffusion layer thickness allows the rate constant, k, for the process given in equation (7.8.) to

be determined. The analysis of the data may be based on the following expression[38] based on the case of a stagnant diffusion layer shown in equation (7.11.).

$$n_{eff} = \frac{I_{lim}}{I_{lim}^{0}} = 2 - \frac{\tanh\sqrt{(\delta^2\, k/D)}}{\sqrt{(\delta^2\, k/D)}} \qquad (7.11.)$$

In this equation I_{lim}^{0} denotes the limiting current expected for the case of a one electron transfer which can be determined for example based on a calibration procedure with the known diffusion coefficient for 3-bromobenzophenone,[11] D_{3BB} = 0.92×10^{-9} m^2 s^{-1}.

In Figure 7.13 data from a series of sonovoltammetric experiments are shown presented analogously to the data on this reaction published recently[11] and extending the range of diffusion layer thicknesses into the range of extreme ultrasonic conditions. The solid line indicates the average sonovoltammetric limiting current for a one electron transfer process and the upper dashed line corresponds to the limiting current associated with a two electron process. The intermediate dashed line corresponds to the limiting current expected for the ECE process with a rate constant of k = 800 s^{-1} taken from literature using cyclic voltammetry data.[37] Analysis of the limiting current data obtained under conditions,

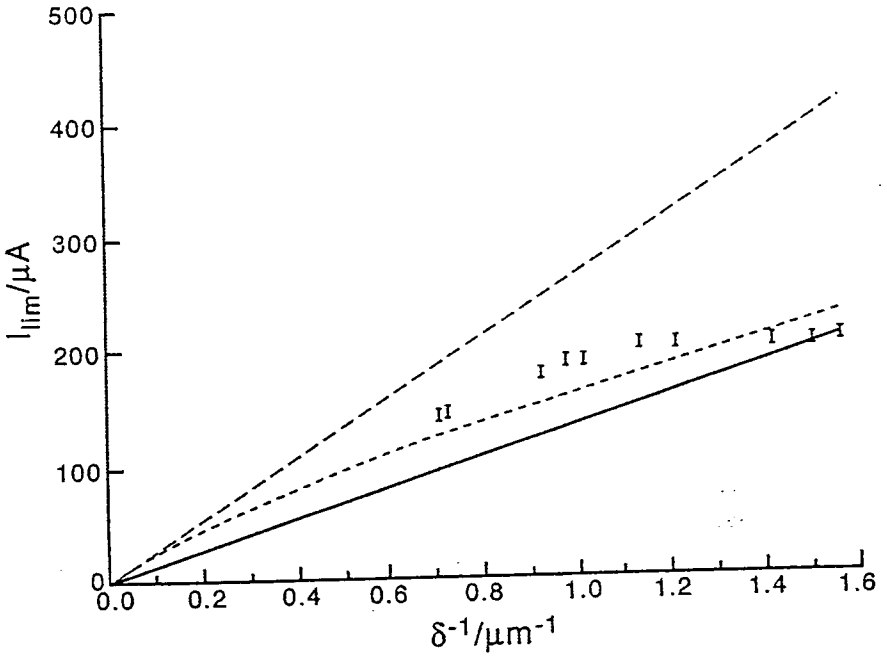


Figure 7.13 Plot of sonovoltammetrically obtained limiting currents versus the reciprocal diffusion layer thickness for the reduction of 0.5 mM 3-bromobenzophenone in dimethylformamide (0.1 M NBu_4PF_6) at a 2.1 mm diameter glassy carbon disk electrode. The theoretically predicted curves for $k \rightarrow 0$ (solid line), $k \rightarrow \infty$ (dashed line), and for k = 800 s^{-1} [29] are also shown.

which are more extreme compared to those published recently,[10] suggests that indeed a marked deviation from the model occurs. As expected the data points follow a trace consistent with a transfer of between one and two electrons. In a range of intermediate diffusion layer thickness, $\delta = 0.8$ to $1.6\mu m$, the data points for the limiting current are higher than expected probably due to a thermal effect. This kind of thermal effect has been noted by Coury *et al.*[32] in aqueous systems and it occurs locally at the electrode/solution interface. However, under even more extreme conditions the data points deviate markedly from the model and apparently a smaller number of electrons is transferred. The purely thermal effect would result in the opposite effect and therefore the negative deviation may be attributed either (i) to a breakdown of the simple mass transport model or (ii) to a change in reactivity on the electrode surface. Although the latter effect is possible under extreme conditions the change in mass transport in the present of more violent cavitation appears to be more plausible.

It is interesting to compare the condition required for the negative deviation with the electrochemical cavitation index introduced above. Conditions required to cause the break-down of the kinetic model in the experiment described here, correspond to a situation in which current points deviating more than 10% from the mean are approximately 6% of the total of current points recorded with 0.1 ms resolution (Figure 7.12).

7.4.3. Correlation of Interfacial and Bulk Cavitation Processes.

It is interesting to compare the presence of interfacial cavitation at the electrode/solution interface with sonochemical processes, which occur predominantly in the bulk solution phase. The presence of violent cavitation at the electrode/solution interface should be correlated to the cavitation in the bulk of the liquid responsible for chemical changes.

The chemical process studied for the purpose of correlating bulk and surface cavitation processes is the sonochemical destruction of cyanide in alkaline solution.[22] The process, which has recently been investigated and which may be of considerable importance in waste water treatment,[39,40] has been proposed to be dominated by a sonochemical mechanism involving $OH^{\bullet}$ radical species,[22] although contributions to the destruction process from high temperature alkaline hydrolysis may also contribute to the process.[41]

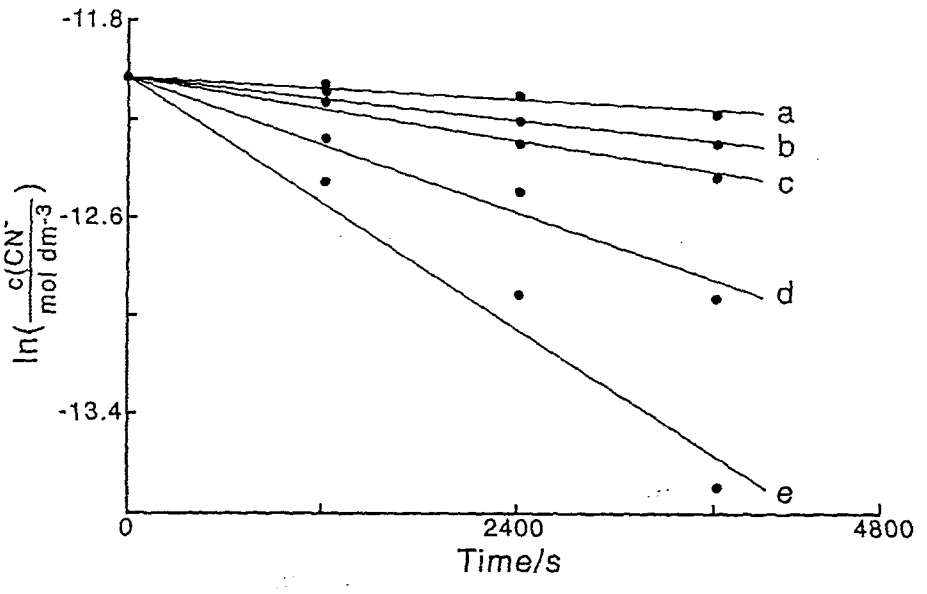


Figure 7.14 Plots of the change in cyanide concentration in aqueous 0.1M NaOH with sonication time (3 mm diameter horn probe, 10 ml volume) for ultrasound intensities of (a) 40 W cm^{-2}, (b) 95 W cm^{-2}, (c) 150 W cm^{-2}, (d) 280 W cm^{-2}, and (e) 400 W cm^{-2}.

A 10 cm^3 volume of 6 μM KCN in aqueous 0.1 M NaOH was placed in a sonochemical reaction vessel[22] with a 3 mm diameter ultrasonic horn immersed and the decrease of the cyanide concentration is followed by ion selective electrode detection. In Figure 7.14 plots of the change in cyanide concentration versus time are shown and the expected first order kinetics for the

degradation process[42] has been verified.[22] The rate for the cyanide destruction is strongly dependent on the ultrasonic power as well as on the solution volume used in the process. Plots in Figure 7.14 are shown for various ultrasound intensities and by plotting the calculated first order rate constants for the cyanide destruction versus the ultrasound intensity (Figure 7.15) a non-linear increase at high intensities can be observed. The volume effect, which causes the rate for the sonochemical process to be approximately proportional to the inverse of the volume of liquid used[22] (see Figure 7.15), arises from the fact that the sonochemical destruction occurs predominantly in the high intensity region near the horn tip and increasing the total reaction volume decreases the apparent rate accordingly.[22] In Figure 7.15 the rate constant observed at a given ultrasound intensity can be compared for two different solution volumes.

Interestingly, there is a pronounced increase in the rate of cyanide destruction at elevated ultrasound intensity and a comparison with the electrochemical cavitation index measurement (see Figure 7.9) shows a clear correlation. Therefore it can be concluded that the violence of cavitation processes responsible for the surface erosion at the solid/solution interface and the forces behind cavitation in the bulk solution phase causing chemical reactions are of a similar origin, possibly the acoustic pressure amplitude near the horn emitter.

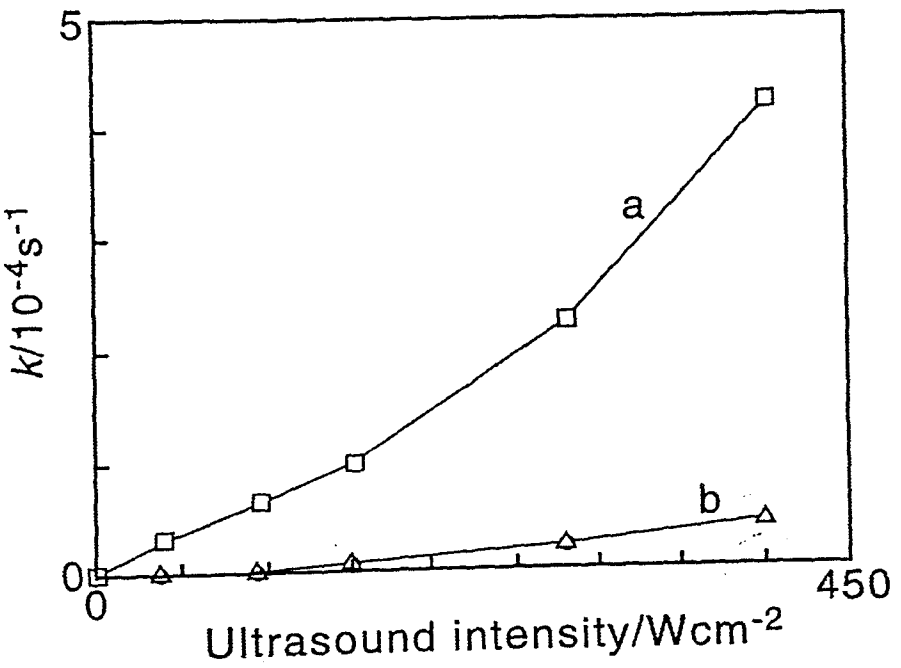


Figure 7.15 Plot of the first order rate constant for the sonochemical destruction (3 mm diameter horn probe) of cyanide in aqueous 0.1 M NaOH for a total sample volume of (a) 10 cm^3 and (b) 150 cm^3

7.5. Conclusions

The effects of cavitation have to been shown to only dominate the mass transport under the most violent conditions. Under mild conditions, that is with low ultrasonic power, acoustic streaming will dominate and the well established Nernst diffusion layer equation is valid. This is not true for high ultrasonic power where it is readily envisaged that the description of diffusion layer does not hold true and therefore the use of equation (7.5.) is not advised. This is borne out in §7.4.2 where chemical effects appear to be seen due to the break down of the mass transport regime proposed. Also the qualitative description of cavitation events can be simulated to good effect using the simulator in §7.2.2 and the amount of cavitation is easily quantified using the counter described in §7.2.1 in a more cost effective manner than a commercial cavitation meter.

References for Chapter 7

[1] D.J. Walton, S.S. Phull, *Adv. Sonochem.*, 4 (1996) 205
[2] R.G. Compton, J.C. Eklund, F. Marken, *Electroanalysis*, 9 (1997) 509
[3] see for example C.R.S. Hagan, L.A. Coury, *Anal. Chem.*, 66 (1994) 399
[4] R.G. Compton, J.C. Eklund, F. Marken, T.O. Rebbitt, R.P. Akkermans, D.N. Waller, *Electrochim. Acta*, 42 (1997) 2919
[5] F. Marken, R.G. Compton, *Ultrasonics Sonochem.*, 3 (1996) S131
[6] D.J. Walton, S.S. Phull, A. Chyla, J.P. Lorimer, T.J. Mason, L.D. Burke,M. Murphy, R.G. Compton, J.C. Eklund, S.D. Page, *J. Appl. Electrochem.*, 25 (1995) 1083
[7] R.G. Compton, J.C. Eklund, S.D. Page, T.J. Mason, D.J. Walton, *J. Appl. Electrohem.*, 26 (1996) 77522
[8] P.R. Birkin, S. Silva-Martinez, *J. Electroanal. Chem.*, 416 (1996) 127
[9] P.R. Birkin, S. Silva-Martinez, *Ultrasonics Sonochem.*, 4 (1997) 121
[10] P.R. Birkin, S. Silva-Martinez, *Anal. Chem.*, 69 (1997) 2055
[11] R.G. Compton, F. Marken, T.O. Rebbitt, *JCS Chem. Commun.*, (1996) 1017
[12] F. Marken, R.G. Compton, J.E.H. Buston, M.G. Moloney, *Electroanal.*, 10 (1998) 1188
[13] M. Atobe, K. Matsuda, T. Nonaka, *Electroanal.*, 8 (1996) 784
[14] F. Marken, R.P. Akkermans, R.G. Compton, *J. Electroanal. Chem.*, 415 (1996) 55
[15] W.H.Press, S.A. Teukolsky, W.T. Vetterling, B.P. Flannery, *Numerical Recipes in C* (CUP, Cambridge, 1996) pp.610-614
[16] W.H.Press, S.A. Teukolsky, W.T. Vetterling, B.P. Flannery, *Numerical Recipes in C* (CUP, Cambridge, 1996) pp.274-328
[17] R.P. Akkermans, M.F. Suárez, S.L. Roberts, Q. Fulian, R.G. Compton, *Electroanal.*, 11 (1999) 1191
[18] T.G. Leighton, *The Acoustic Bubble* (Academic Press, London, 1994) pp75
[19] S. Nishida, *J. Org. Chem.*, 32 (1967) 2692
[20] T.J. Mason, J.P. Lorimer, D.M. Bates, *Ultrasonics*, 30 (1992) 40
[21] M.A. Margulis, A.N. Mal'tsev, *Russ. J. Phys. Chem.*, 43 (1969) 592
[22] Q. Hong, J. L. Hardcastle, R. A. J. McKeown, F. Marken, R. G. Compton, *New J. Chem*, 23 (1999) 845
[23] see for example K.S. Suslick, (Ed.), Ultrasound, its physical, chemical and biological effects (VCH, Weinheim, 1988)
[24] See for example T.G. Leighton, The acoustic bubble (Academic Press, London, 1994)
[25] M. Atobe, T. Nonaka, *Chem. Lett.*, (1997) 323
[26] M. Atobe, Y. Kado, T. Nonaka, *Chem. Lett.*, (1998) 699
[27] G.J. Price , (Ed.), Current trends in sonochemistry (The Royal Society of Chemistry, London, 1992)
[28] See for example H. Kuttruff, Ultrasonics, Fundamentals and Applications (Elsevier, London, 1991)
[29] For a review see D.J. Walton, T.J. Mason, in J.-L. Luche, (Ed.), Synthetic Organic Sonochemistry (Plenum, New York, 1998, p. 263)
[30] R.P. Akkermans, J.C. Ball, T.O. Rebbitt, F. Marken, R.G. Compton, *Electrochim. Acta*, 43 (1998) 3443
[31] C. AgraGutierrez, R.G. Compton, *Electroanal.*, 10 (1998) 603
[32] N.A. Madigan, L.A. Coury, *Anal. Chem.*, 69 (1997) 5
[33] P.R. Birkin, R. O'Connor, C. Rapple, S. Silva-Martinez, *J. Chem. Soc. Faraday Trans.*, 94 (1998) 3365.
[34] F. Marken, J.C. Eklund, R.G. Compton, *J. Electroanal. Chem.*, 395 (1995) 335
[35] J. Klima, C. Bernard, C. Degrand, *J. Electroanal. Chem.*, 399 (1995) 147
[36] see for example T.J. Mason, J.P. Lorimer, Sonochemistry, theory, applications and uses of ultrasound in chemistry (Horwood, Chichester, 1988)
[37] L. Nadjo, J.M. Saveant, *J. Electroanal. Chem.*, 30 (1971) 41
[38] S. Karp, *J. Phys. Chem.*, 72 (1968) 1082
[39] M.R. Hoffmann, I. Hua, R. Höchemer, *Ultrasonics Sonochem.*, 3 (1996) S163
[40] P. Colarusso, N. Serpone, *Res. Chem. Intermed.*, 22 (1996) 61
[41] M. Midler, Jr., C.M. Bagner, A.S. Wildman, E.S. Venkataramani, *Environ. Progress*, 11 (1992) 251
[42] C.M. Sehgal, S.Y. Wang, *J. Am. Chem. Soc.*, 103 (1981) 6606

8. Simulation of Square Wave Voltammetry: Reversible Electrode Processes

The work in this chapter was done in collaboration with Benjamin Brookes, Physical and Theoretical Chemistry Laboratory, Oxford and is published in *Journal of Physical Chemistry B* 103 (1999) 5289.

8.1. Introduction

Square Wave Voltammetry (SWV) is a highly attractive and especially sensitive method for the study of diverse electrochemical processes.[1-4] The technique involves the application of the general potential waveform defined in Figure 6.1 and the measurement of the currents I(1) and I(2) in each cycle of the waveform at the points shown. The current difference (ΔI) given by equation (1.65) is highly discriminating against background currents and the variation of ΔI with potential typically gives rise to symmetrical peak-shaped voltammograms which are also particularly mechanistically revealing. Whilst the SWV behaviour can be satisfactorily modelled by analytical theory for electrochemical processes proceeding via relatively simple mechanisms, the investigation of more complex reactions is necessarily precluded by the absence of suitable theory. In this paper we seek to remedy this situation by formulating a general simulation approach to SWV which should ultimately be readily applicable to relatively elaborate mechanistic schemes.

The numerical simulation of SWV is an especially challenging problem in the computational electrochemistry field, since the concentration profiles near the electrode surface are not only changing temporally very rapidly throughout each pulse, and with potential, but also spatially. In the following transformation of both the time and space variables is suggested to facilitate both accurate and

computationally economical simulations for the specific case of an electrochemically reversible couple. The ready extension to mechanistically rich processes is envisaged.

8.2. Theory

We consider a simple electrode couple,

$RED(\text{aq}) - ne^- \rightleftharpoons OX(\text{aq})$

at the surface of a uniformly accessible electrode. It is assumed that the couple shows fast electrode kinetics so that it is electrochemically reversible. Thus at the electrode surface, we can apply the Nernst Equation,

$$\frac{[\text{RED(aq)}]_{y=0}}{[\text{OX(aq)}]_{y=0}} = \exp\left[-\left(\frac{nF}{RT}\right)\left(E - E^{0'}\right)\right] \qquad (8.1.)$$

where E is the potential of the square-wave scan, $E^{0'}$ the formal potential of the redox couple and y is the co-ordinate normal to the electrode.

Mass transport equations for both species in solution are given by Fick's second law:

$$\frac{\partial[RED]}{\partial t} = D_{RED}\frac{\partial^2[RED]}{\partial y^2} \qquad (8.2.)$$

$$\frac{\partial[OX]}{\partial t} = D_{OX}\frac{\partial^2[OX]}{\partial y^2} \qquad (8.3.)$$

At the electrode surface, we conserve flux of the OX and RED species.

$$D_{RED}\left.\frac{\partial[RED]}{\partial y}\right|_{y=0} = -D_{OX}\left.\frac{\partial[OX]}{\partial y}\right|_{y=0} \qquad (8.4.)$$

Finally the concentration of the reduced species tends to its bulk value far from the electrode, whilst that of the oxidised species approaches zero.

$$[RED]_{y=l} = [RED]_{bulk} \qquad (8.5.)$$

$$[OX]_{y=l} = 0 \qquad (8.6.)$$

where l is a distance large enough not to influence the interfacial process, so that in effect semi-infinite diffusion operates.

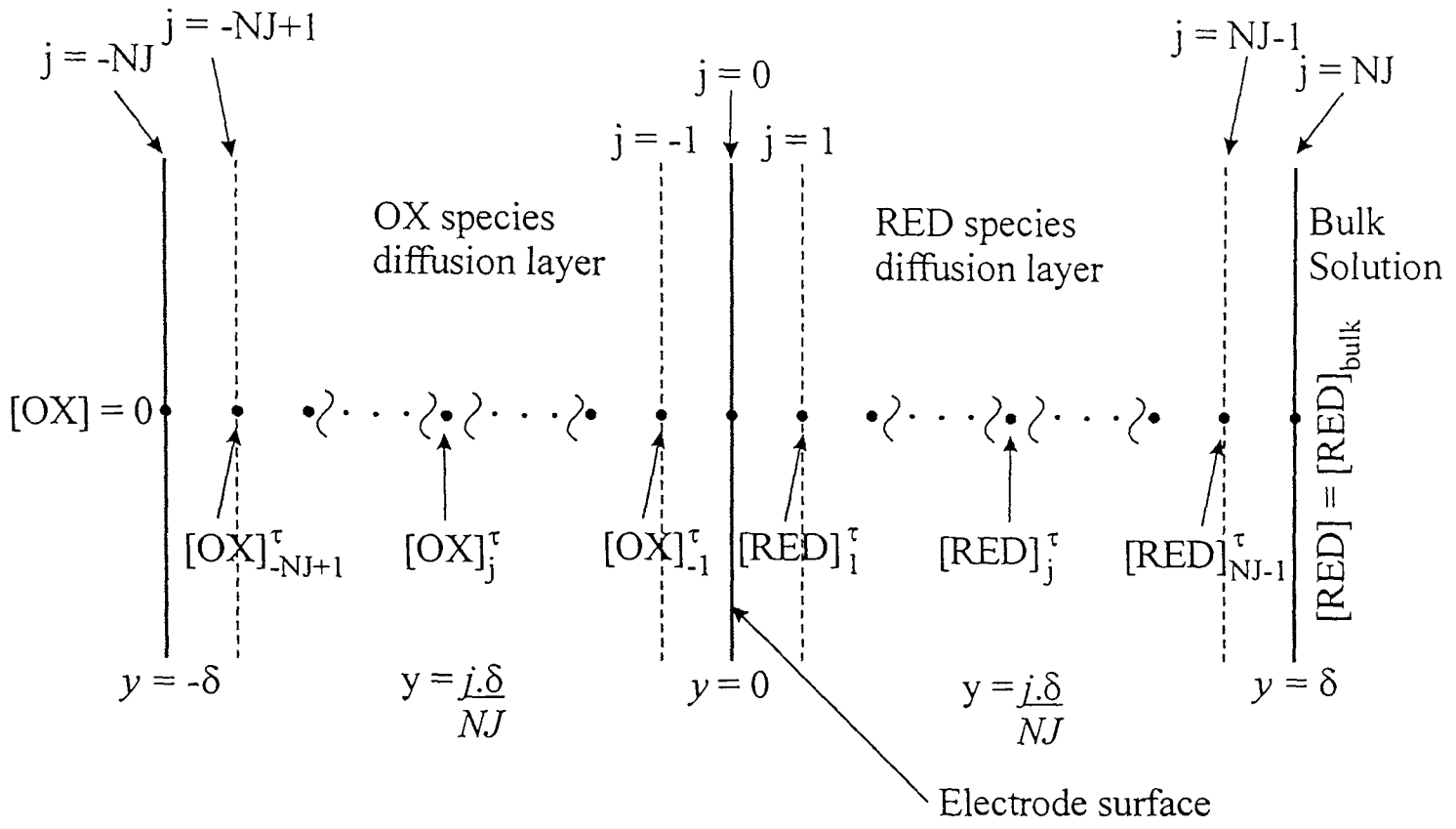


Figure 8.1 Schematic diagram showing the spatial node distribution in the back-to-back grid.

We can simulate the above problem using the Backwards Implicit method.[5-7] It is necessary to simulate both the *OX* and *RED* species that occupy similar space. To most simply accomplish this we use the back-to-back grid,[8-10] shown in Figure 8.1, where a positive y co-ordinate is used to simulate the *RED* species and a negative y co-ordinate for the *OX* species. The electrode surface is placed at $y = 0$. The concentration of *RED* at the surface is allocated to the grid point at $y = 0$; that of *OX* is handled implicitly as detailed below.

The nature of the voltage sweeping causes an increasing amount of *OX* and *RED* species to be inter-converted at the start of every pulse. It may be anticipated that better simulations will be produced if more calculations are made closer to the start of the pulse. The use of Cottrellian time grids[11] provides a "natural" method for accomplishing this. Specifically we introduce two distorted timescales, for the forward pulse:

$$\tau_f = \frac{\sqrt{t_p}}{\sqrt{t-b}} \tag{8.7.}$$

and for the backward pulses:

$$\tau_b = \frac{\sqrt{t_p}}{\sqrt{t-t_p-b}} - \frac{\sqrt{t_p}}{\sqrt{t-b}} \tag{8.8.}$$

where t is real time, t_p is time pulse length (seconds), and b is an offset in the grid

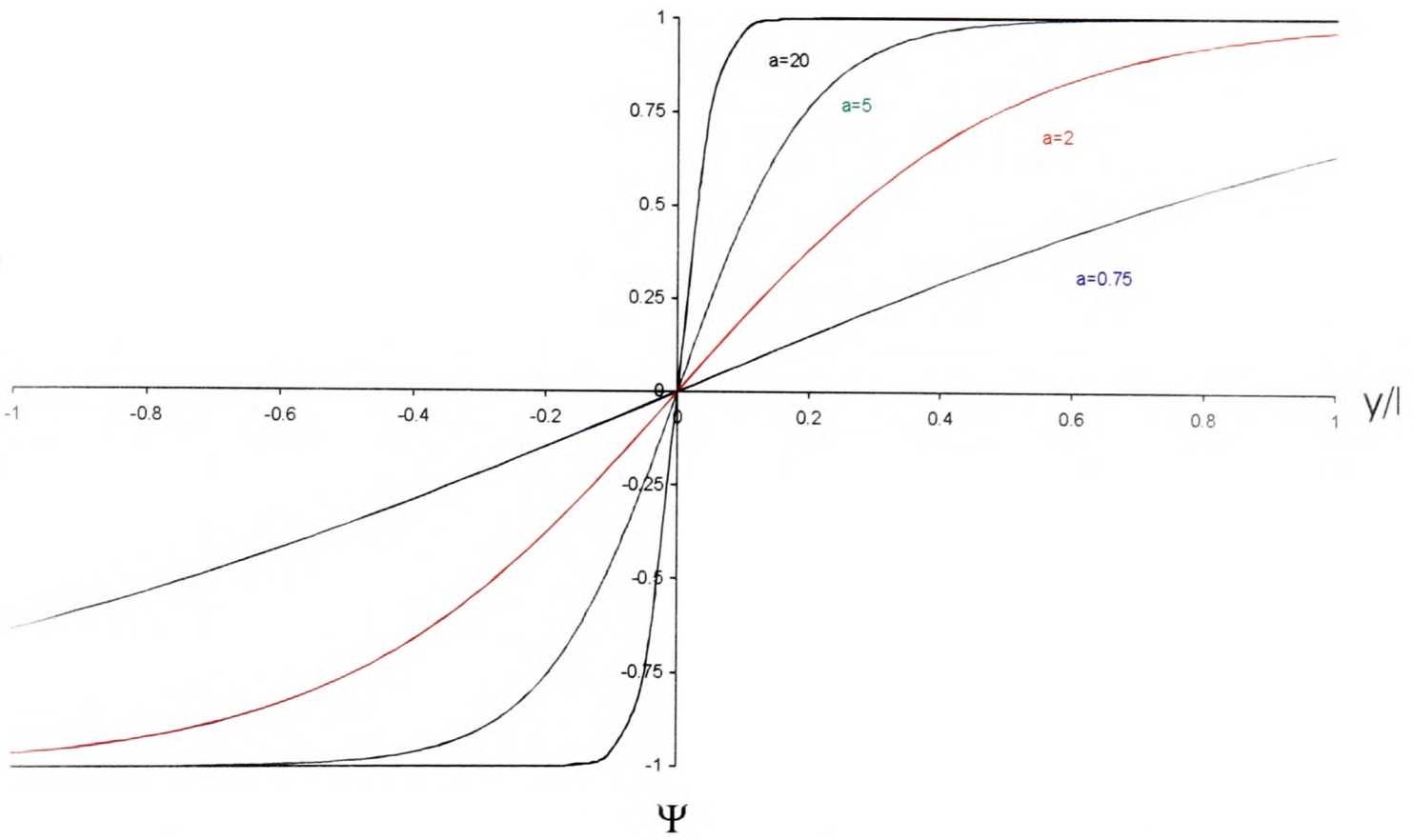


Figure 8.2 Graph showing the variation of the spatial function, ψ, with the ratio y/l.

(seconds) used to optimise the simulations; in practice this was with b about $t_p/500$.

In addition to "Cottrellian time" it is helpful to note that similarly, the largest changes in concentrations of RED and OX species occur at distances closest to the electrode, so that it is necessary to simulate more points closer to the electrode surface than further away. This is done by introducing a transformed spatial function, such that:

$$\psi = \tanh\left(\frac{y.a}{l}\right) \tag{8.9.}$$

where y is the real distance, a, is a scaling parameter, and l the thickness of the semi-diffusion layer. Similar non-linear meshes have been reported by D.J.Gavaghan.[12] Figure 8.2 shows how ψ varies with the dimensionless ratio y/l, for a values between 0.75 and 20. The latter value was used to optimally compute the results reported below.

We next transform the partial derivative equations (8.2.) and (8.3.) into τ and ψ space. Noting first for the temporal variables that

$\left[\frac{\partial}{\partial t}\right]_y = \frac{\partial \tau}{\partial t}.\left[\frac{\partial}{\partial \tau}\right]_y$ by the chain rule, we find that for the forward pulse

$$\frac{\partial}{\partial t} = -\frac{\tau_f^3}{2t_p}.\frac{\partial}{\partial \tau_f}. \qquad (8.10.)$$

For the backward pulse, there is no explicit form of t in terms of τ_b. It is therefore necessary evaluate the derivative $\frac{\partial \tau}{\partial t}$, by use of the Adam's variable-order variable-step method*.

Turning second to the spatial variables,

$$\frac{\partial}{\partial y} = \frac{\partial \psi}{\partial y}.\frac{\partial}{\partial \psi} \qquad (8.11.)$$

Since $\frac{\partial \psi}{\partial y} = \frac{a}{l}\left(1-\psi^2\right)$, we find

$$\frac{\partial^2}{\partial y^2} = \frac{a}{l}\left(1-\psi^2\right).\frac{\partial}{\partial \psi}\left[\frac{a}{l}\left(1-\psi^2\right).\frac{d}{\partial \psi}\right] = \left(\frac{a}{l}\right)^2\left(1-\psi^2\right).\left[-2\psi.\frac{\partial}{\partial \psi}+\left(1-\psi^2\right).\frac{\partial^2}{\partial \psi^2}\right] \qquad (8.12.)$$

It is now possible to formulate finite-difference equations from the two transport equations. Starting for the general case for the RED species:

---

* D02CJF subroutine in the NAG library (Mark 18)

$$\left(\frac{\partial\tau}{\partial t}\right)\left(\frac{[RED]_j^r - [RED]_j^{r-1}}{\Delta\tau}\right) = \tag{8.13.}$$
$$D_{RED}\left(\frac{a}{l}\right)^2\left[\left(1-\psi_j^2\right)^2\left(\frac{[RED]_{j-1}^r - 2[RED]_j^r - [RED]_{j+1}^r}{(\Delta\psi)^2}\right) - \left(2\psi_j\left(1-\psi_j^2\right)\right)\left(\frac{[RED]_{j+1}^r - [RED]_{j-1}^r}{2\Delta\psi}\right)\right]$$

where $\Delta\psi = \dfrac{\tanh(a)}{NJ}$. An analogous equation applies to OX.

Equation (8.13.) can be simplified to:

$$[RED]_j^{r-1} = -\lambda^{RED}\left(\left(1-\psi_j^2\right) + \psi_j\Delta\psi\right)[RED]_{j-1}^r$$
$$+\left(1+2\lambda^{RED}\left(1-\psi_j{}^2\right)\right)[RED]_j^r \tag{8.14.}$$
$$-\lambda^{RED}\left(\left(1-\psi_j^2\right) - \psi_j\Delta\psi\right)[RED]_{j+1}^r$$

where $\lambda^{RED} = \dfrac{-D_{RED}\Delta\tau\left(1-\psi_j^2\right)\left(\dfrac{a}{l}\right)^2}{(\Delta\psi)^2\left(\dfrac{\partial\tau}{\partial t}\right)}$

At the electrode surface, the finite difference equation is written as:

$$0 = [RED]_0^r\left(\kappa + e^{\theta}\right) - [OX]_{-1}^r - \kappa[RED]_1^r \tag{8.15.}$$

where $\kappa = \dfrac{D_{RED}}{D_{OX}}$ and $\theta = \dfrac{nF}{RT}\left(E - E^{o'}\right)$

Also, as noted before, $[OX]_0^r$ must be treated implicitly, so the matrix elements relating to $[OX]_{-1}^{r-1}$ are found from the following

$$[OX]_{j-1}^{r-1} = -\lambda^{RED}\left(\left(1-\psi_j^2\right) + \psi_j\Delta\psi\right)[OX]_{-2}^r$$
$$+\left(1+2\lambda^{RED}\left(1-\psi_j{}^2\right)\right)[OX]_{-1}^r \tag{8.16.}$$
$$-\lambda^{RED}\left(\left(1-\psi_j^2\right) - \psi_j\Delta\psi\right)[RED]_0^r e^{\theta}$$

The boundary conditions applying to the transport equations are:

$t = 0$

$[OX]_j = 0 \quad \text{for } j = \text{-}1,\text{-}2,\text{-}3,\ldots,\text{-}NJ$

$[RED]_j = [RED]_{bulk} \quad \text{for } j = 0,1,2,3,\ldots,NJ$

$t > 0; y = l \; (j = NJ)$

$[RED]_{NJ} = [RED]_{bulk}$

$t > 0; y = l \; (j = \text{-}NJ)$

$[OX]_j = 0$

The relevant equations may be grouped together to form a tridiagonal matrix similar to the one in equation (6.20).

This matrix is solved using the Thomas Algorithm.[13-14] The currents $I(1)$ and $I(2)$ can then be calculated at the end of each half cycle as:

$$I = nFAD_{RED}\left(\frac{\partial[RED]}{d\psi}\right)_{y=0}\left(\frac{\partial\psi}{\partial y}\right) \tag{8.17.}$$

which tends to $I = nFAD_{RED}\left(\frac{\partial[RED]}{\partial\psi}\right)_{y=0}$ at the electrode surface.

The finite difference form of this is

$$I = nFAD_{RED}\left(\frac{a}{l}\right)^2\left(\frac{[RED]_1^\tau - [RED]_0^\tau}{\Delta\psi}\right) \tag{8.18.}$$

The simulations were compiled using FORTRAN or C and executed on a Silicon Graphics Origin™ 2000 server. Results were analysed using Excel 5.0 and IDL 5.0. In order to assess the merits of the distorted time and space parameters detailed above, simulations were conducted using first Cottrellian time and "tanh" space and second, for comparison, with real time and space. Convergence to within 1% of the fully converged peak current was achieved with NJ=57 for the former cases whereas

NJ=775 was required in the latter. Simulations conducted with one real variable and one transformed variable indicated that the spatial transformation was the most important factor in achieving high efficiency.

8.3. Results and Discussion

We start by considering our results in light of the analytical theory developed by Osteryoung, Aoki and co-workers[16] who demonstrated the SWV peak is characterised by three parameters, first the peak current, ΔI_p, second the peak width at half-height, $W_{1/2}$, and third the total area under the peak, S_T. We consider first the current where ΔI is measured at the end of each square wave cycle, k. This is given by equation (8.19.).[15]

$$\Delta I = nFA[RED]_{bulk} \sum_{j=0}^{k} \left(s_{2j+1} g_{k-j} + s_{2j} g'_{k-j} \right) \qquad (8.19.)$$

where $s_0 = -f\left(\nu/2\right)$

$$s_1 = 2f\left(\nu/2\right) - f(\nu)$$

$$s_j = -f\left(\left\{\frac{j-1}{2}\right\}\nu\right) + 2f\left(\left\{\frac{j}{2}\right\}\nu\right) - f\left(\left\{\frac{j+1}{2}\right\}\nu\right) \qquad (j=2,3,4\ldots k)$$

$$g_k = \left[1 + \exp\left\{-nF\left(E_i - E^{0'} + k\Delta E + E_{SW}\right)/RT\right\}\right]^{-1}$$

$$g'_k = \left[1 + \exp\left\{-nF\left(E_i - E^{0'} + k\Delta E - E_{SW}\right)/RT\right\}\right]^{-1}$$

and $\nu = \sqrt{\frac{D}{\pi t}}$

The quantity $t = \left(k - 1/2\right)\nu$ for the forward pulse

whilst $t = k\nu$ for the backward pulse

The equation is entirely rigorous within the problem as formulated above. Equation (8.19.) permits the calculation of ΔI as a function of the potential peak. However to

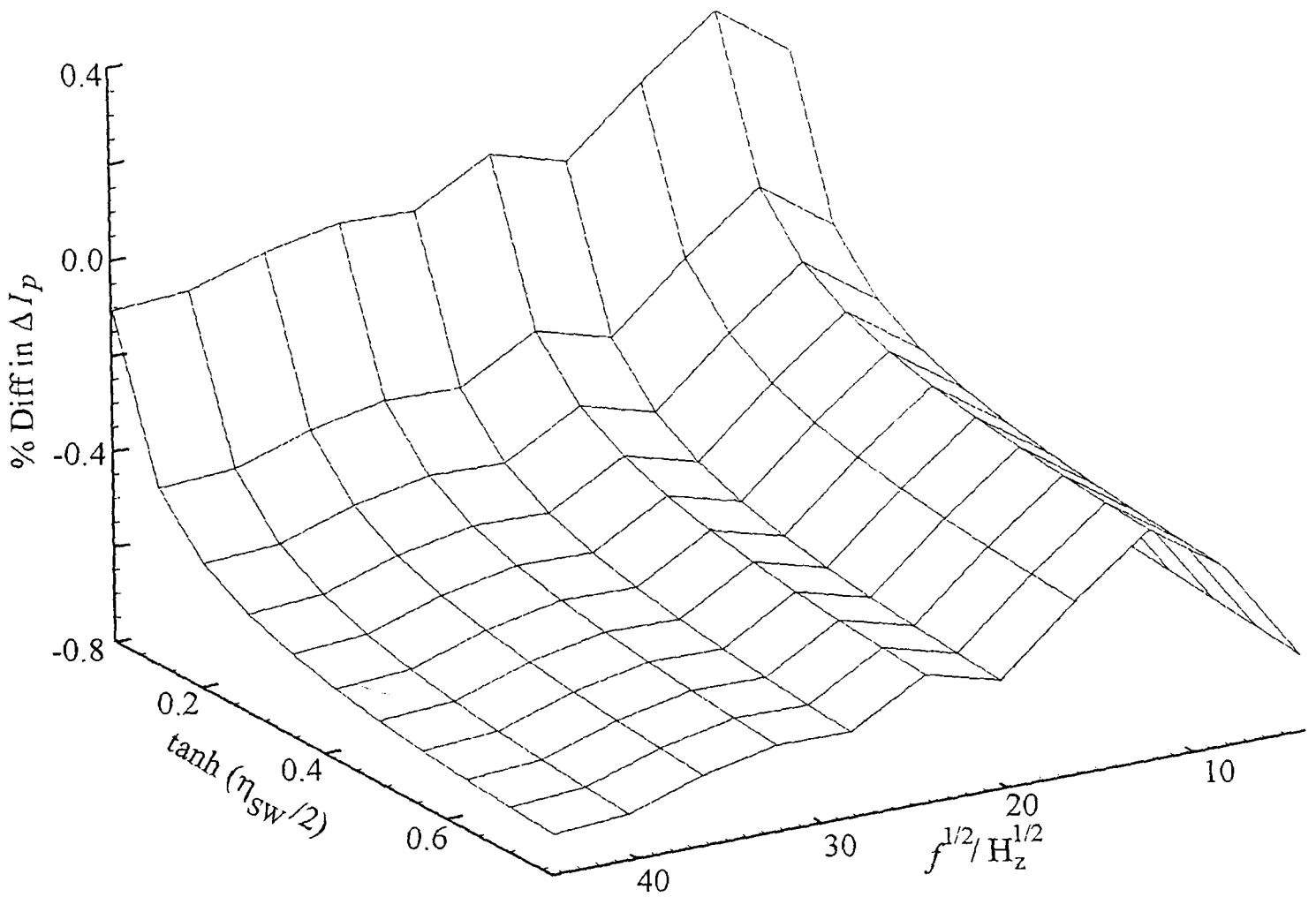


Figure 8.3 Graph showing the percentage difference in ΔIp between the fully converged simulation and the analytical value given by equation (8.19.). The frequency is measured in Hertz.

aid experimentation, approximate forms have been developed. Specifically, work by Osteryoung, Aoki and Maeda[16] shows that ΔI_p should vary linearly with both $\sqrt{f}$ and $\tanh\left(\eta_{SW}/2\right)$:

$$\Delta I_p = 0.9653nF[RED]_{bulk} A\sqrt{Df}\tanh\left(\eta_{SW}/2\right) \qquad (8.20.)$$

where A is the electrode area and

$$\eta_{SW} = \frac{nFE_{SW}}{RT} \qquad (8.21.)$$

Equation (8.20.) was derived under the assumption that $D_{OX} = D_{RED} = D$ and the square wave amplitude dominates over the step height of the base staircase. To assess this approximation, the numerical solution of equation (8.19.) was compared to our

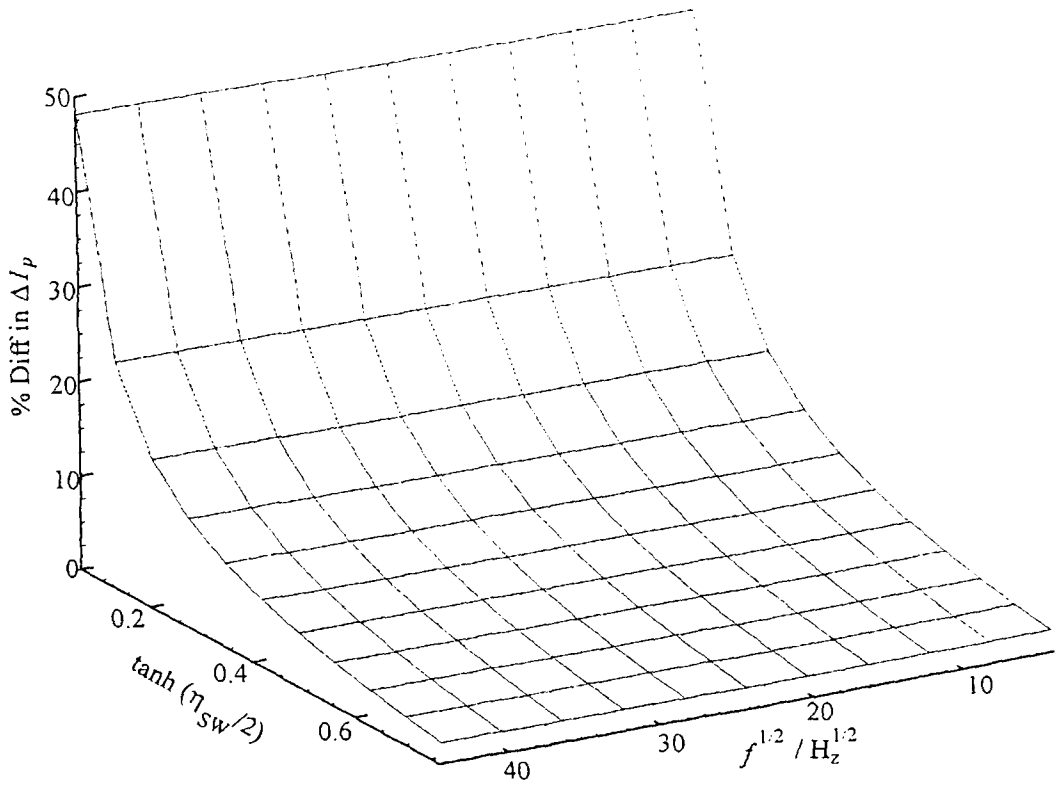


Figure 8.4 Graph showing the percentage difference in ΔIp between that given by the approximate expression in equation (8.20.) and the full analytical solution of equation (8.21.). The frequency is measured in hertz.

simulation results for values of E_{SW} in the range 2 mV to 50 mV and for f in the range 20 to 2000 Hz and a percentage difference calculated. The results[†] are shown in Figure 8.3; agreement was excellent, ranging within -0.7% and 0.3%. Equation (8.20.), however, showed considerable variations from the non-approximate theory. As evident in Figure 8.4, although the frequency dependence of ΔI_p is acceptably accurate, significant errors are seen with variation in E_{SW} and, for example, errors as large as 47% were observed at very low wave amplitudes of 2 mV, with a step potential, ΔE, of 10 mV.

We next turn to consider the parameter $W_{1/2}$. Osteryoung, Aoki and Maeda[16] approximately solved equation (8.19.) to find the peak width at half height:

[†] To collect these data, the following parameter values were used: NJ=140 and NODES=700 where NODES is the number of temporal simulations made in a single pulse. These represent twice the values needed for convergence to 1%.

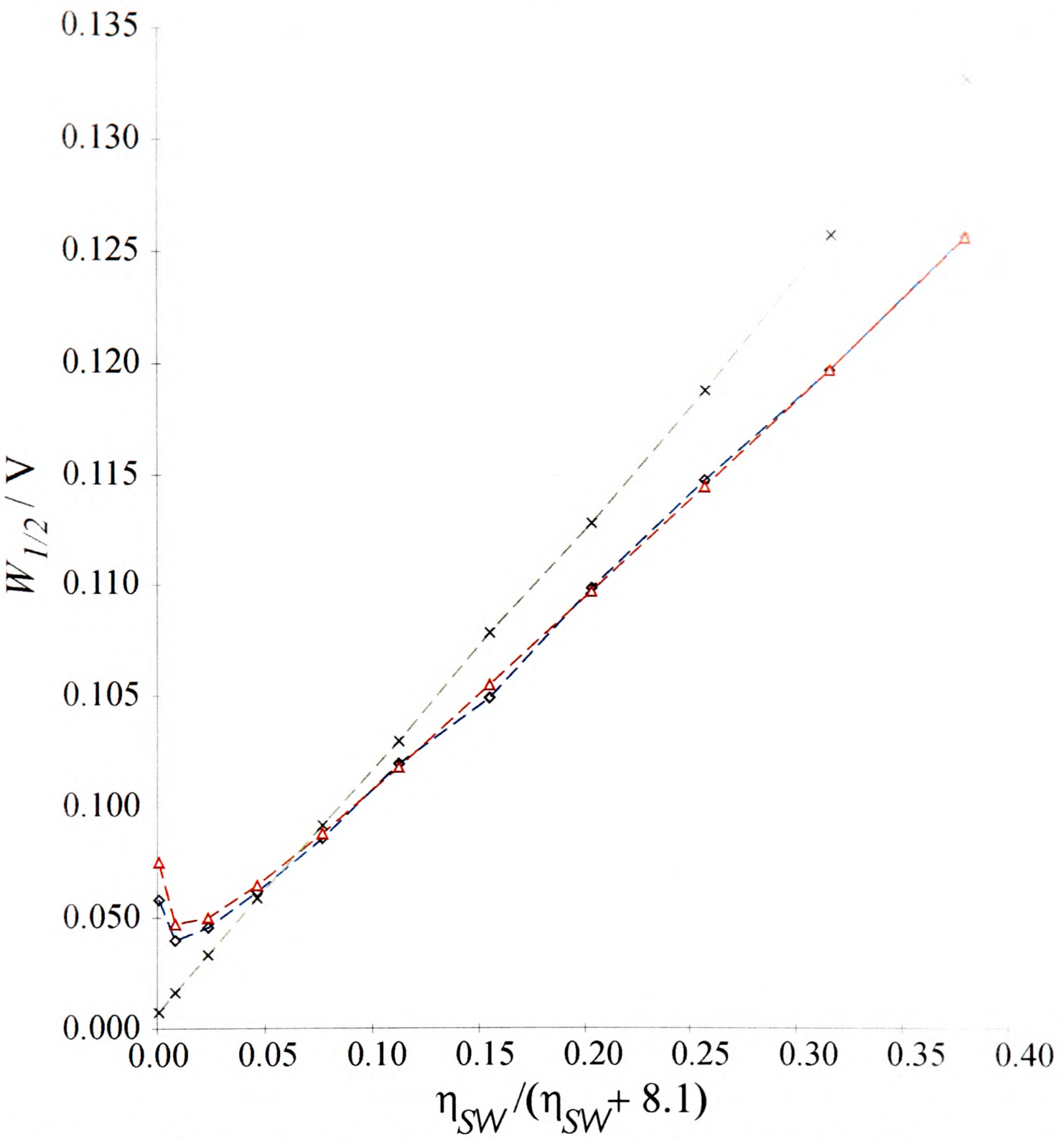


Figure 8.5 Graph showing $W_{1/2}$ calculated from simulation (◇) and equation (8.19.) (△) as a function of $\eta_{SW}{}^2/(\eta_{SW}+8.1)$. The green (×) dashed line shows the approximation of equation (8.22.).

$$W_{1/2} = \frac{RT}{nF}\left\{3.53 + 3.46\left(\frac{\eta_{SW}{}^2}{(\eta_{SW}+8.1)}\right)\right\} \qquad (8.22.)$$

Figure 8.5 shows values of $W_{1/2}$ as deduced first via full simulation and second and third, through equations (8.19.) and (8.22.), plotted against $\frac{\eta_{SW}^{\ 2}}{(\eta_{SW}+8.1)}$ over a range of

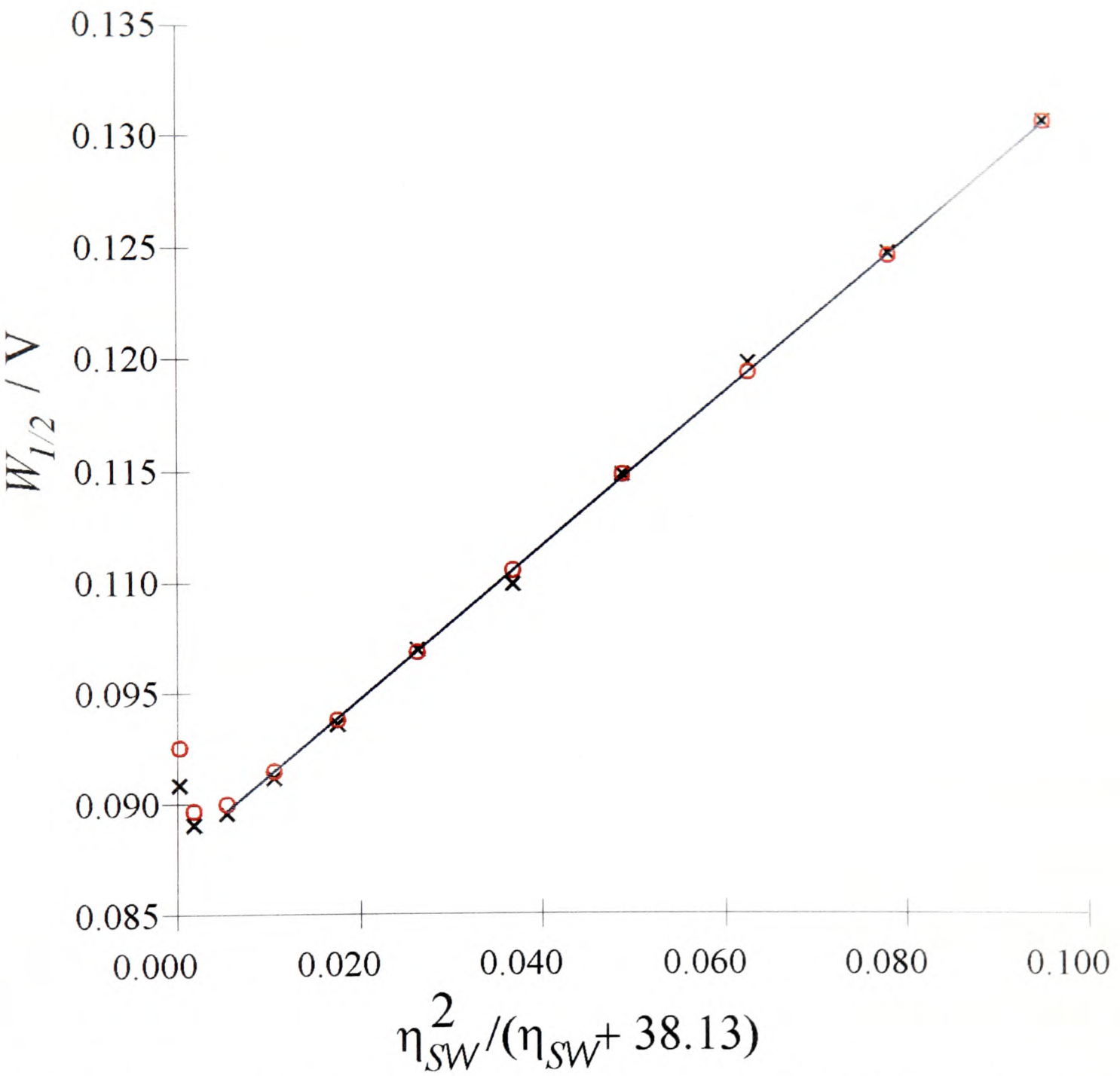


Figure 8.6 Graph showing $W_{1/2}$ calculated from simulation (×) and equation (8.19.) (○) as a function of $\eta_{SW}^{\ 2}/(\eta_{SW}+38.13)$. An R-squared value of 0.9998 is seen for the linear approximation for E_{SW} values higher than 12 mV (see text).

E_{SW} = 2 to 50 mV, taking ΔE as 10 mV. The simulation correlates well with the true analytical value; the agreement is better than 2% over the entire range explored. However the approximate equation is considerably poorer, deviating at worst by up to *ca.* 7% from full analytical theory at low E_{SW}. Using the values given by the numerical solution of equation (8.19.), a new equation was found which fitted data more closely.

The equation was:

$$W_{1/2} = \frac{RT}{nF}\left\{3.61 + \frac{13.73\eta_{SW}{}^{2}}{(\eta_{SW} + 38.13)}\right\} \qquad (8.23.)$$

which accurately predicts $W_{1/2}$ to within 1.7% for E_{SW} greater than 12 mV. The quality of this fit can be seen from Figure 8.6.

Finally we consider the total integration of ΔI with respect to potential:

$$S_T = \int_{-\infty}^{\infty} \Delta I dE \qquad (8.24.)$$

An approximate analytical expression for S_T has been found by Osteryoung, Aoki and Maeda;[16] S_T is a function of root f and E_{SW}.

$$S_T = 1.931nF[RED]_{bulk} AE_{SW}\sqrt{D_{RED}f} \qquad (8.25.)$$

where A is the area of the electrode.

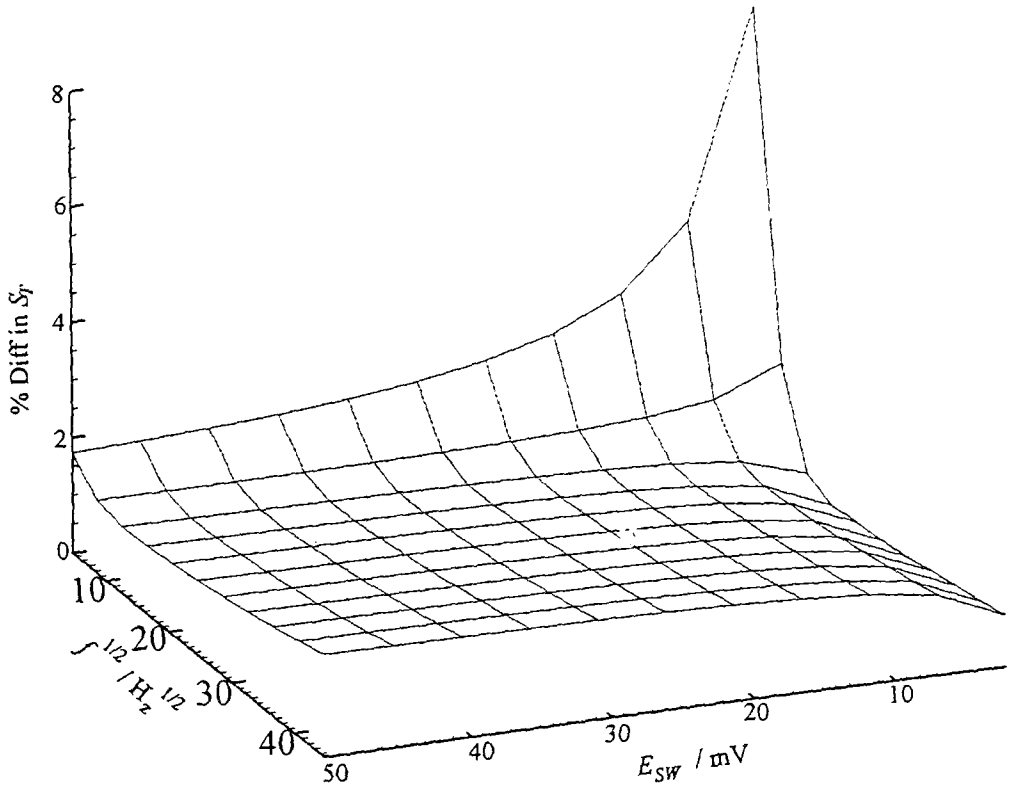


Figure 8.7 Graph showing the percentage difference in the calculated value of S_T between the converged simulation and the analytical value given by equation (8.19.).

A comparison of the results from numerical solution of equation (8.22.) and from the simulation is shown in Figure 8.7 Simulations were carried out for frequencies in the range 20 to 2000 Hz and E_{SW} values in the range 2 to 50 mV. Agreement with equation (8.19.), better than 2%, was found for frequencies greater than 70 Hz and E_{SW} greater than 2 mV. At lower values of E_{SW} and f, the increased deviation may be attributed to errors in the calculation of equation (8.25.),

since the current-potential data points are inherently discrete by virtue of the nature of the experiment.

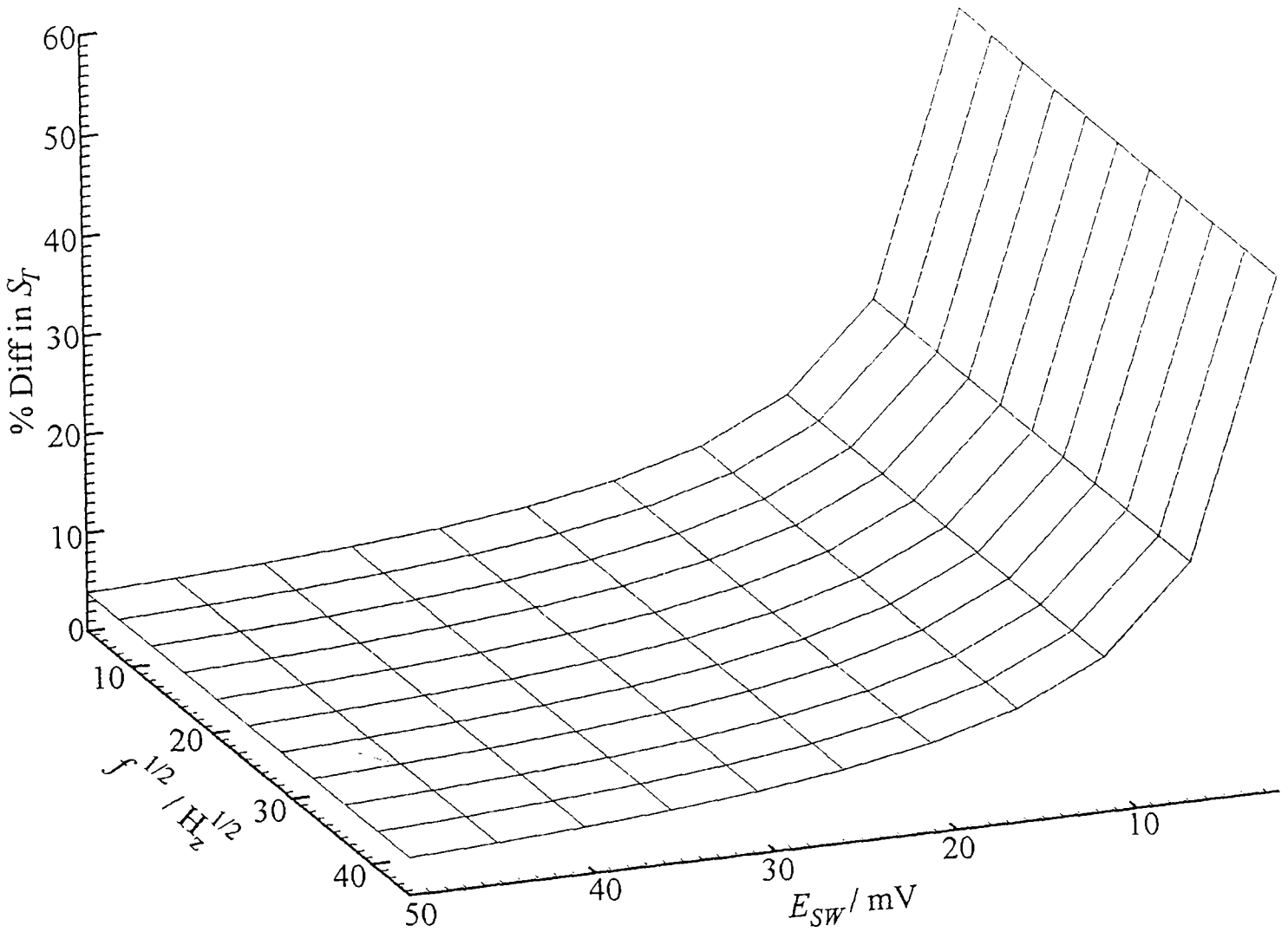


Figure 8.8 Graph showing the percentage difference in the calculated value of S_T given by the approximate analytical expression in equation (8.20.) and the full analytical solution given by equation (8.19.), as a function of frequency(Hz) and E_{SW}(V)

Comparison of equation (8.25.) with full analytical theory shows that the agreement approaches 4% under favourable conditions, as seen in Figure 8.8. Again significant deviation occurs at low values of E_{SW}, since when E_{SW} is 2 mV, equation (8.26.) and equation (8.22.) differ by 60%, for a step potential, ΔE, of 10 mV.

Last a particular merit of the simulation approach to the characterisation of SWV is that concentration profiles close to the electrode surface can be viewed as a function of both potential and time. Figure 8.9 shows a sequence of such profiles simulated for the following parameters: $E_{SW} = 50$ mV; $\Delta E = 10$ mV; $f = 60$ Hz, $E^{0'} = 0$ mV; $E_i = -500$ mV; $E_f = 500$ mV, where E_i and E_f are the initial and final potentials respectively. The potential scan therefore involves 100 cycles or 200 pulses. The

figures show the spatial distribution of OX and RED for forward and backward pulses of two different cycles; the 44^{th} and 54^{th}.

Considering the profiles in Figure 8.9, an increased net depletion of RED is evident as the potential becomes more positive. However the changes in concentration profile induced by the potential steps are inherently sharp and maxima and minima develop in the profiles of both species. These together with the high concentration gradients account for the high complexity of the simulation problem. The use of distorted space and especially spatial grids, advocated above represents a general method to the quantitative study of SWV and the extension to more complicated mechanisms involving coupled homogeneous kinetics should pose no new difficulties .

8.4. Conclusions

An approach to the simulation of square wave voltammetry is developed. This complements the approximate analytical theory developed by Osteryoung and co-workers and is applicable generally, and in particular, under conditions where the square wave amplitude does not dominate the step height as is required for the approximations in the analytical theory to be valid.

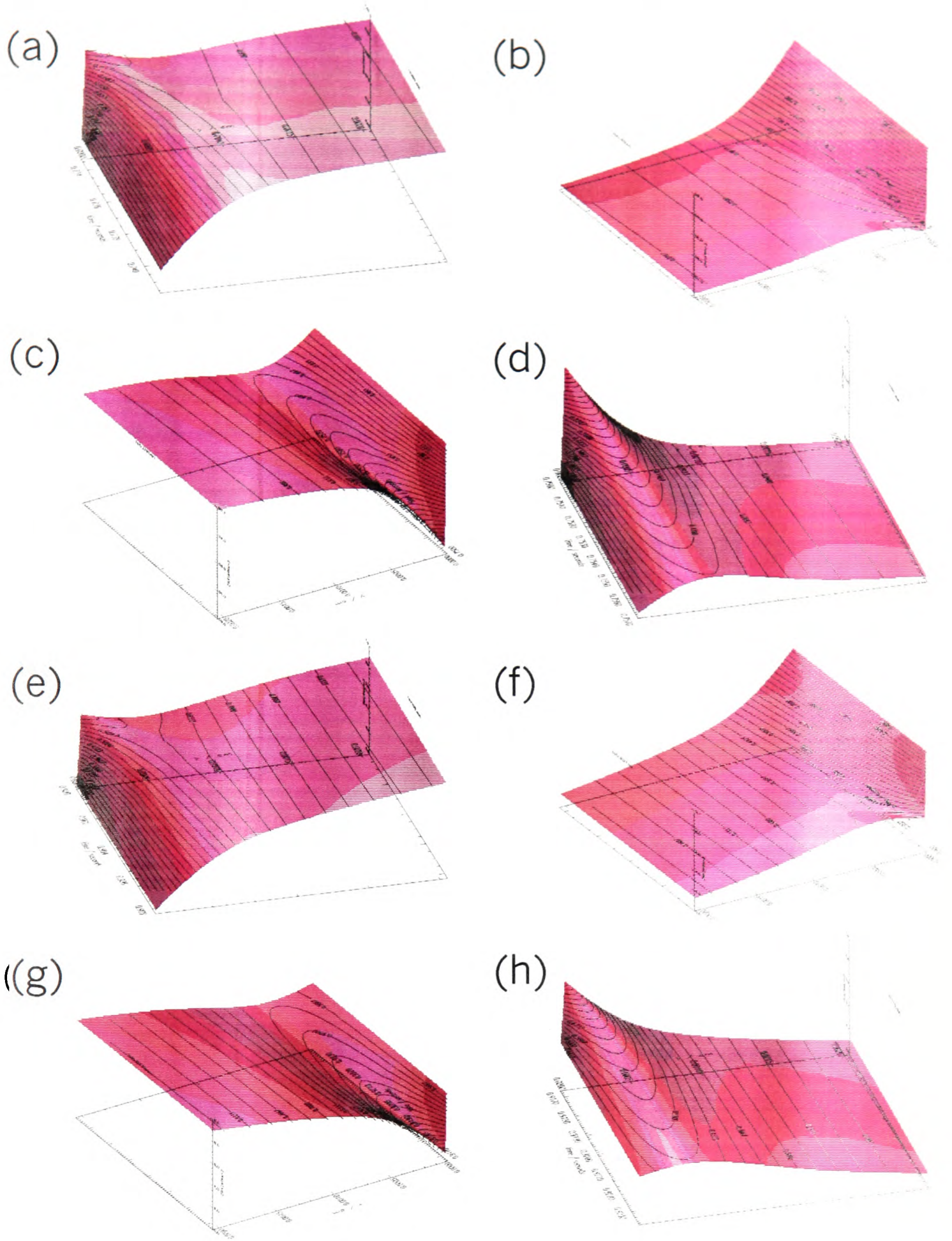


Figure 8.9 Concentration profiles of (a) RED at forward pulse of 44th cycle. E = -10mV. (b) OX at forward pulse of 44th cycle. E = -10mV, (c) RED at backward pulse of 44th cycle. E= -110mV. (d) OX at backward pulse of 44th cycle. E = -110mV, (e) RED at forward pulse of 54th cycle. E = 90mV. (f) OX at forward pulse of 54th cycle. E = 90mV, (g) RED at forward pulse of 54th cycle. E=-10mV. (h) OX at forward pulse of 54th cycle. E = -10mV. It should be noted that the time axes in diagrams 10(b). (c). (f) and (g) have been reversed compared to those in (a). (d). (e) and (h) for clarity of presentation.

References for Chapter 8

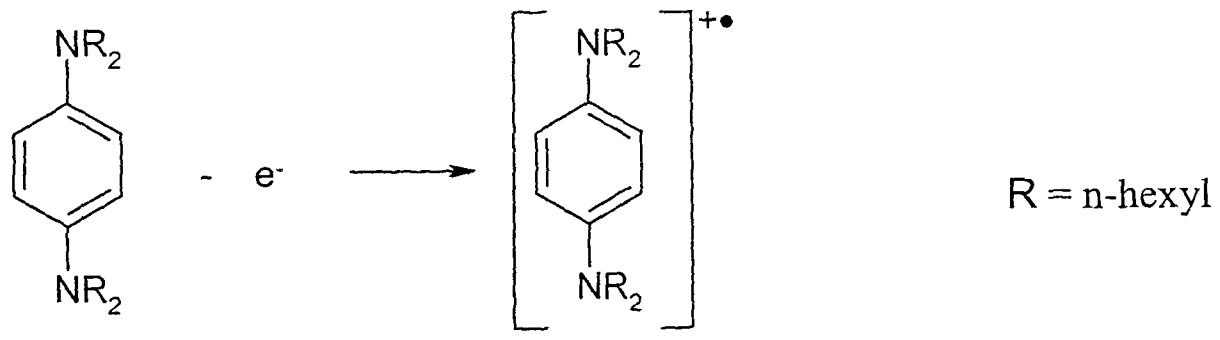
[1] J. Osteryoung, J.J. O'Dea, *Electroanalytical. Chem.*; Bard.A.J., Ed.; Marcel Dekker: New York, 14 (1986) 209
[2] D.P. Whelan, J.J. O'Dea, J. Osteryoung, K. Oaki, *J.Electroanal. Chem.* 202 (1986) 23
[3] N. Fatouros, D. Krulic, *J.Electroanal. Chem.* 443 (1998) 262
[4] K. Aoki, J. Osteryoung, *J. Electroanal. Chem.* 240 (1988) 45
[5] J.L. Anderson S. Moldoveanu, *J.Electroanal. Chem,* 179 (1984) 109
[6] P. Laasonen. *Acta Math.*, 81 (1949) 30917
[7] R.G. Compton, M.B.G. Pilkington, G.M. Stearn, *J.Chem.Soc., Faraday Trans 1*, 84 (1988) 2155
[8] R.A.W. Dryfe, DPhil Thesis, Oxford University, (1995) pp82
[9] M.J. Bidwell, J.A. Alden, R.G. Compton, *J.Electroanal. Chem.* 417 (1996) 119
[10] J.A. Alden, R.G. Compton, *J.Phys.Chem.B.* 101 (1997) 8941
[11] J.C. Ball, R.G. Compton,. *J.Phys.Chem.B.* 102 (1998) 3967
[12] D.J. Gavaghan, *J.Electroanal. Chem*, 456 (1998) 25
[13] L.H. Thomas,. *Eliptical Problems In Linear Difference Equations Over A Network*, (Watson Sci. Comput. Lab. Rept., Columbia University, New York, 1949)
[14] G.H. Bruce, D.W. Peaceman, H.H. Rachford, J.D. Rice, *Trans. Am. Inst. Min. Engrs,*198 (1953) 79
[15] K. Aoki, K. Tokuda, H. Matsuda, J. Osteryoung, *J.Electroanal. Chem*, 202 (1986) 25
[16] K. Aoki, K. Tokuda, H. Matsuda, J. Osteryoung. *J.Electroanal. Chem*, 272 (1989) 17

9. Ionic Liquids: Investigation Using Simulation Techniques to Determine the Mechanism of Electron Transfer by Comparison to Experiment.

The work in this chapter was done in collaboration with Qiu Fulian, Alastair Blythe and Jay Wadhawan, Physical and Theoretical Chemistry Laboratory, Oxford and is currently in press in the form of two papers in *Electroanalysis*.

9.1. Introduction

Microdroplets of the oil THPD (para-(N,N,N',N'-tetrahexyl)-phenylenediamine) can be deposited on an inert solid electrode and then immersed into an aqueous electrolyte with which the oil is immiscible and subjected to a positive potential sweep. This gives a corresponding oxidative current voltage-curve associated with the following electrochemical reaction



with the uptake of charge compensating counter ions from the surrounding solution forming an ionic liquid.[1,2] If the potential sweep is reversed reduction of the droplet occurs and the counter ions are released into solution. The question arises as to the mechanism of electron transfer between the oil or ionic liquid and the electrode surface. Three possibilities can be readily envisaged namely: (i) counter ion injection at the surface of the droplet with rapid surface diffusion of charge to the electrode surface; (ii) electron transfer solely at the three phase boundary between the droplet

aqueous solution and the electrode surface or (iii) a direct charge transfer between the electrode and the oil. The use of digital simulations in electrochemistry to explore mechanistic possibilities is well established.[3,4] Many different approaches may be taken such as Finite Element (FE)[5] methods, Finite Difference (FD)[6,7] methods and Boundary Element Method (BEM).[8-10] This chapter attempts to use three FD methods, Backwards Implicit (BI),[11,12] the Strongly Implicit Procedure (SIP)[13,14] and the Multigrid method (MGD1)[15] to address the three possible electron transfer mechanisms by the use of implicit digital simulations and evaluate the merits of all three mechanisms. The concept of non-ideality[16] will be introduced and incorporated in the simulations as ionic liquids by their very nature are grossly non-ideal. Simulations will be presented for both cyclic voltammetry and current time transients resulting from potential steps.

9.2. Theory

The oil droplets on the surface of the electrode are considered to be sessile hemispheres (see Figure 9.1 which also defines the coordinate system used in the following simulations). The transport of ions in the aqueous phase is assumed to be fast due to solution agitation and is therefore neglected in comparison with the rate of charge movement within the drop. This assumption has been verified by experiments conducted under forced convection.[1,2] Diffusion in the droplet is expected to follow Fick's Laws of diffusion; however we recognise that the

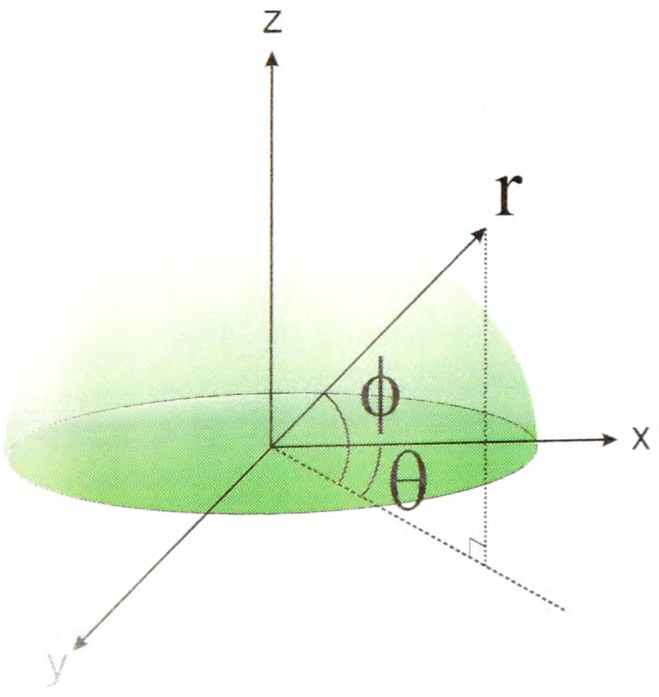


Figure 9.1 Schematic defining the coordinate system of the droplet.

interactions between ions and their precursors are unlikely to be ideal. Accordingly for the redox couple:

$$B(droplet) + X^-(aq.) \rightarrow A(droplet) + e^- \qquad (9.1.)$$

we consider transport within a non-ideal solution of A in B where, for example, B might be THPD so that A would represent $THPD^+X^-$. The flux in a non-ideal solution is given by[17]

$$J_A = -D_{ideal}\frac{d[A]}{dx}\left\{1 + \frac{d\ln\gamma_A}{d\ln a}\right\} \qquad (9.2.)$$

where J_A is the flux of species A, a is the normalised concentration of A ($a = [A]/[B]_{initial}$), $[B]_{initial}$ is the initial concentration of the drop, D_{ideal} is the ideal solution diffusion coefficient and γ_A is the activity coefficient of species A. We also introduce b such the $b = [B]/[B]_{initial}$. The origin and the application of Regular Solution theory is discussed below in §9.2.1.

9.2.1. Regular Solution Theory

Assuming B and A form a regular solution the activity coefficients are given by[16]

$$\ln\gamma_A = \left(\frac{zw}{k_BT}\right)(1-x_A)^2 \qquad (9.3.)$$

$$\ln\gamma_B = \left(\frac{zw}{k_BT}\right)(1-x_B)^2 \qquad (9.4.)$$

where z is the interaction parameter, w the number of nearest neighbours, k_B is the Boltzmann constant and T the temperature. In the simulations the diffusion coefficients of A and B are assumed to be the same so that at any point

$$a + b = 1 \qquad (9.5.)$$

If the Nernst equation is written in the form of standard electrode potential, E^0, concentrations, $[A]$ and $[B]$, and activity coefficients, γ_A and γ_B, we get

$$E - E^0 = \frac{RT}{F} \ln \frac{\gamma_A [A]}{\gamma_B [B]} \tag{9.6.}$$

which can therefore be written as

$$\exp(\theta) = \frac{\gamma_A}{\gamma_B} \frac{[A]}{[B]} = \frac{\gamma_A}{\gamma_B} \frac{x_A}{x_B} \tag{9.7.}$$

Where x_A and x_B are the mole fraction of A and B respectively and $\theta = \frac{F}{RT}(E - E^0)$.

The activity coefficients are defined as

$$\gamma_A = \exp(Z x_B^{\,2}) \tag{9.8.}$$

$$\gamma_B = \exp(Z x_A^{\,2}) \tag{9.9.}$$

where $Z = \frac{zw}{k_B T}$. Combining (9.8.) and (9.9.) we get

$$\frac{\gamma_A}{\gamma_B} = \exp\left(Z\left(x_B^{\,2} - x_A^{\,2}\right)\right) \tag{9.10.}$$

this reduces to

$$\frac{\gamma_A}{\gamma_B} = \exp(Z(1 - 2x_A)) \tag{9.11.}$$

Equation (9.7.) becomes

$$\exp(\theta) = \exp(Z(1 - 2x_A)) \frac{x_A}{1 - x_A} \tag{9.12.}$$

thus if we define a as $[A]/[B]_{initial}$ with no A present to start with

$$a = \frac{1}{1 + \exp(Z(1 - 2a))\exp(-\theta)} \tag{9.13.}$$

where $\theta = \frac{nF}{RT}(E - E^0)$; E^0 is the standard potential of the $A|B$ couple.

9.2.2. Mechanisms of Electron Transfer

In this section three readily envisaged mechanisms for electron transfer are proposed and the finite difference simulations derived.

9.2.2.1. Model 1: Droplet Surface Model.

In this model the charge injection is assumed to occur uniformly at all points on the droplet surface with very fast surface charge hopping to and from the three phase boundary (see Figure 9.2). The droplet symmetry allows us to ignore diffusion in both θ and ϕ co-ordinates so that transport in the droplet can be described by

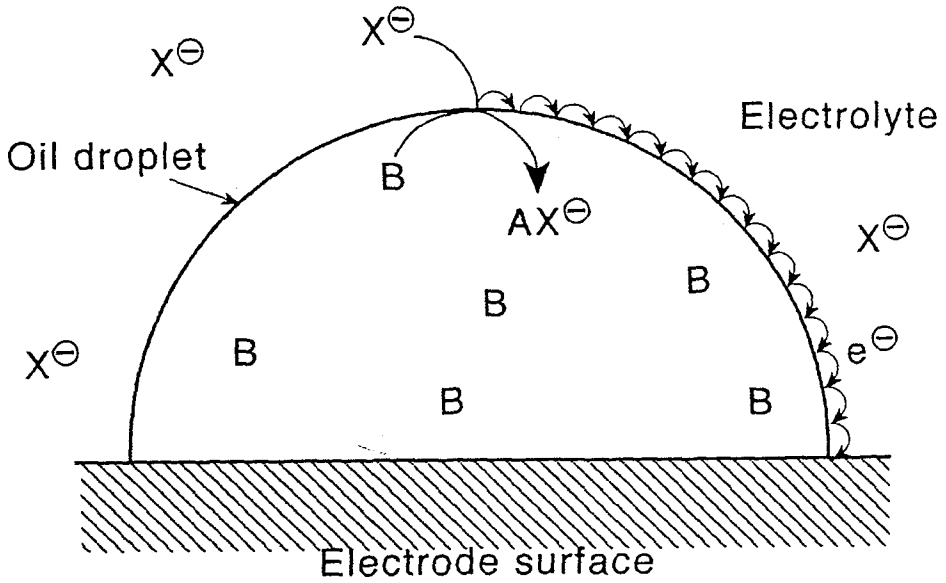


Figure 9.2 A schematic of Model 1: Charge injection at the droplet surface with fast electron migration to the electrode.

$$\frac{\partial a}{\partial t} = D\left(\frac{\partial^2 a}{\partial r^2} + \frac{2}{r}\frac{\partial a}{\partial r}\right) \tag{9.14.}$$

where D is derived from equation (9.2.):

$$D = D_{ideal}\left\{1 + \frac{d\ln\gamma_A}{d\ln a}\right\} \tag{9.15.}$$

Thus equation (9.14.) becomes

$$\frac{\partial a}{\partial t} = D_{ideal}\left\{1 - 2aZ(1-a)\right\}\left(\frac{\partial^2 a}{\partial r^2} + \frac{2}{r}\frac{\partial a}{\partial r}\right) \tag{9.16.}$$

More exactly the general form of the mass transport equation is:[18]

$$\frac{\partial[A]}{\partial t} + \frac{\partial J}{\partial r} + J\frac{\partial \ln A_s}{\partial r} = 0 \tag{9.17.}$$

where J is the flux, $[A]$ is the concentration of the diffusing species, r is the distance, t the time and A_s the surface area of the electrode which in spherical terms is $4\pi r^2$. Thus

$$\frac{\partial \ln A_s}{\partial r} = \frac{\partial}{\partial r}\left[\ln 4\pi + 2\ln r\right] = \frac{2}{r} \tag{9.18.}$$

hence equation (9.17.) becomes

$$\frac{\partial [A]}{\partial t} = -\frac{\partial J}{\partial r} - \frac{2}{r}J \tag{9.19.}$$

the flux is given equation (9.2.) derived from the activity coefficients. Thus equation (9.19.) becomes

$$\frac{\partial [A]}{\partial t} = D_{ideal}\left\{\frac{\partial}{\partial r}\left[1-2aZ(1-a)\right]\frac{\partial [A]}{\partial r} + \frac{2}{r}\left[1-2aZ(1-a)\right]\frac{\partial [A]}{\partial r}\right\} \tag{9.20.}$$

where a is the normalised concentration of species A. (9.20.) reduces to

$$\frac{\partial a}{\partial t} = D_{ideal}\left\{\left[1-2aZ(1-a)\right]\left(\frac{\partial^2 a}{\partial r^2} + \frac{2}{r}\frac{\partial a}{\partial r}\right) - 2Z(1-2a)\left(\frac{\partial a}{\partial r}\right)^2\right\} \tag{9.21.}$$

the derivative squared term may be ignored as it is very small. This then gives us equation (9.16.).

Equation (9.16.) is now turned into centralised finite differences for the transport at a time $t\Delta t$:

$$\frac{a_j^t - a_j^{t-1}}{\Delta t} = D_{ideal}\left\{1-2a_j^{t-1}Z\left(1-a_j^{t-1}\right)\right\}\left[\frac{a_{j+1}^t - 2a_j^t + a_{j-1}^t}{(\Delta r)^2} + \frac{2}{j\Delta r + x_d r_h}\frac{a_{j+1}^t - a_{j-1}^t}{2\Delta r}\right] \tag{9.22.}$$

where x_d is an '*inert*' fraction of the droplet at the centre not simulated (usually about 0.1%), r_h is the radius of the hemisphere, $\Delta r = r_h/NJ$ and NJ is the number of spatial points simulated. The superscript of a refers to which temporal point we are referring and the subscript to the corresponding spatial point. Thus a_j^t indicates the

dimensionless concentration at the point $r = j\Delta r$ and at a time $t\Delta t$. We introduce a spatial and temporal constant λ_j^t such that

$$\lambda_j^t = \frac{D\Delta t}{(\Delta r)^2} \tag{9.23.}$$

and consider two cases: (i) cyclic voltammetry and (ii) current-time transients resulting from a step from a potential at which no current flows to one which is considerably in excess of the potential needed to oxidise species *B*. The boundary conditions for the former case are:

$$0 < j < NJ \text{ and } t = 0 \quad a_j^0 = 0 \tag{9.24.}$$

$$t > 0 \text{ and } j = 1 \quad a_0^t = a_1^t \tag{9.25.}$$

$$t > 0 \text{ and } j = NJ - 1 \quad a_{NJ}^t = \left\{1 + \exp\left[Z\left(1 - 2a_{NJ}^{t-1}\right)\right]\exp(-\theta)\right\}^{-1} \tag{9.26.}$$

In these equations

$$E = E_i + v_s t\Delta t \tag{9.27.}$$

E_I is the initial voltage; v_s the scan rate and $t\Delta t$ the time. Equation (9.26.) is derived from the Regular Solution Theory version of the Nernst equations shown in (9.13.).[16] For the latter case the boundary condition in equation (9.26.) becomes

$$t > 0 \text{ and } j = NJ - 1 \quad a_{NJ}^t = 1 \tag{9.28.}$$

Equation (9.22.) becomes at $j = 1$ and $j = NJ$-1

$$a_1^{t-1} = \left(1 + \lambda_1^t\left(1 + \frac{\Delta r}{\Delta r + x_d r_h}\right)\right)a_1^t - \lambda_1^t\left(1 + \frac{\Delta r}{\Delta r + x_d r_h}\right)a_2^t \tag{9.29.}$$

and

$$\begin{aligned} a_{NJ-1}^{t-1} + \lambda_{NJ-1}^t\left(1 + \frac{\Delta r}{(NJ-1)\Delta r + x_d r_h}\right)\left(\frac{1}{1 + \exp\left(Z\left(1 - 2a_{NJ}^{t-1}\right)\right)\exp(-\theta)}\right) = \\ -\lambda_{NJ-1}^t\left(1 - \frac{\Delta r}{(NJ-1)\Delta r + x_d r_h}\right)a_{NJ-2}^t + \left(1 + 2\lambda_{NJ-1}^t\right)a_{NJ-1}^t \end{aligned} \tag{9.30.}$$

respectively. Equations (9.31.) and (9.30.) can be combined with the general point equation (9.22.) to give a tridiagonal matrix that may be solved using the Thomas Algorithm and the Time Dependent Backward Implicit (TDBI) method.

The current, I, at time at time $t\Delta t$ is calculated from the concentration gradient at the oil droplet surface:

$$I^t = 2F\pi r_h^{\,2} D[B]_{initial} \frac{\partial a}{\partial r}\Bigg)_{r=r_h} \tag{9.32.}$$

where F is the Faraday constant. In finite difference form

$$I^t = 2F\pi r_h^{\,2} D[B]_{initial} \left[\frac{a_{NJ}^t - a_{NJ-1}^t}{\Delta r}\right] \tag{9.33.}$$

An analytical expression for the potential step transient current has been derived[19] for the ideal case.

$$I^t = 2F\pi r_h D_{ideal}[B]_{initial} \sum_{m=1}^{\infty} \exp\left(-\frac{D_{ideal} m^2 \pi^2 t}{r_h^{\,2}}\right) \tag{9.34.}$$

This is compared below with the simulation results.

9.2.2.2. Model 2: The Three Phase Boundary Model

This model has been proposed by Lovrić and solved for transient diffusion in ideal solutions only using explicit digital simulations on a remarkably coarse grid.[20] This mechanism is similar to that postulated for the voltammetry of microcrystals on electrode surfaces.[21-23] The model

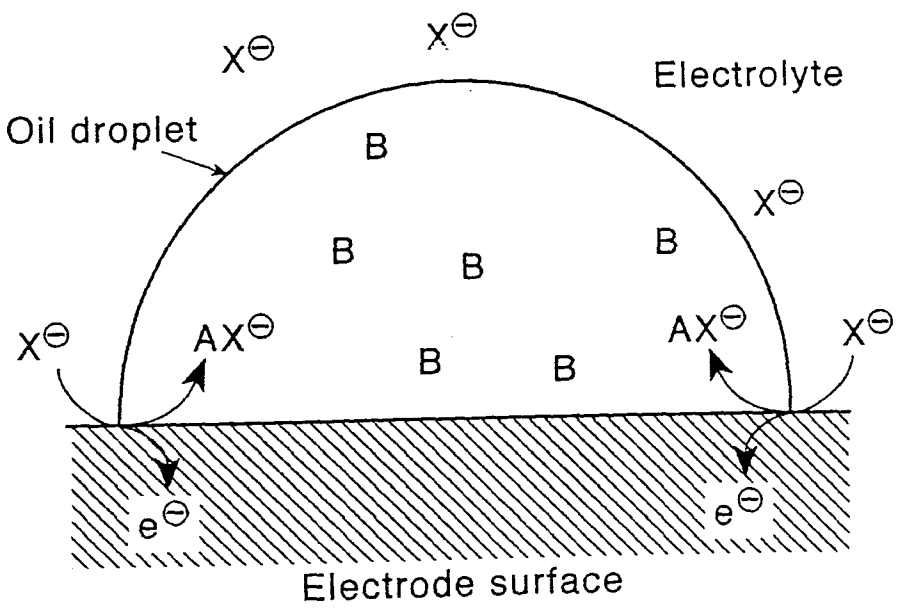


Figure 9.3 A schematic of Model 2: Charge injection electron transfer at the three phase boundary.

allows electron transfer only at the three phase boundary as shown in Figure 9.3. As before we may ignore the ϕ co-ordinate due to axial symmetry but the θ co-ordinate can no longer be neglected. Thus diffusion is given by

$$\frac{\partial a}{\partial t} = D\left(\frac{\partial^2 a}{\partial r^2} + \frac{2}{r}\frac{\partial a}{\partial r} + \frac{1}{r^2}\frac{\partial^2 a}{\partial \theta^2} + \frac{\cos\theta}{r^2 \sin\theta}\frac{\partial a}{\partial \theta}\right) \tag{9.35.}$$

We use a two dimensional finite grid in r and θ space (see Figure 9.4). The centralised finite difference equation has the form:

$$a_{j,k}^{t-1} = \alpha_{j,k} a_{j,k-1}^{t} + \beta_{j,k} a_{j-1,k}^{t} + \gamma_{j,k} a_{j,k}^{t} + \delta_{j,k} a_{j+1,k}^{t} + \varepsilon_{j,k} a_{j,k+1}^{t} \tag{9.36.}$$

which should be easily solved using SIP[13,14] which can be called from the NAG FORTRAN library.*

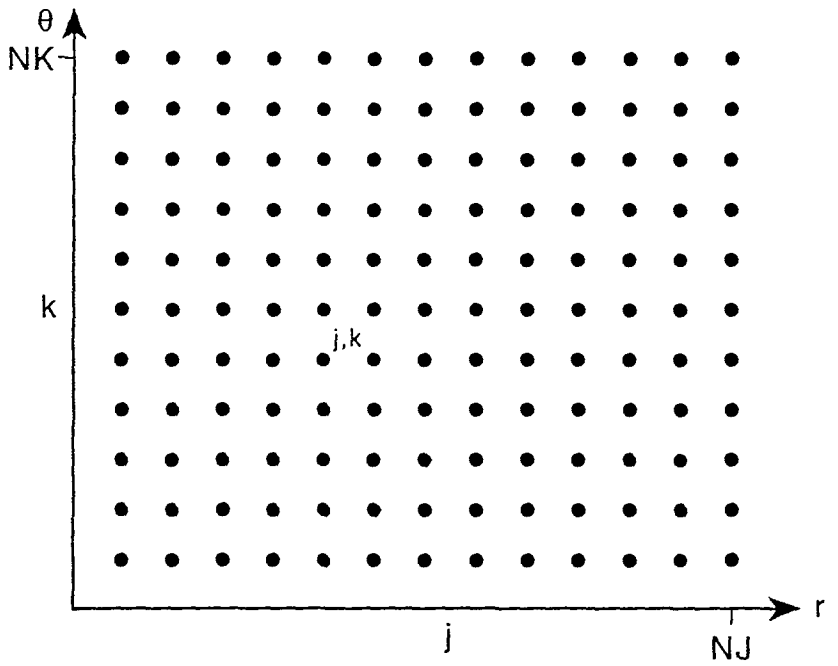


Figure 9.4 The two dimensional grid used in the SIP and MGD1 simulations with each point representing the concentration

The SIP constants are given by

$$\alpha_{j,k} = -\kappa_{j,k}^{t}\left(1 - \frac{\Delta\theta}{2}\cot(k\Delta\theta)\right)$$

$$\beta_{j,k} = -\lambda_{j,k}^{t}\left(1 - \frac{1}{j}\right) \tag{9.38.}$$

$$\gamma_{j,k} = 1 + 2\lambda_{j,k}^{t} + 2\kappa_{j,k}^{t} \tag{9.39.}$$

$$\delta_{j,k} = -\lambda_{j,k}^{t}\left(1 + \frac{1}{j}\right) \tag{9.40.}$$

$$\varepsilon_{j,k} = -\kappa_{j,k}^{t}\left(1 + \frac{\Delta\theta}{2}\cot(k\Delta\theta)\right) \tag{9.41.}$$

* NAG library routine: D03EBF

where $\lambda'_{j,k} = \frac{D\Delta t}{(\Delta r)^2}$, $\kappa'_{j,k} = \frac{D\Delta t}{(j\Delta r)^2(\Delta\theta)^2}$ and D is defined in equation (9.15.) as before. The boundary conditions for this model which apply to both the cyclic voltammetry and the transient problems are:

$$t = 0 \quad 1 \le j \le NJ-1, 1 \le k \le NK-1 \qquad a^0_{j,k} = 0 \tag{9.42.}$$

when t > 0

$$j = 1 \qquad 1 \le k \le NK-1 \qquad a^t_{0,k} = a^t_{1,k} \tag{9.43.}$$

$$k = NK-1 \qquad 1 \le j \le NJ-1 \qquad a^t_{j,NK} = a^t_{j,NK-1} \tag{9.44.}$$

$$j = NJ-1 \qquad 1 \le k \le NK-1 \qquad a^t_{NJ,k} = a^t_{NJ-1,k} \tag{9.45.}$$

$$k = 1 \qquad 1 \le j \le NJ-1 \qquad a^t_{j,0} = a^t_{j,1} \tag{9.46.}$$

At $j = NJ$-1 and $k = 1$ for the cyclic voltammetry simulations:

$$a^t_{NJ,0} = \left\{1 + \exp\left(Z\left(1 - 2a^{t-1}_{NJ,0}\right)\right)\exp(-\theta)\right\}^{-1} \tag{9.47.}$$

whilst for the transient simulations

$$a^t_{NJ,0} = 1 \tag{9.48.}$$

As the point (NJ,0) does not exist on the simulation grid it is incorporated by using the no-flux boundary conditions (9.45.) and (9.46.) such that

$$a^t_{NJ-1,0} = a^t_{NJ,1} = a^t_{NJ,0} \tag{9.49.}$$

The current is calculated by the change of moles per time step such that $I = F\frac{dn}{dt}$ where n is the number of moles of A in the droplet. The latter at the time $t\Delta t$, n^t, is calculated by the volume element method.[24]

$$n^t = [B]_{initial}\int_0^{2\pi}\int_0^{\frac{\pi}{2}}\int_0^{r_h} a^t(r,\theta,\phi)r^2\sin\theta dr d\theta d\phi \tag{9.50.}$$

which in finite difference formulation becomes

$$n^t = 2\pi[B]_{initial} \sum_{k=0}^{NK} \left\{ \sin(k\Delta\theta) \left[\sum_{j=0}^{NJ} a_{j,k}^t (j\Delta r)^2 \Delta r \right] \Delta\theta \right\} \qquad (9.51.)$$

The current at time $t\Delta t$ is given by

$$I^t = F \frac{n^t - n^{t-1}}{\Delta t} \qquad (9.52.)$$

9.2.2.3. Model 3: The Electrode Surface Model

In this model we assume that the oil droplet is saturated with electrolyte partitioned from the surrounding aqueous phase and electron transfer occurs at the electrode surface (see Figure 9.5). The extraction of the aqueous phase ions into the organic layer has been suggested by Anson and Shi.[25-27] This model is similar to that proposed by White and co-workers for the reduction of pure or very concentrated solutions of nitrobenzene.[28-30] The transport is as for the three phase boundary model and the boundary conditions are the same for equations (9.42.) to (9.45.) but equation (9.46.) becomes

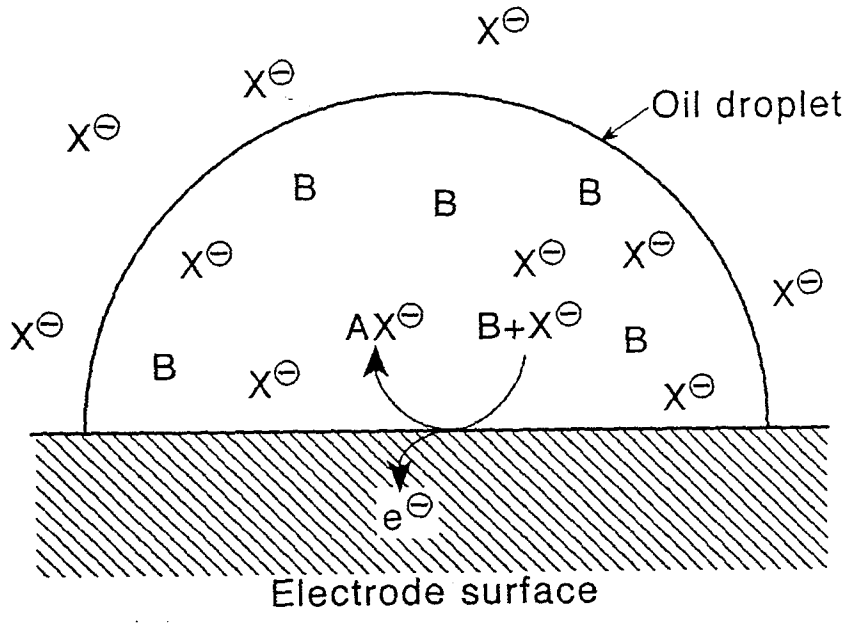


Figure 9.5 A schematic of Model 3: the oil droplet is saturated and electron transfer occurs at the electrode surface.

$$k = 1 \qquad 1 \le j \le NJ - 1 \qquad a_{j,0}^t = \left\{ 1 + \exp\left(Z\left(1 - 2a_{j,0}^{t-1} \right) \right) \exp(-\theta) \right\}^{-1} \qquad (9.53.)$$

for the cyclic voltammetry simulation and

$$k = 1 \qquad 1 \le j \le NJ - 1 \qquad a_{j,0}^t = 1 \qquad (9.54.)$$

for the transient simulation. The current is calculated in the same manner as the three phase boundary model.

9.2.3. Dual Reprocicity Method (DRM)

This was developed by Qiu Fulian to complement the finite difference methods described above. Using again the reaction in (9.1.) the time dependent mass transport equation is

$$D\nabla^2[A] = \frac{\partial[A]}{dt} \tag{9.55.}$$

where ∇^2 is the Laplace operator and D is the diffusion coefficient. The DRM expression for solving equation (9.55.) can be written as in equation (9.56.). More details of the method can be found elsewhere.[31-35]

$$HC - GQ = \left(H\hat{C} - G\hat{Q}\right)F^{-1}\frac{dC}{dt} \tag{9.56.}$$

In this expression G, H and F^{-1} are coefficient matrices depending upon the geometry of interest. C is the concentration and Q is the flux normal to the electrode surface. The $\hat{C}$ and $\hat{Q}$ matrices are both dependent on the distance only as detailed elsewhere.[34,35] For the DRM method, the flux Q is obtained directly rather than calculated indirectly via the concentration difference between two points along the diffusion direction. The expression for flux is given below:

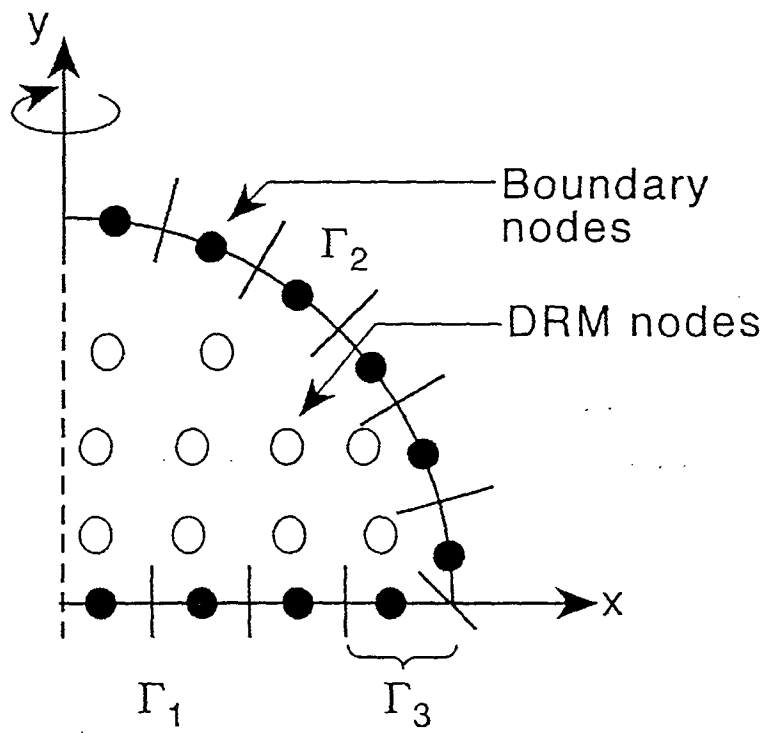


Figure 9.6 Schematic drawing of the grid geometry employed in the DRM simulation for the three mechanistic cases.

$$Q = \frac{IL}{nFCAD} \tag{9.57.}$$

Here I is the current, L is the normalising distance which is chosen as the hemisphere radius r_h, n is the number of electrons per reactant molecule, F is the Faraday constant and A the electrode area. Figure 9.2, Figure 9.3 and Figure 9.5 shows the models to be simulated as before. The boundary conditions are similar to those stated in § 9.2.2.1-9.2.2.3. and are applied, with reference to Figure 9.6,in the following manner:

Model 1: Γ_2 is electroactive

$$\begin{array}{lll} t \le 0 & \Gamma_1, \Gamma_2, \Gamma_3 & C = 1 \\ t > 0 & \Gamma_2 & C = 0 \text{ for chronoamperometry} \\ & & C = \dfrac{1}{(1+\exp(\theta))} \text{ for CV} \\ & \Gamma_1, \Gamma_3 & \dfrac{\partial C}{\partial y} = 0 \end{array} \tag{9.58.}$$

Model 2: Γ_3 is electroactive

$$\begin{array}{lll} t \le 0 & \Gamma_1, \Gamma_2, \Gamma_3 & C = 1 \\ t > 0 & \Gamma_3 & C = 0 \text{ for chronoamperometry} \\ & & C = \dfrac{1}{(1+\exp(\theta))} \text{ for CV} \\ & \Gamma_1, \Gamma_2 & \dfrac{\partial C}{\partial y} = 0 \end{array} \tag{9.59.}$$

Model 3: Γ_1 is electroactive

$$\begin{array}{lll} t \le 0 & \Gamma_1, \Gamma_2, \Gamma_3 & C = 1 \\ t > 0 & \Gamma_1 & C = 0 \text{ for chronoamperometry} \\ & & C = \dfrac{1}{(1+\exp(\theta))} \text{ for CV} \\ & \Gamma_2, \Gamma_3 & \dfrac{\partial C}{\partial y} = 0 \end{array} \tag{9.60.}$$

Efficient meshing was achieved by using 100 boundary element points and a 121 point uniform grid. For the case of model 2 Γ_3 was fixed to $0.0027 r_h$ with an

exponentially expanding grid of boundary nodes along the oil deposit | electrode interface.

9.2.4. Dimensionless Variables

To generalise the results from the simulations next the dimensionless variables are defined which parameterise the observed voltammetry. The mass transport in the general ideal ($Z = 0$) case, ignoring interactions, is given by

$$\frac{\partial a}{\partial t} = D_{ideal}\left[\frac{\partial^2 a}{\partial r^2} + \frac{2}{r}\frac{\partial a}{\partial r} + \frac{1}{r^2}\frac{\partial^2 a}{\partial \theta^2} + \frac{\cos\theta}{r^2 \sin\theta}\frac{\partial a}{\partial \theta} + \frac{1}{r^2 \sin^2\theta}\frac{\partial^2 a}{\partial \phi^2}\right] \qquad (9.61.)$$

Introducing $\xi = \frac{r}{r_h}$ and $\tau = \frac{D_{ideal}}{r_h^{\,2}}t$ equation (9.61.) becomes

$$\frac{\partial a}{\partial \tau} = \frac{\partial^2 a}{\partial \xi^2} + \frac{2}{\xi}\frac{\partial a}{\partial \xi} + \frac{1}{\xi^2}\frac{\partial^2 a}{\partial \theta^2} + \frac{\cos\theta}{\xi^2 \sin\theta}\frac{\partial a}{\partial \theta} + \frac{1}{\xi^2 \sin^2\theta}\frac{\partial^2 a}{\partial \phi^2} \qquad (9.62.)$$

For the peak current and peak to peak potentials on the cyclic voltammogram we consider the following

$$E = E_i + \nu_s t \qquad (9.63.)$$

which in dimensionless variables can be written

$$\widetilde{E} = \widetilde{E}_i + \widetilde{\nu}_s \tau \qquad (9.64.)$$

where $\widetilde{\nu}_s = \frac{F}{RT}\frac{r_h^{\,2}}{D_{ideal}}\nu_s$ and $\widetilde{E} = \frac{F}{RT}E$. It follows from (9.62.) and (9.64.) that

$$a = a\left(\xi, \tau, \widetilde{E}_i, \widetilde{\nu}_s\right) \qquad \text{and} \qquad \left.\frac{\partial a}{\partial \xi}\right)_{r=r_h} = f\left(\tau, \widetilde{E}_i, \widetilde{\nu}_s\right) \qquad (9.65.)$$

where f is some unknown function. The current is given by the concentration gradient at the surface of the drop for the surface model. We can then introduce dimensionless current, $\widetilde{I}$, such that

$$\frac{I}{2\pi r_h F D_{ideal}[B]_{initial}} = \tilde{I} = \frac{\partial a}{\partial \xi}\Big)_{\xi=1} = f\left(\tau, \tilde{E}_t, \tilde{\nu}_s\right) \qquad (9.66.)$$

The peak current is given by

$$\tilde{I}_p = \frac{\partial \tilde{I}}{\partial \tau} = 0 = f\left(\tilde{\nu}_s\right) \qquad (9.67.)$$

The corresponding peak separation

$$\tilde{E}_{p-p} = g\left(\tilde{\nu}_s\right) \qquad (9.68.)$$

where g is another unknown function. If Regular Solution Theory is incorporated then we expect both the peak current and separation also to be a function of Z so that

$$\tilde{I}_p = \tilde{I}_p\left(\tilde{\nu}_s, Z\right) \text{ and } \quad \tilde{E}_{p-p} = \tilde{E}_{p-p}\left(\tilde{\nu}_s, Z\right) \qquad (9.69.)$$

This result applies to all 3 models considered. In the case of the current-time transient

$$\tilde{I} = \tilde{I}\left(\tau\right) \qquad (9.70.)$$

where τ is dimensionless time and defined as

$$\tau = \frac{D_{ideal}}{r_h^{\,2}} t \qquad (9.71.)$$

9.3. Experimental

Reagents used in electrochemical experiments, KSCN (Aldrich), KCl (BDH) and $K_3Fe(CN)_6$ (BDH) were of analytical or the highest commercially available purity. The synthesis and purification of tetrahexylphenylenediamine (THPD) has been reported.[2] Water was taken from an Elgastat filter system (Elga, High Wycombe, UK) with a resistivity of not less than 18 MΩ cm. Electrochemical experiments were conducted in a conventional three-electrode cell with a 4.9 mm diameter basal plane pyrolytic graphite working electrode, a gold or platinum wire counter electrode and a Saturated Calomel (SCE, Radiometer, Kopenhagen) reference electrode. A

commercial potentiostat (Autolab PGSTAT 20, Ecochemie, Netherlands) and an Oxford Electrodes Potentiostat connected to a Lloyd PL3 chart recorder (Lloyd Instruments, Southampton) were used for cyclic voltammetric experiments. The procedure for the deposition of THPD micro-droplets on the surface of the basal plane pyrolytic graphite electrode was based on evaporation of appropriate amounts of a solution of 1 mM THPD in acetonitrile (dried and distilled, Fischer Scientific Limited). Solutions were degassed with argon (Pureshield, BOC, Guildford) for at least 15 minutes prior to experiments. All studies were carried out at a temperature of 20 ± 2 °C. RAM™ electrodes[37] with random arrays of *ca.* 584 carbon fibre microelectrodes of 7 μm diameter (calibrated electrochemically using 2 mM Ferricyanide in 0.1M KCl(*aq.*)) and a total surface area of 0.25 cm^2 were kindly provided by S. Fletcher and M. Horne (CSIRO, Division of Minerals, Clayton VIC 3169, Australia).

Analysis of the electrode surface topography by AFM (atomic force microscopy) was carried out using a TopoMetrix TMX 2010 Discoverer system in the contact mode (typically 3 Hz scan rate) with TopoMetrix standard AFM probes (no. 5200).

Numerical simulations (see §9.2.2.1) were conducted using parameters as follows: $D_{ideal} = 10^{-5}$ cm^2s^{-1}; $[B]_{initial} = 55$ M (the concentration of pure water); $E^0 = 0.0$ V; $NJ = 1000$ and $\Delta t = 1$ ms. The values of NJ and Δt were set such that the solutions were converged to within 1% in all cases. All programs were written in FORTRAN or C and executed on a Silicon Graphics Origin™ 2000 12 processor server. Computation time ranged from less than a minute to 3 minutes for the cyclic voltammograms. Data analysis was completed using Excel 2000 and IDL 5.0.

9.4. Results and Discussion

9.4.1. Theoretical

9.4.1.1. DRM Results

In Figure 9.7 simulated linear sweep voltammograms for all three mechanistic cases, 1, 2, and 3 in Figure 9.2, Figure 9.3 and Figure 9.5 respectively, at the low scan rate limit are shown. It can be seen that for the three cases identical linear sweep voltammograms of Gaussian shape are obtained with a width at half height of 91 mV (at 298 K) in close agreement with the analytical solution. [38] This behaviour can be rationalised in terms of complete conversion to the product during the time scale of the potential sweep so that no effect of mass transport or geometry is evident. In Figure 9.8 simulated linear sweep voltammograms for the three mechanistic cases are shown at a faster scan rate. Unlike for the case of slow scan rates three distinct types of voltammograms can be observed. For the mechanistic case 1 a

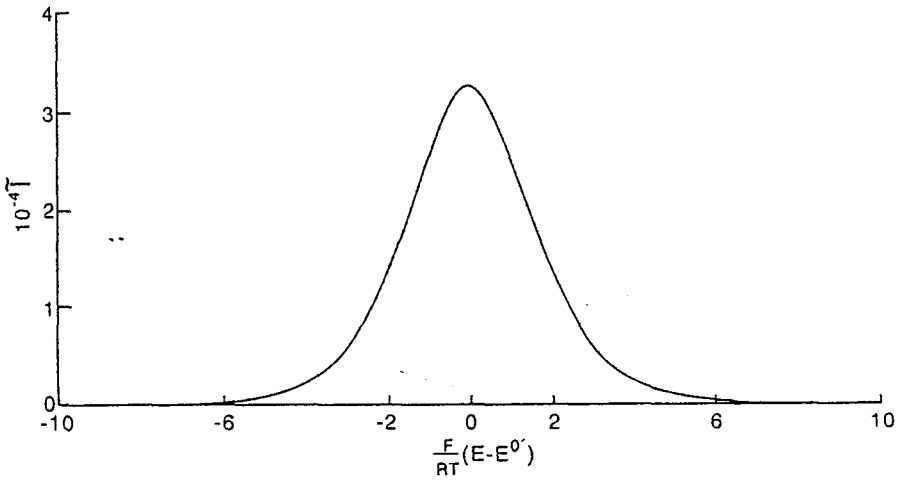


Figure 9.7 Superimposed linear sweep voltammograms for the three mechanistic models for electrochemical processes in droplet deposits on electrode surfaces using a dimensionless scan rate of 3.9×10^{-3} (slow scan rate limit).

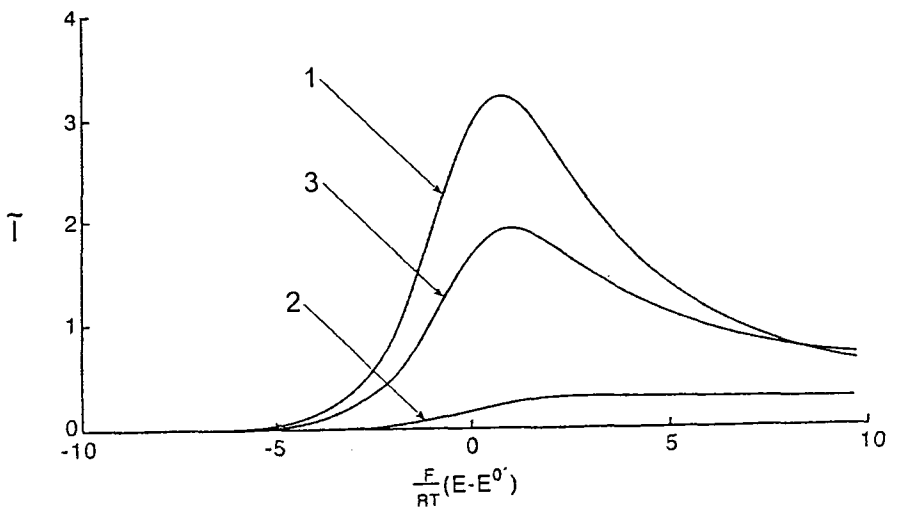


Figure 9.8 Superimposed linear sweep voltammograms for the three mechanistic models for electrochemical processes in droplet deposits on electrode surfaces using a dimensionless scan rate of 78 (intermediate case).

relatively high peak current with a more rapid current decay is observed in agreement with a high electroactive surface area causing rapid conversion. At the same scan rate the voltammogram for the mechanistic case 3 (reaction commencing from the oil | electrode interface) gives a slightly higher peak potential and also gives rise to a considerably lower peak current. A factor of 2 between peak currents for comparing model 3 and 1 may be predicted for the purely diffusion controlled case (ratio of areas) but under conditions simulated here, curve 1 already deviates partly from diffusion control. At sufficiently fast scan rates it is expected that for models 3 and 1 the diffusion layers are nearly identical to the one dimensional diffusion case. The result for model 2 suggests an entirely different behaviour (Figure 9.8). A sigmoidally shaped quasi steady state voltammogram is obtained similar to the standard voltammetric response expected for a microring or band electrode, consistent with diffusion from the edge of the droplet into the bulk.

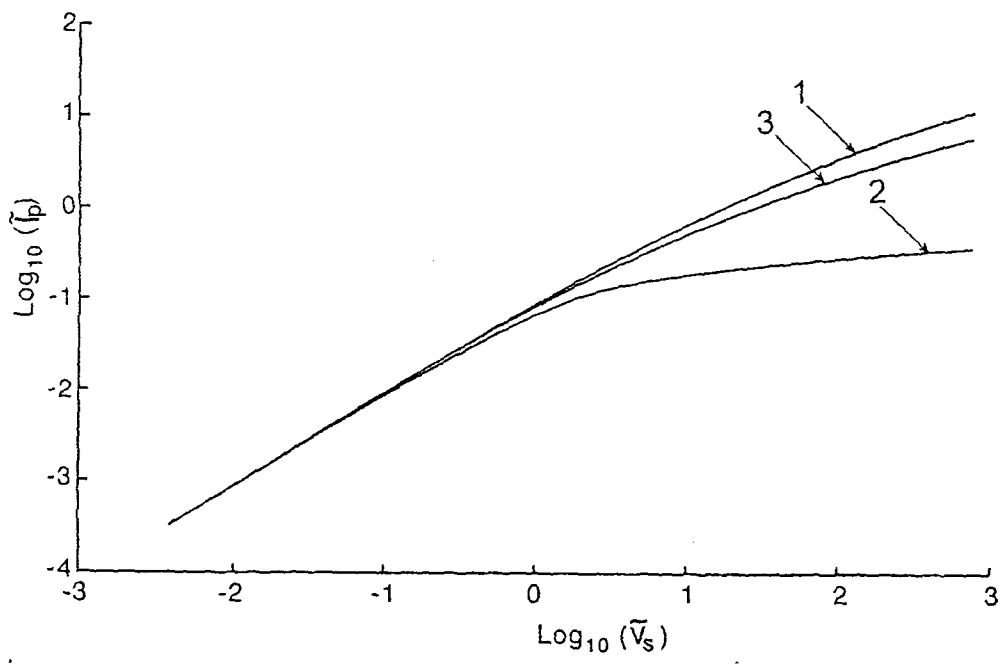


Figure 9.9 Plot of the dimensionless normalised peak current as a function of the dimensionless scan rate for the three models considered.

Next linear sweep voltammograms were simulated for a range of different scan rates. Figure 9.9 shows a plot of the dimensionless peaks currents for models 3, 1, and 2 as a function of dimensionless scan rate. It can be seen that the peak currents, $\log(j_p)$, vary linearly with the dimensionless scan rate, $\log(\tilde{v}_s)$, and the expected slope of 1.0 at

slow scan rate (thin film behaviour) can be observed for all three models. As the scan rate increases different types of behaviour were observed for the three models. The peak currents for models 3 and 1 increase in proportion to the square root of scan rate (slope = 0.5) at the fast scan rate limit and the ratio of the peak currents is 2.0 as predicted. For the normalised peak current in model 2 convergence towards scan rate independent behaviour can be seen which is similar to the case when a microband electrode is employed for conventional voltammetry. The situation corresponds to that of a quasi steady state.

In Figure 9.10 the separations between the peak potential, E_p, and the formal potential, $E^{o'}$, as a function of dimensionless scan rate for the three mechanistic cases are compared. Sigmoidal behaviour was obtained for all three cases with the anticipated zero separation at very slow scan rates (compare Figure 9.7). The peak separation increases slowly as the scan rate increases and gradually converges towards a constant value at faster scan rate. The magnitude of the peak to peak separation in a cyclic voltammogram with forward and back scan, corresponding to twice the separation of E_p and $E^{o'}$, is consistent with the geometric constraints of the distinct mechanistic models. For model 3 *planar* diffusion occurs and the expected 56 mV peak to peak separation (at 298 K) is observed at sufficiently high scan rates. The hemispherical model 1, which has a more

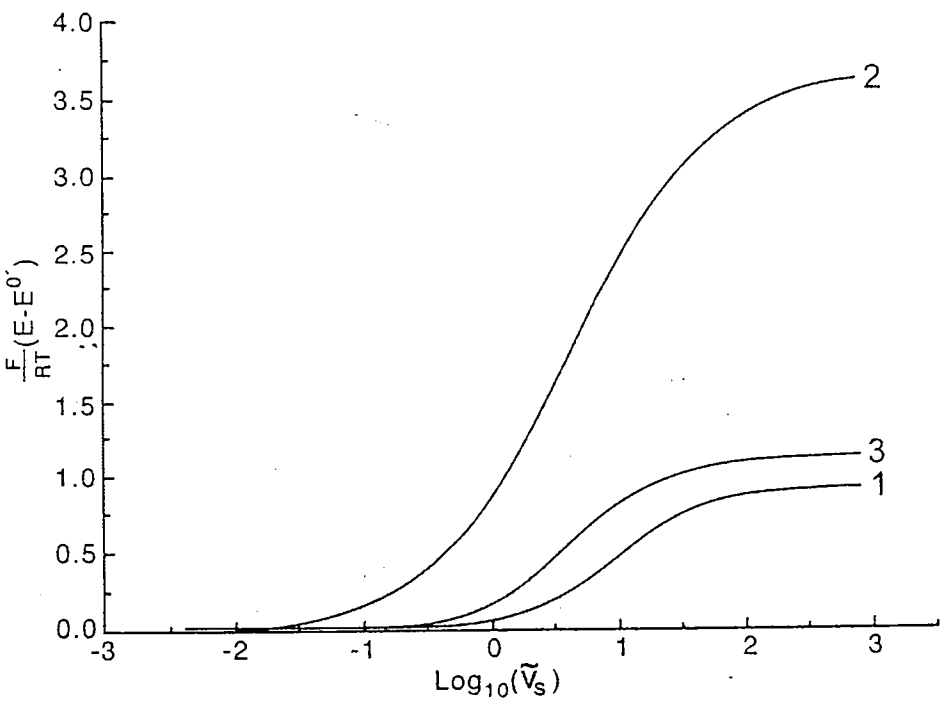


Figure 9.10 Plot of the separation between peak potential and formal potential as a function of dimensionless scan rate.

'concave' diffusion field, in contrast gives rise to a smaller peak to peak separation converging towards *ca.* 49 mV (at 298 K). The reason for this effect is a faster depletion of the solution phase of reactant due to the 'concave' geometry. For the 'convex' three phase boundary model, 2, the peak to peak separation can be seen to converge towards *ca.* 140 mV (at 298 K). For faster scan rates outside the range considered here the peak to peak separation for all three models is expected to converge to 56 mV (at 298 K).

Finally, transient chronoamperometric current responses were simulated for all three mechanistic cases. Figure 9.11 shows dimensionless transient currents as a function of dimensionless time. The fastest conversion of the oil droplet was simulated based on model 1 with a large hemispherical electroactive area. As expected the slowest conversion occurs for model 2, the three phase boundary model, and the quasi steady state nature of the response is apparent.

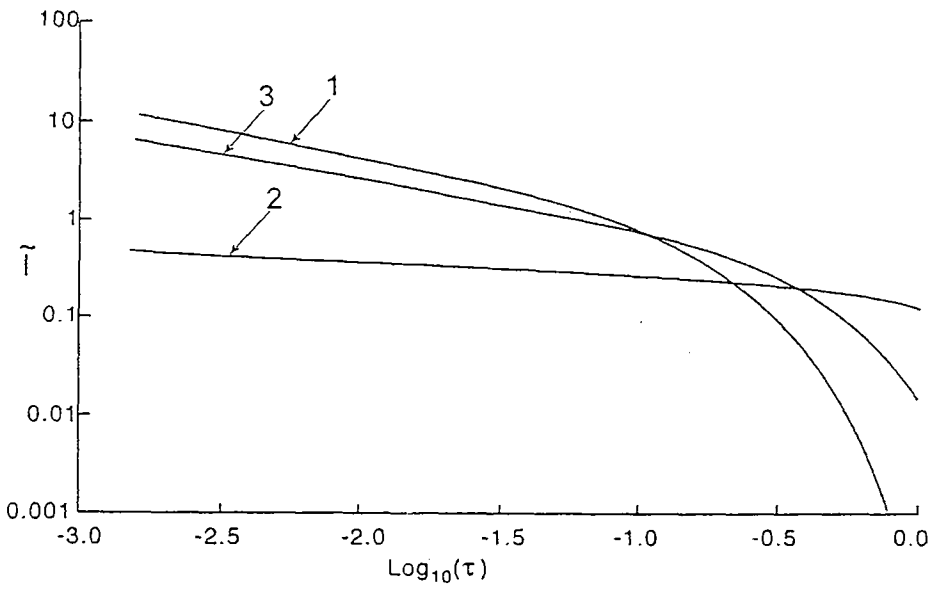


Figure 9.11 Plot of the dimensionless transient current response as a function of dimensionless time.

9.4.1.2. Failure of SIP and MGD1

In the previous section the results for Models 2 and 3 were calculated using the DRM method. The results for Model 1 were calculated using the BI method described in §9.2.2.1 and found to be in agreement with the DRM results. The results obtained using SIP were found to accurate at low scan rates for both models 2 and 3 but deviated greatly at high scan rates. This is attributed to the failure of SIP (documented

in the NAG manuals) due to disparate nature of the matrix coefficients at the faster scan rates causing convergence not to be obtained. To improve the ability of the SIP routine to attain convergence a much larger number of time nodes would be required causing extremely computationally intense simulations. As the DRM method solved these models in a comparatively shorter time this was considered to be an inefficient use of CPU. To increase the computational efficiency the Multigrid method (MGD1) was implemented but this also failed at all scan rates due the diagonal dependence of the coordinate transformation discussed in §3.7.

9.4.1.3. Limitations of DRM

It is not possible to incorporate regular solution theory into the DRM calculations as it is with the point simulations. Fortunately this is of no major consequence as the DRM solutions shows that for experimental scan rates the current response of the same order and shape for all models. This allows the next section to approximately model the voltammograms obtained by experiment using model 1 and the BI method with regular solution theory incorporated.

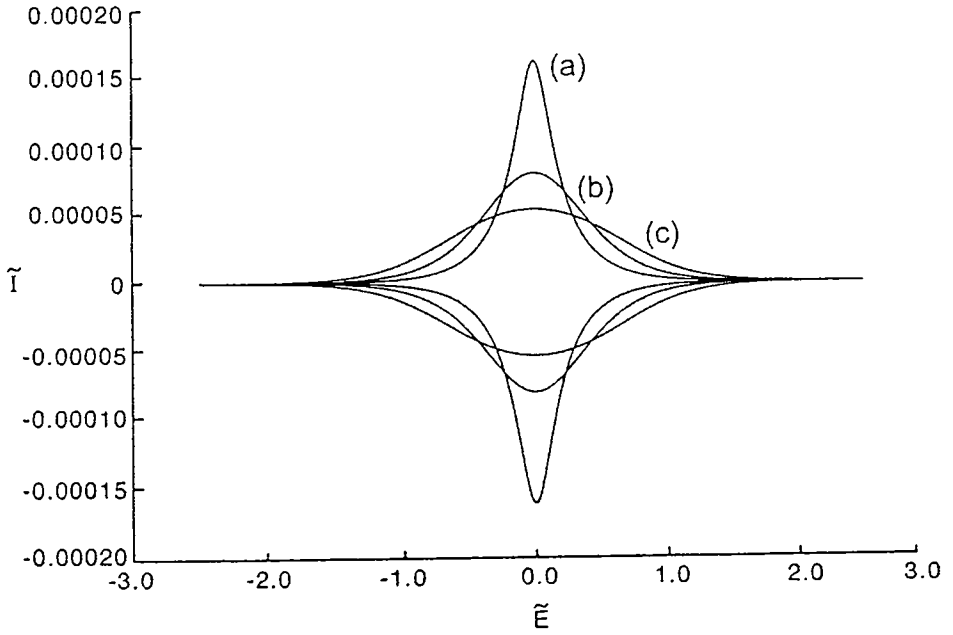


Figure 9.12 Cyclic voltammograms simulated for ν_s = 1 mVs^{-1}, r_h = 5 μm, for (a) Z = 1, (b) Z=0, and (c) Z=-1.

9.4.1.4. BI and Regular Solution Theory

Figure 9.12 shows three cyclic voltammograms simulated for the scan rate $\log_{10}(\tilde{v}_s) = -3.01$ corresponding to $v_s = 1$ mVs^{-1} and $r_h = 5$ μm. Highly symmetric responses are simulated as anticipated for 'thin layer' behaviour without any effect of mass transport. For the repulsive interaction ($Z > 0$) much sharper peaks compared to those in the ideal case are observed and correspondingly for the attractive interactions ($Z < 0$) much broader responses are found.

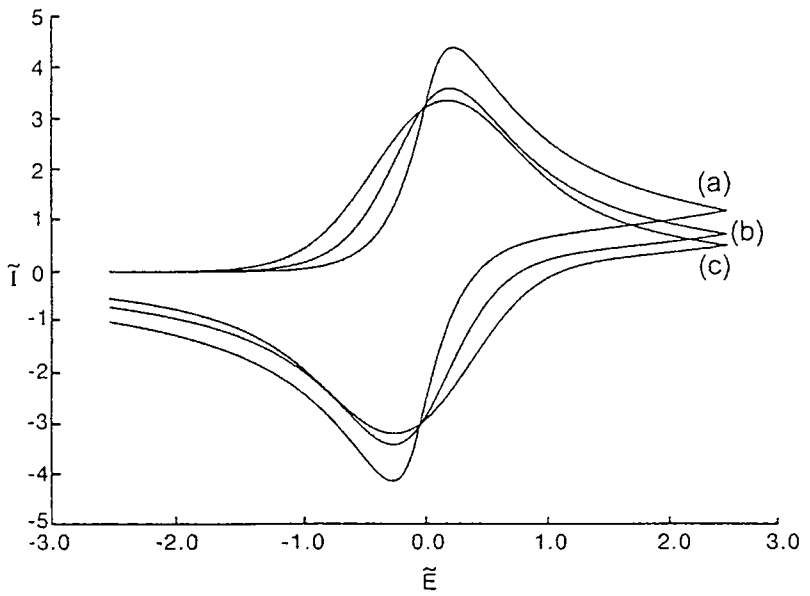
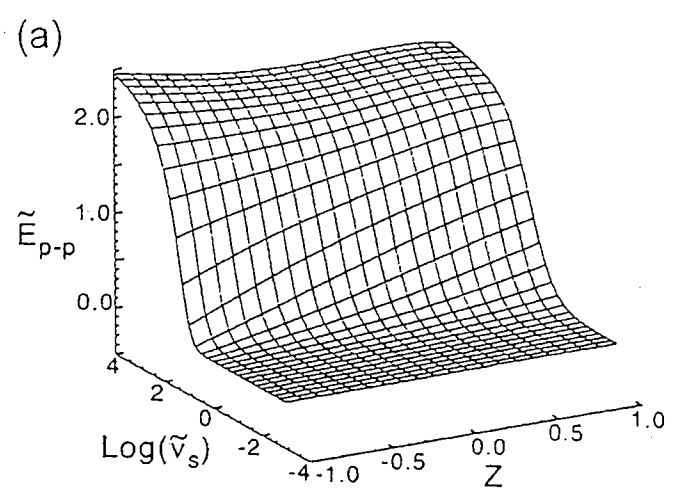


Figure 9.13 Cyclic voltammograms simulated for $v_s = 10$ Vs^{-1}, $r_h = 5$ μm, for (a) $Z = 1$, (b) $Z=0$, and (c) $Z=-1$.

Figure 9.13 shows similar voltammograms simulated for the fast scan rate limit ($\log_{10}(\tilde{v}_s) = 0.998$, corresponding to $v_s = 10$ Vs^{-1} and $r_h = 5$ μm). The dependence on Z shows that the repulsive interactions lead to a sharper peak and the attractive interactions lead to much broader voltammograms compared to those for the ideal case. Figure 9.14(a) shows a 3-dimensional working surface of $\tilde{E}_{p-p}$ against $\tilde{v}_s$ for various parameters Z. As expected, the peak separation reaches a limiting value at high $\tilde{v}_s$ and is zero for low $\tilde{v}_s$. For the case of $Z = 0$ the limiting value is found to be $2.218\frac{RT}{F}$ which is the value expected for reversible cyclic voltammetry under transport controlled conditions.[36] However, for deviations to higher limiting $\tilde{E}_{p-p}$ are found for $Z < 0$ and the limit of $\tilde{E}_{p-p}$ at high scan rates becomes smaller for $Z > 0$. Figure 9.14(b) shows the working surface for $\tilde{I}_p$ against

$\tilde{\nu}_s$ and Z. For positive Z values, corresponding to repulsive interactions, the peak height is bigger as would be expected under ideal conditions. The converse is true for attractive Z values ($Z < 0$). However, the characteristic dependence of $I_p \propto \nu^{1/2}$ at sufficiently fast scan rates remains valid even for $Z \neq 0$.



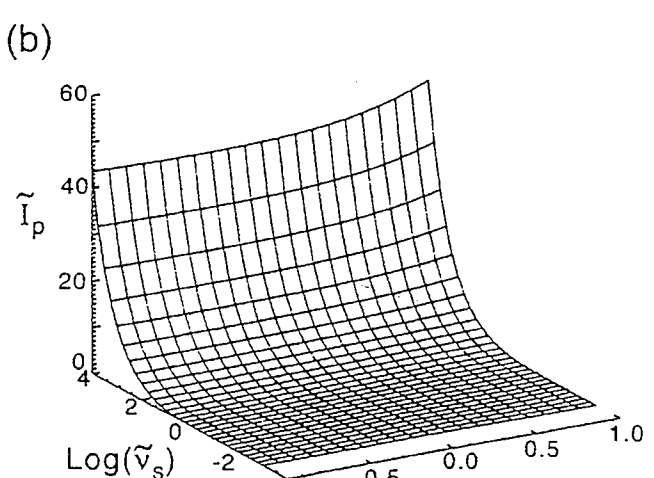


Figure 9.14 Working surfaces for (a) $\tilde{E}_{p-p}$ and (b) $\tilde{I}_p$ as a function of scan rate, $\tilde{\nu}_s$, and Z for the regular solution case.

Next we consider the simulations relating to current-time transients. Figure 9.15 is a dimensionless transient response for the ideal case which fits all parameters and can be simulated for all values of Z. The results in Figure 9.15 were verified against the analytical theory expression, (9.34.), to check the correctness of the simulation and was found to be within 1% for the total transient simulated.

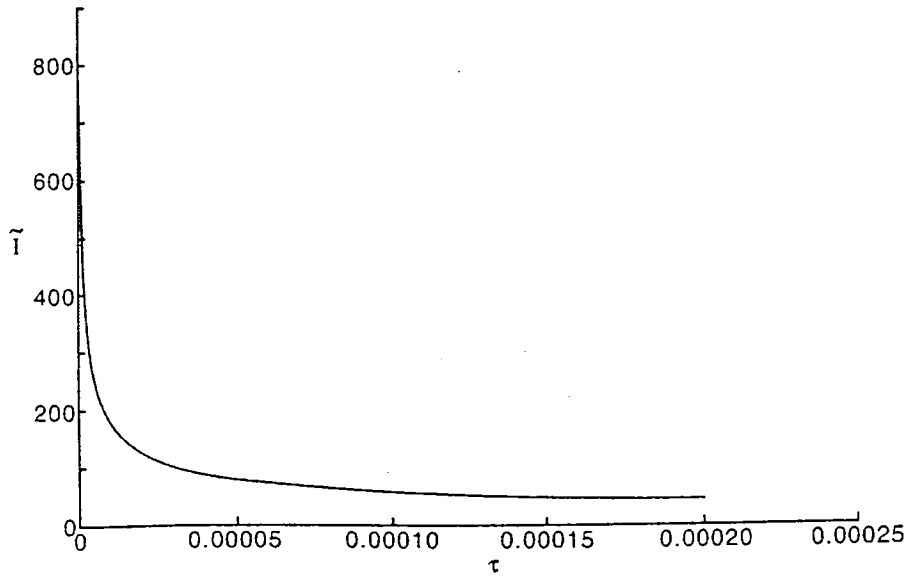


Figure 9.15 Dimensionless current time transient response for the ideal case (Model 1) with the analytical solution overlaid perfectly.

Experimental

9.4.2.1. Electrochemically Induced Anion Insertion in Tetrahexylphenylenediamine

It was reported earlier[1] that the electro-insertion of thiocyanate anions into tetrahexylphenylenediamine (THPD) led to the formation of a stable ionic liquid [$THPD^+SCN^-$]. Figure 9.16(a) shows cyclic voltammograms for the oxidation of 5.3 nmols of THPD deposited on the surface of a 4.9 mm diameter basal plane pyrolytic graphite electrode and immersed in aqueous 0.1 M KSCN. Seven consecutive cycles with a scan rate of 0.1 Vs^{-1} are shown and it can be seen that the voltammetric behaviour is stable after the first cycle.

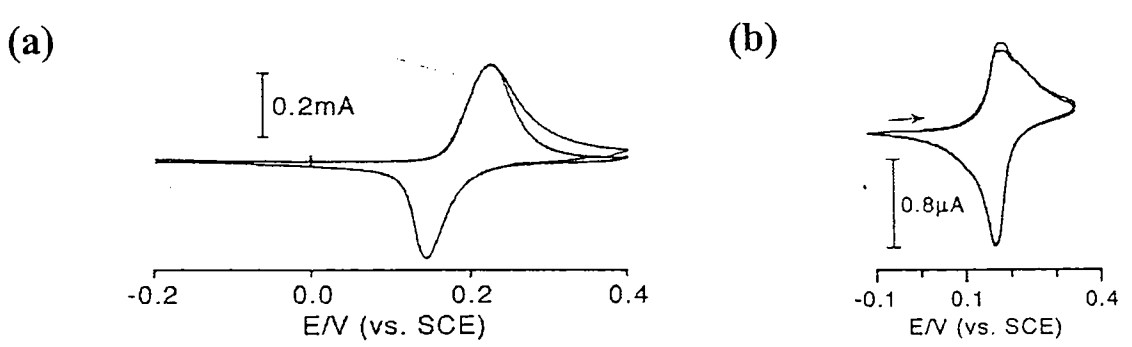


Figure 9.16 (a) Cyclic voltammograms (seven consecutive cycles, scan rate 100 mV s^{-1}) for the oxidation of 5.3 nmoles THPD deposited onto a 4.9 mm diameter basal plane pyrolytic graphite electrode and immersed in 0.1 M KSCN. (b) Cyclic voltammograms (5 consecutive cycles, scan rate 100 mV s^{-1}) recorded with a RAM™ electrode with 40 nmoles THPD deposited on an array of 584 individual 7 μm diameter glassy carbon microdisc electrodes immersed in 0.1 M KSCN.

The degree of conversion of THPD to [$THPD^+SCN^-$] can be shown to be strongly affected by both the scan rate and the coverage of the electrode surface. For sufficiently slow scan rates of *ca.* 1 mV s^{-1} and a small amount of THPD deposited on the electrode surface, *ca.* 10 nmoles or 4.5 μg, the theoretically expected amount of charge is associated with oxidation and re-reduction of the organic liquid. Based on this slow scan electrolysis experiment as well as on ESR evidence[2] the overall mechanism for the oxidation process may be expressed as in equation (9.72)

$$THPD(oil) + SCN^-(aq.) \rightarrow [THPD^+SCN^-](oil) + e^- \qquad (9.72)$$

Further proof for this mechanism comes from experiments in which the concentration of the aqueous electrolyte is varied. Based on equation (9.72) the Nernst equation for the redox system [$THPD^+SCN^-$]/THPD can be written (equation (9.73.)).

$$E = E^{o\,\prime} - \frac{RT}{F}\ln\left[\frac{a\{THPD^+(oil)\}\;\; a\{SCN^-(oil)\}}{a\{THPD(oil)\}}\right] + \frac{RT}{F}\ln[a\{SCN^-(aq.)\}] \qquad (9.73.)$$

Based on this equation a shift in the reversible potential, $E_{mid} = (E_p^{ox} + E_p^{red})/2$, of 59 mV per decade change in the $a\{SCN^-(aq.)\}$ can be expected. The experimental value of 55 mV obtained over a concentration range from 10 mM to 1.0 M SCN^- is in close agreement and consistent with equation (9.73.).

In order to test the contribution that anion diffusion in the aqueous phase makes to the overall transport process, rotating disc experiments were conducted for the oxidation of THPD deposited on basal plane pyrolytic graphite electrodes and immersed in aqueous solutions of KSCN of various ionic strengths. The concentration of SCN^- was varied from 1 M to 10 mM and experiments conducted for 1 – 30 Hz. Consistent with results obtained in the presence of ClO_4^- anions,[2] no significant change in the shape of the cyclic voltammograms upon rotating the electrode was detected in all cases. Therefore diffusion of SCN^- anions in the aqueous phase can be ruled out as a limiting factor in the mass transport process accompanying the oxidation and re-reduction of THPD.

In Figure 9.16(b) five consecutive voltammograms for the oxidation of 40 nmoles of THPD deposited onto a Random Array of Microelectrodes (RAM^{TM})[37] is shown. The deposition procedure causes the 7 μm diameter carbon microelectrodes to be partially covered with the organic oil and a process consistent with that observed on the basal plane pyrolytic graphite is detected. Again after the initial potential cycle the voltammetric response remains stable. Although an even distribution of material over

all 584 electrodes is unlikely and exhaustive electrolysis is not achieved at a scan rate of 100 mV s^{-1} (see Figure 9.16(b)), integration of the current response allows an average thickness of the THPD film on the microelectrodes of *ca.* 0.25 μm to be estimated. The magnitude of the peak current, $I_p = 0.8$ μA, remains considerably lower than $I_{lim} = (584 \times 4)nFDr_e[SCN^-(aq.)] = 80$ μA, the hypothetical limiting current expected for the case that diffusion of anions in the solution phase is rate determining. That is, in agreement with results from the rotating disc electrode experiment diffusion in the aqueous solution can be judged to have no significant effect on the voltammetric response for the electrochemically driven oil droplet oxidation process.

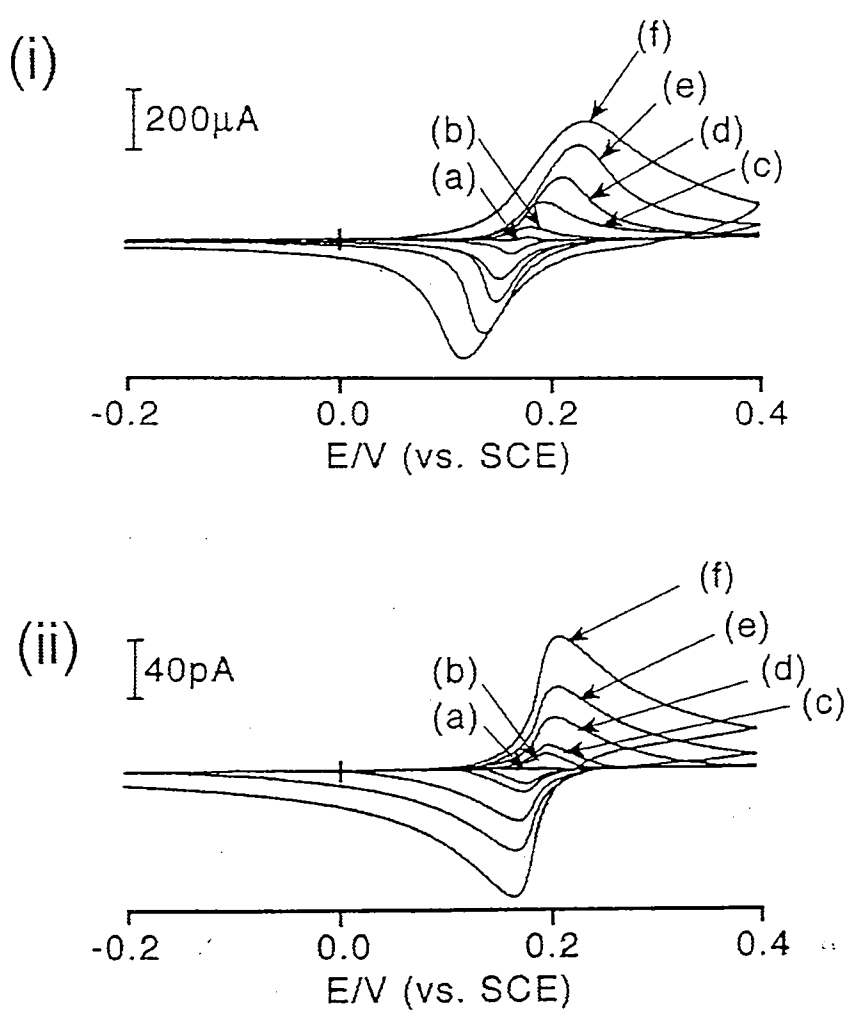


Figure 9.17 (i) Cyclic voltammograms for the oxidation of 10.6 nmoles THPD deposited onto a 4.9 mm diameter basal plane pyrolytic graphite electrode and immersed in 0.1 M KSCN recorded with a scan rate of (a) 1 mVs^{-1}, (b) 9 mVs^{-1}, (c) 25 mVs^{-1}, (d) 49 mVs^{-1}, (e) 100 mVs^{-1}, (f) 225 mVs^{-1}. (ii) Simulation based on model B with $Z = 1.39$, $r_h = 0.5$ μm, $D_{ideal} = 1.0 \times 10^{-5}$ cm^2s^{-1}, and conditions equivalent to those used in (i).

It is interesting to study the effect of scan rate on the peak current of experimental voltammograms in order to gain insight into the details of the mass transport in the microdroplet deposit. Figure 9.17(i) shows a set of experimental cyclic voltammograms for the oxidation of 10.6 nmols of THPD deposited onto a basal plane pyrolytic graphite electrode and immersed in aqueous 0.1 M KSCN.

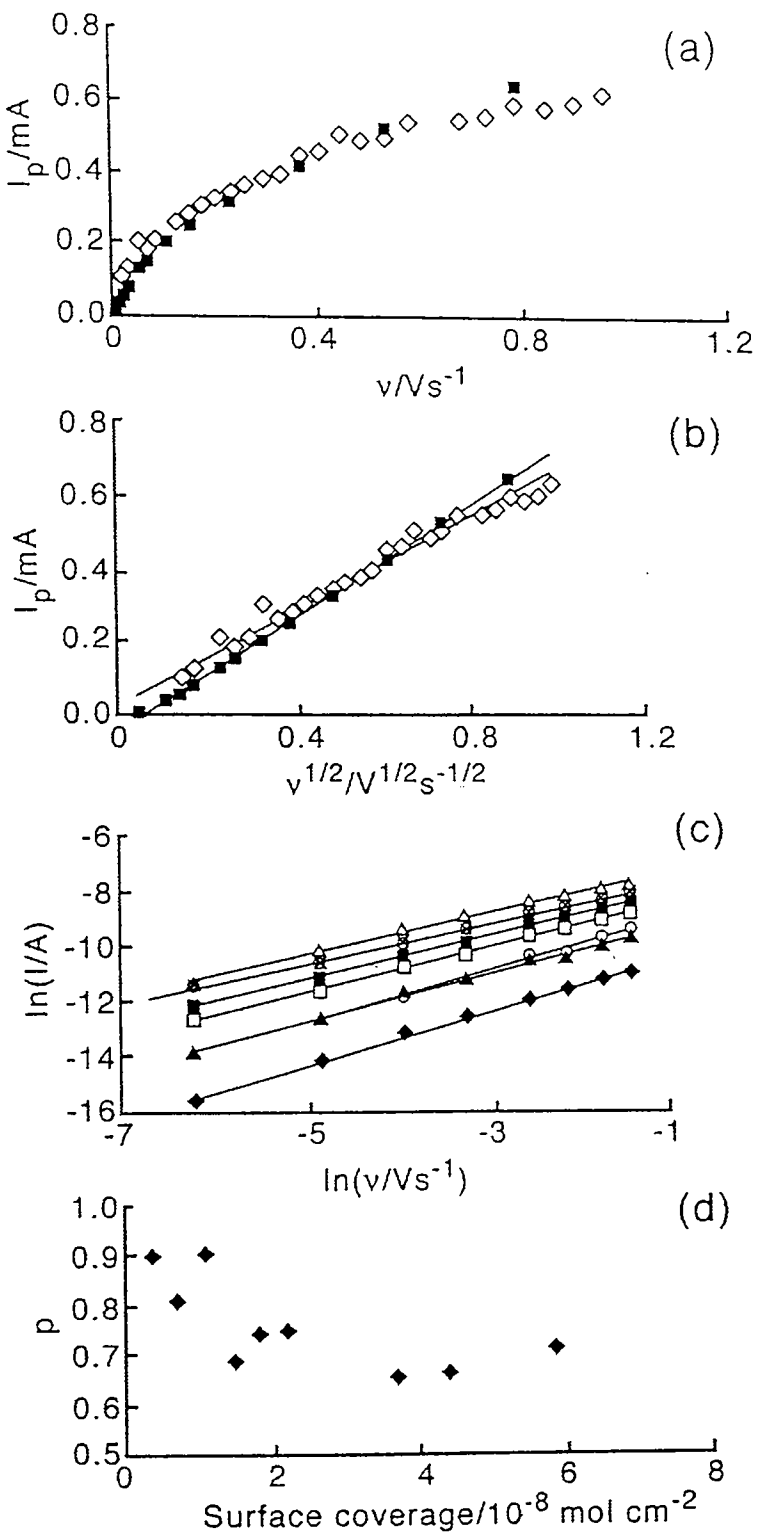


Figure 9.18 Voltammetric data for the oxidation of THPD deposited onto a 4.9 mm diameter basal plane pyrolytic graphite electrode and immersed in 0.1 M KSCN. (a) Peak current for the oxidation of 10.6 nmoles THPD as a function of scan rate (open squares: experimental, filled squares: simulation). (b) Peak current for the oxidation of 10.6 nmoles THPD as a function of square root scan rate (open squares: experimental, filled squares: simulation). (c) Plot of the natural logarithm of the peak current versus logarithm of the scan rate for various amounts of deposit. (d) The slope, p, of graphs given in (c) as a function of surface coverage.

Increasing the scan rate causes the peak current to increase and the dependence of the peak current on the scan rate allows conclusions to be drawn concerning the ease of transport in the micro-droplet deposit. For very fast mass transport there will be only a minor perturbation from equilibrium and therefore no effect of mass transport on the shape of the voltammetric peak. Under these conditions the area under the peak and the peak current show a linear dependence on scan rate, $I_p \propto \nu$. For the case of slow mass transport the electrolysis of the deposit is not complete and mass transport effects dominate the shape of the voltammogram. For the case of diffusion control the expected characteristic is $I_p \propto \nu^{1/2}$. In Figure 9.18 experimental peak currents for the oxidation of 10.6 nmoles of THPD deposited onto a basal plane pyrolytic graphite electrode have been plotted (open squares) versus scan rate. It can be seen that over a

wide range of scan rates a $I_p \propto \nu^{1/2}$ dependence is obeyed and therefore mass transport in the droplet strongly affects the process.

By plotting the logarithm of the peak current versus the logarithm of the scan rate the two cases of fast and slow mass transport as well as intermediate cases can be distinguished. In Figure 9.18(d) data for a wide range of electrode coverage is plotted and it can be seen that the slope of the individual plots varies. A trend strongly indicating mass transport effects for high coverage and nearly thin layer behaviour, $I_p \propto \nu$, for low coverage can be seen. This is not surprising because the average size of the droplet deposit will increase at higher coverage. This kind of transition is therefore dependent on the droplet size as well as the scan rate and may be used as a experimental observation for the comparison of experimental with simulation data.

In the approach to numerical simulation of cyclic voltammetric data used here it is recognised that the interactions between ionic and neutral forms of THPD are unlikely to be ideal. Therefore a model based on regular solution theory (see §9.2.2.1) is employed to account for the effects of non-ideality in terms of an interaction parameter Z.

9.4.2.2. The Low Scan Rate Limit: Matching the Interaction Parameter Z

In order to stepwise solve this simulation problem (see §9.2.2.1) parameters such as the average droplet radius, r_h, the interaction parameter, Z, the diffusion coefficient, D_{ideal}, and reversible potential, $E^{o'}$, have to be determined consecutively. In the slow scan rate limit and for the case of a low coverage of the electrode with the THPD deposit the effect of mass transport can be minimised and the experimental voltammogram essentially yields only thermodynamic information. In this case there is no difference between the three theoretical models (Figure 9.2, Figure 9.3 and

Figure 9.5). An experimental and a simulated voltammogram are shown in Figure 9.19.

It can be seen that the interaction parameter Z has a considerable effect on the shape of the simulated voltammogram. An increase in this parameter causes the interaction of the product-product (B-B) and starting material-starting material (A-A) type to dominate over the product-starting material (A-B) *i.e.* 'repulsive' interaction.

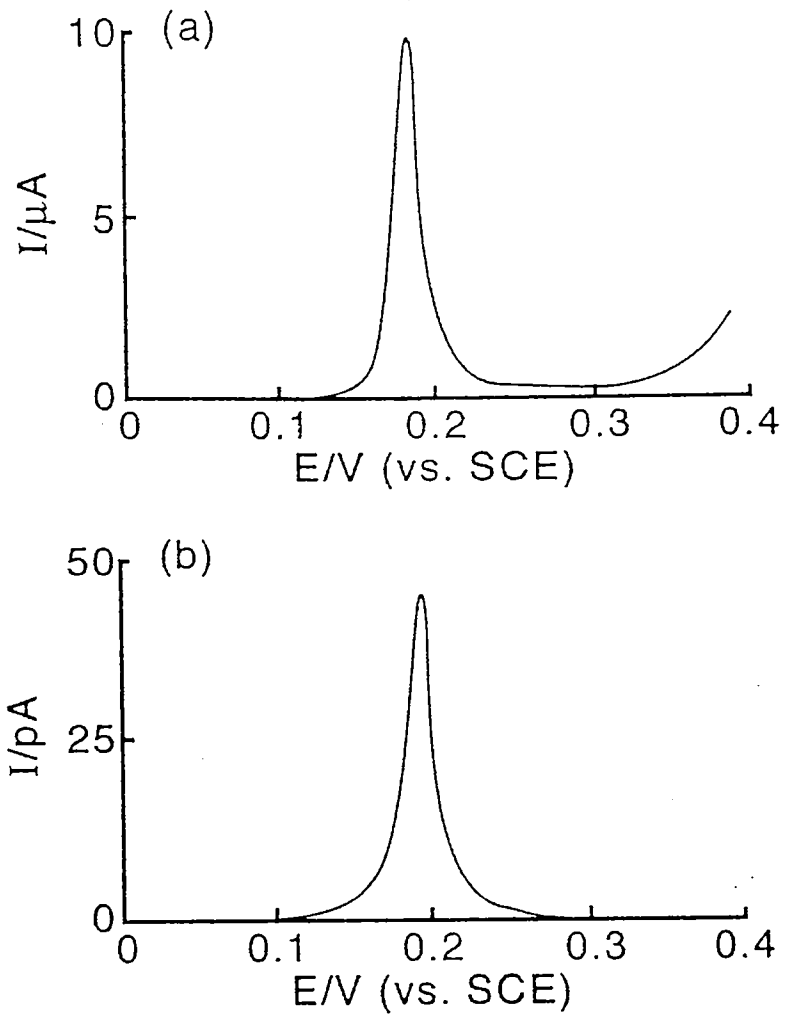


Figure 9.19 Experimental (a) and simulated (b) voltammograms (scan rate 1 mVs^{-1}, Z = 1.39, r_h = 0.5 μm, D_{ideal} = 1 x 10^{-5} cm^2s^{-1}) for the oxidation of 10.6 nmoles of THPD deposited onto a 4.9 mm diameter basal plane pyrolytic graphite electrode immersed in 0.1 M KSCN.

The width of the voltammogram at half height deviates from the theoretical value for the case of no interaction, ΔE_{hh} = 91 mV.[38] Towards the limit of Z = 2 the model ceases to apply because the peak width at half height tends to zero and nucleation/phase separation occurs. The experimental voltammogram (Figure 9.19(a)) recorded at a scan rate of 1 mV s^{-1} for the oxidation of a deposit of 10.6 nmoles of THPD shows a peak width at half height, ΔE_{hh} = 20 mV, and was successfully simulated with an interaction parameter of Z = 1.4 (Figure 9.19(b)).

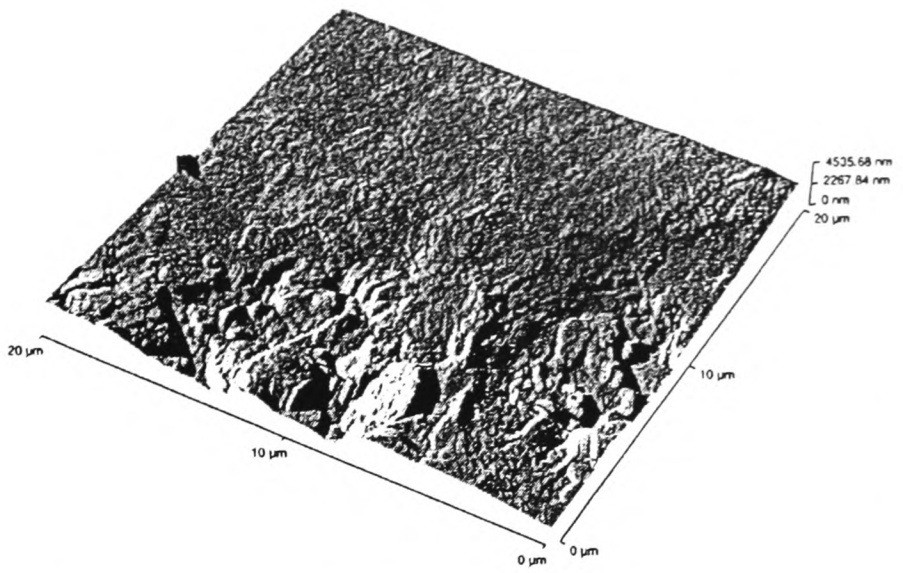


Figure 9.20 Atomic force microscopy topographic image of the surface of a basal plane pyrolytic graphite electrode.

For the simulation of mass transport effects the average radius of the droplet has to be estimated. Estimates were based on the surface roughness of the basal plane pyrolytic graphite electrode used. Figure 9.20 shows a typical AFM image of the surface morphology. The deposition of 10.6 nmoles of THPD can be calculated to correspond to a film of *ca.* 0.25 μm thickness evenly distributed over the electrode geometric surface area. Based on this estimate and the roughness of the surface an estimate of the average droplet size, r_h = 0.5 μm, can be made. This order of magnitude estimate is sufficient for the use in the simulation and important for the conclusions to be drawn from the comparison of experimental and simulation data. The diffusion coefficient, $D_{ideal} = 1.0 \times 10^{-5}$ cm^2s^{-1}, has been chosen arbitrarily and is kept constant for the time being but discussed later.

9.4.2.3. The Intermediate Scan Rate Regime: Transition from Thin Film to Diffusion Characteristics

Next, attention is focused on the more complex case when mass transport affects the voltammetric responses. In Figure 9.17(i) experimental voltammograms for the oxidation of 10.6 nmoles of THPD deposited on a basal plane pyrolytic graphite electrode and immersed in aqueous 0.1 M KSCN are shown. The peak current under these conditions varies as a function of scan rate with $I_p \propto \nu^{1/2}$. The simulated voltammograms for $D_{ideal} = 1.0 \times 10^{-5}$ cm^2s^{-1} follow the same dependence (see Figure

9.17(ii)) and data for this simulation are also shown in the plots in Figure 9.18(a) and (b) (filled squares). Here, data for the model 1 consistent with diffusion from the oil | aqueous electrolyte into the droplet is shown as the most plausible limiting case for the simulation (vide infra). It can be seen that the transition from thin film behaviour to diffusion control is accurately reproduced.

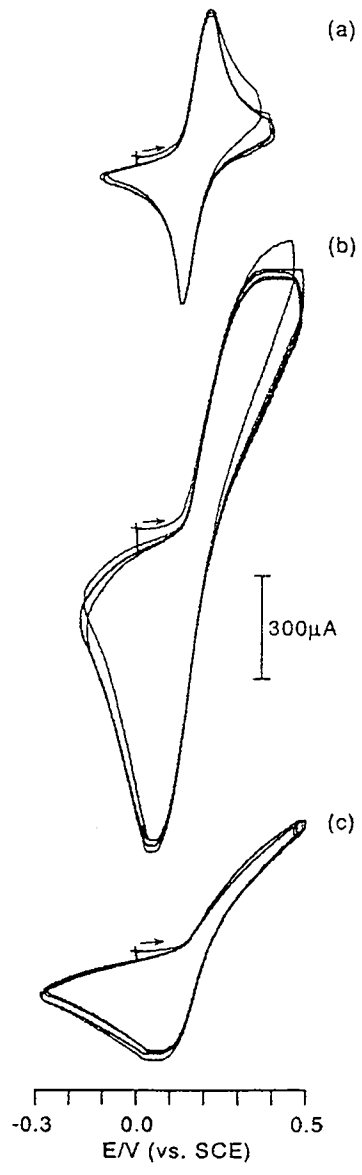


Figure 9.21 Cyclic voltammograms for the oxidation of (a) 10 (b) 160 (c) 640 nmoles of THPD deposited onto a 4.9 mm diameter basal plane pyrolytic graphite electrode and immersed in 0.1 M KSCN.

A major difference in the three simulation models is introduced by the geometries (see §9.2.2.1). A distinction of the models may therefore be based on the effect of mass transport on the shape of the voltammograms. The active surface area from which the electrochemical process commences is maximised in model 1 (surface of the hemisphere). For model 3 and especially for model 2 a considerably slower process can be predicted based on the smaller 'active' surface. Accordingly, voltammograms with a transition between thin film and diffusion behaviour equivalent to those shown in Figure 9.17(ii) can be generated by applying a *larger* diffusion coefficient for the simulation with models 3 and 2. In complementary experiments (vide infra) it can be shown that the theoretical model 3 is not realistic for the case of THPD microdroplet oxidation and this model can therefore be discarded.

Model 3 requires partitioning of the electrolyte into the organic phase and is independent of the presence of the triple phase boundary. The voltammetric response for the oxidation of THPD can be predicted to increase if the coverage of the electrode surface with oil is increased.

However, experimentally it can be observed (Figure 9.21) that increasing the amount of the oil droplet deposit first increases the current, then causes a step-shaped rather than a peak-shaped current response, and finally causes the current response to decrease. All three observations are in good agreement with a process, which

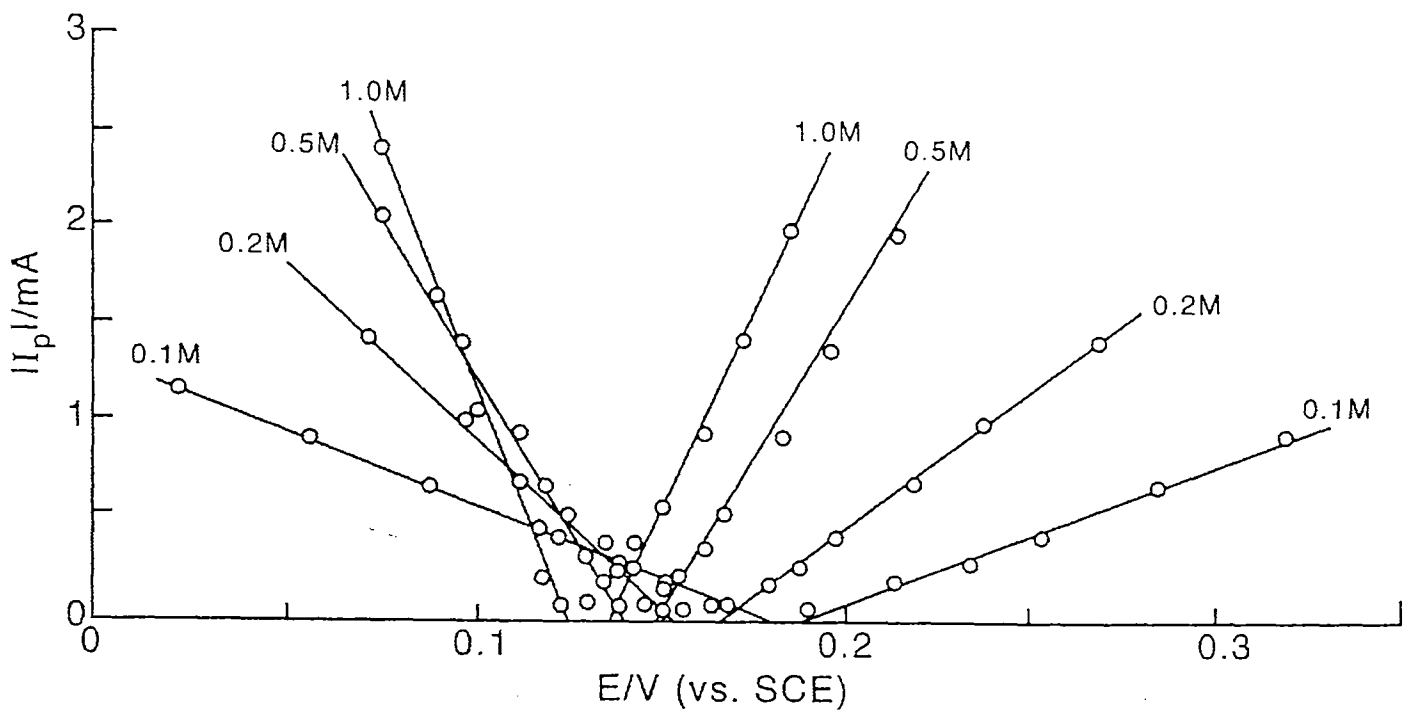


Figure 9.22 Plot of the absolute anodic and cathodic peak currents for the oxidaiton and re-reduction of 20 nmoles THPD deposited on a 4.9 mm diameter basal plane pyrolytic graphite electrode and immersed in aqueous KSCN of various concentration (scan rates 20, 50, 100, 200, 500, 1000, 2000 mV s^{-1}).

commences from the three phase boundary and then progresses towards the centre of the droplet and therefore support model 2.

Model 1 requires very fast electron transfer between droplet deposit and the electrode surface coupled to fast electron conduction at the oil | aqueous electrolyte phase boundary. Experimental voltammograms especially at fast scan rates can be seen to be severely distorted with peak to peak separations of more than 100 mV (Figure 9.17(i)). By varying the concentration of the aqueous electrolyte even more pronounced peak to peak separation can be achieved. In Figure 9.22 anodic and cathodic peak potentials for voltammograms obtained for the oxidation of 20 nmoles of THPD deposited on a basal plane pyrolytic graphite electrode are shown. It can be

seen that increasing the scan rate causes the peak to peak separation to increase with 'ohmic' characteristics dependent on the concentration of the aqueous electrolyte. This unusual observation has also been described for solid state voltammetric processes[39,40] and attributed to charge or mass transport in the microcrystalline deposit. A model based only on diffusion in the oil droplet deposit cannot account for this kind of behaviour and therefore Model 2 appears to be more realistic compared to Model 1. This conclusion is supported by optical micrographs presented recently,[2] which clearly indicate that for large THPD droplets the electrolysis process commences at the triple interface deposit | aqueous electrolyte | electrode. However, a transition from model 2 to model 1 is possible for small droplets and slow scan rates. Model 1 was applied for simulation purposes (see §9.2.2.1) and experimental and theoretical data are contrasted in Figure 9.17 and Figure 9.18. Agreement between experiment and simulation is good apart from the effect of increasing peak separation with increasing scan rate. However, in all cases diffusion coefficients determined via simulation of the experimental data, $D_{ideal} = 1.0 \times 10^{-5}$ cm^2s^{-1}, are surprisingly high. An order of magnitude estimate of a realistic diffusion coefficient can be based on the Wilke-Chang expression[41] which takes into account temperature, viscosity, and volume effects (equation (9.74.))

$$D = 7.4\times10^{-8} \frac{(xM)^{1/2} T}{\eta V^{0.6}} \qquad (9.74.)$$

In this equation the diffusion coefficient D is estimated based on an association parameter, $x = 1$ (corresponding to a non-associated solvent), the molecular mass of the solvent, $M = 444$ g mol^{-1}, the temperature, $T = 298$ K, the viscosity, $\eta = 1$ Pa s (approximate value based on the viscosity of glycerol), and the molecular volume, $V =$ 56.[41] By assuming only thiocyanate anions to diffuse and electron hopping as the

mechanism for keeping charge neutrality, an upper limit for the diffusion coefficient of $D = 4.2 \times 10^{-8}$ cm^2s^{-1} can be calculated. This diffusion coefficient can be seen to be approximately three orders of magnitude below the value obtained by comparison of experimental data with simulation data. Further, applying the simulation model 2 rather than 1 will further *increase* the value D_{ideal} necessary to match simulation and experimental data! It can be concluded that although diffusion is possible and the low scan rate case allows the determination of interaction data, the mass transport process under fast scan rate conditions is orders of magnitude faster than possible by diffusion only. Processes at liquid | liquid interfaces can be greatly accelerated by Marangoni-type convection processes[42] or convection due to bulk expansion or contraction and this may be responsible for the unusually high diffusion coefficient observed for the electroinsertion of SCN^- in microdroplets of THPD.

9.4.2.4. The Fast Scan Rate Limit: Geometry Dependent Wave Shape Effects

It is interesting to consider the case of fast scan rate voltammetric responses because in principle further insight into the mechanism can be gained. The geometries for the two simulation models 3 and 1 compared to the model 2 may be described as 'concave' for 3 and 1 compared to 'convex' for 2 (Figure 9.5, Figure 9.2 and Figure 9.3 repectively). This causes a very different voltammetric characteristic at high scan rates (or for large droplets) as shown in Figure 9.21. In the case of convex diffusion a spherical component causes sigmoidally shaped voltammetric responses similar to those expected for microelctrode steady state voltammetry. In the case of models 3 and 1, however, only semi-infinite or confined diffusion is possible. Experimentally the fast scan rate limit is not accessible due to the considerable increase in the peak to peak separation (see Figure 9.22). However, the voltammetric responses observed in

the presence of large droplets (Figure 9.21) are consistent with model 2, diffusion from the three phase boundary.

9.5. Conclusions

Linear sweep voltammograms and potential step chronoamperograms were simulated for three different mechanistic models for droplet electrodes using the DRM methodology. Reliable and efficient simulations were possible and distinct voltammetric features for the three mechanistic cases have been described. In particular quasi steady state behaviour can be observed for the three phase boundary model and different peak to peak separations for linear sweep voltammetry were observed according to convex, planar, or concave diffusion geometries. The three mechanistic models have been first refined, where possible, to allow for non-ideal diffusion and second compared to experimental data.

It has been shown that the direct comparison of simulation data with cyclic voltammetric data for the oxidation of microdroplet deposits of THPD can be employed to gain important insights into the electrochemical mechanism. In particular the regular solution theory approach has been successful in explaining the peak shape of voltammograms at slow scan rates. More important, the conclusive experimental evidence for simulation model 2 together with the determination of a diffusion coefficient, which is orders of magnitude too large, suggest Marangoni-type convection processes even for very small microdroplet deposits. This is consistent with observations made by optical microscopy for larger droplets. The role of this kind of process in other related electrochemical systems[43] deserve further study.

References for Chapter 9

[1] F. Marken, R.G. Compton, C.H. Goeting, J.S. Foord, S.D. Bull, S.G. Davies, *Electroanal.* 10 (1998) 821
[2] F. Marken, R.D. Webster, S.D. Bull, S.G. Davies, *J. Electroanal. Chem.* 437 (1997) 209
[3] Speiser, B. *Electroanalytical Chemistry* Ed. A.J. Bard, Marcel-Dekker: New York 19 (1997) 1
[4] D. Britz, *Digital Simulation in Electrochemistry* (2nd Ed.) Springer-Verlag: Berlin, (1998)
[5] T. Nann, J. Heinze, *Electrochem. Commun.* 1 (1999) 289
[6] J.A. Alden, R.G. Compton, *J. Phys Chem. B* 101 (1997) 8941
[7] J.A. Alden, R.G. Compton, *J. Phys Chem. B* 101 (1997) 9606
[8] Q. Fulian, N.A. Williams, A.C. Fisher, *Electrochem. Commun.* 1 (1999) 124
[9] Q. Fulian, A.C. Fisher, G. Denault, *J. Phys. Chem. B.* 103 (1999) 4387
[10] Q. Fulian, A.C. Fisher, *J. Phys. Chem. B* 102 (1998) 9647
[11] A.C. Fisher, R.G. Compton, *J. Phys. Chem.* 95 (1991) 7538
[12] A.C. Fisher, R.G. Compton, *J. Appl. Electrochem.* 22 (1992) 38
[13] J.A. Alden, R.G. Compton, R.A.W. Dryfe, *J. Appl. Electrochem.* 26 (1996) 865
[14] R.G. Compton, R.A.W. Dryfe, R.G. Wellington, J. Hirst,. *J. Electroanal. Chem.* 383 (1995) 13
[15] A. Brandt, *Math. Comp.*, 31 (1977) 333
[16] R.G. Compton, M.E. Laing, A. Ledwith, I.I. Abu-Abdoun, *J. Appl. Electrochem.* 18 (1988) 431
[17] B.E. Conway, *Physical Chemistry: An Advanced Treatise vol. IXA* Eds. H. Eyring, D.Henderson, W. Jost, Academic Press: New York, (1970) pp121
[18] K.B. Oldham, C.G. Zoski, *Comp. Chem. Kinetics* Eds C.H. Bamford, R.G. Compton, Elsevier: Amsterdam, NL, 26 (1986) 96
[19] J. Crank, *Mathematics of Diffusion*; OUP: Oxford, UK, (1975) pp89-103
[20] M. Lovrić, *Electrochem. Commun.* 1 (1999) 207
[21] M. Lovrić, F. Scholz, *J. Solid State, Electrochem.* 1 (1997) 108
[22] M. Lovrić, F. Scholz, *J. Solid State, Electrochem.* 3 (1999) 172
[23] K.B. Oldham, *J. Solid State, Electrochem.* 2 (1998) 367
[24] Steiner, E. *The Chemistry Maths Book*; OUP: Oxford, UK, (1996) pp233
[25] C. Shi, F.C. Anson, *J. Phys. Chem. B.* 102 (1998) 9850
[26] C. Shi, F.C. Anson, *Anal. Chem.* 70 (1998) 3114
[27] C. Shi, F.C. Anson, *J. Phys. Chem. B.* 103 (1999) 6283
[28] S.R. Ragsdale, H.S. White, *J. Electroanal. Chem.* 432 (1997) 199
[29] S.C. Paulson, N.D. Okerlund, H.S. White, *Anal. Chem.* 68 (1996) 581
[30] J.D. Norton, S.A. Anderson, H.S. White, *J. Phys. Chem.* 96 (1992) 3
[31] L.C. Wrobel, J.C.F. Telles, C.A.A. Brebbia, *Dual Reciprocity Boundary Element Formation for Axisymmetric Diffusion Problem, in Boundary elements VIII*, Springer – Verlag: Berlin, (1986)
[32] P.W. Partridge, *Engineering Analysis with Boundary Elements*, 14 (1994) 349
[33] P.W. Partridge, C.A. Brebbia, L.C. Wrobel, *The Dual Reciprocity Boundary Element Method*, Elsevier: Southampton, (1992)
[34] Q. Fulian, A.C. Fisher, *DRM for Time – Dependent Diffusion Simulation,* to be submitted
[35] Q. Fulian, *Mechanistic Electrochemistry*, PhD Thesis, Bath University, (1999)
[36] A.C. Fisher, *Electrode Dynamics*, Oxford University Press, Oxford, (1996)
[37] S. Fletcher, M.D. Horne, *Electrochemistry Commun.*, 1 (1999) 502
[38] A.J. Bard, L.R. Faulkner, *Electrochemical Methods*; Wiley: New York, (1980) pp411
[39] A.M. Bond, R. Colton, F. Marken, J.N. Walter, *Organometallics.*, 13 (1994) 5122.
[40] A. Dostal, B. Meyer, F. Scholz, U. Schröder, A.M. Bond, F. Marken, S.J. Shaw, *J. Phys. Chem.*, 99 (1995) 2096.
[41] C. R. Wilke, P. Chang, *A.I.Ch.E. Journal*, (1955) 264.
[42] H.J. Lee, D.J. Fermin, R.M. Corn, H.H. Girault, *Electrochem. Commun.*, 1 (1999) 190.
[43] W. Hyk, Z. Stojek, *J. Phys. Chem.* B, 102 (1998) 577

10. Square Wave Anodic Stripping Voltammetry at Mercury Plated Electrodes. Simulation of Surface Morphology Effects

The work in this chapter was done in collaboration with Matthew Powell, Physical and Theoretical Chemistry Laboratory Oxford and is currently in press at the *Journal of Physical Chemistry*.

10.1. Introduction

There are numerous reports about the nature of mercury thin films (MTFs) on a range of electrode materials. Literature[1–3] is especially prevalent for mercury on glassy-carbon electrodes (GCEs). Štulíková[1] has shown that the manner in which the mercury is deposited affects the nature of the film, ranging from large mercury drops at relatively large separations to a wider distribution of smaller mercury droplets. Furthermore, upon electrode drying mechanical joining of fine drops occurs. The work of Wu[2] supports the view that larger more dispersed droplets occur under certain conditions, although disagrees with Štulíková's[1] explanation of how they are formed, emphasising their association with a transformation, resulting from, for example, evaporation of water from the surface and also as a result of surface perturbation of rapid potential changes under the anodic stripping voltammetry (ASV) condition. Zakharchuk and Brainina[3] also show evidence that microdroplets coalesce giving a few large (>10 μm) droplets.

The experimental papers[1-3] support the tendency of MTF coatings on GCEs to exist in a state of larger microdroplets, typically of the order of 1 μm in diameter, but up to > 10 μm depending on the treatment. Whether this is due to a transformation to a

more stable state triggered by various surface perturbations[2,3] or whether this is their initial state[1] is uncertain.

The formation of droplets is not, however, limited to MTFs on GCEs. Evidence including visualisation via atomic force microscopy for mercury droplets on platinum, ranging from submicron to ca. six microns in diameter can be found in the literature.[4,5] Mercury can also be electroplated on iridium giving rise to a uniform film or hemispherical coverage.[6,7]

These observations have lead Štulíková [1] to note the need for a refined theoretical treatment of ASV at a MTF on GCEs that treats the surface as a large number of spherical drops rather than a thin, homogeneous mercury film.

This chapter develops the theory of ASV via square wave voltammetry for the case of quasi-reversible electrode kinetics considering the electrode both as a uniform thin film experiencing semi-infinite linear diffusion and as an isolated droplet to which mass transport occurs via hemispherical diffusion. The behaviour of the two are contrasted particularly in the limit of drops of small radius where the enhanced mass transport displays a significant effect on the apparent electrochemical reversibility of the redox couple under investigation. It additionally reports experimental atomic force microscopy (AFM) data for mercury deposited on copper and iridium substrates to further illustrate the need for some caution in the application of linear diffusion theory based on the thin film assumption to MTF electrodes.

10.2. Theory

We examine the following redox reaction

$$RED(\text{amalgam}) \overset{k_b^a}{\rightleftharpoons} OX(\text{aq.}) + 2e^- \tag{10.1.}$$

which is considered to occur at the surface of a hemispherical mercury electrode, where k_b^a is the apparent rate constant for the reduction (back) reaction. The net flux at the electrode surface is given by[8]

$$j = -k_b^a \left\{ [\text{OX}] - [\text{RED}] e^{\theta} \right\} \tag{10.2.}$$

where

$$\theta = \frac{2F}{RT}\left(E - E^{\circ\prime}\right), \tag{10.3.}$$

E is the potential of the square wave scan and $E^{0'}$ the formal potential of the redox couple. The two electron process takes place in two steps[8]

$$RED(\text{amalgam}) \underset{k_{-1}}{\overset{k_1}{\rightleftharpoons}} Y(\text{aq.}) + e^- \tag{10.4.}$$

$$Y(\text{aq.}) \underset{k_{-2}}{\overset{k_2}{\rightleftharpoons}} OX(\text{aq.}) + e^- \tag{10.5.}$$

where Y is an intermediate. If the first step is rate determining[8]

$$k_b^a = A_1 \exp\left(-\frac{1}{2}(1+\alpha_1)\theta \right) \tag{10.6.}$$

whereas if the second step is rate determining[8]

$$k_b^a = A_1 \exp\left(-\frac{1}{2}\alpha_2\theta \right) \tag{10.7.}$$

where A_1 is a constant for a particular reaction and α_1 and α_2 are the Tafel coefficients describing the individual electron transfer steps.

In square wave ASV the electrode is subjected to the square wave voltammetric sweep where E changes as shown in Figure 6.1, where ΔE is the step voltage of the staircase, E_{SW} is the pulse amplitude, E_i the starting voltage for the scan and t_p is period of the pulse. During the square wave experiment the current flowing is measured at the points shown for each pulse; $I(1)$ is known as the forward current and $I(2)$ as the backward current. The difference current

$$\Delta I = I(1) - I(2) \tag{10.8.}$$

is recorded and plotted against the average potential of the corresponding forward and backward pulses. RED and OX are both assumed kinetically stable, and initially only RED is present in the mercury electrode at a concentration of $[RED]_{t=0}$. No reduced species is presumed to exist in the solution, nor any oxidised species in the mercury electrode.

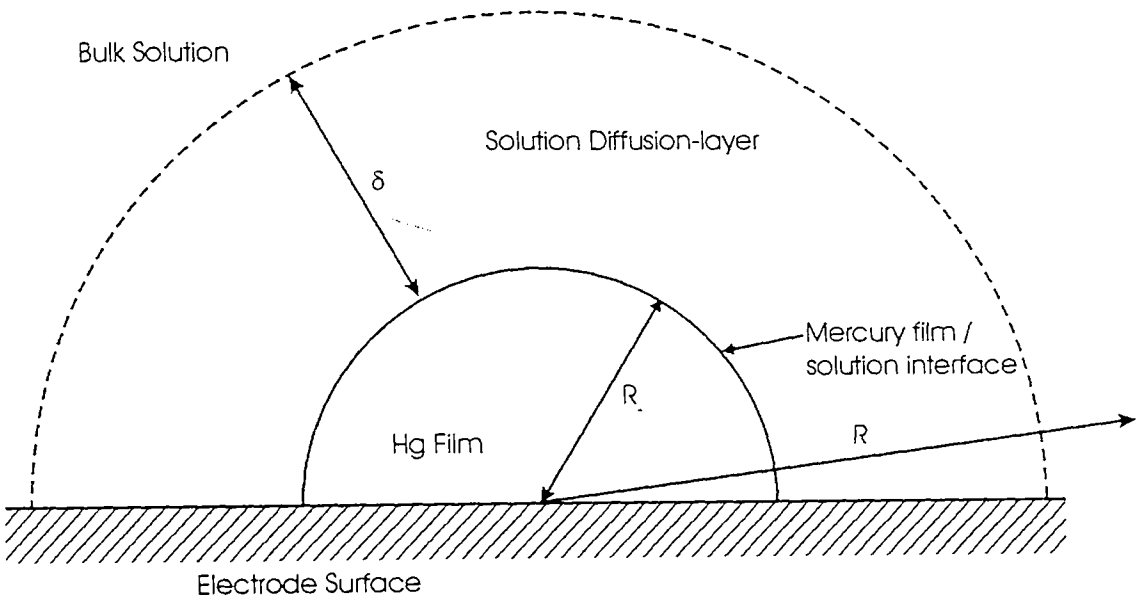


Figure 10.1 Schematic diagram showing coordinates and principal dimensions of the hemispherical system.

Time-dependent mass transport equations for both species are given by Fick's second law. These are given as a function of the radial coordinate, R (Figure 10.1), to take advantage of the symmetry of the hemispherical system.[9]

$$\frac{\partial a}{\partial t} = D_a \left\{ \frac{\partial^2 a}{\partial R^2} + \frac{2}{R}\frac{\partial a}{\partial R} \right\} \tag{10.9.}$$

$$\frac{\partial b}{\partial t} = D_b \left\{ \frac{\partial^2 b}{\partial R^2} + \frac{2}{R}\frac{\partial b}{\partial R} \right\} \tag{10.10.}$$

where D_a and D_b are respectively the applicable diffusion coefficients for the reduced and oxidised species, and a and b are defined as follows

$$a = \frac{[RED]}{[RED]_{t=0}} \tag{10.11.}$$

$$b = \frac{[OX]}{[RED]_{t=0}} \tag{10.12.}$$

The introduction of a new coordinate,[10] ψ, where

$$\psi = 1 - \frac{R_e}{R} \tag{10.13.}$$

and R_e is the electrode radius, transforms mass transport equation (10.10.) to

$$\frac{\partial b}{\partial t} = D_b \left(\frac{(1-\psi)^2}{R_e} \right)^2 \frac{\partial^2 b}{\partial \psi^2} \tag{10.14.}$$

which is valid for $0 \leq \psi < 1$ (where $R \geq R_e$). This transformation is computationally efficient as it distorts space such that there is a higher density of node points close to the electrode surface, where there is a maximum variation in concentrations (see Figure 10.2).

For the reduced species we introduce the spatial distortion φ

$$\varphi = \frac{R_e - R}{R_e} \tag{10.15.}$$

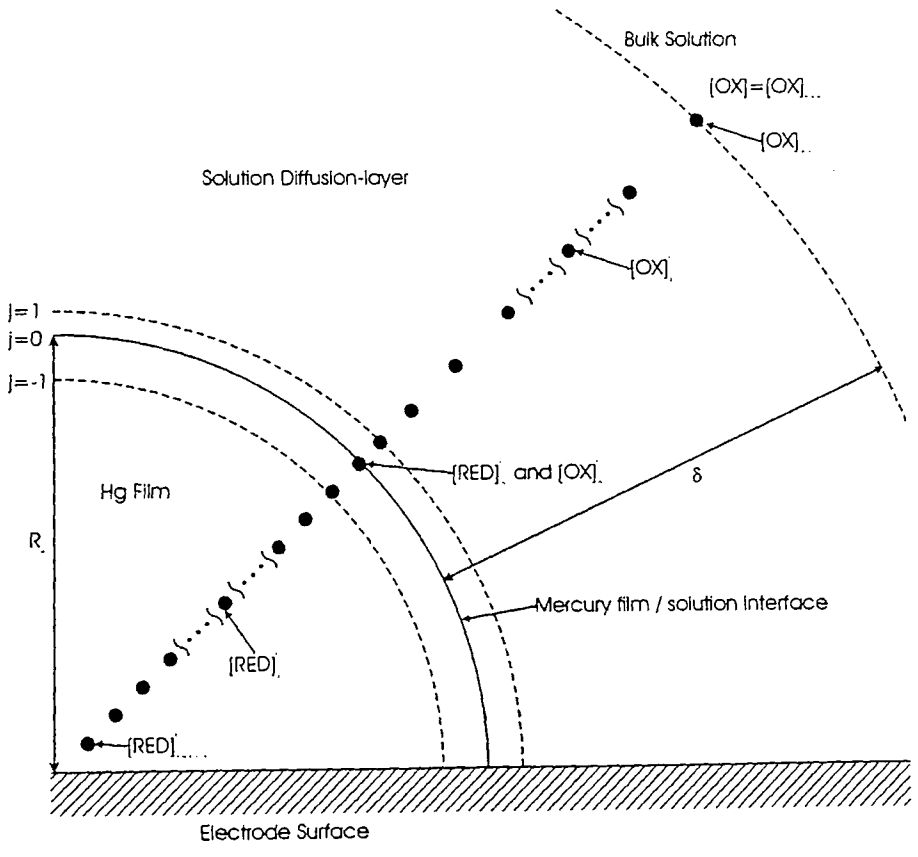


Figure 10.2 Schematic diagram showing the spatial node distribution used in the model, for the hemispherical system.

which transforms equation (10.9.) to

$$\frac{\partial a}{\partial t} = \frac{D_a}{R_e^2}\left(\frac{\partial^2 a}{\partial \varphi^2} - \frac{2}{(1-\varphi)}\frac{\partial a}{\partial \varphi}\right) \qquad (10.16.)$$

This is valid for $0 \leq \varphi \leq 1$ (i.e. where $0 \leq R \leq R_e$). This gives rise to evenly spaced grid nodes (see Figure 10.2).

A back-to-back grid[11-13] based on the coordinates ψ and φ is introduced. The grid is defined such that negative spatial node labels, where the coordinate φ operates, are used to simulate RED species, and positive values, where the coordinate ψ operates, for OX species. The electrode surface is placed at $R = R_e$, corresponding to the node label zero, and a finite diffusion layer boundary at $R = R_e + \delta$ (δ is defined as the thickness of the diffusion layer). Equations (10.14.) and (10.16.) can be simply cast into finite difference form, the first step in the backward implicit method,[14,15] to give

$$a_j^{t-1} = (\lambda_{2a,j} - \lambda_{1a})a_{j-1}^t + (1 + 2\lambda_{1a})a_j^t - (\lambda_{1a} + \lambda_{2a,j})a_{j+1}^t \qquad (10.17.)$$

$$b_j^{t-1} = -\lambda_{b,j}b_{j-1}^t + (1 + 2\lambda_{b,j})b_j^t - \lambda_{b,j}b_{j+1}^t \qquad (10.18.)$$

where t is the temporal node label in a single pulse denoting the time $t\Delta t$, j is the spatial node label, separated by distance,

$$\Delta\psi = \frac{\delta}{(R_e + \delta)NJ} \qquad (10.19.)$$

$$\Delta\varphi = \frac{1}{NF} \qquad (10.20.)$$

NF is the number of node points in the film and NJ the number of node points in solution. The coefficients have the following definitions

$$\lambda_{1a} = \frac{D_a \Delta t}{R_e^2(\Delta\varphi)^2} \qquad (10.21.)$$

$$\lambda_{2a,j} = \frac{D_a \Delta t}{RR_e\Delta\varphi} = \frac{D_a \Delta t}{(1-\varphi_j)R_e^2\Delta\varphi} \qquad (10.22.)$$

$$\lambda_{b,j} = \frac{D_b \Delta t \left(1-\psi_j\right)^4}{R_e^2 \left(\Delta\psi\right)^2} \qquad (10.23.)$$

At the start of SWV experiment, the concentration of the reduced species is at its initial value, whilst that of OX is very close to zero. Hence the following boundary conditions apply.

At $t\Delta t = 0$;

for $R > R_e$ $\qquad b = 0;$

for $0 < R < R_e$ $\qquad a = 1.$

At the electrode surface the flux of OX and RED species is conserved, and its magnitude depends on diffusion as well as the rate of kinetic inter-conversion. These considerations generate further boundary conditions, and using equation (10.2.) it follows that

$$D_a \frac{\partial a}{\partial R}\Big)_{R=R_e} = D_b \frac{\partial b}{\partial R}\Big)_{R=R_e} \qquad (10.24.)$$

$$-D_a \frac{\partial a}{\partial R}\Big)_{R=R_e} = -k_b^a \left\{b_0^l - a_0^l e^{\theta}\right\} \qquad (10.25.)$$

Conversion of equation (10.24.) into finite-difference form gives

$$D_a \frac{(a_0 - a_{-1})}{\Delta\varphi} = D_b \frac{(b_1 - b_0)}{\Delta\psi} \qquad (10.26.)$$

Combining equation (10.25.) and equation (10.26.) gives explicit solutions for either a_0 or b_0 in terms of a_{-1} and b_1 as follows

$$a_0 = k_{a1} a_{-1} + k_{a2} b_1 \qquad (10.27.)$$

where $k_{a1} = \dfrac{1 + k_b^a \phi_b}{1 + k_b^a \phi_a e^{\theta} + k_b^a \phi_b}$ and $k_{a2} = \dfrac{k_b^a \phi_a}{1 + k_b^a \phi_a e^{\theta} + k_b^a \phi_b}$

$$b_0 = k_{b1} a_{-1} + k_{b2} b_1 \qquad (10.28.)$$

where $k_{b1} = \dfrac{k_b^a \phi_b e^{\theta}}{k_b^a \phi_a e^{\theta} + k_b^a \phi_b + 1}$ and $k_{b2} = \dfrac{k_b^a \phi_a e^{\theta} + 1}{k_b^a \phi_a e^{\theta} + k_b^a \phi_b + 1}$

where $\phi_a = \dfrac{R_e \Delta\varphi}{D_a}$, $\phi_b = \dfrac{R_e \Delta\psi}{D_b}$.

Accordingly we can handle the normalised concentrations a and b at the electrode surface implicitly. The finite-difference equations at the electrode surface are therefore written as

$$\begin{aligned} a_{-1}^{t-1} &= (-\lambda_{1a} + \lambda_{2a,-1}) a_{-2}^{t} \\ &+ (1 + 2\lambda_{1a} - \lambda_{1a} k_{a1} - \lambda_{2a,-1} k_{a1}) a_{-1}^{t} \\ &- (\lambda_{1a} k_{a2} + \lambda_{2a,-1} k_{a2}) b_1^{t} \end{aligned} \qquad (10.29.)$$

$$\begin{aligned} b_1^{t-1} &= -\lambda_{b,1} k_{b1} a_{-1}^{t} \\ &+ (1 + 2\lambda_{b,1} - \lambda_{b,1} k_{b2}) b_1^{t} \\ &- \lambda_{b,1} b_2^{t} \end{aligned} \qquad (10.30.)$$

Far from the electrode (at $R_e + \delta$) the concentration of the oxidised species tends to its bulk value of zero, whilst at $R = 0$ there is a no flux boundary for the reduced species. These requirements provide the following boundary conditions

$$\begin{aligned} a_{-NF+1}^{t-1} &= (1 + \lambda_{1a} + \lambda_{2a,-NF+1}) a_{-NF+1}^{t} \\ &- (\lambda_{1a} + \lambda_{2a,-NF+1}) a_{-NF+2}^{t} \end{aligned} \qquad (10.31.)$$

$$\begin{aligned} b_{NJ-1}^{t-1} &= -\lambda_{b,NJ-1} b_{NJ-2}^{t} \\ &(1 + 2\lambda_{b,NJ-1}) b_{NJ-1}^{t} \end{aligned} \qquad (10.32.)$$

All the relevant equations may now be grouped together to form a single matrix equation. This tridiagonal matrix is solvable using the Thomas Algorithm.[16–20] The solution provides the full concentration profile of both species as a function of time throughout the experiment.

The flux of species being oxidised is given by equation (10.2.). This in turn allows the current to be calculated, so by comparison with equation (10.25.)

$$I = nFAj = nFAD_a \frac{(a_{-1} - a_0)}{R_e \Delta\varphi}[\mathrm{RED}]_{t=0} \qquad (10.33.)$$

where the value of a_0 is given by equation (10.27.) and a_{-1} is generated by the simulation. To correspond with experimental practice the difference current ΔI is recorded. This is calculated (equation (10.8.)) by subtracting the simulated backward current $I(2)$ from the simulated forward current $I(1)$: these two currents are calculated using equation (10.33.) at the points in the pulse shown in Figure 6.1.

A variation to the simulation is to consider the limit where the electrode process is totally irreversible, that is no reduction at all occurs at the electrode surface. The electrode process becomes

$$\mathrm{RED(amalgam)} \xrightarrow{k_f} \mathrm{OX(aq)} + 2\mathrm{e}^- \qquad (10.34.)$$

This can be simulated by simplifying equation (10.2.) to

$$j = k_b^a [\mathrm{RED}] e^{\theta} \qquad (10.35.)$$

which modifies equations (10.27.) and (10.28.) to

$$a_0 = k_{a1} a_{-1} \qquad (10.36.)$$

where $k_{a1} = \dfrac{1}{1 + k_b^a \phi_a e^{\theta}}$

and

$$b_0 = k_{b1} a_{-1} + b_1 \qquad (10.37.)$$

where $k_{b1} = \dfrac{k_b^a \phi_b e^{\theta}}{k_b^a \phi_a e^{\theta} + 1}$

10.2.1. Uniform Thin Film

We can model a uniform thin film by considering, rather than a hemisphere of mercury, an electrode consisting of a thin film of mercury on the outside of an inert hemispherical centre (Figure 10.3). When the radius of the inert centre is large,

$R_e \rightarrow \infty$, the system will be equivalent to a uniform planar electrode. This will allow for comparison with previous work in chapter 6, by Kounaves *et al.*[21] and for contrast with the hemispherical case developed above.

The derivation is mostly the same as for the hemispherical electrode system described above. However, the reduced species does not exist in the region of $0 \leq R \leq R_e$ but in the range $(R_e - l) \leq R \leq R_e$, where l is the thickness of the mercury film. R_e remains the radius of the surface of the mercury film.

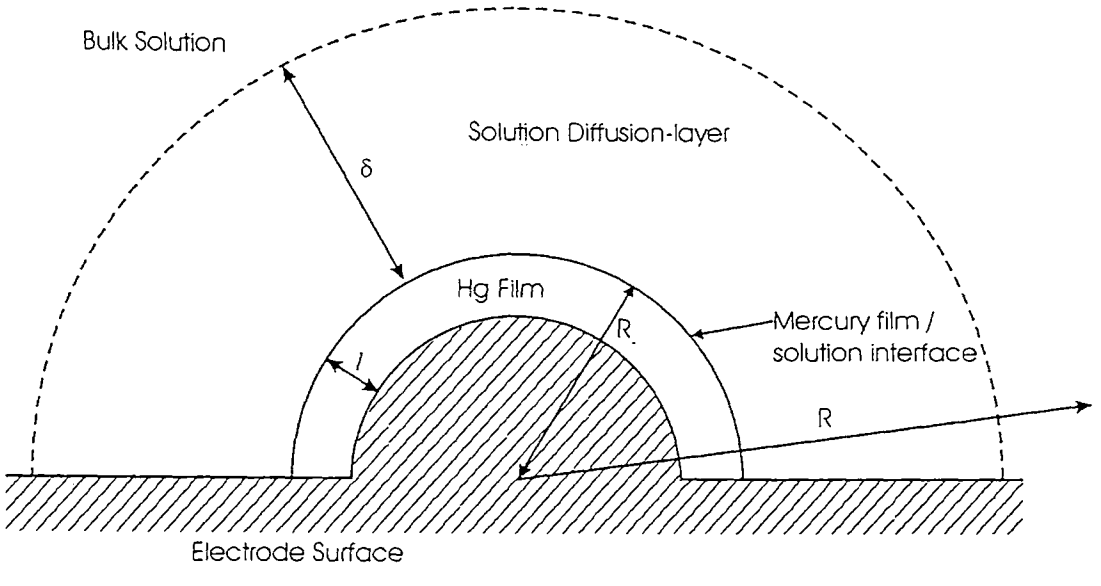


Figure 10.3 Schematic diagram showing coordinates and principal dimensions of the inert centred system

Accordingly we modify equation (10.20.) to become

$$\Delta\varphi = \frac{l}{R_e NF} \tag{10.38.}$$

All other equations remain the same.

10.2.2. Computation

All programs were written in FORTRAN 77 and executed on a Silicon Graphics origin 2000 server. Results were analysed using Microsoft Excel 7.0 or IDL 5.0. The simulations were converged to 1% (as estimated by comparison with a number of 'over converged' runs covering the range of parameters investigated). Typical values of $NJ = 4000$, $NF = 1000$, $nodes = 500$ (where *nodes* is the number of time nodes per pulse) were found to be appropriate.

10.3. Experimental

10.3.1. Apparatus

The electrochemical deposition experiments were performed using either a computer-controlled PGSTAT20 Autolab potentiostat (Eco-Chemie, Utrecht, Netherlands) or a μAUTOLAB® (Eco-Chemie, Utrecht, Netherlands). All experiments were carried out in a previously described electrochemical cell,[22] employing a platinum coil as an auxiliary electrode and a saturated calomel electrode, SCE, as the reference electrode (Radiometer, Copenhagen, Denmark). Atomic Force Microscopy, AFM, measurements were conducted using a TopoMetrix TMX 2010 Discoverer system operating in contact mode (10 Hz scan rate). Pyramidal silicon nitride tips (TopoMetrix AFM PROBES 1520) were employed. Images were obtained *ex situ*, after the electrode substrate had been treated as explained further below.

10.3.2. Reagents

Reagents used were mercury (II) perchlorate hydrate (98 %) and perchloric acid (70 % A.C.S.), both supplied by Aldrich (Poole, Dorset, UK). Solutions were prepared using UHQ grade water of resistivity not less than 18 MΩ cm^{-1} (Elgastat, High Wycombe, Bucks., UK).

10.3.3. Experimental Procedure

A 1 mm diameter iridium electrode and a 5 mm diameter copper electrode, each mounted in a Teflon™ support were used as substrates for mercury deposition experiments. Prior to each experiment, the electrodes were polished using diamond pastes of progressively finer particle size down to 1 μm (Kemet, Kent, UK) and rinsed with UHQ water.

The iridium electrode was plated with mercury using 250 mL of a mercury plating solution,[23] consisting of 0.02 M perchloric acid and 0.1 M mercury (II) perchlorate, by holding the potential of the working electrode at 0.00 V (vs. SCE) for various deposition times.

The copper electrode was plated in a voltammetric cell containing 100 mL of a mercury plating solution, consisting of 0.03 M perchloric acid and 0.003 M mercury (II) perchlorate. Plating was carried out by holding the potential of the working electrode at – 1.00 V (vs. SCE) for various lengths of time and immediately removing the electrode from the solution after plating was complete.

After removal from the solution the electrode was rinsed with UHQ water and AFM images obtained. Imaging was carried out with each metal for a number of different deposition times. In the copper electrode case, some further AFM images were recorded 24 hrs later to see if the nature of the surface had changed.

10.4. Experimental Results and Discussion

The effect of mercury plating copper and iridium electrodes was investigated using AFM imaging. A number of different deposition times were used as shown in Table 10.1.

Substrate Material	Deposition Time *s*	Deposition Potential *V (vs. SCE)*
Iridium	60	0.0
	120	0.0
	360	0.0
Copper	10	–1.0

Table 10.1 Deposition times and potentials used for carrying out the mercury plating.

The resulting AFM images are shown in Figure 10.4 and Figure 10.5. Uncoated electrodes are also shown for comparison. The images in Figure 10.4b, c and d show the presence of droplets on iridium.

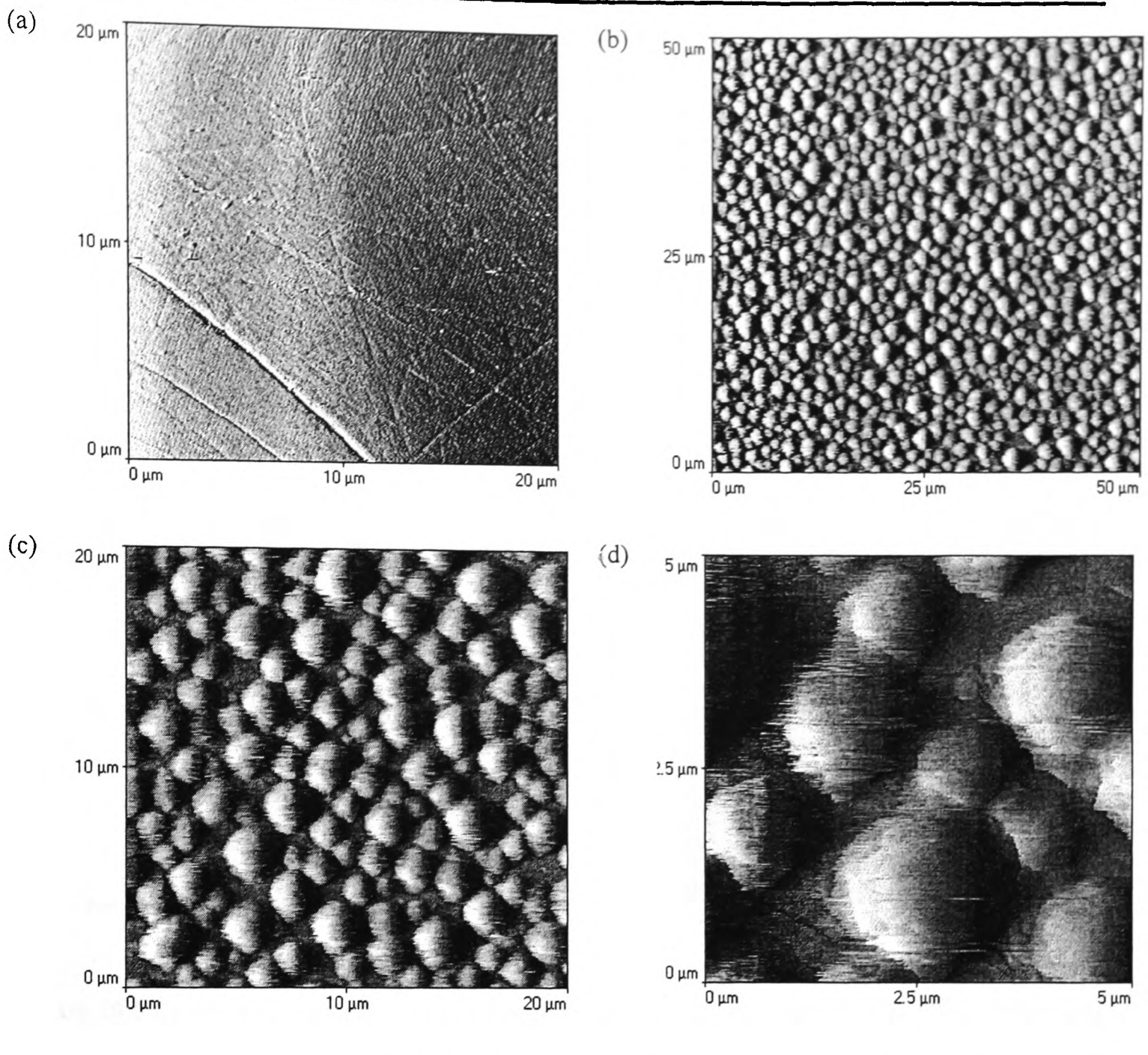


Figure 10.4 *Ex situ* AFM images of a) a polished iridium electrode, b), c) and d) same electrode as in (a) after 360 s of mercury deposition at 0.0 V (shown at different magnifications).

Droplets were formed over a large range of deposition times, although the range of sizes observed varied; the droplets ranged from 0.5 to 1.0 µm in diameter after 60 s deposition time, 0.5 to 1.2 µm after 120 s and from 1.0 to 2.5 µm in diameter after 360 s deposition time.

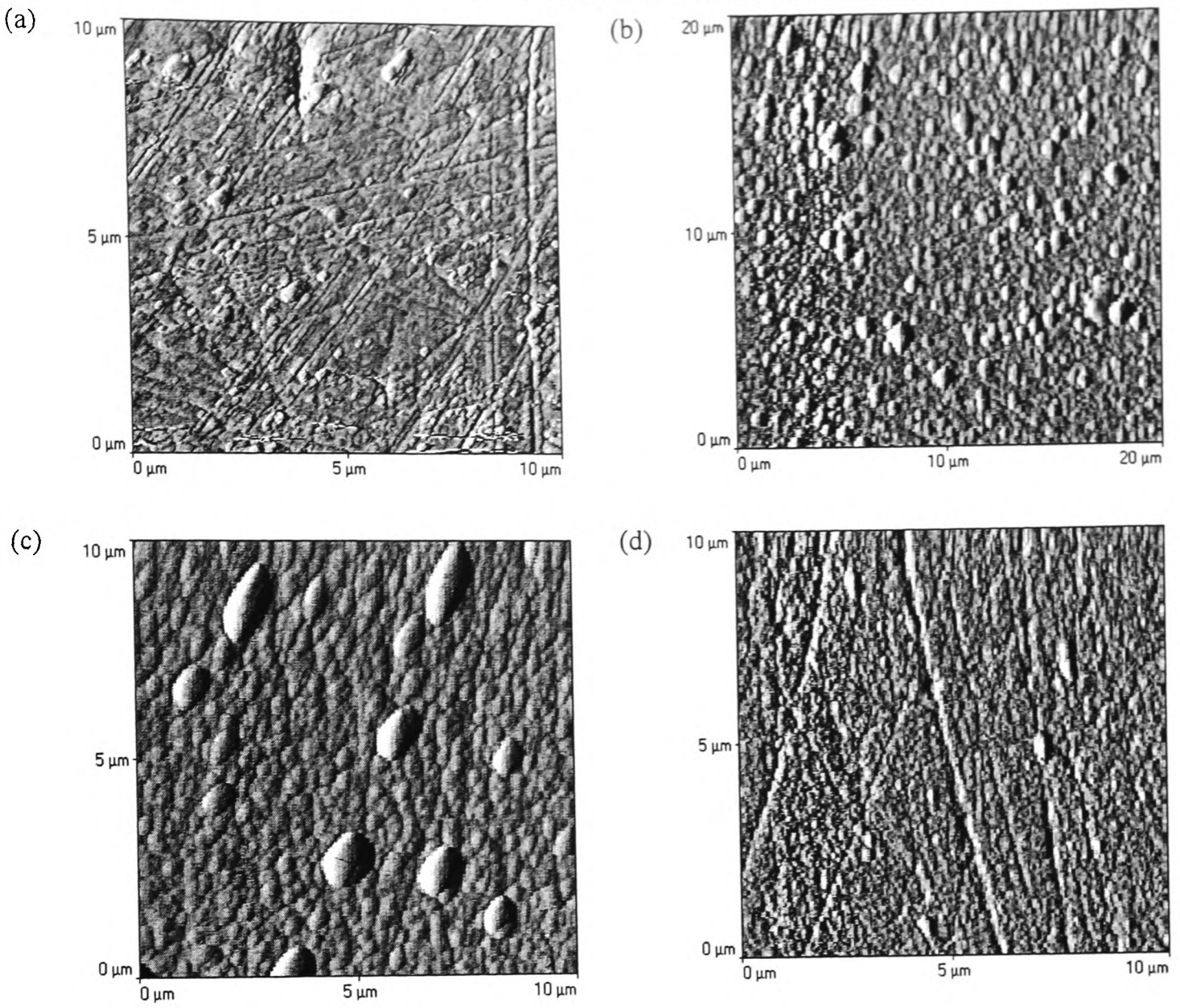


Figure 10.5 *Ex situ* AFM images of a) a polished copper electrode, b) and c) same electrode as in (a) after 10 s of mercury deposition at –1.0 V, and d) the same mercury plated copper electrode as in (b) and (c) after 24 hrs stored in UHQ water.

Repeated scanning of an area 10 µm square showed that the mercury droplets reduced in size, possibly due to the AFM tip removing the mercury. A 20 µm square area was then scanned, that contained the original area, and it was visible that the droplets had been largely removed in the area that had been repeatedly scanned, supporting the interpretation that they were indeed droplets of mercury.

The images in Figure 10.5b and c show the presence of droplets, typically with a diameter of 0.8 to 1.2 µm, on the surface of copper. It is noted from the phase diagram of the Cu-Hg system (see Figure 10.6)[24,25] that the phase consisting of mercury with some dissolved copper is unstable with respect to a copper-mercury alloy, and ultimately in the presence of excess copper this alloy is unstable with respect to

mercury dissolved in copper. A significant change in the nature of the surface is evident in Figure 10.5d, this AFM being recorded 24 hrs after the deposition was carried out.

The AFM images in both Figure 10.4 and Figure 10.5 provide firm support for the existence of mercury in the form of approximately hemispherical droplets, rather than a continuous film, under certain conditions on both iridium and copper substrates. Accordingly we next turn to the results of the simulations to predict the effects of surface morphology on the voltammetric response to the square wave anodic stripping experiment.

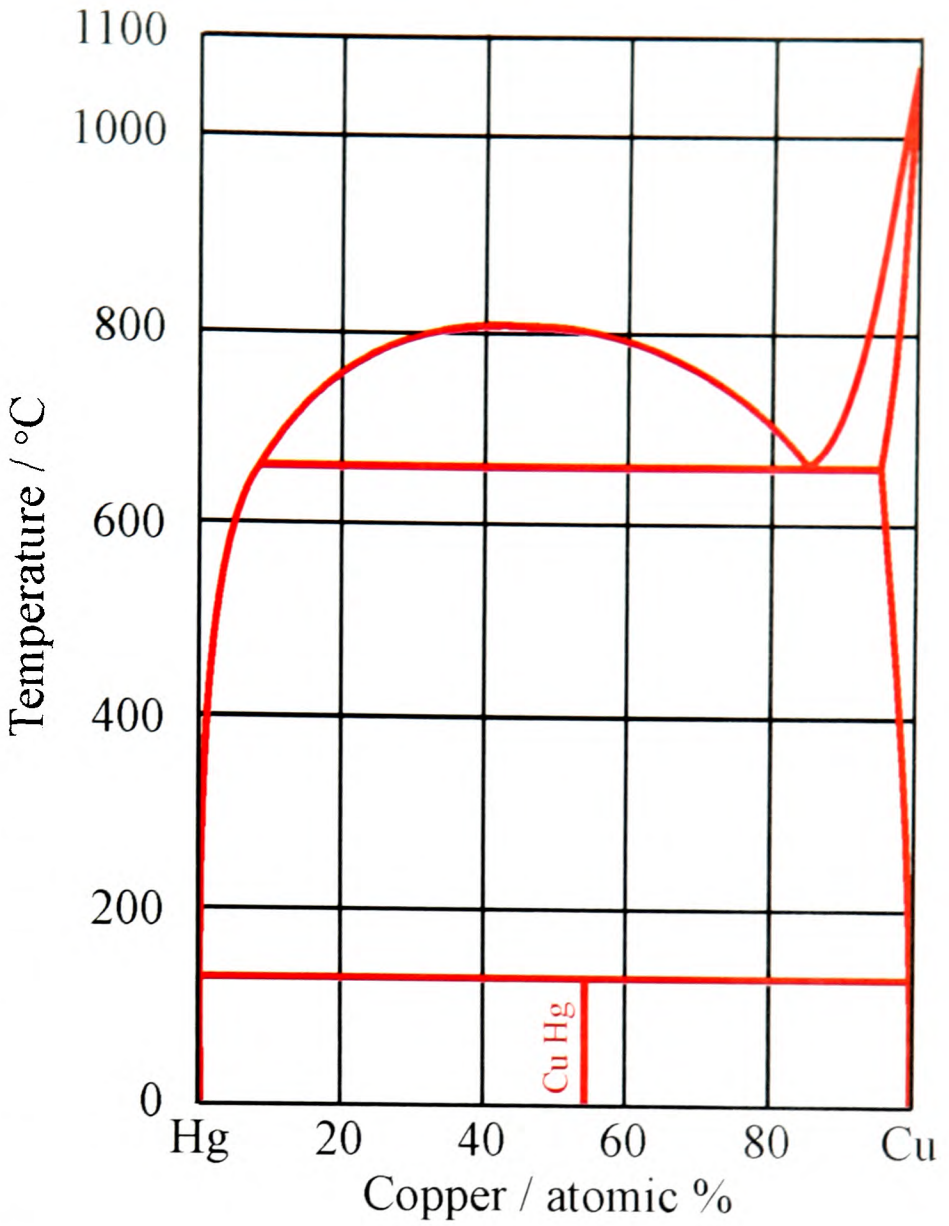


Figure 10.6 The copper-mercury phase diagram.

10.5. Theoretical Results and Discussion

10.5.1. Validation

We consider first results obtained for transport to a planar electrode (simulated using an inert centre system with $R_e = 1000$ μm) under conditions of semi-infinite diffusion noting that this limit has been explored via simulation earlier in chapter 6 and analytically by Kounaves et al[21] for the case of electrochemically reversible systems. A value of $A_1 = 10$ cm s^{-1} was chosen to simulate the electrochemically reversible limit. Voltammograms were obtained for a range of values of film thickness, from $m = 0.03$ μm to $m = 300$ μm, and the characteristic peak shift (the voltage at which the peak in the voltammogram occurs measured relative to $E^{o\prime}$) value recorded in each case. The film thickness values and other parameters were chosen to duplicate Figure 6.4 in §6.3. The satisfying correlation with the literature of simulated values of peak shift versus log Λ, where Λ is[21]

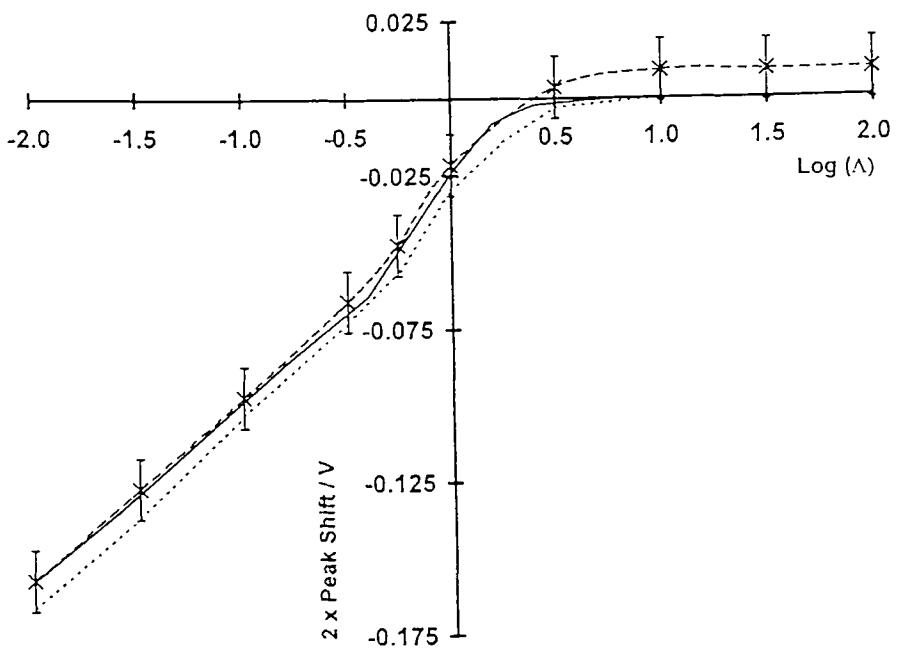


Figure 10.7 Dependence of the peak shift on log Λ. Other parameters are as discussed in the text. The long dashed line shows the results of the simulation, while the solid line shows the work from chapter 6 and the short dashed line that of Kounaves and co-workers.[21] The error bars* and the y-axis scale† are discussed below.

* The error bars in Figure 10.7 and Figure 10.8 arise form the fact that the voltage steps in the simulation are of 5 mV amplitude so that the potential shift values associated with any value of Λ have a maximum uncertainty of this size. For all the points the predictions of the previous work lie within the error bars.

$$\Lambda = m\left(\frac{f}{D_a}\right)^{1/2} \qquad (10.39.)$$

can be seen in Figure 10.7, where f is the frequency in hertz. Similarly voltammograms for a range of values of nE_{SW}, from 1 mV to 100 mV, were simulated and characteristic peak shifts and peak widths (the width of the voltammogram peak at half its maximum height) recorded, to replicate Table I in reference 21. The excellent agreement is shown in Figure 10.8. The ability to quantitatively reproduce results in the literature vindicates both the general method and approach used here and its implementation.

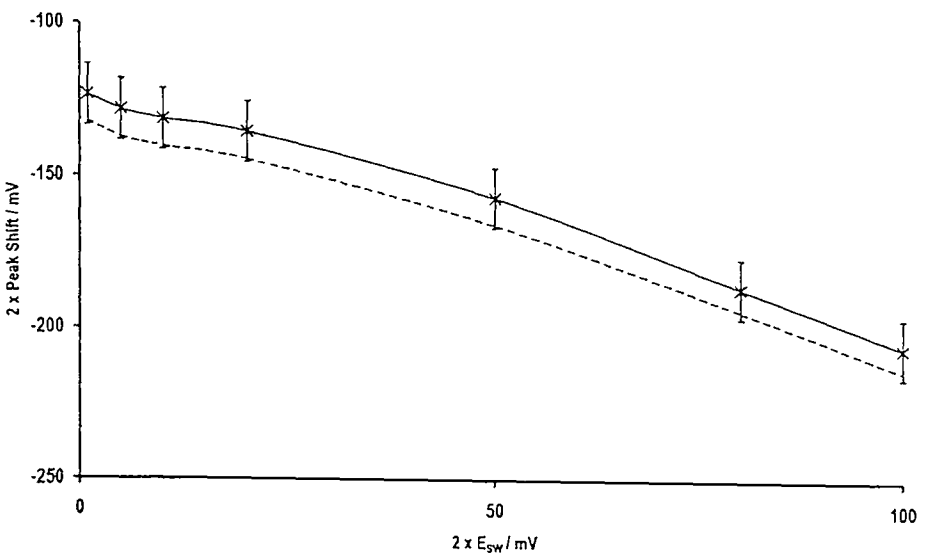


Figure 10.8 Variation in a) peak shift* with nE_{SW} and b) peak width with nE_{SW}. The solid line shows the results of the simulation, while the dashed line shows the work of Kounaves and co-workers.[21] Plotted values are multiplied by two.†

10.5.2. Quasi-reversible and Irreversible Response of Planar Electrodes

The simulation is not limited to electrochemically reversible systems, but can be readily extended to consider quasi-reversible and irreversible electrode kinetics for various film and diffusion layer thicknesses. In order to investigate the influence of both the kinetics and film thickness on the square wave ASV, voltammograms were simulated for films of varying thickness (m = 0.1, 1.0, 3.0, 6.0, 10.0 and 16.0 μm) at a range of different values of A_1 from 1×10^{-5} cm s^{-1} to 10 cm s^{-1}. For all combinations

† All plotted values of peak shift, peak width and square wave amplitude are shown multiplied by two (where two is the number of electrons transferred in the redox couple being simulated). This is done for consistency with the literature[21] and chapter 6 where values are plotted, for example, as nE_{SW}.

simulations were performed where either the first step or second step is rate limiting, using equations (10.6.) and (10.7.) respectively. Other experimental parameters are given in Table 10.2. The characteristic peak shift and peak widths of each voltammogram were recorded, and their dependence on film thickness, rate determining step and A_1 is shown in Figure 10.9.

Parameter	**Symbol**	**Value**	**Units**
Electrode radius	R_e	1000.0	μm
Diffusion layer thickness	δ	200.0	μm
Diffusion constant – reduced species[i]	D_a	1.0×10^{-5}	$cm^2\ s^{-1}$
Diffusion constant – oxidised species	D_b	1.0×10^{-5}	$cm^2\ s^{-1}$
Rate constant	A_1	10.0	$cm\ s^{-1}$
Tafel coefficients	$\alpha_1 = \alpha_2$	0.5	
Starting voltage of scan	E_i	-1.0	V
Finishing voltage of scan	E_f	0.0	V
Pulse amplitude	E_{SW}	0.05	V
Step voltage of the staircase	ΔE	0.01	V
Formal potential of redox couple	$E^{o\prime}$	-0.5	V
Frequency	f	200	Hz
Temperature	T	298	K
Initial concentration of reduced species	$[RED]_{t=0}$	1.0×10^{-3}	M

Table 10.2 Parameters used for the simulations. These values were used unless another value is specified in the text.[i] This value was used for all calculations except the validation (comparison with results obtained in chapter 6 and reference 21), where the value 2×10^{-5} $cm^2\ s^{-1}$ was used.

As the value of A_1 is lowered from 10 $cm\ s^{-1}$ (beyond the totally reversible limit) there is initially no alteration in peak shift or peak width, regardless of the film thickness or which step is rate determining (Figure 10.9a and b). However, when the value of A_1 is dropped below a certain critical value peak shifts move to increasingly positive potentials. A lower value of A_1 makes both the backward and forward reaction rates smaller, thus as A_1 is decreased more positive potentials are required to achieve equivalent oxidation rates and consequently the maximum current occurs at a higher potential.

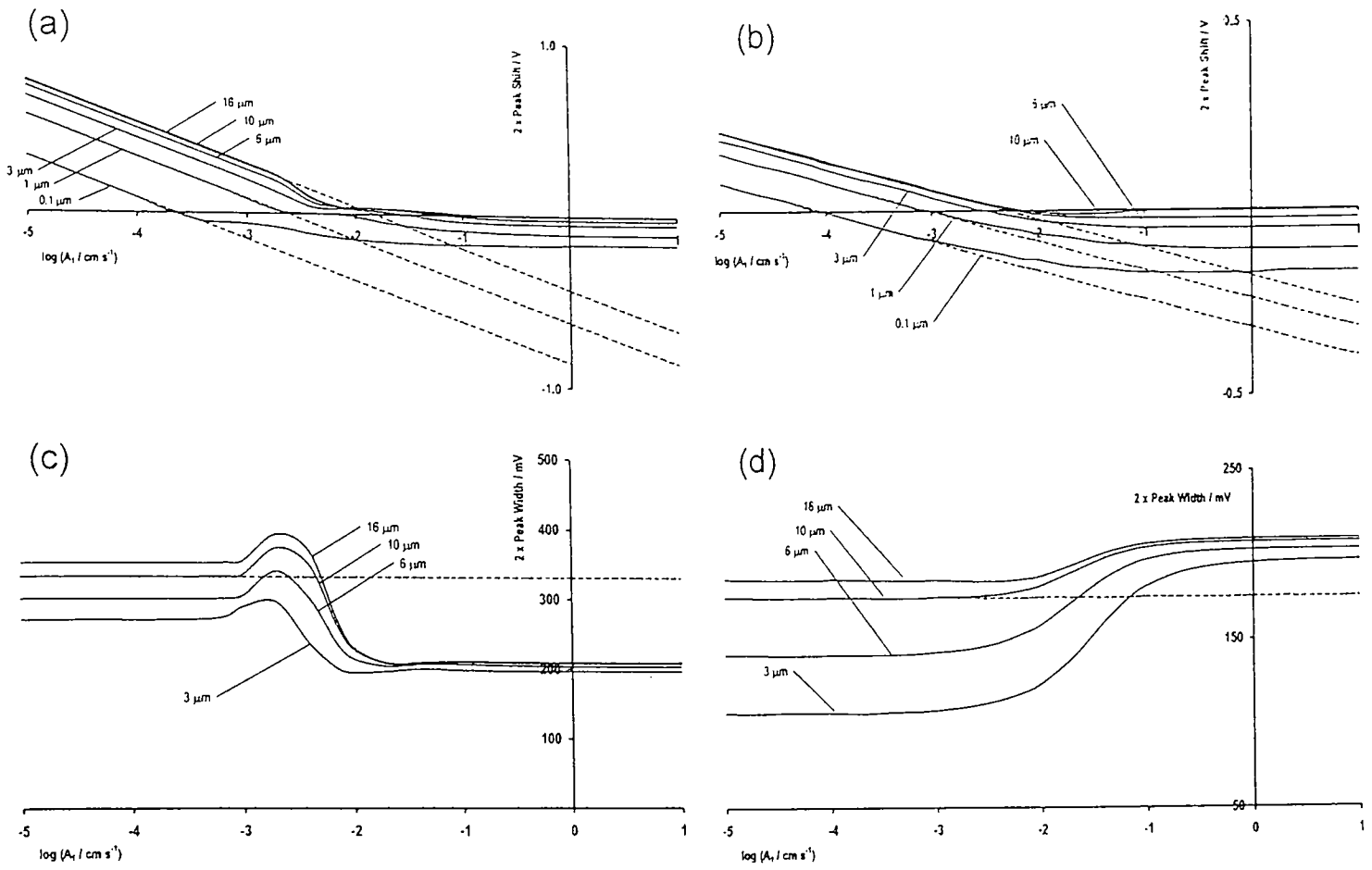


Figure 10.9 Simulated results for thin film system: a) peak shift, first step rate determining [as introduced in text] b) peak shift, second step rate determining c) peak width, first step rate determining d) peak width, second step rate determining as a function of the logarithm of heterogeneous rate constant, A_1. The different lines correspond to mercury films of differing thickness. The solid lines show the results for the quasi–reversible system, while the dashed lines show the results for pure irreversible kinetics (only shown for three of the film thicknesses for clarity).

The critical value of A_1 provides the boundary between two distinct regions in the variation of peak shift with A_1. At high A_1 values the peak shift shows no dependence on the rate constant. This is the diffusion controlled regime. At low A_1 values an increase in peak shift with decreasing A_1 is observed; the (electrode) kinetically controlled region.

When a totally irreversible electrode process is simulated, Figure 10.9a and b, the linear variation of peak shift with the logarithm of the rate constant seen at low A_1 values (the kinetically controlled regime) continues for all values of A_1. This is because the absence of the reverse step means that product materials present near the electrode cannot be converted back into the starting material, thus their rate of diffusion from the electrode surface is no longer significant. The rate of diffusion of the starting material to the electrode is still important in determining the overall rate of conversion of material, but as this is constant the peak position is now controlled

by the rate constant as it is this that controls how quickly an equilibrium concentration profile is set up, and thus the position of the peak in the voltammogram.

The peak shift is also observed, Figure 10.9a and b, to become more positive when the thickness of the electrode is increased. The increased film thickness means there is a larger volume of mercury, and hence a larger amount of analyte to be oxidised, leading the maximum in the voltammogram to occur at a higher potential.

Another property of the system that the simulation allows us to vary is the rate determining step (rds). No alteration in peak shift with variation in the rds is observed in the diffusion controlled regime, as would be expected. The influence of the rds is, however, clearly seen in the kinetically controlled regime where changing the rate determining process from the first to the second step leads to a decreased dependence of peak shift on the rate constant. This results from more rapid changes in k_b^a close to $E^{o\prime}$ when the second step is rate determining. Thus once the forward pulse potential increases above $E^{o\prime}$ so the oxidation occurs more rapidly, and the maximum current occurs closer to $E^{o\prime}$ and less variation in the peak shift is observed.

The variations in peak width seen in Figure 10.9c and d are more complex, each plot showing three distinct regions. There are two regions where peak width is invariant with changes in A_1, at both low and high values of A_1, and an intermediate, more complex region where peak width varies with A_1. The position of this central region corresponds to values of A_1 at the transition between diffusion controlled and kinetically controlled regimes discussed above.

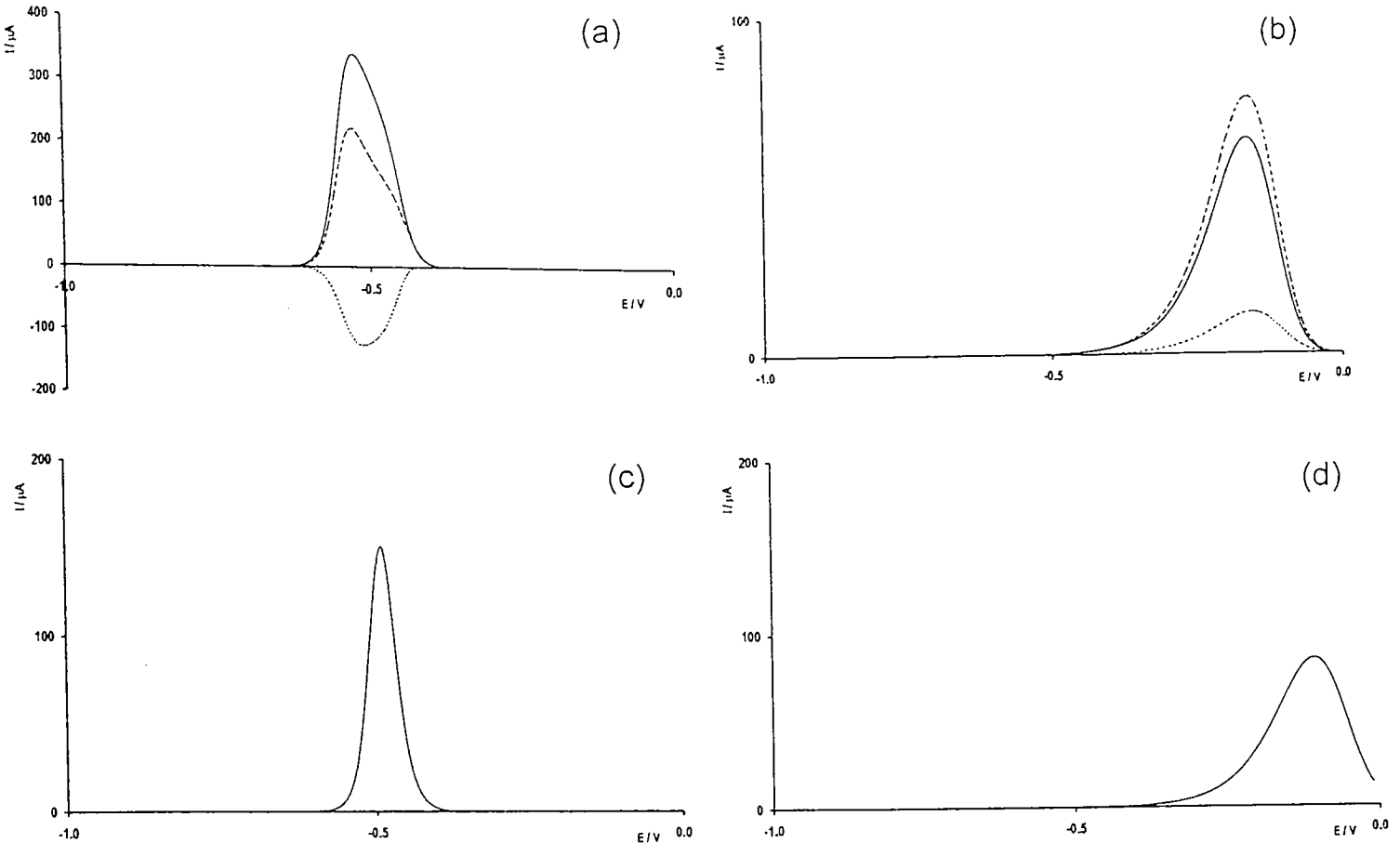


Figure 10.10 Simulated voltammograms for system with first step rate determining [as introduced in text] for R_e = 3 μm and: a) SWV, A_1 = 10.0 cm s^{-1}, b) SWV, A_1 = 1.0 × 10^{-5} cm s^{-1}, c) LSV, A_1 = 10.0 cm s^{-1}, d) LSV, A_1 = 1.0 × 10^{-5} cm s^{-1}. The linear scan voltammograms were obtained by using a modified potential wave form in the simulation.[26]

Examination of Figure 10.9c and d shows the variation in the peak width as A_1 is reduced from large values corresponding to the diffusion controlled, electrochemically reversible limit to those pertaining to the kinetically controlled extreme. Interestingly there is a net increase in peak width on moving from high to low values of A_1 when the first step is rate determining (Figure 10.9c), but a decrease when the second is rate determining (Figure 10.9d). The explanation of this can be most readily appreciated if the square wave voltammograms, together with their individual components $I(1)$ and $I(2)$, are compared with the corresponding linear sweep voltammograms (LSVs). Figure 10.10 and Figure 10.11 make these comparisons for the two kinetic cases of interest. Comparison of the LSVs show that there is a progressive broadening of the voltammetric peak on changing from conditions of electrochemical reversibility (Figure 10.10c and Figure 10.11c) to the cases where there is kinetic control. If the second step (Figure 10.11d) is rate

determining there is a sharper voltammetric response than the case of the first step being rate determining (Figure 10.10d) as would be expected from simple 'Tafel' considerations. On examining the SWVs the reversible limit gives rise to the voltammograms seen in Figure 10.10a and Figure 10.11a. Note the asymmetry of the peak which is due to the large, 50 mV, amplitude of the square wave (E_{SW}) which leads to a significant $I(2)$ component even at relatively positive potentials. In comparison, Figure 10.11b, for the case of the second step being rate determining there is a narrowing of the peak largely because the near-irreversibility of the electrode kinetics shifts the voltammetric feature anodically so that the $I(2)$ component is negligible. In contrast for the case (Figure 10.10b) where the first step is rate determining there remains a significant $I(2)$ component, despite the greater anodic shift, because of the increased sensitivity of the back (reduction) reaction to the electrode potential: this leads to the peak being broadened in comparison with the reversible case.

It is observed that the peak width increases with increasing film thickness (Figure 10.9c and d), attributable to the larger amount of material to oxidise and the longer time this will take (and hence the greater scan width encompassed in the peak). It is further observed that as expected the peak widths vary more with electrode thickness at low heterogeneous rate constants than they do at high A_1 values.

The effect of a totally irreversible electrode process on peak widths is consistent with the behaviour of peak shifts; the pattern observed at low values of A_1 continues throughout. That is the peak width transition from the kinetically controlled to diffusion controlled characteristic widths is not observed, but the width remains constant at the width characteristic of the kinetically controlled system, as diffusion of products away from the electrode is no longer a limiting factor.

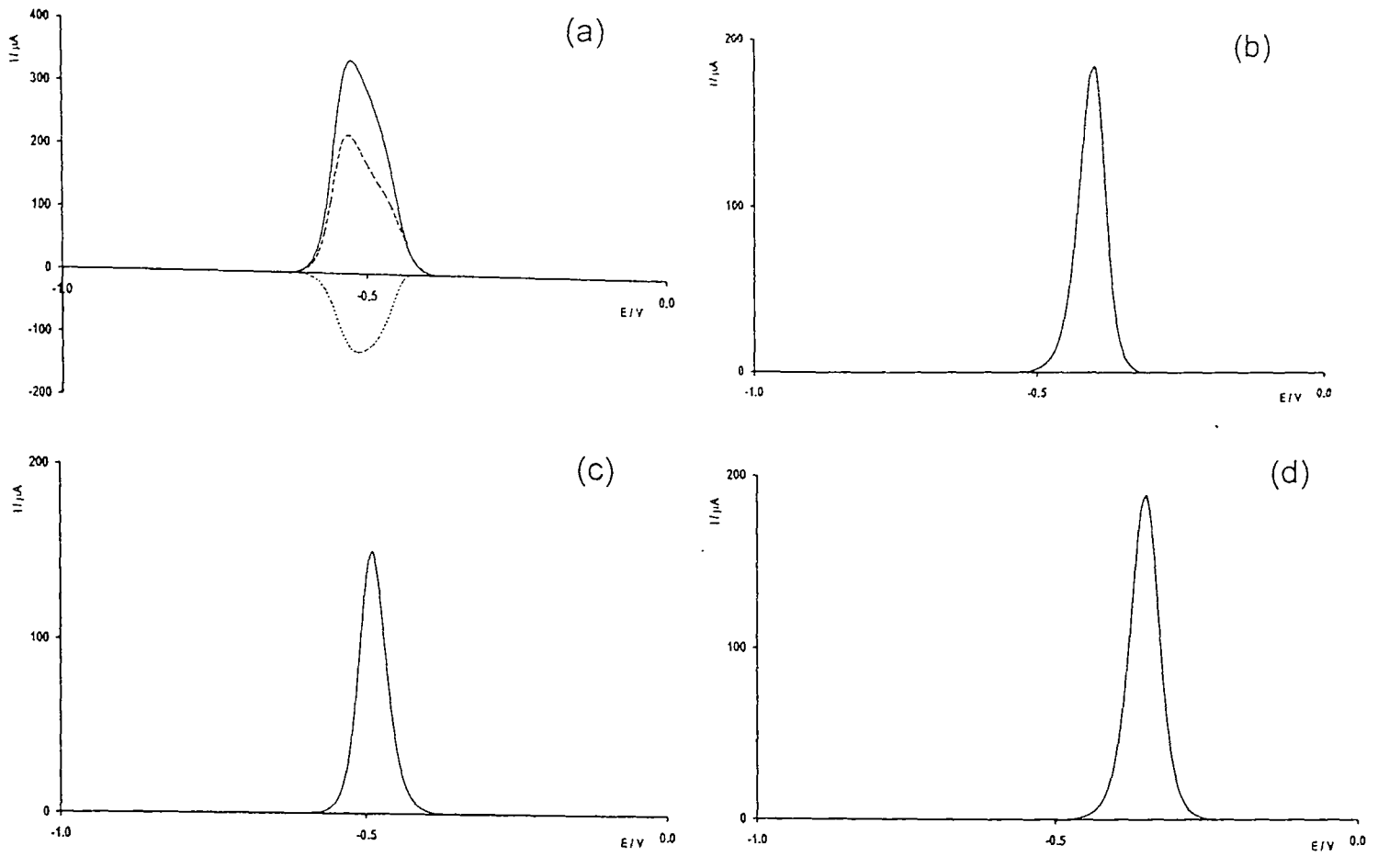


Figure 10.11 Simulated voltammograms for system with second step rate determining [as introduced in text] for R_e = 3 μm and: a) SWV, A_1 = 10.0 cm s^{-1}, b) SWV, A_1 = 1.0 × 10^{-5} cm s^{-1}, c) LSV, A_1 = 10.0 cm s^{-1}, d) LSV, A_1 = 1.0 × 10^{-5} cm s^{-1}. The linear scan voltammograms were obtained by using a modified potential wave form in the simulation.[26]

10.5.3. Hemispherical Electrodes

The simulation allows the modelling of a hemispherical electrode system. To investigate the influence of both the kinetics and electrode radius on the square wave ASV for this system characteristic voltammograms were again simulated and characteristic peak shift and peak width values recorded. The results of simulations of several electrode radii (R_e = 0.1, 1.0, 3.0, 6.0, 10.0 and 16.0 μm) at a range of different values of A_1 from 1 × 10^{-5} cm s^{-1} to 10 cm s^{-1}, for systems where both the first and second step are rate determining (other experimental parameters are given in Table 10.2) can be seen in Figure 10.12

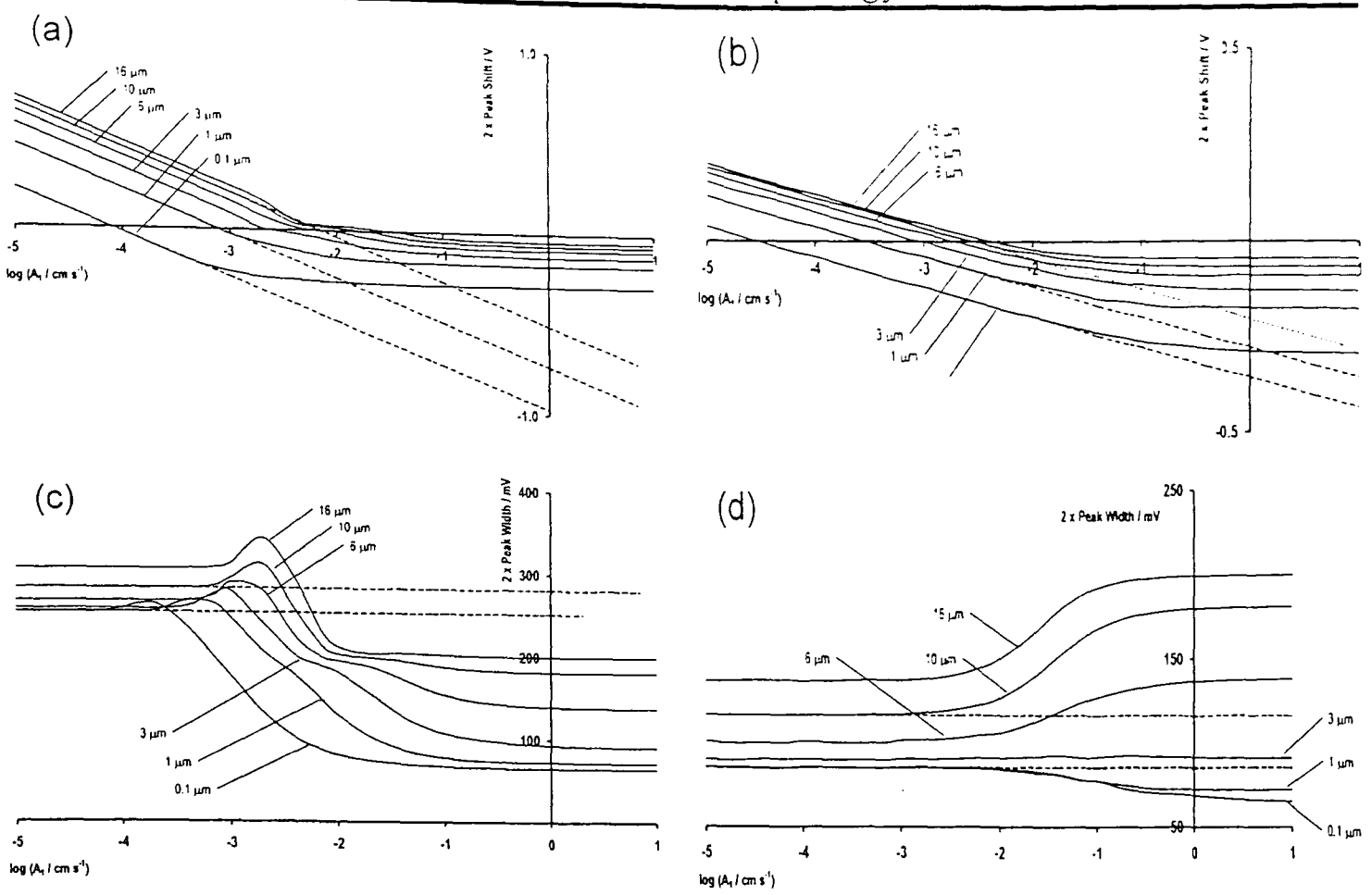


Figure 10.12 Simulated results for droplet system: a) peak shift, first step rate determining [as introduced in text] b) peak shift, second step rate determining c) peak width, first step rate determining d) peak width, second step rate determining as a function of the logarithm of heterogeneous rate constant, A_1. The different lines correspond to mercury hemispheres of differing radius. The solid lines show the results for the quasi–reversible system, while the dashed lines show the results for pure irreversible kinetics (only shown for three of the electrode radii for clarity)

The broad trends are qualitatively similar to those observed for the inert centred system discussed earlier, but the quantitative details differ significantly. The diffusion and kinetic control regimes are still present, as is the increase in peak shift value with decreasing A_1, below a critical value of A_1 (the quasi-reversible region) and at all values of A_1 in the totally irreversible limit.

It is observed that the peak shift potential increases with increasing electrode radius, as a result of the increased amount of analyte (Figure 10.12a and b). However, there is a greater dependency of peak shift on variation in the electrode radius than with an equivalent variation in the film thickness in the inert centred electrode case, Figure 10.13a. This results in part from a more marked increase in the volume of mercury, and hence analyte, with electrode radius in the hemispherical case (doubling the diameter of the hemispherical electrode causes the volume of mercury to go up eight-

fold, but increasing the film thickness in the inert centred cases has a much smaller effect on the volume of mercury as it is around a large inert centre), but also from the enhanced mass transport at the hemispherical electrode.

Peak widths again show three distinct regions, reducing to the peak width being invariant with A_1 in the totally irreversible limit, but there are marked differences. In the inert centre case there is a net decrease in peak width on moving to higher values of A_1 when the first step is the rate determining (Figure 10.9c), and an increase when the second step is the rate determining (Figure 10.9d). The hemispherical system, however, is more interesting. It again shows a decrease when the first step is rate determining (Figure 10.12c), but the relative widths lead to a spreading out of peak width with increasing A_1 when the second step is rate determining (Figure 10.12d).

In all cases, for both electrode geometries, the peak width increases with increasing electrode diameter / film thickness[‡], attributable to the larger amount of material to oxidise (and hence the greater scan width encompassed in the peak). However in the inert centre case, whilst the peak widths increase more with electrode thickness, at low values of A_1 than they do at high A_1 values (Figure 10.9c and d), the opposite is true in the case of the hemispherical system (Figure 10.12c and d). In the kinetically controlled limit for the hemispherical system, with increasing radius there is also a large increase in surface area for electrode reaction. So although there is an increase in the amount of material to oxidise and a reduction in the enhanced mass transport, there is also an increase in surface area at which this kinetically limited process can be carried out, hence minimising the increase in peak width with increase in electrode radius. In the system with an inert centre the change in surface area is less relative to

‡ Thickness applies to the thickness of mercury, outside the inert centre, in the case of the pseudo thin film electrode system, and electrode diameter applies to the diameter of the hemisphere of mercury in the hemispherical system.

the volume, as an alteration in the film thickness only has a small effect on the overall radius of the electrode, so the dependence of peak width on film thickness is greater. In the diffusion controlled limit of the hemispherical system, the peak width increases rapidly with electrode radius due to the equally sharp increase in material available for oxidation and decrease in

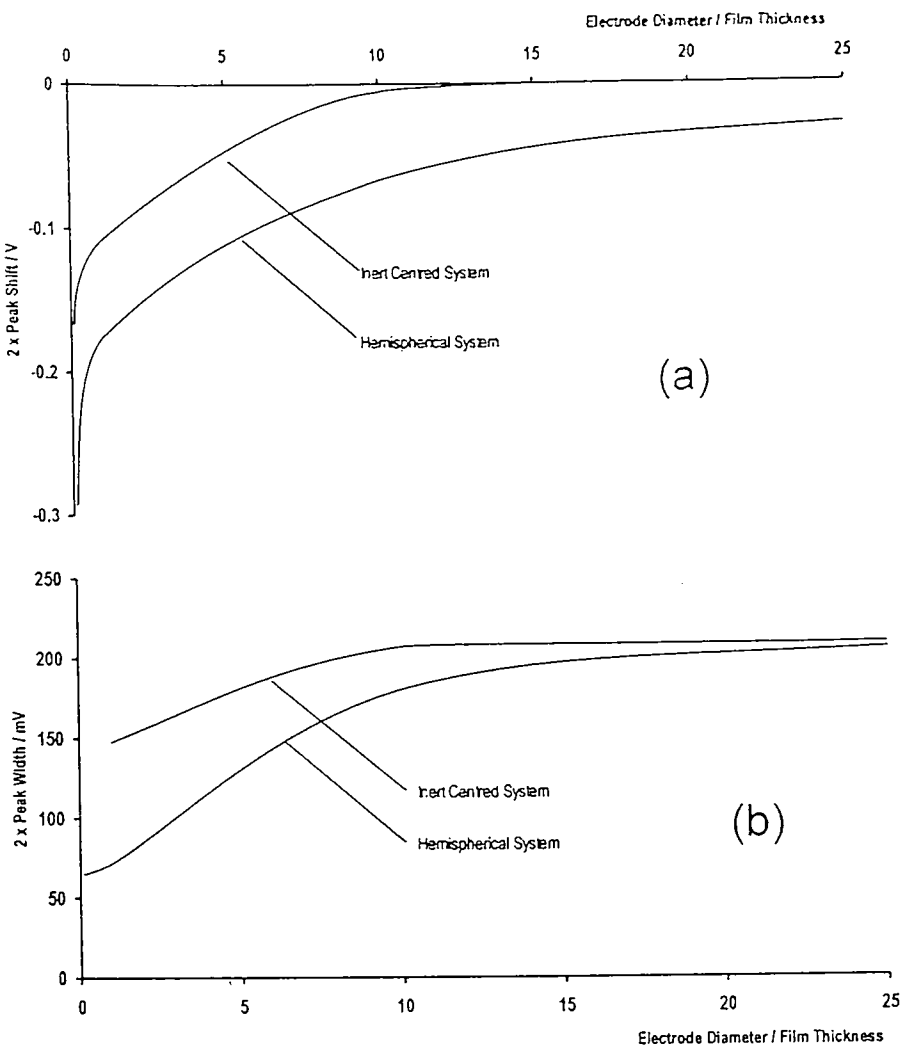


Figure 10.13 Variation with electrode radius / film thickness‡ of a) peak shift and b) peak width. Results are simulated for the reversible limit (A_1 = 10.0 cm s^{-1}) in all cases.

the enhanced mass transport, whereas the effect of film thickness in the inert centre case is less marked as the electrode is already of substantial radius. Further trends are also visible in the peak width variation.

Firstly, the peak widths show a greater variation with changes in electrode radius in the hemispherical system than for an equivalent variation in the film thickness of the inert centred system, as was observed with the peak shift and for the same reasons, Figure 10.13b.

Secondly, with increasing electrode radius the enhanced mass transport that exists to the hemispherical electrode is depleted, and the diffusion become increasingly like that to a uniform film. Consequently both the characteristic peak widths, and peak shifts, of the inert centred and hemispherical systems tend to the same value as the electrode radius / film thickness‡ is increased (Figure 10.13).

10.6. Conclusions

AFM evidence of mercury existing as droplets of mercury on both iridium and copper substrates, under certain conditions, has been presented. Simulations of square wave ASV at hemispherical electrodes have been produced for reversible, irreversible and quasi-reversible redox couples. The simulation of square wave ASV at uniform thin films has been extended, from the reversible limit, to encompass irreversible and quasi-reversible redox couples. The simulations have revealed significant quantitative differences between the behaviour at electrodes of these two geometries. Moreover the value of simulations in facilitating the understanding of the voltammetric responses, as illustrated for example by the generation of Figure 10.10 and Figure 10.11 in respect of gaining insight into Figure 10.9, is again evident.

References for Chapter 10

[1] M. Štulíková, *J. Electroanal. Chem.* 48 (1973) 33
[2] H.P. Wu, *Anal. Chem.* 66 (1994) 3151
[3] N.F. Zakharchuk, K.Z. Brainina, *Electroanalysis* 10 (1998) 379
[4] R.P. Akkermans, J.C. Ball, F. Marken, R.G. Compton, *Electroanalysis* 10 (1998) 26
[5] W.S. Kruijt, M. Sluyters-Rehbach, J.H. Sluyters, A. Milchev, *J. Electroanal. Chem.* 371 (1994) 13
[6] S.P. Kounaves, W. Deng, *J. Electroanal. Chem.* 301 (1991) 77
[7] S.P. Kounaves, J. Buffle, *J. Electroanal. Chem.* 216 (1987) 53
[8] T.G.J. Van Venrooij, M. Sluyters-Rehbach, J.H. Sluyters, *J. Electroanal. Chem.* 419 (1996) 61
[9] J.A. Alden, F. Hutchinson, R.G. Compton, *J. Phys. Chem. B.* 101 (1997) 949
[10] C. Amatore, B. Fosset, *Anal. Chem.* 68 (1996) 4377
[11] R.A.W. Dryfe, DPhil Thesis, Oxford University, (1995) pp82
[12] M.J. Bidwell, J.A. Alden, R.G. Compton, *J. Electroanal. Chem.* 417 (1996) 119
[13] J.A. Alden, R.G. Compton, *J. Phys. Chem. B* 101 (1997) 8941
[14] J.L. Anderson, S. Moldoveanu, *J. Electroanal. Chem.* 179 (1984) 107
[15] R.G. Compton, M.B.G. Pilkington, G.M. Stearn, *J. Chem. Soc., Faraday Trans. I*, 84 (1988) 2155
[16] L.H. Thomas, *Elliptical problems in linear equations over a network*, Watson Sci. Comput. Lab. Rept., Columbia University, New York, (1949)
[17] P. Laasonen, *Acta Math.*, 81 (1949) 30917
[18] G.H. Bruce, D.W. Peaceman, H.H. Rachford, J.D. Rice, *Trans. Am. Inst. Min. Engrs.* 198 (1953) 79
[19] A.C. Fisher, R.G. Compton, *J. Phys. Chem.* 95 (1991) 7538
[20] A.C. Fisher, R.G. Compton, *J. Appl. Electrochem.* 22 (1992) 38
[21] S.P. Kounaves, J.J. O'Dea, P. Chandresekhar, J. Osteryoung, *Anal. Chem.* 59 (1987) 386
[22] R.G. Compton, J.C. Eklund, S.D. Page, *J. Phys. Chem.* 99 (1995) 4211
[23] J. Wang, J. Wang, B. Tian, M. Jiang, *Anal. Chem.* 69 (1997) 1657
[24] D.J. Chakrabarti, D.E. Laughlin, *Bull. Alloy Phase Diagrams* 6 (1985) 522
[25] E. Lugscheider, J. Gerhard, *Z. Metallk.* 62 (1971) 548
[26] J.C. Ball, R.G. Compton, *Electroanalysis* 9 (1997) 1305

A1 Effluent Data from BP Chemicals Ltd, Hull Site

This appendix details the data supplied by BP Chemicals, Hull for the average composition of the effluent data for the run-off of the Acetate plant. The data contained is from the year 1997.

A1.1. pH Data

Figure A1.1 shows a frequency histogram for the pH of the effluent . Table A1.1 shows the statistics for the histogram. From both the histogram and the statistics we can see that the most commonly encountered pH range is 4.5-8.5. This is why the experiments in chapter 4 were designed using acetate buffer of approximately pH 5-5.5. The next section looks at the daily composition of copper in the effluent outflow and sets the values that detection limits in chapter 4 must be below for the methodology developed to be useful in an online industrial sense.

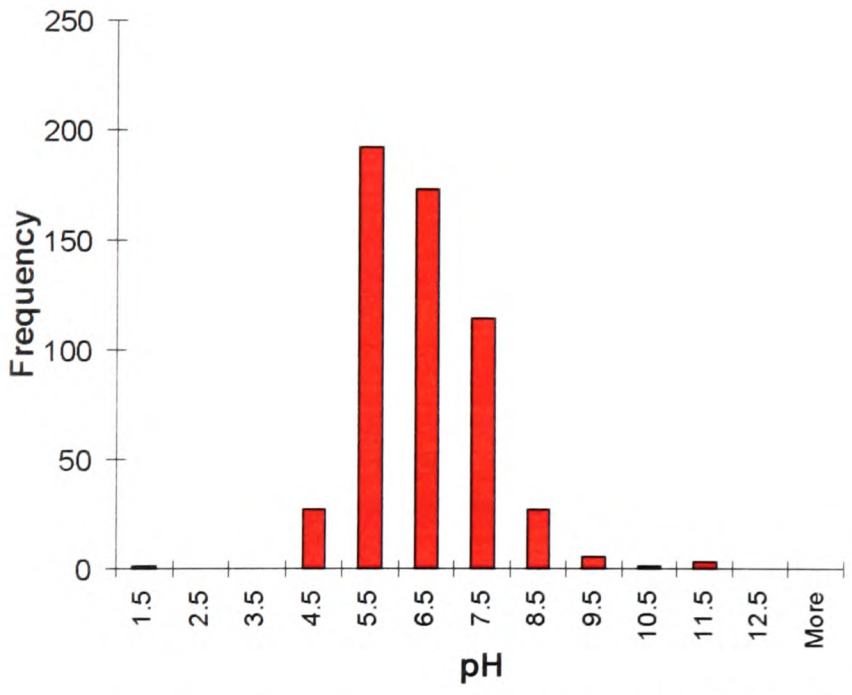


Figure A1.1 A frequency histogram showing the variation of pH of the effluent for the year 1997.

Statistics	pH
Size	548.0000
Mean	5.9708
Median	5.9000
Variance	1.1789
Standard Deviation	1.0858

Table A1.1 Showing the sample size and main statistics for the pH distribution shown in Figure A1.1

A1.2. Copper Data

The data in Figure A1.2 shows the distribution of copper concentrations using ICPMS (Inductively Coupled Plasma Mass Spectrometry) at 8 hour intervals for the year 1997 at the BP Chemicals site. The relevant statistics are shown in Table A1.2. From both of these it can be easily seen that the methodology described in chapter 4 is perfectly capable of detecting the concentrations of copper present in the effluent. The Acetate buffer solution used as a laboratory model is a good substitute for testing the methodology as the pH is within the region expected and it is reasonable to expect that the run off from the acetate plant would indeed contain acetate.

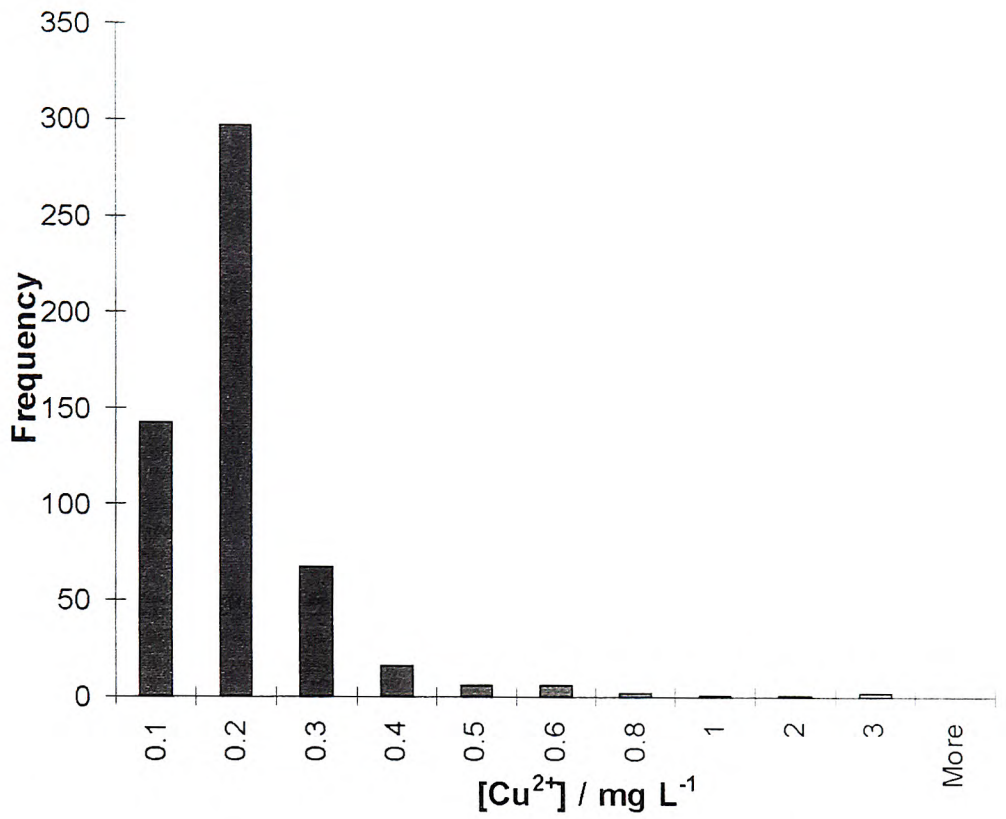


Figure A1.2 A histogram showing the frequency of the copper concentration from the output from the BP Chemicals acetate plant.

Statistics	C1
Size	543.0000
Mean	0.2110
Median	0.2000
Variance	0.0286
Standard Deviation	0.1692

Table A1.2 Showing the sample size and main statistics for the Cu concentration distribution shown in Figure A1.2

A2 Computer Program Source Code Listings

This appendix contains the source code listing for many of the programs used in the main body of the thesis. Some are omitted as they are very similar to previous ones.

A2.1. The Online Buffer Calculator (C/C++)

```
//Main.c++ : Main program //

#include "cgiutil.h"
#include <math.h>
#include <stdlib.h>
#include <stdio.h>
#include <string.h>
#include <iostream.h>
#include <iomanip.h>

#define MAX_ENTRIES 10000
#define BGSHADE "#000040"

double x,y,z,pKa,*beta,K12,K22,KD,KA;
int n,i;

double sumsim(int n,double *,double ,int m=0);  // m is the derivative
double sumderiv(int,double*,double);
double deriv(double);
double rtsafe(void (*funcd)(double, double *,double *),double ,double ,double ,int);
void buffer(double ,double *,double *);
void get_log_K_values(char*,double*,double*,int);
int length_of_lK(char *);

int main(int argc,char *argv[])
{
        double *K,*u,lK,a,b,c,d;
        int j,MAXIT;
        entry entries[MAX_ENTRIES];
        register int i,xx,mm=0;
        int cl;


        printf("Content-type: text/html%c%c",10,10);

        // Standard CGI parsing
        if(strcmp(getenv("REQUEST_METHOD"),"POST"))
        {
                printf("This script should be referenced with a METHOD of POST.\n");
                printf("If you don't understand this, see this ");
                printf("<A
HREF=\"http://www.ncsa.uiuc.edu/SDG/Software/Mosaic/Docs/fill-out-
forms/overview.html\">forms overview</A>.%c",10);
                exit(1);
        }
        if(strcmp(getenv("CONTENT_TYPE"),"application/x-www-form-urlencoded"))
        {
                printf("This script can only be used to decode form results. \n");
                exit(1);
        }
        cl = atoi(getenv("CONTENT_LENGTH"));

        for(xx=0;cl && (!feof(stdin));xx++)
        {
                mm=xx;
                entries[xx].val = fmakeword(stdin,'&',&cl);
                plustospace(entries[xx].val);
                unescape_url(entries[xx].val);
                entries[xx].name = makeword(entries[xx].val,'=');
        }

        /* Web Page */
        printf("<!DOCTYPE HTML PUBLIC \"-//IMECHF//DTD HTML//EN\"><HTML
VERSION=\"2.0\">\n");
        printf("<HEAD><TITLE>Buffer Speciation Calculator: Results</TITLE></HEAD>\n");
        printf("<BODY LINK=\"#CFCFFF\" VLINK=\"#9F9FFF\" TEXT=\"#D9D9D9\"
BGCOLOR=\"%s\"> \n",BGSHADE);
```

```
        printf("<TABLE WIDTH=\"100%%\" VALIGN=\"CENTER\"><TR><TD><FONT SIZE=7>Buffer
Speciation Calculator: Results</FONT></TD><TD ALIGN=\"RIGHT\"><IMG
SRC=\"../../icons/calc.gif\" ALIGN=\"MIDDLE\"></TD></TR></TABLE>\n<IMG
SRC=\"../../icons/line2.gif\" WIDTH=\"100%%\" HEIGHT=\"4\">\n");

        //Parse for input parameters
        for(xx=0; xx <= mm; xx++)
        {
                if(strcmp(entries[xx].name,"x")==0) sscanf(entries[xx].val,"%lf",&x);
                if(strcmp(entries[xx].name,"y")==0) sscanf(entries[xx].val,"%lf",&y);
                if(strcmp(entries[xx].name,"z")==0) sscanf(entries[xx].val,"%lf",&z);
                if(strcmp(entries[xx].name,"pKa")==0)
sscanf(entries[xx].val,"%lf",&pKa);
                if(strcmp(entries[xx].name,"MAXIT")==0)
sscanf(entries[xx].val,"%d",&MAXIT);
                if(strcmp(entries[xx].name,"K12")==0)
sscanf(entries[xx].val,"%lf",&K12);
                if(strcmp(entries[xx].name,"K22")==0)
sscanf(entries[xx].val,"%lf",&K22);
                if(strcmp(entries[xx].name,"KD")==0) sscanf(entries[xx].val,"%lf",&KD);
                if(strcmp(entries[xx].name,"lK")==0)
                {


                        n=length_of_lK(entries[xx].val);

                        if(n>0)
                        {
                                // Allocate memory for arrays

                                K = new double [n];
                                beta = new double [n];
                                u = new double [n];

                                get_log_K_values(entries[xx].val,K,beta,n);


                                beta[0]=K[0];
                                for (j=1;j<n;j++)
                                        beta[j]=beta[j-1]*K[j];
                        }
                }
        }


        // Convert the logs to real values

        KA=pow(10,-pKa);
        K12=pow(10,K12);
        K22=pow(10,K22);
        KD=pow(10,KD);

        // call Newton-Raphson method to calculate [A-]

        if (MAXIT >10000 && x >0.0)
                b=rtsafe(&buffer,z-y,z+y,x/10000,10000);
        else if(MAXIT <10000 && x > 0.0)
                b=rtsafe(&buffer,z-y,z+y,x/10000,MAXIT);
        else
                b=rtsafe(&buffer,z-y,z+y,z/10000,MAXIT);

        //Calculate the resulting equilibrium concentrations

        a=(y-b-(z*sumsim(n,beta,b)/(1+sumsim(n,beta,b))))/(K12*b-KA/b);  // AH
concentration
        c=z/(1+sumsim(n,beta,b)); // free M concentration
        d=pKa+log10(b/a); //pH of solution

        //Calculate concentration of each metal species
        for (j=0;j<n;j++)
                u[j]=beta[j]*c*pow(b,j+1);

        // Output for Web Page

        printf("<P><TABLE WIDTH=\"100%%\"><TR><TD
WIDTH=\"25%%\"><B>pH</B></TD><TD>%4.2lf</TD></TR>\n",d);
        if(x!=0.0)
        {
                printf("<TR><TD WIDTH=\"25%%\"></TD><TD></TD><TD VALIGN=\"MIDDLE\"
ROWSPAN=%d>%%MA<SUB>j</SUB><SUP>(n-j)+</SUP> = [MA<SUB>j</SUB><SUP>(n-
j)+</SUP>]/[M<SUP>n+</SUP>]<SUB>i</SUB></TD>\n",n+1);
                printf("<TR><TD WIDTH=\"25%%\"><B>%% &quot;Free&quot;
M<SUP>n+</SUP></B></TD><TD>%6.2lf</TD></TR>\n",(c/z)*100);
                for (j=0;j<n;j++)
                        printf("<TR><TD WIDTH=\"25%%\"><B>%% MA<SUB>%d</SUB><SUP>(n-
%d)+</SUP></B></TD><TD>%6.2lf</TD></TR>\n",j+1,j+1,(u[j]/z)*100);
                printf("</TABLE>\n<HR>\n<TABLE WIDTH=\"100%%\">\n");
```

```
                printf("<TR><TD WIDTH=\"25%%\"></TD><TD></TD><TD VALIGN=\"MIDDLE\"
ROWSPAN=2>%%HA<SUB>2</SUB><SUP>-</SUP> = [HA<SUB>2</SUB><SUP>-
</SUP>]/([HA]<SUB>i</SUB>+[A-]<SUB>i</SUB>)</TD>\n");
                printf("<TR><TD WIDTH=\"25%%\"><B>%% HA<SUB>2</SUB><SUP>-
</SUP></B></TD><TD>%6.2lf</TD></TR>\n",(K12*a*b/(x+y))*100);
                printf("<TR><TD WIDTH=\"25%%\"><B>%%
H<SUB>2</SUB>A<SUB>2</SUB></B></TD><TD>%6.2lf</TD></TR>\n",(KD*a*a/(x+y))*100);
//              printf("<TR><TD WIDTH=\"25%%\"><B>[A<SUP>-
</SUP>]</TD><TD>%6.2lf</TD>\n",b);
        }
        printf("</TABLE>");
        printf("<HR COLOR=\"#000070\"><TABLE CELLPADDING=10 CELLSPACING=0 BORDER=0
WIDTH=100%%><TR>\n");
        printf("<TD ALIGN=LEFT>Email : <a
href=\"mailto:richard.compton@chem.ox.ac.uk\">richard.compton@chem.ox.ac.uk</a></TD>\n
");
        printf("<TD ALIGN=RIGHT><FONT SIZE=2>Managed by Jon
Ball.</FONT></TD></TR></TABLE>\n");
        puts("</BODY></HTML>\n");

        return 0;
}

// Newton Raphson Method Algorithm
// Original code can be found on pp362-367 in Numerical Recipes in C (2nd Ed.)

double rtsafe(void (*funcd)(double, double *,double *), double x1, double x2,double
xacc, int MAXIT)
{
        int j;
        double df,dx,dxold,f,fh,fl;
        double temp,xh,xl,rts;

        (*funcd)(x1,&fl,&df);
        (*funcd)(x2,&fh,&df);
        if ((fl > 0.0 && fh >0.0) || (fl < 0.0 && fh <0.0))
                printf("<P><FONT SIZE=5 COLOR=\"#FF0000\"><BLINK>Root cannot be
found</BLINK></FONT>\n");
        if (fl == 0.0) return x1;
        if (fh == 0.0) return x2;
        if (fl < 0.0)
        {  // Orient the search on so that f(x1)<0
                xl=x1;
                xh=x2;
        }
        else
        {
                xh=x1;
                xl=x2;
        }
        rts=0.5*(x1+x2);
        dxold=fabs(x2-x1);
        dx=dxold;
        (*funcd)(rts,&f,&df);
        for (j=1;j<=MAXIT;j++)
        {
                if ((((rts-xh)*df-f)*((rts-xl)*df-f) >=0.0)||(fabs(2.0*f) >
fabs(dxold*df)))
                {
                        dxold=dx;
                        dx=0.5*(xh-xl);
                        rts=xl+dx;
                        if (xl == rts) return rts;
                }
                else
                {
                        dxold=dx;
                        dx=f/df;
                        temp=rts;
                        rts -= dx;
                        if (temp == rts) return rts;
                }
                if (fabs(dx) < xacc) return rts;
                (*funcd)(rts,&f,&df);
                if (f < 0.0)
                        xl=rts;
                else
                        xh=rts;
        }
        printf("<P><FONT SIZE=5 COLOR=\"#FF0000\"><BLINK>Maximum number of iterations
too small for Newton-Raphson algorithm</BLINK></FONT>\n");
        printf("<P><CENTER><FONT SIZE=5 COLOR=\"#FFFF00\">Process
stopped</FONT></CENTER>");
        printf("<P><CENTER>Click <A HREF=\"/research/buffer/buffer.shtml\">HERE</A> to
go back to form page</CENTER>");
        printf("<P>If this problem persists please contact: <A
HREF=\"mailto:richard.compton@chem.ox.ac.uk\">richard.compton@chem.ox.ac.uk</A>
```

```
stating what parameters you used.</p>");
        exit(0);
        return 0.0;
}

// Equations to be solved

void buffer(double c,double *fn,double *df)
{
        double p1,p2,p3,p4;

        p1=z*sumsim(n,beta,c);
        p2=1+sumsim(n,beta,c);
        p3=(y-c-(p1/p2))/(K12*c-KA/c);
        *fn=p3+(KA*p3/c)+K12*p3*c+2*KD*p3*p3-x;
        p4=deriv(c);
        *df=p4+KA*((p4/c)-p3/c/c)+K12*(p3+c*p4)+2*p3*KD*p4;
        return;
}

double deriv(double c)
{
        double p1,p2,value;

        p1=z*sumderiv(n,beta,c)/pow((1+sumsim(n,beta,c)),2);
        p2=z*sumsim(n,beta,c)/(1+sumsim(n,beta,c));


        value=(K12*c-KA/c)*(-1-p1)-(y-c-p2)*(K12+KA/c);
        value=value/pow((K12*c-KA/c),2);
        return value;
}

// Sumation tools

double sumsim(int n,double *val,double c,int m)
{
        double tot=0;
        for (int j=0;j<n;j++)
        {
                tot+=*val*pow(c,(j+1)-m);
                val++;
        }
        return tot;
}

double sumderiv(int n,double *val,double c)
{
        double tot=0;
        for (int j=0;j<n;j++)
        {
                tot+=*val*(j+1)*pow(c,j);
                val++;
        }
        return tot;
}


// Web parsing tools (for textboxes)


int length_of_lK(char *lK)
{
        int count=0;
        char *p=lK,*temp=new char [strlen(lK)];
        while(*p!='\0')
        {
                if(*p=='\n') count++;
                p++;
        }
        if(*(p-1)!='\n') count++;
        strcpy(temp,lK);
        if(strtok(temp,"\n")==NULL)
                return 0;
        else
                return count;
}


void get_log_K_values(char *lK,double *K,double *beta,int n)
{
        char *num;
        int count;
        for(count=0;count<n;count++)
        {
                if(count==0)
                        num=strtok(lK,"\n");
```

```
                else
                        num=strtok(NULL,"\n");
                sscanf(num,"%lf",K);
                *K=pow(10,*K);
                K++;
        }
        return;
}
```

A2.2. Reversible Anodic Stripping Voltammetry using a Square Wave Voltammetric Sweep (FORTRAN 77)

```
**************************************
** asv square wave using bi method **
** ------------------------------ **
**      expanding time grids        **
**************************************

      integer nj,ntau,debug,nf,nt
      parameter(nj=8000,ntau=600,nt=10000,debug=1,nf=4000)

      integer counter,ne,np,t,j,k,l,s
      real*8 a(-nf:nj),b(-nf:nj),c(-nf:nj),d(-nf:nj)
      real*8 alpha(-nf:nj),beta(-nf:nj),f(-nf:nj),u(-nf:nj)
      real*8 area,diff,layr,simt,ampl,r
      real*8 lam,dtauf,dy,hgl,estand,e,dtaub,ldtau
      real*8 red,ei,kap,theta,pi,ay,bee,tauinitb
      real*8 scan,oxbulk,nn,tauf,taustart,dtaudt(0:ntau)
      real*8 curr,freq,tp,de,ejump,dr,hhi,dimip,dl
      real*8 lamred,ti,rt(0:(ntau*2)+1)
      real*8 dele,tauend,tauendb
      character*15 file1,file2,file3,file4,file5,file6
      common /nag/ freq,ay


*     .. nag routine parameters ..

      real*8 x01aaf
      external  d02caf,fcn,x01aaf
      integer  n,ni
      parameter (n=1,ni=6)
      integer ifail
      real*8  tol,x,xend,y(n),w(21*n+23)

**  data storage i  **
      file1="c1.dat"
      file2="c2.dat"
      file3="curr600.dat"
      file4="redsi56.dat"
      file5="oxsi56.dat"
      file6="realtime.dat"


**    cell parameters (all cm, v or s)

      layr   = 200.e-4
      pi     = x01aaf(0.00e0)
      r      = 0.15
      area   = pi*(r**2)
      diff   = 1.e-5
      ei     = -1.0
      ef     = 0.0
      ampl   = 0.025
      ejump  = 2.*ampl
      red    = 1.e-3
      dr     = 2.e-5
      estand = -0.50
      nn     = 2.0
      freq   = 200.
c      hgl    = 0.1e-4
      hgl = (10**-0.03377)*(Dr/freq)**0.5
      tp     = 1./2./freq
      de     = 0.005
      scan   = freq*de
      simt   = (ef-ei)/scan
      np     = simt/tp
      ti     = tp/real(nt)


**    data storage ii **

      open(10,file=file1,status="unknown")
      open(11,file=file2,status="unknown")
      open(999,file=file4,status="unknown")
      open(998,file=file5,status="unknown")
      open(997,file=file6,status="unknown")


**    cartesian grid
```

```
      dy=layr/real(nj)
      dl=hgl/real(nf)

      ay=1.
      taustart=(1/(ti))**0.5
      tauend=(1/(tp**0.5))
      dtauf=(taustart-tauend)/real(ntau)
      do 555 t=0,ntau
         y(1)=taustart-t*dtauf
         rt(t)=1/(y(1)*y(1))
555   continue

**    backward temporal grid

      tauinitb=ay*(1/((ti)**.5)-1/((tp+ti)**.5))
      tauendb=ay*(1/(tp**0.5)-1/((2*tp)**.5))
      dtaub=(tauinitb-tauendb)/real(ntau)
      x=tauendb
      y(1)=2*tp
      rt((ntau*2)+1)=y(1)
      dtaudt(ntau)=ay*(-0.5*((tp)**-1.5)+.5*((2*tp)**-1.5))
      do 10 t=ntau-1,0,-1
         xend=x+dtaub
         tol =1.e-6
         ifail=0
         call d02caf(x,xend,n,y,tol,fcn,w,ifail)
         rt(t+(ntau+1))=y(1)
         dtaudt(t)=ay*(-0.5*((y(1)-tp)**-1.5)+.5*(y(1)**-1.5))
         x=xend
10    continue

**    output real time data file

      do 556 t=0,(ntau*2)+1
         write(997,700)rt(t)
         call flush(997)
556   continue

**    calculate oxbulk
*       oxbulk=red*exp((nn*96485.0)/(8.314*298.0)*(ei-estand))
      oxbulk=1.e-9

**    initial concentration of ox and red
      do 20 j=1,nj-1
         u(j)=1.
20    continue

      do 22 j=-nf+1,-1
         u(j)=red/oxbulk
22    continue

*****************
*** scan loop ***
*****************

      do 100 t=1,np

**    square-wave scan

      if(t.eq.1) e=ei+ampl
      if(t.ne.1) then
         e=e-((-1.)**real(t))*ejump
         if(mod(t,2).ne.0) e=e+de
      endif


**    calculate theta

       theta =(nn*96485.0/8.3143/298.0)*(e-estand)

*****************
** pulse loop  **
*****************


       do 150 l=0,ntau

          if(mod(t,2).ne.0) then
             tauf=taustart-dtauf*l

**    set the matrix elements

             lam = 2.*diff*ay*ay*dtauf/dy/dy/tauf/tauf/tauf
             lamred = 2.*dr*ay*ay*dtauf/dl/dl/tauf/tauf/tauf
          else
             lam = -diff*dtaub/dy/dy/dtaudt(l)
```

```
            lamred = -dr*dtaub/dl/dl/dtaudt(1)
          endif

          kap = diff*dl/dr/dy

**************************
**    define a,b,c     **
**************************

**      internal nodes

        do 25 j=0,nj-1
        a(j)  = -lam
        b(j)  = 1.0 + 2.0 * lam
        c(j)  = -lam
25      continue

        do 27 j=-nf+1,-1
         a(j)  = -lamred
         b(j)  = 1. + 2.*lamred
         c(j)  = -lamred
27      continue

** copy u -> d **

       do 60 j=-nf+1,nj-1
         d(j)=u(j)
60     continue

**    boundary conditions at bulk solution limit
        d(nj-1)=d(nj-1)-c(nj-1)
        c(nj-1)=0


**    calculate b at electrode substrate boundary

        b(-nf+1)=b(-nf+1)+a(-nf+1)
        a(-nf+1)=0

**    calculate matrix constants at film-solution surface

        b(0) = kap + exp(-theta)
        a(0) = -1.
        c(0) = -kap
        d(0) = 0.

**    at j=-1

        c(-1) = -lamred*exp(-theta)

**    alpha & beta

       do 30 j=-nf+1,nj-1
         alpha(j)=b(j) - a(j)*beta(j-1)
         beta(j)=c(j)/alpha(j)
30     continue


** thomas algorithm

       f(-nf+1) = d(-nf+1)/alpha(-nf+1)
       do 40 j=-nf+2,nj-1
         f(j)=(d(j) - a(j)*f(j-1))/alpha(j)
40     continue

       u(nj-1)=f(nj-1)
       do 50 j=nj-2,-nf+1,-1
         u(j)=f(j) - beta(j)*u(j+1)
50     continue

       if(t.eq.163) then
         do 53 j=-NF+1,-1
           if (mod(-j,40).eq.0) write(999,700)u(j)*oxbulk
53       CONTINUE
         DO 54 j=0,NJ-1
           if (mod(j,80).eq.0) write(998,700)u(j)
54       CONTINUE
       endif

       if(t.eq.164) then
         do 51 j=-NF+1,-1
           if (mod(-j,40).eq.0) write(999,700)u(j)*oxbulk
51       CONTINUE
         DO 52 j=0,NJ-1
           if (mod(j,80).eq.0) write(998,700)u(j)
52       CONTINUE
       endif
```

```
150    continue

* calculate current in ua *


         curr=((u(0)-u(1))/dy)*oxbulk*nn*area*96485.0*1.e6*diff
         if(mod(t,2).ne.0) then
            write(10,600)e,curr
            call flush(10)
         else
            write(11,600)e,curr
            call flush(11)
         endif


100    continue
* end of t loop *

500    format (1x,f12.5,2x,e12.5,2x,e12.5,2x,e12.5)
600    format (1x,e12.5,3x,e12.5)
700    format (1x,e12.5)

       close(10)
       close(11)


       ne=np/2.
       call onefile(ne,file1,file2,file3)


       end


** create one output file of e,i(1),i(2) and i(1)-i(2)

       subroutine onefile(ne,file1,file2,file3)

       integer ne
       real*8 curr1,curr2,e1,e2,eav
       character*15 file1,file2,file3
       open(15,file=file1,status="old")
       open(16,file=file2,status="old")
       open(17,file=file3,status="unknown")

** read in the stored data

** create new data file

      do 2000 e=1,ne
         read(15,600)e1,curr1
         read(16,600)e2,curr2

         eav=(e1+e2)/2.
         write(17,500)eav,curr1,curr2,curr1-curr2

2000  continue

      close(15)
      close(16)
      close(17)

500    format (1x,f12.5,2x,e12.5,2x,e12.5,2x,e12.5)
600    format (1x,e12.5,3x,e12.5)

      return

      end

      subroutine fcn(t,y,f)
      integer n
      parameter(n=1)
      real*8 t
      real*8 f(n),y(n)
      real*8 ay,tp,freq
      common /nag/ freq,ay

      tp=1./2./freq

      f(1)=1./(ay*(-0.5*((y(1)-tp)**-1.5)+.5*(y(1)**-1.5)))
      return
      end
```

A2.3. The Cavitation Counter (C/C++)

```
#include <math.h>
#include <string.h>
#include <limits.h>
#include <stdio.h>
#include <stdlib.h>

void exit_program(int);
void moment(double *,int,double *,double *,double *,double *);
void count_peaks(double *,double,int*,int);

void main(int argv,char *argc[])
        {

/* Setting up the variables */

        int count[8]={0,0,0,0,0,0,0,0},points,j,k;
        double *tdata,*idata,stddev,average,adev,sdev,var,skew,curt;
        double *tstart,*istart;
        char *filename,*output,*temp;
        FILE *fp1,*fp2,*pp1;


        if (argv < 2)
                {
                fprintf(stderr,"%s [GPES filename]\n",argc[0]);
                exit(1);
                }


 /* filenames and opening files */

 /* Memory allocations for filenames */

        filename = (char*) malloc (sizeof(char)*strlen(argc[1]));
        temp = (char*) malloc (sizeof(char)*strlen(filename));
        output = (char*) malloc (sizeof(char)*(strlen(argc[1])+4));

 /* build filenames */

        strcpy(filename,argc[1]);
        strcpy(temp,filename);

        strcpy(output,strtok(temp,"."));
        strcat(output,"res.dat");

 /* open files */

        fp1=fopen(filename,"r");
        fp2=fopen(output,"w");

 /* test files have opened properly */

        if(fp1 == NULL)
                exit_program(0);
        if(fp2 == NULL)
                exit_program(1);

 /* free memory */

        free(filename);
        free(output);
        free(temp);

 /* Calculate the length of the data file */



        pp1=popen(strcat("wc -l ",filename),"r");
        if(pp1 == NULL)
                fprintf(stderr,"error reading in transient data");
        fscanf(pp1,"%d",&points);
        pclose(pp1);

 /* Allocate memory for data arrays */

        tdata = (double*) malloc (sizeof(double)*points);
        idata = (double*) malloc (sizeof(double)*points);
        tstart=tdata;
        istart=idata;

 /* Read data file */
```

```
        fscanf(fp1,"\n,\n");

        for(k=0;k<points;k++)
                {
                fscanf(fp1,"  %lf %lf\n",tdata,idata);
                tdata++;
                idata++;
                }

        idata=istart;
        tdata=tstart;

        fclose(fp1);

/* call variance function (pre written numerical recipe) */

        moment(idata,points,&average,&adev,&sdev,&var);

/* count occurances of cavitation */

        count_peaks(idata,average,count,points);

/* output data file */

        fprintf(fp2,"n\tnstd\t ocurrances\n");
        printf("n\tdev from mean\t ocurrances\n");
        for(j=0;j<8;j++)
                {

        fprintf(fp2,"%d\t%lf\t%6.2lf\n",j+1,fabs((j+1)*0.1*average),(double)((double)co
unt[j]/(double)points)*100.);

        printf("%d\t%lf\t%6.2lf\n",j+1,fabs((j+1)*0.1*average),(double)((double)count[j
]/(double)points)*100.);
                }
        free(tdata);
        free(idata);
        return;
        }

void exit_program(int err)
        {
        switch (err)
                {
                case(0):printf("file error");exit(1);break;
                case(1):printf("file2");exit(1);
                }
        return;
        }

/* Code adapted from Numerical Recipes in C, 2nd Ed., pp 610-613*/

void moment(double *data,int n,double *ave,double *adev,double *sdev,double *svar)
        {
        int j;
        double s=0.0,p;
        if (n <= 1) fprintf(stderr,"n must be at least 2 in MOMENT");
        for (j=1;j<=n;j++) s += data[j];
        *ave=s/n;
        *adev=(*svar)=0.0;
        for (j=1;j<=n;j++)
                {
                *adev += fabs(s=data[j]-(*ave));
                *svar += (p=s*s);
                }
        *adev /= n;
        *svar /= (n-1);
        *sdev=sqrt(*svar);
        }

/* End of recipe */

void count_peaks(double *array,double average,int *count,int n)
        {
        int j=0,k;

        while(j<n)
                {
                for (k=0;k<8;k++)
                        if(fabs(*array-average)>fabs((k+1)*0.1*average)) count[k]++;
                array++;
                j++;
                }
        return;
        }
```

A2.4. The Cavitation Simulator (C/C++)

```
/* Cavitation Simulator

       Ver 1.4b Working with blocking of the electrode surface*/

#define MBIG 1000000000
#define MSEED 161803398
#define MZ 0
#define FAC (1.0/MBIG)
#define map(j,k,n) (k)*(n)+(x)-1
#define M 714025
#define IA 1366
#define IC 150889

#include <math.h>
#include <stdio.h>
#include <stdlib.h>
#include <string.h>
#include <limits.h>
#include <sys/types.h>  /* Unix specific */
#include <unistd.h>     /* header files  */

typedef struct occurance1 {                                          // Define a
Structure for storing and remembering cavitating points and currents
                          int occur,time_since;                      // Has
cavitation occured,time since last occurance
                          double ielem;                              // Element
current
                          }occurance;                                //
Structure name

typedef struct param1  {                                             //
Structure for storing system parameters
                          int n;                                     // No. of
electrons
                          double diff,conc,delta,area,tint;     // Diffusion
Coefficient,concentration,diffusion layer,element area,time ineterval
                          }param;                                    //
Structure name

float ran2(long*);
       /* Random Number Generator */
float ran3(long*);
       /* Random Number Generator */
void moment(double *,int,double *,double *,double *,double *);             /*
Statistcal routine for testing RNG */
float prob(float,int,float);                                               /*
Calculate the probabilty of an event */
void transient(occurance*,param*,int,float*,float*,int);                   /*
Calculates the Transient current */
void nernst(occurance*,param*,int);                                        /*
Calculates the Nernst diffusion layer current */
void read_transient_data(char*,float*,float*,int);                         /* Read in
transient data file */
float inter_trans(float*,float*,int,int,param*);                           /*
Interpolate transient data file for current */
void count_peaks(double *,double,int,int);                                 /*
Parts of cavitation */
void cav_counter(char*,float,float,int*);                                  /*
counter        */

void main (int argv, char *argc[])
{
       long idum;                                                    // RNG
intialisation value

       int i,nt,n,transdata,temp,count=0;                       // Counter,number of time
steps,number of grid elements,length of transient data file,temp for reading in data
       int t,x,y,counter=0,run=-1;                              // Time and electrode grid
counters,cavitation counter

       float p,events,time,el,*inorm,*tau;                      // Probability,events per
second(s-1),length of transient(s),electrode length(cm),Normalised transient
current,normalised time
       float temp1,mapx,mapy;                                   // Temporary for reading
in data,for mapping random point x,y
       double accum=0,bd;                                            // Current
accumulator,bubble diameter
       float k;                                                             // Array to
store RGNs and test at the end
       double average,adev,sdev,var;                            // Stats routine
variables: mean,average deviation,standard deviation,variance
```

```
        char *filename;

        occurance *curr;                                        // Structure for
storing and remembering cavitating points and currents
        param *system = (param*) malloc(sizeof(param));      // Structure for system
parameters

        FILE *pp1,*fp1;                                                 // A pipe
pointer,file pointer

/* Check for datafile name existance */

        if (argv == 1)
        {
                fprintf(stderr,"No data file name: %s [filename]\n",argc[0]);
                exit(1);
        }

/* Set initialisation value to the negative of the PID number of the program */

        idum = (long) -getpid();

/* Input the system parameters */

        printf("\n\nPlease input the system Parameters using cm and s as the primary
units\n");



        printf("\nNo. of Electrons ");
        scanf("%d",&temp);
        system->n=temp;
        printf("\nDiffusion Coefficient ");
        scanf("%e",&temp1);
        system->diff=temp1;
        printf("\nSolution Concentration ");
        scanf("%e",&temp1);
        system->conc=temp1;
        printf("\nDiffusion layer Thickness ");
        scanf("%e",&temp1);
        system->delta=temp1;
        printf("\nBubble diameter ");
        scanf("%lf",&bd);
        printf("\nElectrode length ");
        scanf("%f",&el);
        printf("\nTime of measurement ");
        scanf("%f",&time);
        printf("\nNumber of cavitation events per second ");
        scanf("%f",&events);
        printf("\nSample time (ms)   ");
        scanf("%f",&temp1);
        nt=time/temp1/1.e-3;


/* Start the two nested loops */

        /* check events not too large */

                while(2*events*time > nt)
                {

                        nt=2*events*time;
                        fprintf(stderr,"\nToo many events, incrementing time points to
%d",nt);
                        fprintf(stderr,"\nsample time is now %f
ms",1.e3*time/(float)nt);
                }

        /* Calulate the number of grid elements */
                n = (int)(el/bd);

        /* Calculate system parameters */

                system->area=bd*bd;                                     // set element area
                system->tint=time/((float) nt);                         // set time intervals

        /* Calculate the length of the data file */

                pp1=popen("wc -l transient.dat","r");
                if(pp1 == NULL)
                        fprintf(stderr,"error reading in transient data");
                fscanf(pp1,"%d",&transdata);
                pclose(pp1);

        /* Allocate memory */
```

```
        inorm=(float*) malloc(transdata*sizeof(float));
        tau=(float*) malloc(transdata*sizeof(float));


/* Read the transient data file */

        read_transient_data("transient.dat",tau,inorm,transdata);

/* Calculate the probability of a cavitational event occur for one time step */

        p=prob(events,nt*n*n,time);
        if (p == 1.0)
        {
                printf("Number of events too small. Exiting program!\n");
                exit(0);
        }

/* Allocate memory for current array */

        curr = (occurance*) malloc (n*n*sizeof(occurance));

        if (curr == NULL)
        {
                printf("memory allocation failed");
                exit(0);
        }

        for(y=0;y<n*n;y++)
                curr[y].occur=0;

/* open output file */

        filename = (char*) malloc(strlen(argc[1])*sizeof(char));

        strcpy(filename,argc[1]);

        fp1=fopen(filename,"w");

/* Time Loop */
        for(t=0;t<=nt;t++)
        {
        /* Y loop */
                for (y=0;y<n;y++)
                {
                /* X Loop */
                        for(x=0;x<n;x++)
                        {
                                k=ran3(&idum);
                            //printf("%f\t%f\n",k,p);
                            if (k<p || curr[map(x,y,n)].occur==1)
                                {
                                        if (k<p)
                                        {
                                                count++;
                                                curr[map(x,y,n)].time_since=0;
                                        }

transient(curr,system,map(x,y,n),tau,inorm,transdata);
                                }
                                else
                                        nernst(curr,system,map(x,y,n));
                                accum+=curr[map(x,y,n)].ielem;
                        }
                /* end of X Loop */
                }

        /* end of Y loop */
        fprintf(fp1,"%f\t%lf\n",t*(system->tint),accum*1.e6);
        fflush(fp1);
        accum=0.;
        }

/* End of time loop */

        fclose(fp1);

/* free up memory */

        free(inorm);
        free(tau);
        free(curr);

        printf("\n%d",count);

/* Run cavitation counter */
```

```
//              cav_counter(filename,x,y,&run);

        return;
}

/* RANDOM NUMBER GENERATOR */
/* Original code can be found in Numerical Recipes in C (2nd Ed.) pp283 */

float ran3(long *idum)
{
        static int inext,inextp;
        static long ma[56];
        static int iff=0;
        long mj,mk;
        int i,ii,k;

/* INITIALIZATION */

        if (*idum < 0 || iff == 0)
        {
                iff=1;
                mj=MSEED-(*idum < 0 ? -*idum : *idum);
                mj %= MBIG;
                ma[55]=mj;
                mk=1;
                for (i=1;i<=54;i++)
                {
                        ii=(21*i) % 55;
                        ma[ii]=mk;
                        mk=mj-mk;
                        if (mk < MZ) mk +=MBIG;
                        mj=ma[ii];
                }
                for (k=1;k<=4;k++)
                {
                        for (i=1;i<=55;i++)
                        {
                                ma[i] -=ma [1+(i+30) % 55];
                                if (ma[i] < MZ) ma[i] += MBIG;
                        }
                }
                inext=0;
                inextp=31;
                *idum=1;
        }

/* RANDOM NUMBER GENERATION */

        if (++inext == 56) inext=1;
        if (++inextp == 56) inextp=1;
        mj=ma[inext]-ma[inextp];
        if (mj < MZ) mj +=MBIG;
        ma[inext]=mj;
        return mj*FAC;
}

/* Code adapted from Numerical Recipes in C, 2nd Ed., pp 610-613*/

void moment(double *data,int n,double *ave,double *adev,double *sdev,double *svar)
{
        int j;
        double s=0.0,p;
        if (n <= 1) fprintf(stderr,"n must be at least 2 in MOMENT");
        for (j=1;j<=n;j++) s += data[j];
        *ave=s/n;
        *adev=(*svar)=0.0;
        for (j=1;j<=n;j++)
        {
                *adev += fabs(s=data[j]-(*ave));
                *svar += (p=s*s);
        }
        *adev /= n;
        *svar /= (n-1);
        *sdev=sqrt(*svar);
}

float prob(float events,int points,float time)
{
        float ne,ans,points2;

        ne = events*time;
        points2 = (float) points;
        ans = ne / points2;

        return (ne>0) ? ans : 1.0;
```

```
}

/* Calculate the transient current */

void transient(occurance *data,param *system,int element,float *x,float *y,int n)
{
        nernst(data,system,element);
        data[element].ielem*=inter_trans(x,y,n,data[element].time_since,system);

        if (data[element].time_since==0)
                data[element].ielem=0;

        data[element].time_since++;
        data[element].occur=1;

        return;
}

/* Calculate the Nersnt diffusion layer current */

void nernst(occurance *data,param *system,int element)
{

        data[element].ielem=system->n*system->area*system->diff*system-
>conc*96485/system->delta;
        return;
}

void read_transient_data(char *name,float *x,float *y,int length)
{
        int j;
        FILE *fp1;

        fp1=fopen(name,"r");
        if(fp1==NULL)
                fprintf(stderr,"Cannot open transient data file %s",name);

        for (j=0;j<length;j++)
        {
                fscanf(fp1,"%f\t%f\n",x,y);
                x++;
                y++;
        }
        fclose(fp1);
        return;
}
float inter_trans(float *x,float *y,int length,int point,param *system)
{
        float x1,ans;
        int counter=0;

        /* Convert point into tau */

        x1=system->diff*point*system->tint/pow(system->delta,2);

        /*find point data */

        do
        {
        counter++;
        }while(x1 >= *(x+counter-1) && counter != length);

        if(counter==1)
                return y[0];
        else
                ans=(y[counter-1]-y[counter])*(x1-x[counter-1])/(x[counter]-x[counter-
1])+y[counter];

        return (counter!=length) ? ans : 1.0;

}

/* Alternative random Number generator */
/* Original code can be found in Numerical Recipes in C (2nd Ed.) pp282 */

float ran2(long *idum)
{
        static long iy,ir[98];
        static int iff=0;
        int j;

        if (*idum < 0 || iff == 0) {
                iff=1;
                if ((*idum=(IC-(*idum)) % M) < 0) *idum = -(*idum);
                for (j=1;j<=97;j++) {
                        *idum=(IA*(*idum)+IC) % M;
                        ir[j]=(*idum);
```

```
                }
                *idum=(IA*(*idum)+IC) % M;
                iy=(*idum);
        }
        j=1 + 97.0*iy/M;
        if (j > 97 || j < 1) printf("this cannot happen");
        iy=ir[j];
        *idum=(IA*(*idum)+IC) % M;
        ir[j]=(*idum);
        return (float) iy/M;
}

#undef M
#undef IA
#undef IC

void cav_counter(char *filename,float x,float y,int *run)
        {

/* Setting up the variables */

        int count=0,points,j,k;
        double *tdata,*idata,stddev,average,adev,sdev,var,skew,curt;
        double *tstart,*istart;
        char *output,*temp,*pipe_com;
        FILE *fp1,*fp2,*pp1;



/* filenames and opening files */

/* Memory allocations for filenames */

        temp = (char*) malloc (sizeof(char)*strlen(filename));
        output = (char*) malloc (sizeof(char)*(strlen(filename)+4));
        pipe_com = (char*) malloc (sizeof(char)*(strlen("wc -l ")+strlen(filename)));

/* build filenames */

        if(run<0)
        {
                unlink(output);
                *run=1;
        }
        strcpy(temp,filename);

        strcpy(output,strtok(temp,"."));
        strcat(output,"res.dat");

/* open files */

        fp1=fopen(filename,"r");
        fp2=fopen(output,"a");

/* test files have opened properly */

        if(fp1 == NULL)
                exit(1);
        if(fp2 == NULL)
                exit(1);

/* free memory */

        free(filename);
        free(output);
        free(temp);

/* Calculate the length of the data file */

        strcpy(pipe_com,"wc -l ");
        strcat(pipe_com,filename);

        pp1=popen(strcat("wc -l ",filename),"r");
        if(pp1 == NULL)
                fprintf(stderr,"error reading in transient data");
        fscanf(pp1,"%d",&points);
        pclose(pp1);

/* Allocate memory for data arrays */

        tdata = (double*) malloc (sizeof(double)*points);
        idata = (double*) malloc (sizeof(double)*points);
        tstart=tdata;
        istart=idata;

/* Read data file */
```

```
        for(k=0;k<points;k++)
                {
                fscanf(fp1,"%lf\t %lf\n",tdata,idata);
                tdata++;
                idata++;
                }

        idata=istart;
        tdata=tstart;

        fclose(fp1);

/* call variance function (pre written numerical recipe) */

        moment(idata,points,&average,&adev,&sdev,&var);

/* count occurances of cavitation */

        count_peaks(idata,average,count,points);

/* free up memory from arrays */

        free(tdata);
        free(idata);

/* output data file */

        fprintf(fp2,"%f\t%f\t%6.2lf\n",x,y,(double)((double)count/(double)points)*100.)
;
        printf("%f\t%f\t%6.2lf\n",x,y,(double)((double)count/(double)points)*100.);
        return;
        }

void exit_program(int err)
        {
        switch (err)
                {
                case(0):printf("file error");exit(1);break;
                case(1):printf("file2");exit(1);
                }
        return;
        }

void count_peaks(double *array,double average,int count, int n)
        {
        int j=0;

        while(j<n)
                {
                if(fabs(*array-average)>fabs(0.1*average)) count++;
                array++;
                j++;
                }
        return;
        }
```

A2.5. Modelling of Square Wave Voltammetry for Reversible Systems.

This is not included as it is very similar to the listing in §A2.2 but with slightly different boundary conditions and the tanh grid incorporated (see chapter 8)

A2.6. Oil Droplet (Model 1) with Regular Solution Theory (FORTRAN 77)

```
**********************************
**  Ionic Liquids Simulations   **
**                              **
**       Hemisphere model       **
**                              **
**      Cyclic Voltammetry      **
**                              **
** Electrochemical Inert Centre **
**                              **
**    Regular solution Theory   **
**       (Approximation)        **
**********************************

      PARAMETER(NT=10000,NJ=5000)

      REAL*8 A(NJ),B(NJ),C(NJ)
      REAL*8 ALPHA(NJ),BETA(NJ),F(NJ),U(NJ),D(NJ)
      REAL*8 Area,Da,Rh,SIMt,inert_frac
      REAL*8 LAM,Dt,Dr,Estand,E,flux,ip
      REAL*8 Bbulk,Ei,Ev,theta,zed,iold
      REAL*8 scan,curr,x01aaf,PI,e1,e2
      INTEGER J,T,count,z

      EXTERNAL x01aaf


**    CELL PARAMETERS (all cm or s)


       PI = x01aaf(0.0)
       Da = 1.e-5
       Ei = -0.25
       Ev = 0.25
       Estand = 0.0
       Bbulk = 0.055
       inert_frac=0.001
       zed =0.
       scan = 0.1
c      rh=5.e-4


**    Data Storage

       open(10, file="surface.dat",status="unknown")
       open(20, file="current.dat",status="unknown")

**    Dim variable loop **

      DO 10002 z =-10,10

        zed=real(z)/10.

      DO 10001 count=-12,16
c      count=-3

      rh=real(count)/4.
        rh=10**rh
        rh=rh*8.314*298./96485.
      rh=rh*da/scan
        rh=rh**0.5

      Area  = 2.*PI*Rh*Rh

      ip=0.

      Simt = (dabs(Ei-Ev))/scan


**    Cartesian Grid

       Dr=(1.-inert_frac)*Rh/real(NJ)
       Dt=simt/real(NT)
      print*,Dr

**    Initial concentration of Ox and Red
       DO 20 j=1,NJ-1
          u(j)=0.
```

```
20      CONTINUE

        u(NJ)=1./(1+exp(zed)*exp((96485./8.3143/298)
     +        *(Ei-Estand)))

**************
*** T loop ***
**************

        DO 100 t=0,2*NT

         IF(t.le.NT) THEN
            E = Ei + scan*t*dt
         ELSE
            E = Ev - scan*(t-NT)*dt
         ENDIF

** Copy u -> d **

        DO 60 j=1,NJ-1
          d(j)=u(j)
60      CONTINUE

**     Calculate Theta

        theta =(96485.0/8.3143/298.0)*(E-Estand)

************************
**     Define a,b,c    **
************************

**     Internal nodes

         DO 25 j=1,NJ-1
           LAM = Da*Dt*(1-2*u(j)*zed*(1-u(j)))/Dr/Dr
           a(j)  = -LAM+LAM*Dr*(1./(j*Dr+inert_frac*Rh))
           b(j)  = 1. + 2.*LAM
           c(j)  = -LAM-LAM*Dr*(1./(j*Dr+inert_frac*Rh))
25       CONTINUE

**     Boundary Conditions at Film surface (j=NJ)

        c(NJ-1) = c(NJ-1)*(1/(1+exp(zed*(1-2*u(NJ)))*
     +            exp(-theta)))
        d(NJ-1) = d(NJ-1)-c(NJ-1)
        c(NJ-1) = 0

**     No flux boundaries

        b(1) = b(1)+a(1)
        a(1) = 0

**     Alpha & Beta

        DO 30 j=1,NJ-1
          alpha(j)=b(j) - a(j)*beta(j-1)
          beta(j)=c(j)/alpha(j)
30      CONTINUE

** Thomas Algorithm

        f(1) = d(1)/alpha(1)
        DO 40 j=2,NJ-1
          f(j)=(d(j) - a(j)*f(j-1))/alpha(j)
40      CONTINUE

        u(NJ-1)=f(NJ-1)
        DO 50 J=NJ-2,1,-1
          u(j)=f(j) - beta(j)*u(j+1)
50      CONTINUE

* Calculate current in uA *

        u(NJ)=1./(1+exp(zed*(1-2*u(NJ)))*exp(-theta))

        flux=(u(NJ)-u(NJ-1))*(1-2*u(NJ)*
     +       zed*(1-u(NJ)))/Dr

c        flux=(u(NJ)-u(NJ-1))/dr

        curr=96485.*Da*area*Bbulk*flux
        if (mod(t,10).eq.0) then
          write (20,700) E,curr
        endif

        if(dabs(curr).gt.dabs(iold)) then
          if(t.lt.NT) then
```

```
          ip=curr
          e1=e
         else
          e2=e
         endif
       endif


       iold=curr

c       if(t.eq.700) then
c         do 1001 j=1,NJ-1
c           write(10,700)j*dr+inert_frac*Rh,u(j)
c1001     continue
c       endif


c       if(u(NJ+1).gt.1.0) then
c         print*,u(nj-1),u(NJ+1)
c         stop
c       endif


100    CONTINUE
* End of t loop *

       print*,ip
       ip=ip/96485./Bbulk/Da/2./pi/rh

       e1=e1*96485/8.314/298.
       e2=e2*96485/8.314/298.



       write(10,500)real(z)/10.,real(count)/4.,ip,(e1-e2)
       call flush(10)

10001  CONTINUE

10002  CONTINUE

* end of dimless variable loop *
500    FORMAT (1X,F12.5,F12.5,2E14.5,2e14.5)
600    format (1X,2E12.5,2E12.5)
700    FORMAT (1X,2e12.5,2X,2E12.5)

       close(20)

       END
```

A2.7. Modelling of Square Voltammetry Accounting for Surface Morphology

This is omitted as it is similar to both the listings in §A2.2 and A2.6 with slightly different boundary conditions.

A3 Chronoamperometry Modelling at Uniformly Accessible Electrodes with a Finite Diffusion Layer

This work was developed by John Alden in collaboration with Richard Akkermans *et al.*[1] for the elucidation of mass transport for Laser Activated Voltammetry. It is based on a general approach proposed by Fisher and Compton.[2]

A3.1. Theory

The computation is concerned with the reversible single electron transfer:

$$A \pm e^- \rightleftharpoons B \qquad \text{(A3.1.)}$$

The diffusion equation to be solved is Fick's 2nd law for one dimensional diffusion given by

$$\frac{\partial[A]}{\partial t} = D\frac{\partial^2[A]}{\partial y^2} \qquad \text{(A3.2.)}$$

where y is the coordinate perpendicular to the electrode surface, $[A]$ is the concentration of the electroactive species A, D is the diffusion coefficient of A and t the time. For a finite diffusion layer thickness, δ, equation (A3.2.) is solved subject to the following boundary conditions.

$$t \le 0 \quad 0 \le y \le \delta \quad [A] = [A]_{bulk} \qquad \text{(A3.3.)}$$

$$t > 0 \quad y = 0 \quad [A] = 0 \qquad \text{(A3.4.)}$$

$$t > 0 \quad y = \delta \quad [A] = [A]_{bulk} \qquad \text{(A3.5.)}$$

---

[1] R.P. Akkermans, M.F. Suárez, S.L. Roberts, Q. Fulian, R.G. Compton, *Electroanal.*, 11 (1999) 1191

[2] A.C.Fisher, R.G. Compton, *J. Phys. Chem.*, 95 (1991) 7538

Where $[A]_{bulk}$ is the bulk concentration of the electroactive species A. The BI method (see §3.3)[2] was employed to solve this equation. The results give the values of $[A]$ as a function of y and t. The currents associated with each time step were evaluated from

$$I = nFAD\frac{\partial[A]}{\partial y}\Bigg)_{y=0} \qquad \text{(A3.6.)}$$

The results are shown in Figure A3.1 in the form of dimensionless current, $\tilde{I}$,against dimensionless time, τ. These are given by

$$\tilde{I} = \frac{I(t)}{I(t \to \infty)} \qquad \text{(A3.7.)}$$

$$\tau = \frac{Dt}{\delta^2} \qquad \text{(A3.8.)}$$

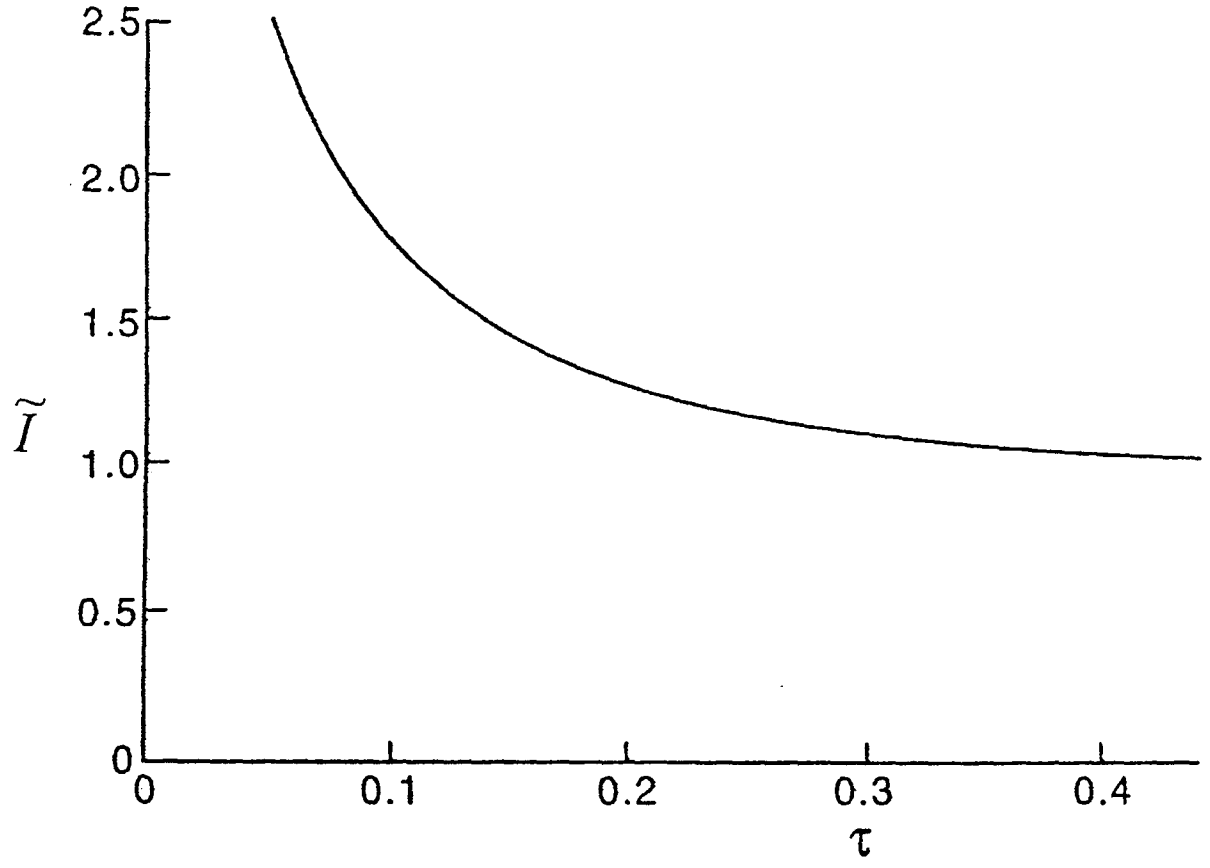


Figure A3.1 Plot of normalised current, $\tilde{I}$, against normalised time for a Backwards Implicit, fixed diffusion layer, one dimensional diffusion model simulation.

A4.1. Fick's 1st Law of Diffusion

For this derivation a simplified model is employed. Consider a volume of electrolyte solution where the concentration of the diffusing ionic species is constant in the *yz*-plane, but varies in the *x*-plane (Figure A4.1). The parallelepiped of solution considered is then evenly divided into two compartments by an imaginary 'transit' plane of area *A*. The diffusion occurs normal to this plane. The outer planes L and R are situated at a distance of $\sqrt{\langle x^2 \rangle}$ (the mean distance travelled by an ion in a time interval *t*) from the transit plane ensuring that, provided the ions are moving in the specified direction, all the ions in each compartment cross the 'transit' plane. As the ions are 'random walking', statistically only half the ions will be moving towards the plane T at any given time. Thus, in a time interval, *t*,

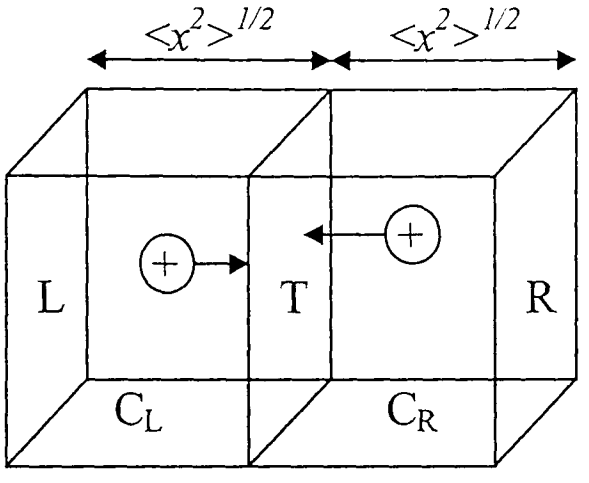


Figure A4.1 Parallelepiped of solution used to model random walk processes

$$\text{Number of ions making the L} \rightarrow \text{T crossing is } \frac{1}{2}\left(\sqrt{\langle x^2 \rangle} A C_L\right)$$

$$\text{Number of ions making the R} \rightarrow \text{T crossing is } \frac{1}{2}\left(\sqrt{\langle x^2 \rangle} A C_R\right)$$

where C_L and C_R are the concentrations of ions in the respective compartments. The total diffusive flux, *J* (mol m^{-2} s^{-1}), of ions across the 'transit' plane in the L → R direction is

$$J = \frac{1}{2}\frac{\sqrt{\langle x^2 \rangle}}{t}\left[C_L - C_R\right]$$

The concentration gradient (*dc/dx*) in the L → R direction can then be written

$$\frac{dc}{dx} = \frac{\left[C_R - C_L\right]}{\sqrt{\langle x^2 \rangle}} \equiv -\frac{\left[C_L - C_R\right]}{\sqrt{\langle x^2 \rangle}}$$

Combination of the two expressions gives the following expression for the flux:

$$J = -\frac{1}{2}\frac{\langle x^2 \rangle}{t}\frac{dc}{dx}$$

This is analogous to Fick's 1st law where $D = \frac{\langle x^2 \rangle}{2t}$. Thus $\langle x^2 \rangle = 2Dt$ and the parameters x and D are shown to be related.

A4.2. Fick's 2nd Law of Diffusion

As for the first law only planar diffusion is considered (Figure A1). Considering a small region of volume Adx and the concentration changes which occur within this region of volume in the time interval t and t + dt,

No. of moles in the region at time t+dt	-	No. of moles in the region at time t	=	No. of moles entering across plane at x	-	No. of moles leaving across plane at x+dx

or

$$c(x,t+dt)Adx - c(x,t)Adx = J(x,t)Adt - J(x+dx,t)Adt$$

where $J(x,t)$ is the flux in the x-direction (mol cm^{-2} s^{-1}) such that

$$\left[c(x,t+dt) - c(x,t)\right]dx = \left[J(x,t) - J(x+dx,t)\right]dt$$

This can be rearranged to give

$$\frac{\partial}{\partial t}c(x,t) + \frac{\partial}{\partial x}J(x,t) = 0$$

If $J(x,t)$ is substituted for Fick's 1st Law then Fick's 2nd law is obtained

$$\frac{\partial}{\partial t}c(x,t) = D\frac{\partial^2}{\partial x^2}c(x,t)$$

From using a simple statistical model the diffusion of molecules can be mathematically expressed in the form of Fick's 1st and 2nd laws.